GFZ

Helmholtz Centre
POTSDAM

HELMHOLTZ CENTRE POTSDAM
GFZ GERMAN RESEARCH CENTRE
FOR GEOSCIENCES

Jungang Wang

Integrated processing of GNSS and VLBI on the observation level

Scientific Technical Report STR21/07

www.gfz-potsdam.de

Recommended citation

Wang, J. (2021): Integrated processing of GNSS and VLBI on the observation level,
(Scientific Technical Report STR; 21/07),
Potsdam: GFZ German Research Centre for Geosciences.
https://doi.org/10.48440/GFZ.b103-21079

Originally published as

Wang, J. (2021): Integrated processing of GNSS and VLBI on the observation level,
Berlin: Technische Universität.
https://doi.org/10.14279/depositonce-12513

Imprint

Helmholtz Centre Potsdam
GFZ German Research Centre
for Geosciences

Telegrafenberg
D-14473 Potsdam

Published in Potsdam, Germany
December 2021

DOI: https://doi.org/10.48440/GFZ.b103-21079
URN: urn:nbn:de:kobv:b103-21079

This work is published in the GFZ series
Scientific Technical Report (STR)
and electronically available at GFZ website
www.gfz-potsdam.de

Integrated Processing of GNSS and VLBI on the Observation Level

vorgelegt von
M. Sc.
Jungang Wang
ORCID: 0000-0002-7060-5342

an der Fakultät VI – Planen, Bauen, Umwelt
der Technischen Universität Berlin
zur Erlangung des akademischen Grades

Doktor der Ingenieurwissenschaften
- Dr.-Ing. -

genehmigte Dissertation

Promotionsausschuss:

Vorsitzender:	Prof. Dr. Jürgen Oberst
Gutachter:	Prof. Dr. Dr. hc Harald Schuh
Gutachter:	Prof. Dr. Thomas Hobiger
Gutachter:	Prof. Dr. Maorong Ge

Tag der wissenschaftlichen Aussprache: 13. April 2021

Berlin 2021

Acknowledgments

This is the place to honor the people who support and help me through my study, without them this work would not be possible.

First of all, I would like to express my deepest appreciation to my supervisors Harald Schuh and Maorong Ge, for giving me the opportunity to stay at GFZ Potsdam, for allowing me to freely explore my scientific investigations, for supporting me to work on the multi-technique integrated processing, for providing all the facilities to conduct my research, for guiding me throughout my study with their deep knowledge in space geodesy, and for always encouraging me to pursue the better. I am also grateful to Thomas Hobiger for agreeing to co-supervise my study. I am honored to have him reviewing my thesis, as he is one of the very first researchers who has successfully implemented the multi-technique integrated processing.

I would like to thank Robert Heinkelmann, Kyriakos Balidakis, and Susanne Glaser, for their support and valuable advices. Further thanks also go to Maximillian Semmling, Florian Zus, James M. Anderson, Georg Beyerle, and the whole VLBI group at GFZ for sharing the knowledge and experiences.

I owe special thanks to Zhiguo Deng, who always provides endless help and guidance with great patience. I would like to acknowledge my former roommates, Shengfeng Gu, Wenju Fu, Haibo Ge, Xinggang Zhang, my colleges, Pan Li, Xinyuan Jiang, Xinghan Chen, Wen Huang, Xuewen Gong, Zhilu Wu, Hanbing Peng, Xiao Chang, Long Jiang Tang, Kai Zheng, for all the fruitful discussions and enlightening ideas that I gained from them. I enjoyed a wonderful time with the Real-Time GNSS group at GFZ.

The technical staff at GFZ provides critical support to this work, and their great efforts enable the efficient data processing capability. I thus deeply thank them.

Last but not the least, I would like to thank my family for their unconditional love and support. I give heartfelt thanks to my girlfriend Zhimeng Ye for her understanding, support, patience, and love.

My stay at GFZ is financially supported by the China Scholarship Council and the ADVANTAGE project.

Jungang Wang

September, 2021

Potsdam

Abstract

The Global Geodetic Reference Frame (GGRF) plays a fundamental role in geodesy and related Positioning, Navigation, and Timing applications, and allows to quantify the Earth's change in space and time. The ITRF and ICRF are the two most important components to realize GGRF, while the determination of these two reference frames relies on the combination of several space geodetic techniques, mainly, VLBI, SLR, GNSS, and DORIS. The combination is currently done on either the parameter level, or the normal equation level. However, the combination on the observation level, or the so-called integrated processing of multi-technique on the observation level, provides the results of best consistency, robustness, and accuracy.

This thesis focuses on the investigation of the integrated processing of GNSS and VLBI on the observation level. The benefits of integrated processing are demonstrated in terms of TRF, CRF, and EOP, while the impact of global ties (EOP), tropospheric ties, and local ties are underlined. Several issues in integrated processing are addressed, including the systematic bias in ties (for instance, LOD and tropospheric ties), the relative weighting. An automatic reweighting strategy based on the normalized residuals is developed, which can properly handle the uncertainty of the ties without losing too much constraint.

A software with state-of-the-art modules is the prerequisite to perform integrated processing. Based on the GNSS data processing software: Positioning And Navigation Data Analyst (PANDA), the VLBI and SLR modules are implemented in the common least-squares estimator. Therefore, the best consistency can be guaranteed. The software capability is demonstrated with the single-technique solutions. The station coordinate precision is at millimeter level for both GNSS and VLBI, while the EOP estimates are comparable to other Analysis Centers and the IERS products. It is also demonstrated that the SLR station coordinate precision is improved by 20% to 30% with additional GLONASS and GRACE satellites to contributing to the LAGEOS and ETALON constellation.

Focusing on the tropospheric ties in GNSS and VLBI integrated processing, its contribution is demonstrated for the first time comprehensively. Applying tropospheric ties improves the VLBI station coordinate precision by 12% on the horizontal components and up to 30% on the vertical component. The network scale repeatability is reduced by up to 33%. The EOP estimates are also improved significantly, for instance, 10% to 30% for polar motion, and up to 10% for other components. Furthermore, applying the gradient ties in the VLBI intensive sessions reduces the systematic bias in UT1-UTC estimates.

The consistent TRF, CRF, and EOP are achieved in the integrated VLBI and GNSS solution. Applying the global ties, tropospheric ties, and local ties stables the reference frame. The ERP estimates in the integrated solution are dominated by the GNSS technique, and the VLBI technique introduces additional 10% improvement on the y-pole component in terms of the day-boundary-discontinuity. The UT1-UTC and celestial pole offsets are also slightly improved

in the integrated solution. It is also demonstrated that applying the LTs inappropriately distorts the network and introduces systematic biases to the ERP estimates, addressing the necessity of updating the local surveys. Moreover, the coordinates of AGN are also enhanced by up to 20% in the integrated solutions, especially the southern ones.

This study reveals the importance of integrated processing of multi-technique on the observation level, as the best consistency can be achieved, and the applied ties improve the solutions significantly. It is strongly recommended that for the future realization of celestial and terrestrial reference frames, the concept of integrated processing on the observation level should be implemented, and all the possible ties should be applied, including the global ties (EOP), local ties, space ties, and tropospheric ties. Such kind of integrated solution of all the four techniques can provide robust estimates of the reference frames and EOP, with the advantage of each technique exploited to its full extend.

Kurzfassung

Der Globale Geodätische Referenzrahmen (*Global Geodetic Reference Frame, GGRF*) spielt eine fundamentale Rolle in der Geodäsie und den damit verbundenen Positionierungs-, Navigations- und Zeitmessungsanwendungen (*Positioning, Navigation, and Timing, PNT*) und ermöglicht die Quantifizierung der Veränderung der Erde in Raum und Zeit. Der ITRF und der ICRF sind die beiden wichtigsten Komponenten zur Realisierung des GGRF, wobei die Bestimmung dieser beiden Referenzrahmen auf der Kombination verschiedener raumgeodätischer Techniken beruht, hauptsächlich VLBI, SLR, GNSS und DORIS. Die Kombination wird derzeit entweder auf der Parameterebene oder auf der Normalgleichungsebene durchgeführt. Die Kombination auf der Beobachtungsebene oder die sogenannte integrierte Daten-Verarbeitung von Multi-Techniken auf der Beobachtungsebene, bietet jedoch eine Lösung mit der besten Konsistenz, Robustheit und Genauigkeit.

Diese Arbeit konzentriert sich auf die Untersuchung der integrierten Daten-Verarbeitung von GNSS und VLBI auf der Beobachtungsebene. Die Vorteile der integrierten Lösung werden in Bezug auf TRF, CRF, und EOP aufgezeigt, während die Auswirkungen von „*Global Ties (EOP), Tropospheric Ties, and Local Ties*“ hervorgehoben werden. Einige Punkte der integrierten Verarbeitung werden in dieser Arbeit untersucht, einschließlich der systematischen Abweichungen von „*Ties*“ (z.B. *LOD und Tropospheric Ties*), der relativen Gewichtung usw. Anhand der normalisierten Residuen wird eine automatische Umgewichtungsstrategie entwickelt, mit der die Unsicherheit der „Ties“ angemessen behandelt werden kann, ohne dass zu viel Einschränkung dabei verloren geht.

Eine Software mit modernsten Modulen ist die Voraussetzung für die integrierte Daten Verarbeitung. Basierend auf der GNSS-Datenverarbeitungssoftware Paket: *Positioning And Navigation Data Analyst (PANDA)* werden die Module VLBI und SLR in demselben Least-Squares-Estimator wie GNSS implementiert, damit kann man die beste Konsistenz in der Datenverarbeitung erreichen. In dieser Arbeit wird die Leistungsfähigkeit der Software mit den Ein-Technik-Lösungen demonstriert. Die Genauigkeit der Stationskoordinaten liegt sowohl für GNSS als auch für VLBI im Millimeterbereich, und die geschätzten EOP-Parameter sind auch mit der anderer Analysezentren und den IERS-Produkten vergleichbar. Es wird auch gezeigt, dass die Koordinatengenauigkeit der SLR-Station um 20-30% verbessert wird, wenn zusätzliche GLONASS- und GRACE-Satelliten zur LAGEOS und ETALON-Konstellation beitragen.

Mit dem Schwerpunkt auf den „*Tropospheric Ties*“ in der integrierten GNSS- und VLBI- Daten Verarbeitung wird ihr Beitrag zum ersten Mal umfassend dargestellt. Die Anwendung der „*Tropospheric Ties*“ verbessert die Genauigkeit der VLBI-Koordinaten um 12% bei der horizontalen Komponente und bis zu 30% bei der vertikalen Komponente. Die Genauigkeit im Netzwerkmaßstab wird um bis zu 33% verbessert. Auch die EOP-Bestimmungen werden deutlich verbessert, z.B. um 10-30% bei polaren Bewegungen und bis zu 10% bei anderen

Komponenten. Darüber hinaus reduziert die Einführung der „*Gradient Ties*“ in der VLBI-Intensivsession die systematische Abweichung in den dUT1-Bestimmungen.

Die konsistente TRF, CRF, und EOP werden bei der integrierten VLBI- und GNSS-Lösung erreicht. Die Anwendung der „*Global Ties, Tropospheric Ties and Local Ties*“ stabilisiert die Bestimmungen des Referenzrahmens. Die ERP-Bestimmungen in der integrierten Lösung werden von der GNSS-Technik dominiert, und die VLBI-Technik bringt eine zusätzliche Verbesserung um 10% auf die Tagesgrenzen-Diskontinuität (*day-boundary-discontinuity, DBD*) für die y-Pol-Komponente. Die dUT1- und CPO werden in der integrierten Lösung ebenfalls leicht verbessert. Es wird auch gezeigt, dass eine ungeeignete Anwendung der LTs das Netzwerk verzerrt und systematische Abweichungen in die ERP-Bestimmungen einführt, wodurch die Notwendigkeit einer Aktualisierung der lokalen Tie Messungen deutlich wird. Darüber hinaus werden die Koordinaten der AGN in den integrierten Lösungen um bis zu 20% verbessert, insbesondere im Süden.

Diese Arbeit zeigt die Bedeutung der integrierten Daten Verarbeitung von Multi-Technik auf der Beobachtungsebene, da die beste Konsistenz erreicht werden kann und die angewandten „*Ties*“ die Lösungen erheblich verbessern. Es wird nachdrücklich empfohlen, für die zukünftige Realisierung von himmelsfesten und erdfesten Referenzrahmen das Konzept der integrierten Verarbeitung auf Beobachtungsebene durchzuführen und alle möglichen „Ties“ anzuwenden, einschließlich der „*Global Ties (EOP), Local Ties, Space Ties, and Tropospheric Ties*“. Eine solche integrierte Lösung aller vier Techniken kann die robusten Bestimmungen der Referenzrahmen und der EOP liefern, wobei die Vorteile jeder Technik voll ausgeschöpft werden.

List of Figures

List of Tables

List of Abbreviations

AAM	Atmospheric Angular Momentum
AC	Analysis Center, for instance, COD, GFZ, BKG
AGN	Active Galactic Nuclei
APL	Atmospheric Pressure Loading
ARP	Antenna Reference Point
ASCII	American Standard Code for Information Interchange
BCRS	Barycentric Celestial Reference System
BDS	The BeiDou Navigation Satellite System
BKG	Bundesamt für Kartographie und Geodäsie, Federal Agency for Cartography and Geodesy
BLR	Baseline Length Repeatability
CC	Combination Center, for instance, DGFI-TUM, IGN, JPL
CODE	Center for Orbit Determination in Europe
CoM	Center of Mass
CONT	VLBI CONTinuous Campaign
CPO	Celestial Pole Offset
CRD	Consolidated Laser Ranging Data Format
CRF	Celestial Reference Frame
CRS	Celestial Reference System
DBC	VLBI DataBase Code
DBD	Day-boundary-discontinuity
DGFI-TUM	Deutsches Geodätisches Forschungsinstitut der Technischen Universität München
DOGS	DGFI Orbit and Geodetic parameter estimation Software
DORIS	Doppler Orbitography and Radiopositioning Integrated by Satellite
DOY	Day of Year
DRF	Dynamic Reference Frame, or satellite reference frame
DTRF	The realization of the ITRS of DGFI-TUM
dUT1	UT1-UTC, the time difference between UT1 and UTC
EOP	Earth Orientation Parameters, including polar motion, UT1-UTC, CPO, and their time derivatives
EPOS	Earth Parameter and Orbit System
ERP	Earth Rotation Parameters, including polar motion and LOD
ESOC	European Space Operations Centre
FDMA	Frequency Division Multiple Access
GCRS	Geocentric Celestial Reference System
G_E	East gradient of the tropospheric delay
GFZ	German Research Centre for Geosciences (Deutsches GeoForschungsZentrum)
GGOS	The Global Geodetic Observing System
GGOS-D	Integration of Space Geodetic Techniques as the Basis for a Global Geodetic-Geophysical Observing System

GGRF	Global Geodetic Reference Frame
GIM	Global Ionospheric Map
GINS	Géodésie par Intégrations Numériques Simultanées
GLONASS	Globalnaya navigatsionnaya sputnikovaya sistema
GMF	Global Mapping Function
G_N	North gradient of tropospheric delay
GNSS	Global Navigation Satellite Systems
GPS	Global Positioning System
GPST	GPS Time
GRACE	Gravity Recovery and Climate Experiment
GRASP	The Geodetic Reference Antenna in Space Mission
GRGS	Groupe de Recherches de Géodésie Spatiale
GSFC	Goddard Space Flight Center
IAU	International Astronomical Union
ICRS	International Celestial Reference System
ICRS	International Celestial Reference Frame
IDS	International Doris Service
IERS	International Earth Rotation and Reference Systems Service
IFB	Inter Frequency Bias
iGMAS	The International GNSS Monitoring & Assessment Service
IG2	The IGS second reprocessing campaign
IGS	International GNSS Service
INT	VLBI INTensive sessions
IRNSS	The Indian Regional Navigation Satellite System
ISB	Inter System Bias
ISDC	Information System and Data Center for geoscientific data, at GFZ
IVS	International VLBI Service
ILRS	International Laser Ranging Service
ITRF	International Terrestrial Reference Frame
ITRS	International Terrestrial Reference System
JASON	Joint Altimetry Satellite Oceanography Network
JPL	NASA Jet Propulsion Laboratory
JTRF	The JPL Kalman filter and smoother realization of the International Terrestrial Reference System
LAGEOS	Laser Geodynamics Satellite or Laser Geometric Environmental Observation Survey
LEO	Low Earth Orbiter
LLR	Laser Lasing Ranging
LOD	Length of Day, the negative value of the first time derivative of UT1-UTC
LRA	Laser Reflector Array
LT	Local Ties
MIT	Massachusetts Institute of Technology
NASA	National Aeronautics and Space Administration

NavIC	Navigation with Indian Constellation
NAPEOS	Navigation Package for Earth Orbiting Satellites
NEQ	Normal Equation
NNR	No-Net-Rotation
NNS	No-Net-Scale
NNT	No-Net-Translation
NWM	Numerical Weather Model
OMC	Observation Minus Calculation
OPA	Paris Observatory (l'Observatoire de Paris)
PANDA	Positioning And Navigation Data Analyst
PCO	Phase Center Offset
PCV	Phase Center Variation
PM	Polar Motion
PMF	Potsdam Mapping Function
PNT	Positioning, Navigation, and Timing
POD	Precise Orbit Determination
PORT	Potsdam Open-source Radio interferometry Tool
PPP	Precise Point Positioning
PRN	Pseudo-Random Noise
PWC	Piece Wise Constant
PWL	Piece Wise Linear
QZSS	The Quasi-Zenith Satellite System
RINEX	Receiver Independent Exchange Format
RWK	Random Walk Process
SINEX	Solution Independent Exchange Format
SLR	Satellite Laser Ranging
SRP	Solar Radiation Pressure
SSB	Solar System Barycenter
STD	Standard Deviation
TC	Technique Center, for instance, IGS, IVS
TEC	Total Electron Content
TRF	Terrestial Reference Frame
TRS	Terrestial Reference System
UHF	Ultra High Frequency, 0.3-3 GHz
VCE	Variance Component Estimation
VGOS	VLBI Global Observing System
VieVS	The Vienna VLBI and Satellite Software
VMF	Vienna Mapping Function
VLBI	Very Long Baseline Interferometry
WBLR	Weighted Baseline Length Repeatability
WMEAN	Weighted Mean
WRMS	Weighted Root Mean Squares

WVR	Water Vapor Radiometer
ZHD	Zenith Hydrostatic Delay
ZWD	Zenith Wet Delay

List of Contents

1 Introduction

1.1 Overview

The science of geodesy deals with the Earth's size, shape, gravity field, orientation, including the temporal variation. The three pillars of geodesy, that is, the Earth's shape (geokinematic), gravity field, and rotation, provide the conceptual and observational basis for the reference frames. On the other hand, the reference frames with high accuracy and temporal stability are of primary importance for the three pillars. The reference frames are necessary for the homogeneous and reliable determination and interpretation of the changes in Earth system temporally and spatially, for sea-level rise and climate change, for natural disaster management. As illustrated in Figure 1.1, the space geodetic techniques and dedicated satellite missions play the major role in the three pillars, and the space geodetic observations together determine the reference frames.

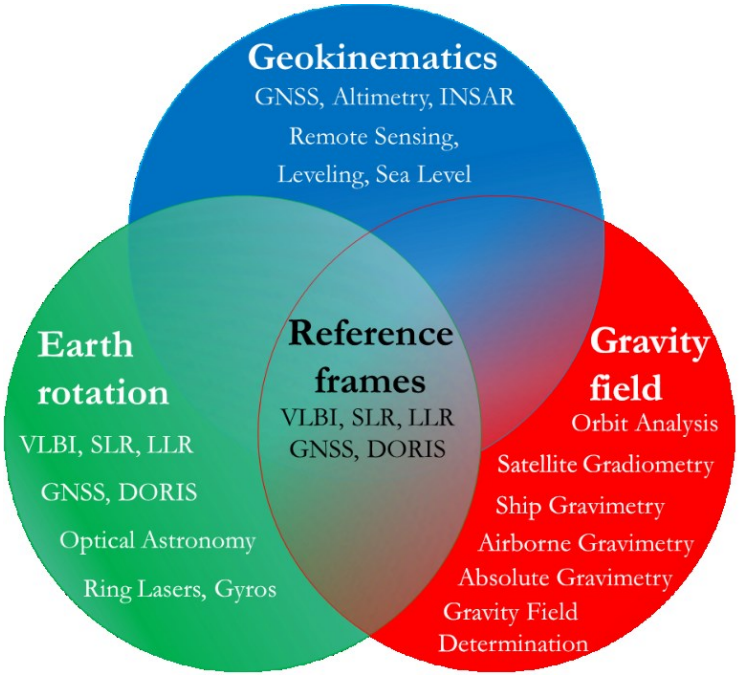

Figure 1.1 The three pillars of geodesy: Earth's shape (geokinematics or geometry), rotation, and gravity field. Modified figure from Rothacher (2003) and GGOS website[1].

The generic term of Global Geodetic Reference Frame[2] (GGRF) describes the framework for the precise determination and description of locations on the Earth, and the quantification of the Earth's change in space and time. The resolution on Global Geodetic Reference Frame for Sustainable Develop was adopted by the United Nations General Assembly in 2015. The

[1] http://www.iag-ggos.org/about_geodesy/the_three_pillars.php
[2] https://www.unggrf.org/

GGRF is realized through the ITRF, ICRF, and physical height system. The reference frames are determined by the four space geodetic techniques, namely, Global Navigation Satellite Systems (GNSS), Very Long Baseline Interferometry (VLBI), Satellite Laser Ranging (SLR), and Doppler Orbitography and Radiopositioning Integrated by Satellite (DORIS), as depicted in Figure 1.2.

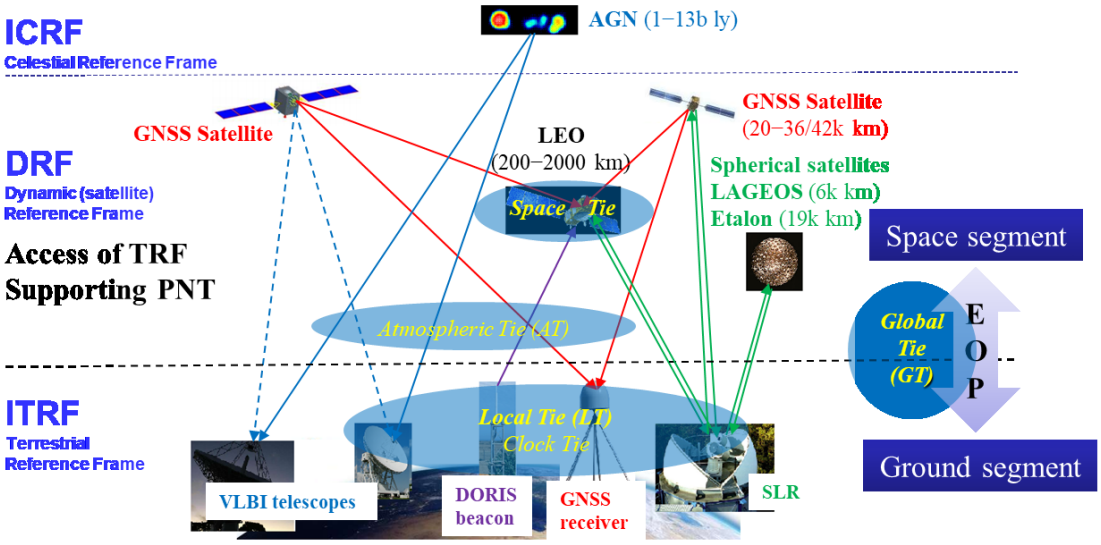

Figure 1.2 Illustration of space geodetic techniques: Global Navigation Satellite Systems (GNSS), Very Long Baseline Interferometry (VLBI), Satellite Laser Lasing (SLR), and Doppler Orbitography and Radiopositioning Integrated by Satellite (DORIS).

In GNSS, the L-band microwave signals from GNSS satellites are observed by ground and space-borne receivers, and the distance between the transmitter and receiver is measured; in VLBI, the ground radio telescopes observe the X/S-band signals from the AGN far away from the Earth and use the time delay between two radio telescopes; in SLR, the ground station emits optical signals to satellite and receives the reflected one; as for DORIS, the Doppler effect of the signals from ground beacons received by the payload on-board Low Earth Orbiter (LEO) is utilized. All these techniques consist of a space segment, that is, satellites or AGN, and a ground segment, that is, the ground stations. The space segment is described in the celestial reference system, and the ground segment is described in the terrestrial reference system, while the Earth Orientation Parameters are used to establish the transformation between these two systems. The celestial reference system is realized by the celestial reference frame representing by a set of AGN coordinates and the terrestrial reference system is realized by the terrestrial reference frame representing by a set of ground geodetic stations. The satellite orbits, which can be referred to as the dynamic (or satellite) reference frame, play a fundamental role in the positioning, navigation, and timing (PNT) service, and provide users the access to terrestrial reference frame.

The four techniques have different sensitivities to different parameters which define the terrestrial reference frame including orientation, origin, and scale, and none of the techniques can determine the reference frames solely. The VLBI technique determines the CRF and EOP but is incapable of monitoring the geocenter motion, meanwhile the satellite techniques

cannot determine the UT1-UTC (or dUT1) and celestial pole offsets. Taking the current ITRF determination to illustrate the terrestrial reference frame, the origin is realized by SLR, and the scale is averaged over VLBI and SLR. The GNSS and DORIS techniques provide globally distributed stations with continuous observations, which densifies the network in both space and time and provides a more precise description of the Earth surface movement. The orientation strongly relies on the GNSS network as it is realized by the no-net-rotation (NNR) condition which mainly involves the GNSS stations.

Moreover, it is expected to have more robust and precise estimates with the multi-technique combined solution than the single-technique solution. Specifically, the VLBI and SLR techniques provide discrete observations but in the sense of absolute measurements, while GNSS and DORIS provide continuous observations but in the sense of relative measurement. As a consequence, the continuous observations provide better estimates of the time-varying parameters, for instance, the tropospheric delays. For instance, a precision of 2 to 4 mm for the zenith total delay (ZTD) can be easily achieved by the GNSS technique, which can be integrated to other microwave-based techniques. Another example is the UT1-UTC component of EOP, which can only be determined by VLBI. However, the discrete observing program of VLBI[3] does not provide continuous UT1-UTC estimates, while the GNSS technique can provide the rate of UT1-UTC with good short-term precision. Integrating these two techniques will produce continuous reliable dUT1 estimates.

To combine different techniques, it is necessary to have common parameters or external observations to link the parameters from different techniques, that is, the so-called tie. The EOP set works as the very first global tie, as physically the same EOP set is applied for all the techniques. The coordinate difference vector between near-by stations, that is, within a few hundred meters, can be measured by local surveys. These external observations work as the local ties (LTs) to connect different techniques. The third one is the space tie, which is the coordinate difference between instruments of different techniques on-board the same satellite. For one satellite equipped with several instruments, for instance, one GNSS satellite with GNSS transmitter and Laser Reflector Array (LRA) can be used to connect GNSS and SLR. Last but not the least, for the microwave-based techniques, that is, GNSS, VLBI, and DORIS, the same troposphere is shared for the co-located stations, meaning that the tropospheric ties can be applied by nature.

Depending on the input data sets, the combination can be done on three different levels: on the solution (or parameter) level, on the normal equation (NEQ) level, and on the observation level. As the details of these three methods will be addressed in the following text (section 2.3.1), it is worth to mention the pros and cons briefly here: (1) it is more feasible to combine on the parameter level or the normal equation level as different software packages can be used; (2) it is more rigorous to combine on the observation level as the same modeling and parameterization implemented for different techniques provide the best consistency; (3) a combination on the normal equation level can be theoretically equivalent to that on the

[3] This may be fixed in future VLBI observing program with continuous daily observations, see the IVS Infrastructure Development Plan 2030

observation level with a lot of special efforts for the pursue of consistency, which is almost impractical in reality.

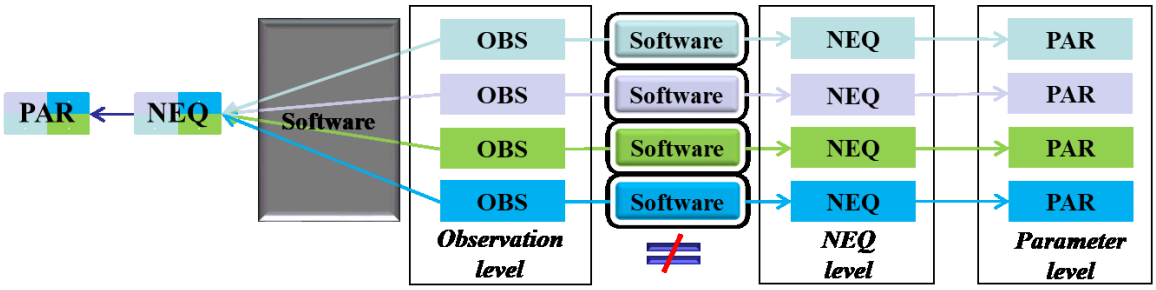

Figure 1.3 Illustration of the three levels for multi-technique combination. Different colors represent different techniques.

1.2 Motivation and objective

The combined solution of more than one technique should be superior to each single-technique solution, as it should have the advantages of each technique fully exploited but the disadvantages minimized to wherever possible. This is a non-trivial work, and plenty of studies have been conducted.

The determination of ITRF always involves all four techniques, as different techniques provide different datum constraints (Altamimi et al., 2002), where the combination is done on the parameter level. Other TRF realizations also adopt the strategy of combination on the parameter level (Wu et al., 2015; Abbondanza et al., 2017) or on the NEQ level (Seitz et al., 2012). Several studies discussed that the combination of EOP from GNSS and VLBI (Ray and Altamimi, 2005; Ray et al., 2005; Thaller et al., 2006), demonstrating the advantages of combining the discrete estimate from VLBI and the continuous estimates from GNSS. The IERS official EOP product is also derived from the multi-technique combined solution (Bizouard et al., 2018). The early-stage studies of homogeneous reprocessing and rigorous combination of GPS, VLBI, and SLR were performed by Thaller et al. (2006), where special care was taken to obtain the consistent NEQs from different software packages. The investigation was continued in GGOS-D[4], where the methodology and results provide valuable experiences for further similar studies (Rothacher et al., 2011). The concept of space co-location was investigated mainly on the LEO platforms, where the GNSS, SLR, and DORIS observations are combined for an optimized orbit solution (Zhu et al., 2004; Otten et al., 2012; Koenig, 2018; Montenbruck et al., 2018a). The VLBI observations to GNSS satellites and LEO platforms were also exploited to connect VLBI with other techniques (Männel, 2016; Anderson et al., 2018; Klopotek, 2020).

The previous combination studies are usually done based on several solutions or normal equations from different software packages, as this is the most feasible way and already

[4] https://www.ggos-d.de/

available. The very first attempts to use the same software were done by Yaya (2002) and Coulot et al. (2007), where the GINS software was used to generate four normal equations from the four techniques and then combined for an ultimate solution. On the other hand, the integrated processing of GPS and VLBI on the observation level was done by Hobiger and Otsubo (2014), where the impact of the local ties, tropospheric ties, and clock ties are investigated. The study is further developed on the VLBI and SLR combination by Hobiger et al. (2014). These studies highlight the station coordinates, as the EOP was not discussed comprehensively.

On the other hand, comprehensive studies on the integrated processing of multi-technique on the observation level with real observations are still rare. However, the best consistency can only be guaranteed with a combination on the observation level. Ideally, the normal equation stacking can achieve an identical result if the two normal equations are from highly-homogeneous processed software, and the same models, conventions, parameterizations are adopted. However, this is no easy way to go. Practically, it is a heavy burden to guarantee the homogeneity of different software packages.

Therefore, the object of this thesis is to investigate the method and result of multi-technique integrated processing, which will naturally be performed in one software. The characteristics of different techniques should be first identified, several issues in integrated processing must be addressed, and the benefits of integrated processing will be demonstrated with real observations. Specifically, the following questions will be discussed.

- What is the agreement of the global ties and local ties between GNSS and VLBI?
    - For the global ties, that is, EOP, what accuracy can be achieved by each technique, and is there any discrepancy?
    - For the local ties, how reliable are they from the local surveys? To what extend can the nominal accuracy from the local surveys be trusted?
    - For the tropospheric ties, what is the agreement between estimates from Numerical Weather Model (NWM) and that from space geodetic solutions? How to explain the potential discrepancy?
- How to process more than one technique in the common least-squares estimator on the observation level?
    - How to properly apply the ties? Should the pseudo-observations be applied or the method of NEQ stacking be adopted?
    - How to handle the discrepancies of the ties? For instance, the LOD from GNSS is precise in short-term but biased over long-term; the tropospheric ties from NWM might not fit those from space geodetic solution perfectly.

  - How to weight the local ties from local surveys? It is well known that the local surveys nominal uncertainty is too optimistic, and cannot be directly used, so an optimal method must be applied.
  - How to weight observations from different techniques? As the observation number of GNSS is much larger than that of VLBI, together the solution will be dominated by GNSS. As this can be easily handled by scaling the normal equations if the combination is done on the normal equation level, it is not easy to be addressed in the integration on the observation level.

- What is the benefit of applying the tropospheric ties? As the tropospheric parameters are one of the limiting factors to achieve high-precision space geodesy solutions and all the microwave-based techniques share the same troposphere at co-locations by physical nature, the impact of tropospheric ties has not been thoroughly investigated yet. Thus, the impact on the integrated solution, especially for the VLBI estimates, will be studied in this study.

- What is expected in the integrated GNSS and VLBI solution? In an integrated solution of GNSS and VLBI where all the possible ties are applied, several issues should be clarified.
  - How to evaluate the integrated solution? What internal and external criteria can be used?
  - Theoretically, will the integrated solution be more robust? And to what extend?
  - Which parameters will be improved and which one will not? How will the applied ties influence the station coordinates, network scale, and EOP? Will any parameter be affected negatively due to the unmodeled systematic errors?
  - How to define the datum in the integrated solution? Will the minimum constraints good enough for a robust solution or the additional constraints are still necessary?

Dedicated to answering the above questions, this thesis is however not limited to GNSS and VLBI. The impact of including LEO and GNSS satellites in determining the SLR station coordinates is also investigated. The fact that only a small piece of SLR observations are used for SLR TRF determination raises the question of whether an enhanced SLR solution is available by including the SLR observations to LEO and GNSS satellites.

As it is not possible to make bricks without straw, a software package with the capability of processing different space geodetic techniques is the prerequisite for any further multi-technique processing and corresponding investigations. Indeed, the investigation can also be conducted by simulation, on the condition that everything works as expected. However, it is not the case in reality, as there are always inconsistencies when using different software packages. Moreover, there are already enough real observations available for the investigation. Another example is that by simulation it is not possible to figure out which tropospheric tie

from NWM is biased to what extend. Therefore, a lot of efforts have been put into the implementation of the VLBI and SLR modules in the PANDA software. The existing modules in the software should be cautiously revised and unified, especially those related to the VLBI and SLR. It is also necessary to evaluate the reliability of the modules with single-technique solutions, which is the very first object of this thesis. Such an evaluation not only demonstrates the software capability, but also helps to diagnose characteristics of different techniques, and serves as a basic reference to evaluate the following integrated solutions.

Despite that the SLR capability is also available, this thesis focuses more on GNSS and VLBI. Adding SLR and potentially DORIS in the near future will contribute to a complete multi-technique solution, which leads to the consistent realization of TRF, CRF, and EOP ultimately. However, the important issues in integrated processing, for instance, handling the global, local, and tropospheric ties, weighting different types of observations, can be very well demonstrated using the combination of GNSS and VLBI as a prototype. It should be pointed out that determining a long-term TRF is not the goal of this thesis. Instead, the single-session or daily solutions of five VLBI CONT campaigns since 2005 are used to demonstrate the capability of the software and the effect of the integrated solution. The VLBI CONT campaigns are 15-days continuous observing program with 24-hour observations arc per session, organized by IVS every three years from 2002 to 2017. The successfully performed single-session solutions pave the way for further reference frame determination.

1.3 Outline

This section describes the structure of the thesis. Starting with the basic theory of space geodetic techniques and the data processing method, the software implementation is then presented and validated with the single-technique solution. The contribution of the GNSS–VLBI tropospheric ties is then demonstrated, followed by the analysis of the integrated GNSS and VLBI solutions with all the ties applied. The overall contribution of this thesis and the future work are summarized at the last.

Following this introduction, Chapter 2 briefly describes the basic theoretical backgrounds of space geodetic techniques and the data processing methods. The modeling of GNSS, VLBI, and SLR are introduced, together with the basic concepts of terrestrial and celestial reference frames, signal delay models, station displacements. The least-squares adjustment is then presented in brief. The multi-technique combination methods are also described with focuses on handling the ties.

With the theoretical knowledge described in Chapter 2, the software implementation is given in Chapter 3. Information on different software packages in space geodetic data processing is first collected. Second, the PANDA software is introduced, which is used as base for the implementation of VLBI and SLR. Third, the basic GNSS data processing procedure is described. The newly implemented VLBI and SLR modules are then presented, with a focus on several critical issues, including handling the VLBI clock breaks, baseline clock offsets, and

outliers. This chapter ends with the integrated processing strategy, where the key factors are discussed in-depth and in details, including handling the ties an weighting strategies.

The single-technique solutions are presented in Chapter 4. The single-technique solutions help to identify the features of different techniques. Ensuring the accuracy of single-technique solutions is a prerequisite for integrated processing, especially for the newly implemented VLBI and SLR modules. The criteria for evaluation is first introduced, which also applies to the rest of this thesis. The data processing procedure of both GNSS and VLBI are summarized second. Third, the GNSS precise orbit determination results are evaluated in terms of station coordinate repeatability, orbit precision compared to IGS products, and EOP agreement to the IERS product and IGS (and ACs) solutions. The single-session solutions of VLBI CONT campaigns (CONT05–CONT17) are then analyzed in terms of the residuals, the coordinate repeatability of ground stations and AGN, and the EOP agreement to IERS product and IVS and AC solutions. The inter-technique agreement of tropospheric parameters and the EOP estimates are further analyzed in detail, which is important in the following integrated processing. Moreover, the VLBI intensive sessions (INT1 and INT2) in the period of 2001–2016 are further processed. The SLR solution is briefly demonstrated at the end of this chapter.

In Chapter 5, the main focus lies on how the tropospheric ties between GNSS and VLBI can contribute to the integrated solution, especially for the VLBI estimates. Both the VLBI CONT campaigns and the INT sessions are integrated with the GNSS in the Precise Point Positioning mode, where the tropospheric ties are applied. For the CONT campaigns, the contribution of the tropospheric ties is evaluated in terms of the precision of terrestrial reference frame and EOP. As for the INT sessions, the UT1-UTC and LOD are evaluated using IERS and GNSS products, respectively.

The full integration of GNSS observations in Precise Orbit Determination mode and VLBI is presented and demonstrated using the data during the VLBI CONT campaigns in Chapter 6, where not only the tropospheric ties, but also the global ties (EOP) and local ties are applied. The impact of adding different types of ties one by one on the terrestrial reference frame, celestial reference frame, and EOP is investigated.

The major findings and conclusions are summarized in Chapter 7, together with the further prospects of multi-technique integrated processing, such as adding SLR and space ties.

2 Space geodetic techniques

In this Chapter, the theoretical background of space geodetic techniques is introduced. The four techniques, that is, GNSS, VLBI, SLR, and DORIS, are presented in general. The data processing methods of the techniques, including the delay models and the least-squares adjustment, are then introduced concisely, which serve as the fundamental role for the software implementation in the following chapter. Unlike previous studies where the delay models of different techniques are usually described separately, in this chapter they are presented in a more general way, which suits the concept of multi-technique integrated processing on the observation level. The next section describes the integrated processing of multi-technique, where several critical issues are addressed, including the integration level, the handling of the ties, and the relative weighting of different techniques. This chapter ends with a summary of the main findings and conclusions.

2.1 Overview of space geodetic techniques

In this section the very basic background about space geodetic techniques is described. As all the four techniques have been developed for decades and the technical details are very well documented, they shall not be described again but referred to the related literatures given below.

2.1.1 Global Navigation Satellite System

The concept of satellite navigation refers to a satellite constellation transmitting signals from space to receivers, where both positioning and timing information modulated in the signals can be used to determine the receiver location. Such a system that provides global coverage is termed as Global Navigation Satellite System.

The very first GNSS refers to the Global Positioning System (GPS) from the United States, which is designed to have at least four satellites simultaneously visible anywhere on Earth, enabling the basic trilateration positioning. To satisfy this requirement, the GPS constellation is designed to have a minimum of 24 satellites orbiting in six orbit planes, with an inclination of 55° and an altitude of about 20 200 km. For robustness, there are usually around 32 GPS satellites available. The fundamental GPS observation is the time delay (in the forms of the code and carrier phase observation) between the signal emitting epoch from the satellite end and signal receiving epoch at the receiver end, which is acquired at ground tracking receivers by the correlation between the signals from satellite and the one generated by the receiver. These code and carrier phase observations are then used for satellite orbit determination and clock estimation at the ground control center. The satellite orbit and clock estimates are predicted and uploaded to the satellites by the ground control stations, and then broadcasted to the users as the ephemeris, together with the code and carrier phase observations, allowing

the positioning at the user end. Noted that this broadcast ephemeris is for providing the standard positioning service of the system with an accuracy at the level of meter.

Another option for positioning at the user end is using the products from the IGS and its Analysis Centers (ACs), including the post-processing, (ultra-) rapid, and real-time products, with an accuracy of 2.5 cm for orbits and 75 ps for clocks in the case of the post-processing one[5]. Additional products, for instance, the ERP and atmospheric delay parameters, are also available from the IGS and ACs. A comprehensive understanding of GPS principles, signals, observation modeling, applications., can be acquired in the literature (Seeber, 2003; Leick et al., 2015; Teunissen and Montenbruck, 2016).

Following the GPS, there are three other GNSSs available, namely, the Russian GLONASS, the Chinese BDS, and the European Galileo. Despite the different space constellations, signal frequencies, satellite clock performances., all the GNSSs follow the very basic concept of GPS. Besides, two regional satellite navigation systems are also available, that is, the Japanese QZSS, and the Indian IRNSS (operational name NavIC). For details about these systems, it is referred to their corresponding websites for BDS[6], GLONASS[7], Galileo[8], QZSS[9], and IRNSS[10] and literature (Prange et al., 2016; Montenbruck et al., 2017; Montenbruck et al., 2018b).

2.1.2 Very Long Baseline Interferometry

The concise concept of geodetic Very Long Baseline Interferometry is to measure the signal time delay (arrival time difference) between two radio telescopes, where the signal is from extragalactic radio sources and usually observed in the X-band (8.2 to 8.9 GHz) and the S-band (2.2 to 2.4 GHz). Currently, this time delay can be observed with a precision of 10 to30 ps (3 to 10 mm) (Robertson, 1991; Sovers et al., 1998). The design of observing dual-frequency signals is dedicated to mitigating the first-order ionospheric delay. In the VLBI Global Observing System (VGOS) era, four or more bands are observed with the frequency ranging from 2.5 to 14 GHz, using the fast-slewing, 12-m class antennas at a high data rate of 8 Gbps and above[11] (Petrachenko et al., 2012).

The basic principle of VLBI is shown in Figure 2.1. a basic VLBI time delay observable τ, that is, the arrival time difference between the two radio telescopes 1 and 2 pointing at the same radio source simultaneously, times the light of speed c, can be calculated as the scalar product of the baseline vector $\mathbf{b}$ and the unit vector to the source $\mathbf{k}$. Worth mentioning that this geometrical delay model only works for the planar wavefront. For the modeling of near-field objects, it is referred to the literature (Klioner, 2003; Sekido and Fukushima, 2006; Kikuchi et al., 2009; Duev et al., 2012).

[5] http://www.igs.org/products
[6] http://en.beidou.gov.cn
[7] https://www.glonass-iac.ru
[8] https://www.gsa.europa.eu
[9] https://qzss.go.jp
[10] https://www.isro.gov.in/irnss-programme
[11] http://ivscc.bkg.bund.de/technology/vgos-general.html

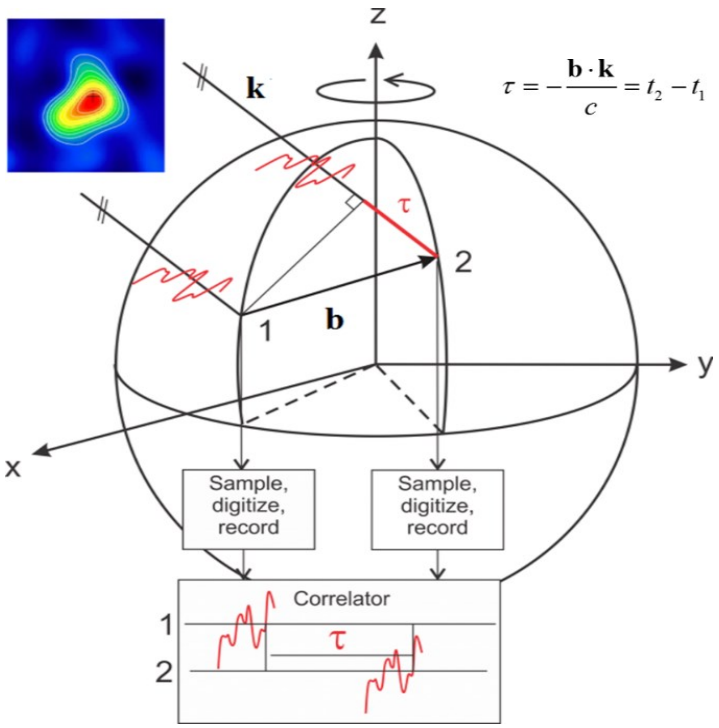

Figure 2.1 Basic concept of Very Long Baseline Interferometry. This is a modified version from the VieVS wiki[12].

A typical VLBI program usually starts with the scheduling, which writes the information of observing time and AGN to the radio telescopes. Depending on the interested parameters, several factors have to be considered in scheduling, for instance, the sky-coverage, the number of scans and observations, slew rate (Sun et al., 2014; Schartner and Böhm, 2019; Schartner and Bohm, 2020). The second step is observing, that is, collecting and recording the signals at each antenna. Then the signals are combined pairwise, producing an interference pattern. This procedure is called correlation and is usually done by a correlator. To put it simply, the correlator compares the recorded bitstreams at the two telescopes and determines the difference in arrival times. This correlation is usually performed for many frequency channels in parallel, and the results are saved for the next step: post-correlation. Post-correlation prepares the data for final delay modeling and parameter estimation. Several tasks are done in post-correlation, for instance, rejecting unreliable data, determine the reference time and frequency, phase calibration. The products of post-correlation are the phase delay, group delay, phase delay rate, and amplitude, while the group delay rate is usually not accurate enough for geodetic purposes. Last but not the least, the observations (usually group delays) are modeled, and the parameters are estimated with the least-squares adjustment, or Kalman filter (Soja et al., 2015). For details about the above-mentioned steps, it is referred to Sovers et al. (1998). The final products are the EOP, station and AGN coordinates, and the auxiliary atmospheric parameters, receiver clocks. Most of these activities are conducted within the IVS [13] coordination.

[12] https://vievswiki.geo.tuwien.ac.at
[13] https://ivscc.gsfc.nasa.gov

2.1.3 Satellite Laser Ranging

Satellite Laser Ranging is a straightforward technique measuring the round-trip optical signal traveling time, which is emitted by a ground station, reflected by a corner-cube retro-reflector on-board a satellite, and then received by the same ground station. The signal traveling time is calculated by a timer at the ground station, which starts counting as the laser pulse is emitted, and gives the time delay when the reflected signal is detected. In addition to the reflector on-board a satellite, several reflector arrays are located on the surface of the Moon, which is called Lunar Laser Ranging (LLR). The latter one is out of the scope of this thesis and is referred to the corresponding literature (Müller and Nordtvedt, 1998; Müller et al., 2009; Müller et al., 2019).

In terms of SLR, the tracked satellites can be categorized into three groups: the spherical satellites such as the two LAGEOS satellites (LAGEOS-1 and LAGEOS-2), the GNSS satellites equipped with retro-reflectors, for instance, the GPS-35/36 and the GLONASS constellation, and the LEO satellites equipped with retro-reflectors, for instance, the GRACE and JASON satellites. The spherical satellites are designed with very low area-to-mass ratio and a favorable symmetry for modeling non-conservative forces (Luceri et al., 2019), and the center of mass offset can also be easily calculated. Thus, the two LAGEOS and two ETALON satellites are majorly used to maintain the SLR TRF and determine low-degree coefficients of the Earth's gravity field (Sośnica et al., 2015a; Bloßfeld et al., 2018a; Glaser et al., 2019). SLR works as the determining factor for the origin realization and a critical one for the scale realization of ITRF (Altamimi et al., 2016). Moreover, the SLR observations to the LEO and GNSS satellites serve as an important and independent source for the orbit accuracy validation (Fritsche et al., 2014; Arnold et al., 2018).

To have a straightforward illustration of the SLR observations to different types of satellites, the session (or pass) number from 2017 to 2019 is shown in Figure 2.2. The daily normal point files in this period are scanned and the total number in each year is counted. Only the SLR spherical satellites, GNSS satellites, and LEO satellites equipped with GNSS receivers are counted. Other LEO satellites tracked by SLR but not GNSS, such as Envisat, CryoSat, and ICESat, are not counted here. In total, around 0.2 million sessions are available per year.

As shown in Figure 2.2, the typical SLR spherical satellite, for instance, the two LAGEOS satellites, only contribute to about 10% of the available sessions (or scans). Even with the two ETALON satellites, only around 13% of sessions are used. Other SLR satellites including LARES, Larets, Ajisai, contribute to about 20–25% of the sessions in total. Therefore, using all the SLR spherical satellites can provide a more robust solution with the session number increased by a factor of three to four (Sośnica et al., 2014; Bloßfeld et al., 2018a). However, it should be noted that these satellites are only observed by the SLR technique. In other words, there is no other way for the orbit determination of these satellites besides the SLR observations. As a result, for each satellite, the limited observation number is still a drawback for precise orbit determination, despite the feasibility of dynamic modeling.

On the other hand, the SLR sessions to GNSS satellites contribute to around 30–40% of the total sessions, especially the GLONASS and Galileo satellites, with 10–20% contributions for each of them. More importantly, the GNSS satellites do not rely on the SLR observations for precise orbit determination. The continuous GNSS observations collected at more than 400 globally distributed IGS stations can very well determine the satellite orbits with an accuracy of 1–3 cm for most of them. The well-determined GNSS satellite orbits can contribute to determining the station coordinates with a significantly increased observation number and better geometry. The newly launched satellites, for instance, the Galileo satellites, have precisely calibrated antenna PCO and LRA offset. Therefore, these GNSS satellites can also contribute the TRF scale, and provide a direct link between the GNSS TRF and SLR TRF in addition to the local ties (Thaller et al., 2011; Bury et al., 2018; Sośnica et al., 2018).

Besides the SLR observations to GNSS satellites, additional 30% of SLR sessions to the LEO satellites are available. Note that all these LEO satellites are equipped with GNSS receivers, and the satellite orbits can be precisely determined from the GNSS observations, and DORIS if the payload is available. Therefore, these SLR sessions can also enhance the SLR TRF with additional observations and improved geometry (Arnold et al., 2018; Montenbruck et al., 2018a).

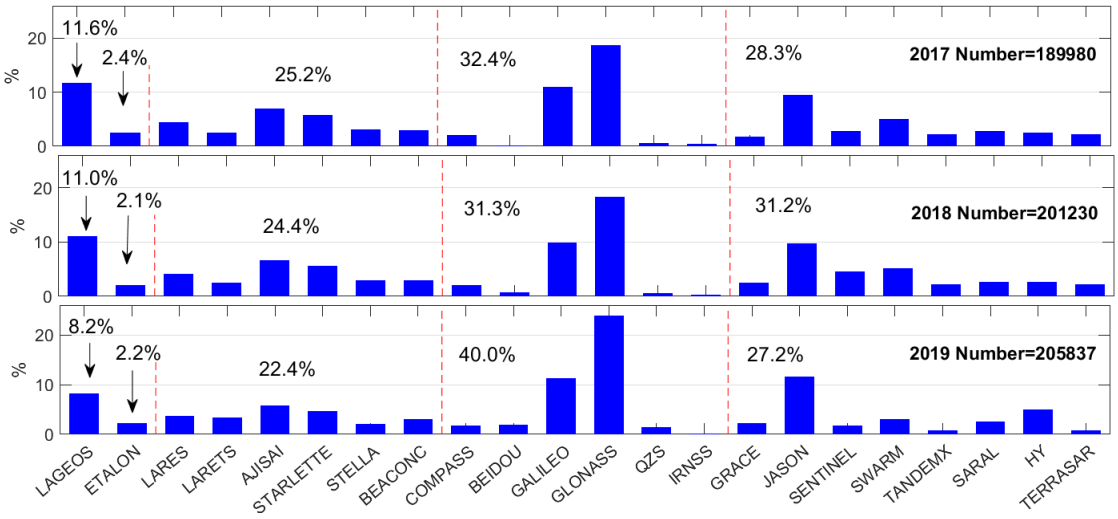

Figure 2.2 SLR session percentage of different satellites in 2017–2019. The LEO satellite list are taken from Table A.1 in Männel (2016). The horizontal axis is the satellite name.

Taking all the available SLR observations together, the usable sessions can be increased by a factor of 10 compared to the current typical SLR solution with only LAGEOS satellites, and the corresponding SLR solution will be significantly improved. The instrument offsets, that is, the LRA offset or GNSS antenna phase center offset, do not change during the lifetime of one satellite, and for some satellites the carefully calibrated values are available. Therefore, these offsets work as the space ties to provide a perfect opportunity for the integrated processing of GNSS and SLR and further connect the two TRFs.

2.1.4 Doppler Orbitography and Radiopositioning Integrated by Satellite

Even the DORIS is out of the scopes of this thesis, it is still mentioned for the sake of completeness. DORIS is a one-way Doppler tracking system based on the Doppler effect, with two-frequency microwave signals (401.25 MHz and 2036.25 MHz) emitting from ground beacons continuously to the payload on-board LEO satellites, for instance, JASON and SPOT. The DORIS technique is mainly used for the precise orbit determination of these LEO satellites, and also contributes to the TRF determination and ERP estimation. For the technique details, observation file format, tracking network and satellite list, and products, the IDS website[14] provides well-organized documents. It is also referred to the AVISO website[15] and other related literature (Jayles et al., 2010; Mercier et al., 2010; Zelensky et al., 2010; Lemoine et al., 2016).

2.1.5 Characteristics of space geodetic techniques

With the basic knowledge of the four space geodetic techniques presented above, here their characteristics are summarized for comparison.

First, all the techniques involve a space segment and a ground segment. For GNSS and VLBI, the signal comes from space (satellite and AGN, respectively) and is acquired by the ground-based receivers. In the case of GNSS, any platform within the coverage of the GNSS signal, if equipped with the corresponding receiver and antenna, can work as the signal receiving end, including the ground static and kinematic objects, airplanes, ships, and LEO satellites. For SLR, the signal is emitted from the ground station, reflected by the LRA on-board satellite (spherical, GNSS, and LEO satellites), and then acquired by the same ground station. It can also be considered as similar to GNSS, if the one-way delay model is used. The DORIS signal is from the ground beacons to the payload on-board LEO satellites. Additional, the VLBI signals can not only from the AGN but also from the spacecraft with a VLBI transmitter equipped, such as a LEO or GNSS satellite (Bar-Sever et al., 2009; Anderson et al., 2018; Klopotek et al., 2020), or the space exploration spacecraft (Klopotek et al., 2017).

In terms of the signal, SLR operates on the optical regime (usually 532 nm), while the other three techniques work with the microwave. As a consequence, the dual-frequency design is not necessary for SLR, but critical for the others to eliminate the first-order ionospheric delay. It is also worth mentioning that the tropospheric delay for the microwave-based techniques follows the same rule and is independent of the frequency, while for the optical signal the tropospheric delay is frequency-dependent.

[14] https://ids-doris.org
[15] https://www.aviso.altimetry.fr

As for the observing scheme, both VLBI and SLR provide discrete observations, whereas GNSS and DORIS provide continuous observations which can usually be sampled up to a few seconds. The VLBI observing programs are always pre-scheduled and observed routinely. For instance, aiming to provide twice-weekly EOP results on a timely basis, the VLBI R1 and R4 sessions observe on Monday and Thursday with 24-hour arc length. The Intensive sessions observe daily with 1-hour arc length. The interval between two epochs (two scans) depends on the schedule and correlation, but usually varies from a few seconds to several minutes. As for SLR, the stations usually observe one satellite for a while as a pass. The SLR full-rate points are resampled to about 5-sec within one pass as the normal points. However, SLR usually works at night and cannot work on rainy or cloudy days, introducing the blue-sky effect (Sośnica et al., 2013). In the case of GNSS, the 30-sec sampling is mostly used by the ground stations, while the high-frequency (1 Hz, or even 10 Hz) observations are also used quite often on kinematic platforms. The DORIS observations are usually sampled to 10 seconds.

The comparison of delay models and parameter sensitivities of different techniques will be presented in the next section.

2.2 Data processing of space geodetic techniques

In this section, the focus lies on the mathematical modeling of the time delay in GNSS, VLBI, and SLR. The delay models are first presented in a general way, and the involving items are then explained one by one. The least-squares adjustment used in this work is also briefly described.

2.2.1 Delay modeling of GNSS, VLBI, and SLR

The basic observable in geodesy is usually distance or angle. For GNSS, VLBI, and SLR, the basic observable is the distance derived from the signal traveling time delay between the transmitter and the receiver in the case of GNSS, or that between two telescopes in the case of VLBI, or a two-way delay between the ground station and the retroreflector on-board satellite in the case of SLR. The SLR two-way delay can also be re-written in a one-way delay method for convenience (Arnold et al., 2018). Therefore, a general delay model can be written as:

$$dist = c \cdot \tau_{geom} \tag{2.1}$$

where τ_{geom} is the geometry time delay between the two objects (satellite to receiver, or receiver to receiver), d is the corresponding distance, and c is the speed of light. For VLBI, the time delay is the product of the baseline $\mathbf{b}$ between the two receivers and the unit vector $\mathbf{k}$ from the radio telescope to the AGN (as shown in Figure 2.1).

$$\mathbf{b} \cdot \mathbf{k} = c \cdot \tau_{geom} \tag{2.2}$$

As for GNSS and SLR, considering the coordinates of the two objects $(x_1 \quad y_1 \quad z_1)^{\mathrm{T}}$ and $(x_2 \quad y_2 \quad z_2)^{\mathrm{T}}$, the geometrical distance can be written as:

$$dist = \sqrt{(x_1 - x_2)^2 + (y_1 - y_2)^2 + (z_1 - z_2)^2} \tag{2.3}$$

Defining coordinates of the two objects as $\mathbf{x_1} = (x_1 \quad y_1 \quad z_1)^{\mathrm{T}}$ and $\mathbf{x_2} = (x_2 \quad y_2 \quad z_2)^{\mathrm{T}}$, one would have the delay model for VLBI, GNSS and SLR as follows.

$$(\mathbf{x_1} - \mathbf{x_2}) \cdot \mathbf{k} = c \cdot \tau_{geom}; |\mathbf{x_1} - \mathbf{x_2}| \cdot \mathbf{k} = c \cdot \tau_{geom} \tag{2.4}$$

For a ground station, the coordinates provided by ITRF usually refer to a reference epoch t_0, and thus the instantaneous coordinates in TRS at epoch t_i are derived as:

$$\mathbf{x}_{\mathrm{r,TRS}}(t_i) = \mathbf{x}_{\mathrm{r,TRS}}(t_0) + (t_i - t_0) \cdot \mathbf{v} \tag{2.5}$$

where $\mathbf{v}$ is the station velocity. The Earth surface deformation due to the geophysical process, for instance, the tides, should be further corrected:

$$\mathbf{x}_{\mathrm{r,TRS}}(t_i) = \mathbf{x}_{\mathrm{r,TRS}}(t_0) + (t_i - t_0) \cdot \mathbf{v} + \sum_{i=1}^{n} \mathbf{dx}_i \tag{2.6}$$

where $\sum_{i=1}^{n} \mathbf{dx}_i$ are the deformation corrections.

Considering that the signal reference point usually does not coincide with the marker defined in ITRS, this offset must be corrected:

$$\mathbf{x}_{\mathrm{r,TRS}}(t_i) = \mathbf{x}_{\mathrm{r,TRS}}(t_0) + (t_i - t_0) \cdot \mathbf{v} + \sum_{i=1}^{n} \mathbf{dx}_i + \mathbf{dx}_{\mathrm{marker-ref}} \tag{2.7}$$

where $\mathbf{dx}_{\mathrm{marker-ref}}$ is the offset between the marker and the signal reference point. As for the satellite, the coordinates at the epoch t_i can be derived using the Lagrange interpolation from the numerically integrated orbit. Nevertheless, the satellite coordinates at epoch t_i can be described using the function $F(\mathbf{x_0}, \mathbf{v_0}, \mathbf{s_0}, t_i)$, where $(\mathbf{x_0}, \mathbf{v_0}, \mathbf{s_0})$ denotes the satellite orbit parameters at reference epoch, i.e, the initial position, velocity, and solar radiation pressure parameters. By considering the satellite body coordinate system, the coordinates of the signal reference point of the satellite read:

$$\mathbf{x}_{\mathrm{s,CRS}}(t_i) = F(\mathbf{x_0}, \mathbf{v_0}, \mathbf{s_0}, t_i) - \mathbf{dx}_{\mathrm{CoM}} + \mathbf{dx}_{\mathrm{arp}} \tag{2.8}$$

where $\mathbf{dx}_{\mathrm{CoM}}$ and $\mathbf{dx}_{\mathrm{arp}}$ are the satellite center of mass (CoM) vector and the signal reference point (antenna) vector in the satellite body coordinate system. The latter one ($\mathbf{dx}_{\mathrm{arp}}$) refers to the LRA offset in SLR, and includes the satellite antenna phase center offset and variation corrections in GNSS.

On the right side of Eq. 2.1, the time delay is measured by the signal correlation in GNSS and VLBI. However, the clock synchronization between the emiting and receiving instruments is not accurate enough, and thus the clock offset has to be considered when clock synchronization is used.

$$\tau_{obs} = \tau_{geom} - dt_{emit} + dt_{recv} \tag{2.9}$$

Where dt_{emit} and dt_{recv} are the clock offsets at the emitting and receiving instruments, respectively. For SLR, the signals are emitted and received by the same instrument, hence it is not necessary to consider this clock offset.

Transmitting through the atmosphere, the signal delays caused by the ionosphere dt_{iono} and troposphere dt_{trop} should also be considered.

$$\tau_{obs} = \tau_{geom} - dt_{emit} + dt_{trop} + dt_{iono} \tag{2.10}$$

Other terms, such as the ambiguity and multi-path in GNSS, the cable calibration in VLBI, and the range bias in SLR, are not listed in the above equation.

As the ground stations are defined in the TRS, while the satellite orbit and AGN coordinates are usually provided in CRS, the EOP connects the two systems by several rotation matrices. Details will be given later.

In VLBI, the construction of the delay model is not as easy as GNSS and SLR. It involves transformation between the ITRS, GCRS, and BCRS, including performing the Lorentz transformation. The details have been described previously (Sovers et al., 1998; Plank, 2013). On the other hand, the consensus model recommended by IERS Conventions (Chapter 11) can be easily adopted (Petit and Luzum, 2010).

Terrestrial reference system and frame

The terrestrial reference system is used to describe the points attached to the Earth's solid surface, and is co-rotating with the Earth in space. In TRS the coordinates are supposed to be stable in time with only small temporal variation due to the geophysical effects. The ITRS is defined by IERS[16] as[17]:

- *It is geocentric, its origin being the center of mass for the whole Earth, including oceans and atmosphere;*
- *The unit of length is the meter (SI). The scale is consistent with the TCG time coordinate for a geocentric local frame, in agreement with IAU and IUGG (1991) resolutions. This is obtained by appropriate relativistic modeling;*
- *Its orientation was initially given by the BIH orientation at 1984.0;*
- *The time evolution of the orientation is ensured by using a no-net-rotation condition with regards to horizontal tectonic motions over the whole Earth.*

The realization of ITRS is the ITRF, which uses the global solutions of the four space geodetic techniques, that is, VLBI, SLR, GNSS, and DORIS (Altamimi et al., 2002; Altamimi et al., 2016). The latest realization of ITRF is the ITRF2014, which is determined using decades of solutions from IVS, IGS, ILRS, and IDS. The network of ITRF2014 is given in Figure 2.3, including ~1500 stations located in 975 sites. The stations from different techniques are

[16] https://www.iers.org/IERS/EN/Science/ITRS/ITRS.html
[17] This is a direction quotation of the original description. In this thesis the direct quotations are marked as an indented freestanding block of text in *Italic*. The source is given in the footnote.

connected by local ties at the co-locations. One can see that there are more GNSS stations than other techniques, while only the GNSS and DORSI stations have a global distribution. The GNSS, VLBI, and SLR stations are more concentrated in North America and Europe. These clusters will dominate the transformation of the global network and over-represent the geophysical effects if not handled properly.

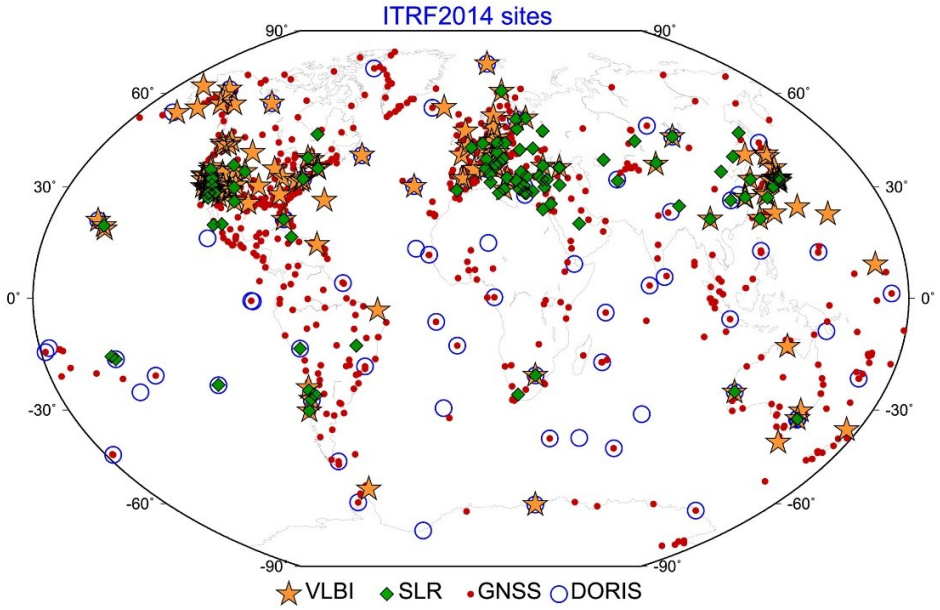

Figure 2.3 Station distribution of the ITRF2014 network. This figure is taken from Altamimi et al. (2016).

Celestial reference system and frame

The celestial reference system is used to describe the celestial body coordinates, for instance, the Earth-orbiting satellite coordinates, solar system ephemerides (Sun, Moon, and so on), galactic and extragalactic bodies. The ICRS is adopted by IAU in 1998 as the standard celestial reference system to describe the extragalactic bodies. The ICRS is defined as[18]:

> *Its origin is located at the barycenter of the solar system through appropriate modelling of VLBI observations in the framework of General Relativity. Its pole is in the direction defined by the conventional IAU models for precession (Lieske et al., 1977) and nutation (Seidelmann, 1982). Its origin of right ascensions was implicitly defined by fixing the right ascension of 3C 273B to the Hazard et al. (1971) FK5 value transferred at J2000.0.*

The ICRF is the realization of the ICRS and is determined by the VLBI technique solely. The latest realization is ICRF3, which uses ~4,500 extragalactic objects, and 303 of them are used for defining. Unlike the previous ICRF, in ICRF3 the galactic aberration is considered, that is, the rotation of the solar system barycenter (SSB) around the galactic center. The ICRF can be accessed at the IERS ICRS Center[19] where the right ascension α and declination δ of the AGN are given. Then the direction of this AGN on the sky is described as the following equation.

[18] https://www.iers.org/IERS/EN/Science/ICRS/ICRS.html
[19] http://hpiers.obspm.fr/icrs-pc/newwww/index.php

$$\mathbf{r} = \begin{pmatrix} \cos\delta\cos\alpha \\ \cos\delta\sin\alpha \\ \sin\delta \end{pmatrix} \tag{2.11}$$

Shifting the origin from the Barycenter to Earth's geocenter, the resulting GCRS is more appropriate to describe the earth-orbiting objects, for instance, the satellites. It is also widely adopted for modeling satellite geodetic techniques. In the ideal Newtonian thinking, the BCRS can be converted into the GCRS given the barycentric position of geocenter $\mathbf{x_E}(t)$:

$$t_{GCRS} = t_{BCRS}; \mathbf{x_{GCRS}} = \mathbf{x_{BCRS}} - \mathbf{x_E}(t) \tag{2.12}$$

Considering the relativity theory, it becomes a 4-dimensional space-time transformation, which is non-trivial. Nevertheless, the IERS Conventions (Petit and Luzum, 2010) give the equations to transform between BCRS and GCRS with an uncertainty below 1 mm.

The solar system bodies are usually described by the ephemeris as a function of time, and one commonly used ephemeris is the JPL Solar System ephemerides (DE 405, DE 421). The positions and velocities of the Sun, the Earth, the Moon, Pluto, and other planets are provided in the BCRS. The ephemeris can be accessed from the JPL server[20].

Transformation between terrestrial and celestial reference systems

As the ground stations are defined in TRS, while the satellite orbits and AGN coordinates are described in the CRS, the transformation between these two systems is necessary in modeling the signal time delay of space geodetic techniques. The GCRS and ITRS have the same origin, and thus the transformation at the time t consistents three rotation matrices:

$$\mathbf{x_{GCRS}} = \mathbf{Q}_{PN}(t) \cdot \mathbf{R}_{ERA}(t) \cdot \mathbf{W}_{PM}(t) \cdot \mathbf{x_{ITRS}} \tag{2.13}$$

where $\mathbf{Q}_{PN}(t)$, $\mathbf{R}_{ERA}(t)$, and $\mathbf{W}_{PM}(t)$ are the transformation matrices to account for the motion of the celestial pole in the celestial reference system (precession and nutation), the rotation of the Earth around the axis associated with the pole, and the polar motion, respectively.

The transformation matrices are constructed by the five Earth Orientation Parameter components, namely, the two celestial pole offsets (CPO) dX and dY, the Earth rotation angle, and the two polar motion components (PM) x-pole and y-pole. The EOP set describes the Earth rotation irregularities, caused by the gravitational torque exerted by the Sun, Moon, and planets, displacements of the Earth surface planet and other excitation mechanisms.

Station displacement

For the solutions with daily (or several days) station coordinates estimated as constant, the a priori coordinates are usually taken from the ITRF solution, using the coordinates at reference epoch and the velocity, plus the postseismic deformation (PSD) if necessary. Taking the ITRF2014 as an example, the coordinates at epoch t_i are derived with the following equation:

$$\mathbf{x}(t_i) = \mathbf{x}(t_0) + (t_i - t_0) \cdot \mathbf{v} + \mathbf{dx_{psd}} \tag{2.14}$$

[20] ftp://ssd.jpl.nasa.gov/pub/eph/planets/ascii/

Moreover, the instantaneous station coordinates are also affected by the Earth's surface displacement due to the mass re-distribution and corresponding loading effects. Most of the displacement models have been presented in the IERS Conventions in detail (Petit and Luzum, 2010). Here they are only listed briefly.

- Solid Earth tides displacement. The solid Earth tides are caused by the gravitational forces of the Sun and Moon, which further induce the Earth's surface tidal deformation. The deformation includes time-independent and time-dependent signals with periods from hours to 18.6 years, and can reach up to 40 cm (peak-to-peak) vertically and several centimeters horizontally. Solid earth tides displacement must be corrected in the geodetic data processing.

- Ocean tides loading displacement. The ocean tides are also caused by the gravitational forces of the Sun and Moon. The water mass re-distribution introduces the loading displacement on the oceanic crust, mainly on the vertical component. The vertical displacement for coastal stations can be up to several centimeters, while for the continental stations it is usually less than one centimeter. The ocean tides loading displacement has to be corrected, but can also be estimated in data processing (Schuh and Moehlmann, 1989; Sovers, 1994; Thomas et al., 2006; Yuan et al., 2009). The ocean tide loading models which describe the ocean tides with each have their own periods (usually 11 harmonics) are usually available at the Onsala Space Observatory website[21].

- S_1-S_2 tidal atmospheric pressure loading displacement. The APL is dominated by the diurnal S_1 and semidiurnal S_2 signals caused by the atmospheric pressure oscillations. It is usually less than a few millimeters and is recommended to be corrected.

- Rotational deformation due to polar motion. The variation of station coordinate from pole tide can be as large as 25 mm vertically and 7 mm horizontally, and is usually corrected.

- Ocean pole tide loading displacement. The centrifugal effect of polar motion on the oceans causes the water mass re-distribution and the corresponding ocean pole tide loading displacement. It is usually less than 1.8 mm and 0.5 mm on the vertical and horizontal components, respectively.

- Non-tidal atmospheric pressure loading displacement. Besides the S_1-S_2 tidal atmospheric pressure loading, the annual part and non-tidal parts can be as large as 1 cm. However, modeling this displacement is not easy and the accuracies of several products are still under investigation. Regarding its impact, plenty of studies have been conducted in the data processing of GNSS, SLR, and VLBI (Boehm et al., 2009; Dach et al., 2010; Spicakova et al., 2011; Bury et al., 2019; Männel et al., 2019; Glomsda et al., 2020; Mémin et al., 2020). However, modeling non-tidal APL displacement is only a standard for the VLBI community, not for other techniques[22]. Several sources are

[21] http://holt.oso.chalmers.se/loading/index.html
[22] https://ivscc.gsfc.nasa.gov/IVS_AC/IVS-AC_ITRF2020.htm

available, including the Global Geophysical Fluid Center[23], the Vienna product[24], the ESMGFZ product[25].

- Other effects, such as the post-glacial rebound, hydrological effects, non-tidal oceanic loading, sea level loading, are currently not considered in geodetic data processing.

Instrumental offset

For a ground station, the coordinate refers to the marker, while for the satellite the orbit describes the motion of the satellite center of mass. As they usually do not coincide with the signal emitting and receiving points, it is necessary to apply the corresponding correction.

For a GNSS receiver, the correction from the station marker to the antenna reference point (ARP), which is usually available from the station log file, is first applied. And then the antenna PCO and PCV should be corrected. On the satellite end, the center of mass and center of the spacecraft body coordinate system usually coincides with each other for the old satellites but not for the newly launched satellites. Nevertheless, the satellite antenna PCO and PCV should also be applied together considering the CoM offset and the antenna ARP offset. The PCO and PCV information is available from the IGS atx file[26]. As for the LEO satellites, the ARP, PCO, and PCV should always be applied, and the time-varying CoM corrections should be considered. The satellite body coordinate system definition of multi-GNSS satellites has been described by Montenbruck et al. (2015), and the satellite CoM and ARP information are available from the IGS metadata file[27].

For SLR, both the station eccentricity and the satellite LRA offset are available from the ILRS website. The CoM value for spherical satellite satellites are station-dependent and the corresponding files are also available[28].

For VLBI, the station axis offset and the thermal deformation are usually corrected as the time delay item on the right side of Eq. 2.2. The AGN source structure correction (Anderson and Xu, 2018; Xu et al., 2019) is no standard, as the data have already been cleaned and those suffer from large AGN source structure variation are marked in the observation file.

Tropospheric and ionospheric delays

The very basic observable of GNSS, VLBI, and SLR is the signal running time delay, which is then converted into the distance using the speed of light. However, the signal (microwave and optical parts) from space to the ground stations goes through the atmosphere, where the propagation speed is modified by the ionosphere charged particles; the signal is slowed down by the neutral molecules and the path is changed by the refractive bending.

The ionized part by solar radiation of Earth's upper atmosphere from 40 to 1000 km altitude is called the ionosphere. The ionosphere causes a delay in the GNSS code observations and

[23] https://geophy.uni.lu/atmosphere/tide-loading-calculator/
[24] https://vmf.geo.tuwien.ac.at/APL_products/
[25] http://rz-vm115.gfz-potsdam.de:8080/repository/entry/show?entryid=e0fff81f-dcae-469e-8e0a-eb10caf2975b
[26] ftp://ftp.igs.org/pub/station/general/
[27] http://mgex.igs.org/IGS_MGEX_Metadata.php
[28] https://ilrs.dgfi.tum.de/index.php?id=6

VLBI group delay observations, while an acceleration in the GNSS carrier phase observations. As the ionosphere is a dispersive medium, the ionospheric delay magnitude is linearly dependent on the squares of wavelength. In the GNSS and VLBI data processing, the dual-frequency observations are usually available and can be used to eliminate the first-order ionospheric delay by a linear combination (Hobiger, 2005; Hobiger et al., 2006). In the case of single-frequency observations, the external total electron content (TEC) map generated using the global GNSS network is available for both GNSS and VLBI users (Sekido et al., 2003; Hernández-Pajares et al., 2009; Gordon, 2010), while the broadcast models are available for GNSS real-time navigation (Hoque et al., 2017). It is also possible to estimate the ionospheric delay using the GNSS single-frequency observations (Shi et al., 2012; Lou et al., 2015). As for the higher-order (second and third) terms, they usually account for about 0.1% of the ionospheric delay, and are more often considered in POD (Fritsche et al., 2005; Hernández-Pajares et al., 2007; Chen et al., 2019) than in PPP (Hoque and Jakowski, 2008; Banville et al., 2017; Hadas et al., 2017). The higher-order ionospheric delay in VLBI was investigated but usually not considered due to its limited impact (Hawarey, 2005). As for SLR, the ionospheric delay effect can be neglected due to the insensitivity of the high-frequency signal to the ionosphere.

When going through the troposphere (0–60 km altitude), the signals are delayed, which is called the tropospheric delay (Böhm and Schuh, 2013). As the troposphere is a non-dispersive medium to electromagnetic waves up to 15 GHz, the tropospheric delay is frequency-independent for the GNSS and VLBI observations, but frequency-dependent for the SLR observations. The tropospheric delay is related to the atmospheric pressure, temperature, and water vapor content, and is one of the limiting factors in high-precision space geodesy, as the rapid fluctuation of water vapor in both space and time can be hardly modeled. The tropospheric delay at the signal path of elevation angle e and azimuth angle e can be written as the sum of the dry (hydrostatic) part and the wet (non-hydrostatic) part plus the azimuth related gradients:

$$L(e,a) = mf_H(e) \cdot Z_H + mf_W(e) \cdot Z_W + mf_G(e) \cdot (G_N \cos a + G_E \sin a) \quad (2.15)$$

where Z_H and Z_W are the zenith hydrostatic delay and zenith wet delay, respectively; mf_H and mf_W are the hydrostatic and wet mapping functions, respectively. G_N and G_E are the north and east gradients, respectively, and mf_G is the gradient mapping function. The zenith hydrostatic delay is usually about 2.3 m in GNSS and VLBI at the sea surface, and can be calculated accurately given the accurate atmospheric pressure value using the Saastamoinen equation (Saastamoinen, 1972). The zenith wet delay and gradients are usually estimated as unknowns. The mapping functions are generated from radiosonde observations or NWM, and are provided either as empirical function, for instance, the Global Mapping Function (Boehm et al., 2006a), or as epoch-wise global grid files, for instance, the Vienna Mapping Function series (Boehm et al., 2006b; Böhm et al., 2015; Landskron and Böhm, 2017) and the Potsdam Mapping Function[29] (Zus et al., 2014; Balidakis et al., 2018). In SLR, the tropospheric delay is usually corrected with models using the in situ meteorological data (Marini and Murray, 1973;

29 ftp://ftp.gfz-potsdam.de/GNSS/products/gfz-vmf1/

Mendes et al., 2002; Mendes, 2004), and the subroutine is provided by IERS[30]. As for the gradients, the estimation of the first order term has to be applied in GNSS and VLBI data processing, while in SLR it is not a standard yet. Studies have shown a reduction in the PM biases by applying the tropospheric gradients from NWM in SLR processing (Drożdżewski et al., 2019). The higher-order gradients in GNSS and VLBI can be applied if external high-precision data from NWM is available, but yet it is difficult to be estimated in data processing due to the parameter correlation and imperfect geometry.

Receiver and satellite clock offsets

As the time delay is usually derived from the signal correlation either between the transmitter and the receiver (GNSS) or between two receivers (VLBI), it is necessary to consider the time differences between the two instruments, that is, the clock offset. For SLR, the same instrument is used to emit and receive the signal and count the time, and thus the clock offset can usually be ignored. Note that the clock refers to two critical applications: (1) measuring the delay and (2) giving the time tag, and the latter one is indispensable for all the four space geodetic technique but usually can be precisely provided in most cases. Therefore, in this section only the first one is focused. Biases related to the time tag in SLR is referred to as the time bias and will be presented later.

The GNSS satellites are usually equipped with stable Caesium, Rubidium, or Hydrogen clocks. As for clock estimation, the fact of continuous observations from a global network of hundreds of stations to tens of satellites (for instance, 32 for GPS) allows the epoch-wise estimation of satellite and receiver clocks, and the mm-level carrier phase observations guarantee the high precision. Therefore, the satellite and receiver clocks are usually estimated as epoch-wise white noise. Applying the between-epoch constraint utilizing the clock stable nature in case of a very stable clock can help to reduce the correlation between satellite orbit and clock at the satellite end, and that between receiver clock, vertical coordinate, and tropospheric parameters at the receiver end. However, this is highly dependent on the clock performance. Fruitful studies have been done using the receiver clock modeling to improve the positioning and troposphere estimation (Wang and Rothacher, 2013; Krawinkel and Schön, 2015; Chen et al., 2018), while the satellite clock modeling has also been studied (Qing et al., 2017). Nevertheless, the white noise is still more often used in GNSS data processing, especially for precise orbit determination and clock estimation using a global network, where applying the constraints to clocks can be a time-consuming job.

As for VLBI, a very stable receiver clock is the prerequisite for both the correlation and the estimation. The Active Hydrogen Maser is used for all the VLBI sites (Pazamickas et al., 2015). The observation number in one scan is limited, and thus it is not optimal to estimate the receiver clock as white noise. Figure 2.4 shows the observation number per epoch of one session. Despite the statistic of 6.6 observations per epoch on average, about 43% of the epochs have only one observation, and 75% of epochs have no more than 6 observations. Therefore, modeling the clock as white noise is simply not practical. Also shown in the figure,

30 ftp://tai.bipm.org/iers/conv2010/chapter9

the interval between two consecutive epochs varies from a few seconds to several minutes, and the average interval is 56 sec in this session.

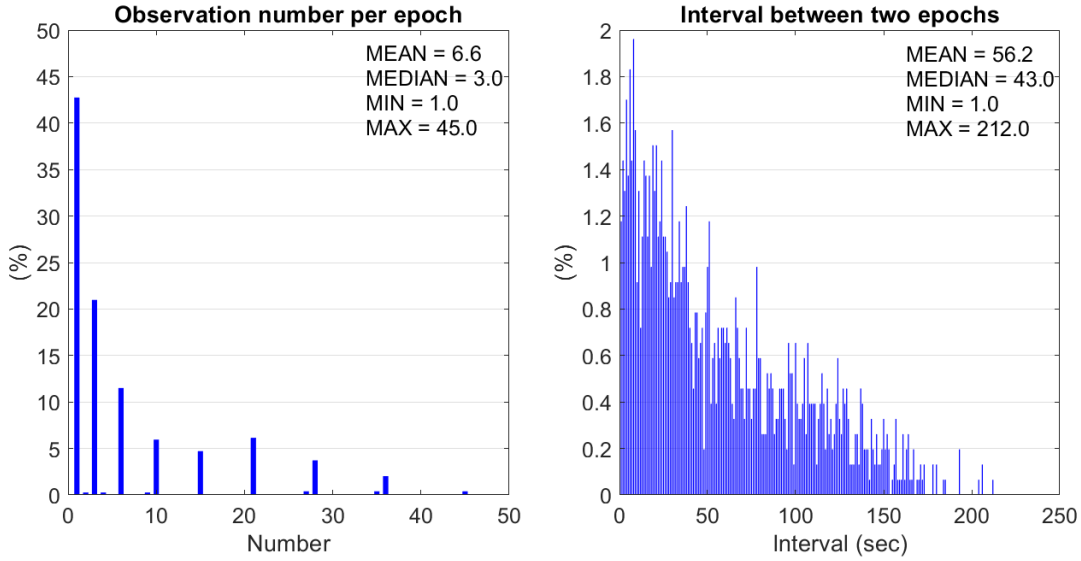

Figure 2.4 The observation number in one epoch (left panel) and the interval between two consecutive epochs (right panel) in the VLBI session CONT1704 in CONT17 (NGSCARD file: 17DEC01XB_N004). Note the different vertical axis scales.

Therefore, the receiver clock modeling has to be applied in VLBI data processing. The most commonly used method is using either a piece-wise-linear (PWL) function or a polynomial function, which both work perfectly (e.g, in Calc/SOLVE and VieVS). On the other hand, the Kalman filter can also be adopted in modeling the VLBI receiver clock (for instance, in PORT). The random walk process can also be applied for clock estimation. However, the power spectral density should be chosen carefully, as it is station-dependent and can affect the solution significantly. As long as the clock modeling is applied, the clock break should always be diagnosed with great caution.

Not related to this thesis, but worth mentioning that the polynomial function is usually used in DORIS data processing.

As already mentioned, in SLR there is no receiver clock offset. However, the time bias can be a serious problem and should be handled properly (Luceri et al., 2019). The time bias is more like a receiver clock offset, but is usually stable and can be modeled as constant (plus a drift in some cases) over a long period.

Technique-specific biases

In addition to different delay items, several biases should be considered in different techniques.

In GNSS data processing, the ambiguities should be estimated if the carrier phase observations are used. The ambiguity is modeled as constant within one continuous arc if no cycle slip occurs. On the other hand, by the ambiguity resolution to fix the values to integers, both network solution and PPP solution can be improved significantly (Ge et al., 2005a; Ge et al.,

2007). If different types of code are used the differential code biases (DCB) should be considered using the IGS product. The differences between different frequencies (ISB and IFB) are usually modeled as daily constants in the case of a multi-GNSS solution or when the FDMA-based GLONASS constellation involved. The phase wind-up correction can be well modeled by Wu et al. (1993); while correcting the multi-path effect is currently not a standard.

For VLBI, the baseline dependent clock offset should be carefully checked and estimated if possible. According to Petrov, the baseline dependent clock offsets are possible due to[31]:

- *Unmodeled source structure effects;*
- *Systematic clock misclosure introduced by correlation and post-correlation procedures;*
- *Presence of strong outliers;*
- *Errors during resolving group delay ambiguities what may result in appearance of permanent clock misclosures at X or S band to be a multiple of group delay ambiguity spacings.*

The baseline dependent clock offset is usually within 100 ps and should be estimated. It also helps to absorb the uncalibrated instrumental and correlator bias (Petrov, 2000; Petrov et al., 2009). The cable calibration can be corrected using the value from the observation file.

In SLR processing, despite the elegant concept of a simple distance measurement without the clock bias, the time bias and range bias do exist and might distort the network. Using the ILRS data handling file is a standard in the SLR community.

Delay model comparison between different techniques

In this section, a comparison of the delay model between different techniques is presented. Starting from the space part (AGN, satellites), the parameter sensitivity of different techniques is analyzed.

The parameter sensitivity of different techniques is shown in Table 2.1. The AGN coordinates can only be determined by the VLBI technique, either by the NNR minimal constraint, or freely estimated with some other AGN coordinate constrained (for instance, fixing one radio source is enough for the solving the normal equation). It is also possible to fix all AGN coordinates to the accurate values in single-session processing, especially for the sessions with weak observation geometry, for instance, the INT sessions. As for the GNSS satellite, the orbits are usually estimated in POD, but fixed in positioning solutions. SLR has the capability of determining GNSS satellite orbits, but currently it is more of a tool for orbit evaluation due to the limited observation number and discrete observing scheme. Despite the simulation studies of orbit determination using VLBI observations (Klopotek et al., 2020), fixing the orbits is expected to be a safer way due to the limited observation number; and this also applies to the LEO satellites in future missions (Bar-Sever et al., 2009; Anderson et al., 2018). The LEO satellite orbits can be precisely determined by GNSS, SLR, and DORIS independently; and using these techniques together can provide a more robust solution. It should be noted that for both SLR and VLBI, given enough observations the POD solution can always be

[31] http://astrogeo.org/petrov/discussion/basdep_clo/basdep_clo.html

performed in the near future. The satellite clock, either for GNSS or LEO satellite, should always be estimated as unknown parameters. On the other hand, the pre-determined GNSS satellite clock is often used in positioning and navigation services. The spherical satellite (for instance, LAGEOS) orbits can only be determined by SLR.

Table 2.1 Comparison of different space geodetic techniques in terms of the observation and the contribution to geodetic parameters. "X" means the parameter contribution is direct or dominant, and "(X)" means the contribution is indirect or not commonly adopted yet.

Technique		VLBI	SLR	GNSS	DORIS
Signal	Type	X/S-band	Optical	L-Band	UHF
	Frequency (GHz)	2.4 & 8.4	~10^5	1.2 & 1.6	0.4 & 2.0
Observation	Sampling	Discrete		Continuous	
	Observable	Time delay			Phase difference
Space	AGN	X			
	GNSS orbit	X	X	X	
	GNSS clock			X	
	LEO orbit	X	X	X	X
	LEO clock			X	X
	Spherical Sat. Orbit[32]		X		
Atmosphere	Ionosphere	X		X	X
	Troposphere	X	X	X	X
Ground	Coordinate	X	X	X	X
	Clock	X		X	X
EOP	PM	X	X	X	X
	UT1-UTC	X	(X)	(X)	(X)
	CPO	X	(X)	(X)	(X)
TRF	Origin		X	(X)	(X)
	Scale	X	X	(X)	(X)
CRF		X			

The ionospheric delay is usually corrected by the dual-frequency combination in VLBI, GNSS, and DORIS, and it is negligible in SLR. GNSS is the major technique to determine the ionospheric parameters on a global scale with high accuracy, that is, the TEC map. As for the tropospheric delay, it is always recommended to be estimated in GNSS, VLBI, and DORIS; and in SLR it is optimal to correct using meteorological observations or NWM. An alternative option for handling the tropospheric delay in SLR is to use the two-color observations, if available.

On the ground station part, the coordinates can be determined by all four techniques. However, different constraints have to be applied to the station coordinates in different techniques, which corresponds to the contribution to ITRF realization. The clock modeling (for instance,

[32] The SLR tracking passive satellites, such as LAGEOS and ETALON.

using the polynomial function) is necessary for VLBI and DORIS, while white noise is good enough for GNSS. In SLR the receiver clock term does not exist.

In terms of EOP, VLBI is the only technique to determine the five components, namely, the two polar motion components, the dUT1, and the two celestial pole offsets. The PM components can be estimated by all four techniques, whereas dUT1 can only be determined by VLBI due to its correlation to satellite dynamic parameters. The first time derivative of UT1-UTC (or LOD) can also be derived from the satellite techniques, despite the long-term biases (Ray, 1996). Moreover, the rates of CPO can also be determined from satellite techniques, as long as the orbit perturbing acceleration can be modeled accurately enough (Rothacher et al., 1999). The PM and dUT1 components are usually estimated as daily offset and rate in data analysis, whereas the daily offset is more applicable for the CPO components. As for the high-frequency (sub-daily) EOP estimation, studies have been conducted using GNSS and VLBI observations (Nilsson et al., 2014), but further investigations are required for a reliable solution.

The TRF determination involves different techniques, although each technique can determine its own TRF with different datum constraints. The orientation is realized by the NNR constraint to the a priori TRF. The origin of current ITRF is determined by the SLR observations to the spherical satellites (Altamimi et al., 2002), even though other satellite techniques including both GNSS and DORIS are capable of determining geocenter motion (Meindl et al., 2013; Männel and Rothacher, 2017; Couhert et al., 2018; Zajdel et al., 2019). Therefore, the NNT constraint should be applied for a GNSS (and SLR, DORIS) network if the geocenter is estimated. As VLBI observes the station coordinate differences, the geocenter is not available, and the NNR+NNT should always be applied. In the case of the TRF scale, both VLBI and SLR provide a stable absolute scale estimate over the long-term. However, it should be noted that for SLR (especially with the uneven station distribution), the imperfect modeling of range bias and CoM, and even the neglected tropospheric horizontal gradients, all might introduce bias to scale estimates. Due to the high correlation between the antenna PCO-Z and scale, the GNSS technique is usually considered incapable of determining the absolute scale as the PCO-Z is not available. Therefore, the additional NNS constraint should be applied when estimating the satellite antenna PCO (Ge et al., 2005b). In this case, the PCO-Z estimates are aligned to a prior TRF. However, for the newly launched Galileo constellation with carefully calibrated PCO information, the scale from GNSS is also possible (Villiger et al., 2020). The GNSS observations on-board LEO satellites can also contribute to scale estimation as long as the accurate LEO PCO information is available (Huang et al., 2020a). The DORIS technique is capable of scale determination, even though it is not adopted by the ITRF solution (Štěpánek and Filler, 2018).

It is worth mentioning the observation file format briefly. The RINEX observation file is mostly used in the GNSS community, which is an ASCII file with the epoch-wise observations stored. In SLR the CRD files (Ricklefs, 2009) are used to provide the flexible, extensible format for both the full-rate and normal point data. It is also an ASCII file format, where the observations are stored pass by pass (or session by session). However, in the CRD file, the

observations are not rigorously chronological. The DORIS uses the DORIS Data Exchange Format previously, but now adopts the RINEX-like format, which follows the GNSS RINEX observation file format with some modifications (Lemoine et al., 2016). As for VLBI, the binary Goddard database format was used to store all the usable information, while the NGSCARD[33] was used to store the necessary delay data (mainly the group delay, ionospheric correction, cable calibration) in the ASCII file. Currently, the vgosDB file in the format of NetCDF is superseding the NGSCARD (Gipson, 2015).

2.2.2 Least-squares adjustment

The least-squares adjustment is well known and widely used in the geodetic data processing. However, several issues should be addressed, which are important in multi-technique integrated processing. The comprehensive background is referred to the literature (Koch, 1999; Kotsakis, 2018)

Starting with a basic function to describe the observation $\mathbf{y}$ with a set of unknown parameters:

$$\mathbf{y} = F(\mathbf{x}) \tag{2.16}$$

where $\mathbf{x}$ is the vector of unknowns. Given the a priori value of $\mathbf{x_0}$, one would have:

$$\mathbf{y} = F(\mathbf{x_0} + \hat{\mathbf{x}}) \tag{2.17}$$

where $\hat{\mathbf{x}}$ is the correction of the unknown. It can be linearized as:

$$\mathbf{y} = \frac{\partial F}{\partial \mathbf{x_0}}\hat{\mathbf{x}} + F(\mathbf{x_0}) \tag{2.18}$$

Considering the observation noise, the equation should be written as:

$$\mathbf{v} = \mathbf{A}\hat{\mathbf{x}} - \mathbf{l}; \mathbf{A} = \frac{\boldsymbol{\partial F}}{\boldsymbol{\partial \mathbf{x_0}}}; \mathbf{l} = \mathbf{y} - \mathbf{y_0} \tag{2.19}$$

where $\mathbf{v}$ is the vector of observation residuals, $\mathbf{l}$ is the vector of observation minus calculation (OMC), $\mathbf{A}$ is the design matrix; and this is the basic observation equation. The equation can be solved with the goal of the minimization of the sum of the weighted squares of the residuals:

$$\min(\mathbf{v^T P v}) \tag{2.20}$$

where $\mathbf{P}$ is the weight matrix of the observations. The observations are usually considered as uncorrelated, and thus $\mathbf{P}$ is diagonal. For the ith obsevation, the weight is defined as the squares of the ratio of the a priori sigma value σ_0 to the observation noise σ_i:

$$P_i = \left(\frac{\sigma_0}{\sigma_i}\right)^2 \tag{2.21}$$

[33] https://cddis.nasa.gov/archive/reports/formats/ngs_card.format

Back to the observation equation, the minimization of the sum of the weighted squares of the residuals is solved as:

$$\hat{\mathbf{x}} = \mathbf{N}^{-1}\mathbf{U}; \mathbf{N} = \mathbf{A}^{\mathbf{T}}\mathbf{P}\mathbf{A}; \mathbf{U} = \mathbf{A}^{\mathbf{T}}\mathbf{P}\mathbf{L} \tag{2.22}$$

where $\mathbf{N}$ is called the normal equation (NEQ).

A datum-free normal equation is usually singular and cannot be inverted. Therefore, the external information should be used, that is, either constrain some parameters to a priori value with the corresponding uncertainties or constrain a set of parameters with certain conditions. This can be done by applying the pseudo-observation equation.

To constrain a parameter to a value x_c with the corresponding uncertainty σ_c, the pseudo-observation equation reads:

$$x_0 + \hat{x} = x_c, P = \left(\frac{\sigma_0}{\sigma_c}\right)^2 \tag{2.23}$$

The constraint can also be applied between two parameters x_a and x_b given the uncertainty σ_{ab}, for instance, the two parameters at consecutive epochs in the random walk process, or a tropospheric tie between the ZTD parameter from GNSS and that from VLBI. The equation reads:

$$x_a - x_b = \Delta_{ab}, P = \left(\frac{\sigma_0}{\sigma_{ab}}\right)^2 \tag{2.24}$$

where Δ_{ab} is the difference, for instance, zero in case of RWK process.

Datum constraint of a network

Another option to remedy the rank deficiency in a datum-free network is to align the datum to a previous network by applying the minimum constraint. The no-net-translation (NNT), no-net-rotation (NNR), and no-net-scale (NNS) constraints are the three constraints usually applied to a network (Sillard and Boucher, 2001; Kotsakis, 2018).

The datum defining condition matrix $\mathbf{B}$ is usually applied as:

$$\mathbf{B}\hat{\mathbf{x}} = \mathbf{0} \tag{2.25}$$

where $\hat{\mathbf{x}}$ is the vector of coordinate corrections. This condition equation can contribute to the datum-free network normal equation to obtain the solution.

For the celestial reference frame, the NNR conditions for one AGN q read:

$$\mathbf{B}_{CRS,NNR,q} = \begin{bmatrix} \cos\alpha_q \sin\delta_q & -\sin\alpha_q \\ \sin\alpha_q \sin\delta_q & \cos\alpha_q \\ \sin\delta_q & 0 \end{bmatrix} \tag{2.26}$$

where (α_q, δ_q) are the right ascension and declination, respectively. This means that there is no global rotation with respect to the a priori CRF.

As for the ground stations, the NNR means the orientation cannot be changed to the a priori TRF. The sum of the rotations from station coordinate corrections of a network is zero. For a station s, the NNR reads:

$$\mathbf{B}_{TRS,NNR,s} = \begin{bmatrix} 0 & z_s & -y_s \\ z_s & 0 & x_s \\ y_s & -x_s & 0 \end{bmatrix} \tag{2.27}$$

The NNT conditions mean that no translation between the a priori network and the estimated one, that is, the sum of all the corrections of the network stations is zero on each of the x, y, and z components. The NNT conditions for the station s read:

$$\mathbf{B}_{TRS,NNT,s} = \begin{bmatrix} 1 & 0 & 0 \\ 0 & 1 & 0 \\ 0 & 0 & 1 \end{bmatrix} \tag{2.28}$$

The NNS conditions mean the scale of the a priori network is the same as the estimated one. The matrix reads:

$$\mathbf{B}_{TRS,NNS,s} = \begin{bmatrix} x_s \\ y_s \\ z_s \end{bmatrix} \tag{2.29}$$

The NNS is usually not applied, as the scale is one of the most parameters to be estimated in geodetic techniques. One applicable scenario for NNS is to estimate the GNSS satellite antenna phase offset and variation (Ge et al., 2005b; Schmid et al., 2007).

2.3 Multi-technique combination

As mentioned in Table 2.1, the four space geodetic techniques have different sensitivities to different parameters and contribute to different aspects of the ITRF realization. For instance, the ITRF2014 is specified as (Altamimi et al., 2016): (1) origin defined by the ILRS SLR solution, (2) scale defined as the average of VLBI and SLR solutions; (3) orientation defined as zero rotation between ITF2014 and ITRF2008. On the other hand, the GNSS and DORIS solutions (especially the large number of GNSS stations) densify the global network and contribute to modeling the postseismic deformation.

The combination can be implemented on the observation level, on the normal equation level, and on the parameter level. The concept of these three levels is first introduced in this section. As mentioned in Section 1.1, the combination of different techniques needs common parameters or external measurements to connect these parameters, that is, the global tie, local tie, space tie, and tropospheric tie. The methods of handling these ties are also presented in this section.

2.3.1 Combination level

One of the major goals to combine different techniques is the realization of the reference frame, especially the terrestrial reference frame. Here the procedure to realize the TRF is used to demonstrate the three levels of combination.

The three levels of TRF determination depicted in Figure 2.5. From left to right: on the parameter level (red), on the normal equation level (blue), and on the observation level (green).

According to Altamimi et al. (2016), the two steps to determine ITRF on the parameter level from the session-wise solutions of the four techniques are:

> *(1) stacking the individual time series to estimate a long-term solution per technique comprising station positions at a reference epoch, station velocities, and daily EOPs, and*
>
> *(2) combining the resulting long-term solutions of the four techniques together with the local ties at colocation sites.*

However, before the first step, the session-wise solutions (NEQs) of each technique have to be generated from the raw observations, which is the input for ITRF and usually done by the Technique Centers (TC) and corresponding Analysis Centers (AC). Therefore, the procedure is expanded to three steps, which start from the raw observations.

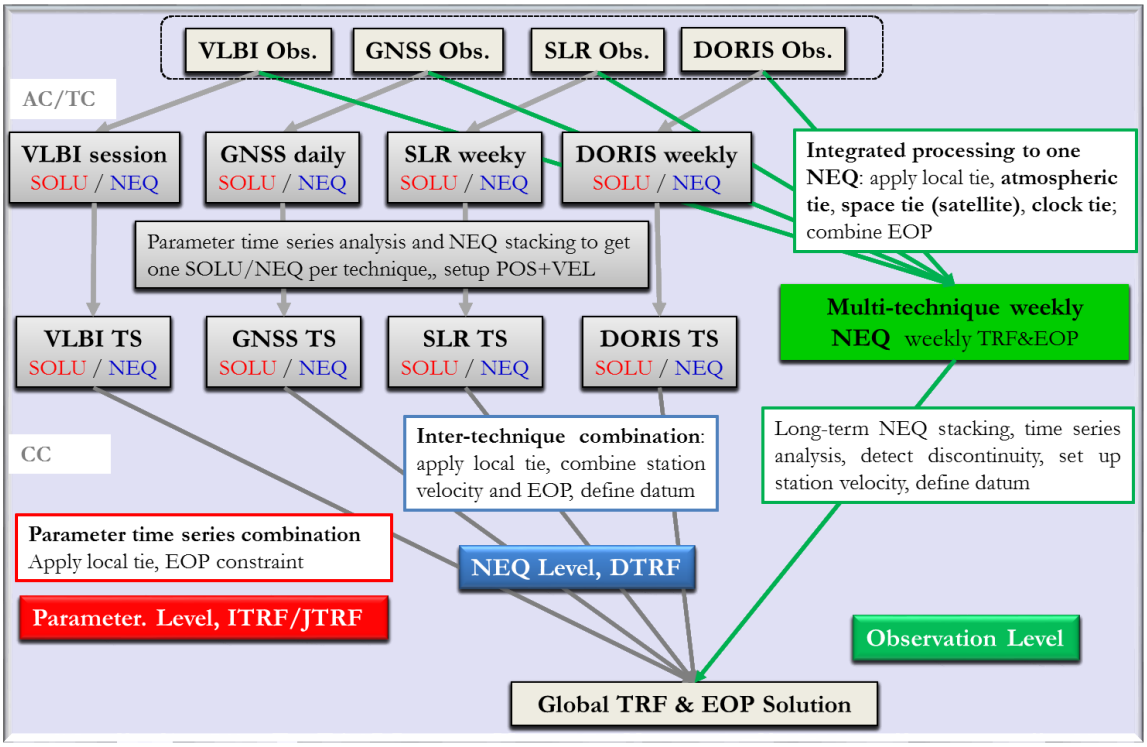

Figure 2.5 Description of the TRF determination method: on parameter level (in red), on normal equation level (in blue), and on observation level (in green). "TS" means time series in this figure. TC, AC, and CC for technique center, analysis center, and combination center, respectively.

For each technique, the session-wise (or daily, weekly) solutions and (or) NEQs are submitted to the TC (that is, IGS, IVS, ILRS, and IDS), which performs the intra-technique combination. Usually only the EOP and station coordinates are kept in the submitted NEQ. Other parameters, .for instance, the satellite orbits, tropospheric parameters, clocks, are all pre-eliminated. It is also required that the NEQ should be datum-free, that is, without any constraints. However, it is not always the case, as some minimum or loose constraints might be applied by some ACs, see Table 1 in Altamimi et al. (2016). Each TC then generates the combined session-wise (or daily, weekly) solution.

In the second step, the long-term time series are generated for each technique. This is the "step 1" in the ITRF determination. The station position time series analysis aims to capture both the linear and non-linear motions. The latter includes discontinuities, periodic signals, postseismic deformation. The outlier elimination is also performed based on the time series analysis.

In the third step, the four long-term solutions are combined, with the LTs and velocity constraints at co-located stations applied and the EOP ties applied. The weights of different techniques and the LTs are tested iteratively, aiming to achieve the comparable a posteriori variance factors for the four technique solutions (variation within 10% of the unity). After adjusting the weights, the EOP ties are applied. The weight will be re-adjusted after applying EOP ties if necessary. Then the final combined TRF and EOP is achieved.

The method of combination on the parameter level is also adopted by the ITRF realization at JPL: JTRF (Abbondanza et al., 2017). The unique feature of JTRF is the Kalman filter. Instead of using the least-squares adjustment to determine the positioning at the reference epoch and the corresponding velocity, the JTRF determines the time-varying weekly TRF.

On the other hand, a combination on the NEQ level is always the pursue of the TRF realization at DGFI-TUM: DTRF. It also consists of three steps: (1) session-wise (or daily, weekly) NEQ determination by the TC and AC; (2) intra-technique combination of accumulating the long-term normal equations for each technique; (3) inter-technique combination of the four long-term NEQs. The time series analysis and the reweighting are applied. The most important difference compared to the combination on the parameter level is that the correlation information between the parameters is saved (Rudenko et al., 2018).

The combination on the observation level, however, is quite different from the above two methods. Instead of single-technique TRF determination, the multi-technique NEQ is directly derived from the raw observations. Then the long-term NEQs can be analyzed, stacked, and form the TRF, either using the least-squares adjustment or using the Kalman filter.

Therefore, it is clear that combination on parameter level and NEQ level both need an intra-technique combination and long-term time series analysis, which can be done with different software packages. If no special care is taken, the inconsistencies of the a priori models, the parameterization, and the processing method will be obvious, which will further affect the parameter estimates. Even if special efforts are made to guarantee the best consistency of the

single-technique NEQs there are still the following differences between combination on the parameter level and that on the NEQ level (Seitz et al., 2012):

- *When combining normal equation systems, corrections of the original observations are estimated. In case of combining solutions, the parameters of the input solutions are corrected.*
- *If normal equation systems are used as input data, in principle no a priori datum conditions in form of pseudoobservations are added to the individual input normal equations. In case of combination of solutions the input solutions have to be generated applying datum conditions. In order to ensure undeformed input data sets, the so-called minimum conditions are necessary.*
- *In order to be free to select the geodetic datum of the reference frame, in case of combination of solutions it is necessary to estimate parameters of a similarity transformation between the final and the input solutions. The estimated transformation parameters, which should represent the datum differences, might absorb non-modelled station movements. This can lead to biases in the estimated station coordinates and can affect the realization of the geodetic datum parameters origin and scale (Drewes, 2008). A further aspect to be kept in mind is that the results depend on the selection of stations used for the transformation.*

To summarize it up, the combination on parameter level loses the correlation information between different parameters, and mixes the datum definition.

On the other hand, a combination on the observation level can remedy all the above-mentioned inconsistencies. First, the best consistency in conventions, modeling, and parameterizatoion between different techniques can be easily achieved as the same software is used. Despite the continuous efforts in pursuing the consisntency between different software, it is not easy to keep fundamental constants, conventions, and parameterization exactly the same, especially for some of the sophisticated software packages with decades of ongoing development. Second, the pre-eliminated parameters can also be tied when combining on the observation level, for instance, the tropospheric delay and clock parameters. Of course it is theoretically possible to keep all these parameters in the NEQ and then apply the ties. However, it is not practical as an enormous NEQ is required. Taking the GNSS and VLBI combination as an example, to keep the tropospheric parametes at 20 co-location sites, additional 800 parameters (hourly ZTD and 3-hourly gradients) have to be kept in a dail NEQ per technique, not to mention the huge amount of epoch-wise clock parameters. Third, the inter-technique outlier detection is also possible, meaning that the solution will be more robust. Thanks to the contribution of multi-technique, the combined solution will be stronger and so that the capablity of detecting and identifying irregular observations and inaccurate modelling will be increased. Last but not the least, using one software for multi-technique integrated processing allows one to diagnose the systematic biases in parameter estimates. For example, the LOD biases in satellite techniques can hardly be handled in the single-technique solutions. Having LOD aligned with the VLBI estimate in the integrated solution will introduce systematic biases to other parameters, for instance, the orbit dynamic parameters, and these parameters can then be investigated for a better dynamic orbit modeling.

2.3.2 Handling the ties

The common parameters and external observations are necessary to combine different techniques. Namely, the global ties (EOP), the local ties, and the space tie. The tropospheric clock ties contribute to a more robust solution, but solely it does not provide any datum constraints.

To apply the ties, two methods are available: (1) using the pseudo-observation, and (2) directly stacking the NEQs of the common parameter. The first one can be applied for all the ties and is more convenient to be handled. However, the corresponding weights for the pseudo-observations should be determined with great caution, as a constraint too loose cannot rigorously tie the parameters whereas one too tight could cause numerical problem in solving the NEQ due to the extreme large weight. On the other hand, directly stacking the NEQs for the common parameters only works for the global tie, the tropospheric tie, and the space tie, on the condition that the differences can be modeled to the a priori value. This method is especially recommended for the space tie as the dynamic orbit cannot be described with pseudo-observation.

Global ties (EOP)

The global ties refer to the common parameters observed by different techniques, that is, EOP (Seitz et al., 2012; Glaser et al., 2017). Specifically, global ties refer to the polar motion and LOD, as they are the only EOP components that are observed by all the techniques. The nutation rates can also be used as global ties (Thaller et al., 2006; Thaller, 2008), but they are usually not included in the solutions of satellite techniques. Moreover, the LOD estimates from satellite techniques are well known biased in the long-term signals, which requires special handling. Thus, the polar motion offsets and rates are the most used global ties.

For the global tie modeling, the piece-wise linear function is most used. In this way, the EOP offsets and rates can be effectively connected, and any session time can fit in. For more details about the PWL function, it is referred to Rothacher et al. (2011).

The LOD differences of different GNSS solutions compared to the IERS 14 C04 product (also referred to as the C04 product in the following chapters) are shown in Figure 2.6. The 14-day smoothed values are shown in red. The LOD estimates of all the AC solutions except for the IGS combination show visible biases, including both constant and annual (and semi-annual) signals. However, the IGS combined LOD is not a GNSS-only solution, as it is calibrated with a sliding window of 9-day (or 14-day) using the LOD estimates from the IERS rapid product (the Bulletin A product), which is derived from VLBI. Despite the slightly larger fluctuation in 2006–2007, the 14-day STD values are about 9–11 μs/day for all the solutions.

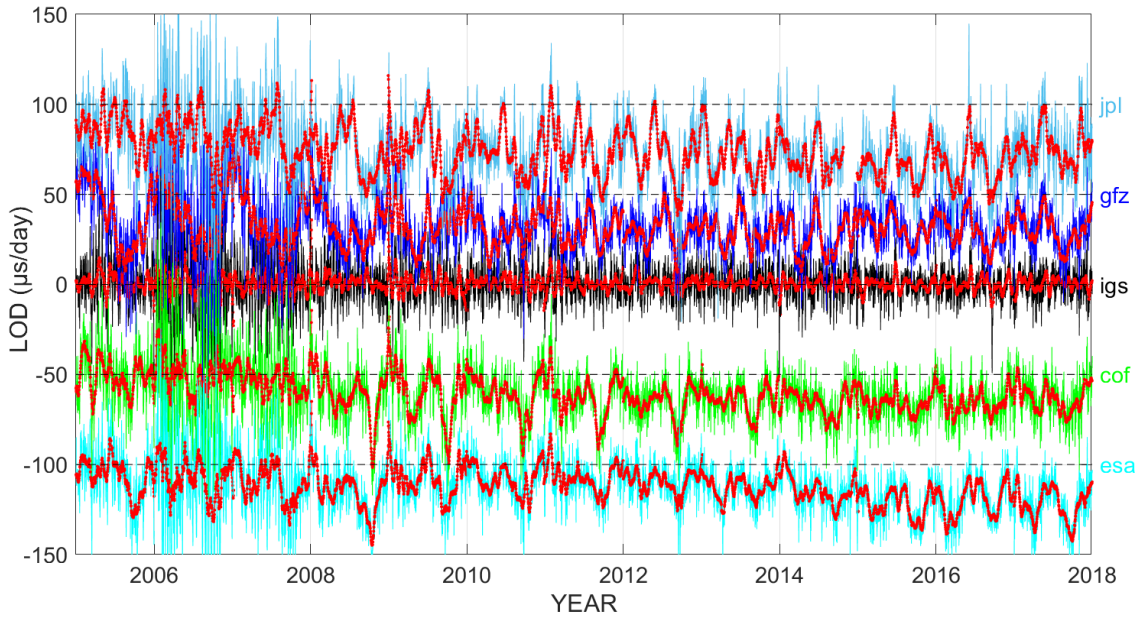

Figure 2.6 LOD differences between the solutions of IGS and ACs and the IERS EOP 14 C04 product in 2005–2017, offset by multiples of 50 μs/day for clarity. The smoothed bias (14-day window moving mean values) of each solution is shown in red.

Local tie

The co-location is defined as two or more space geodetic instruments close to each other with the three-dimension station coordinate differences precisely surveyed using either classical (total station) or GNSS surveys. Usually, the co-located instruments are within a few hundred meters, but sometimes the distance can be tens of kilometers. The local tie is defined as the station coordinate difference vector between the different instruments. Additionally, the co-located stations also share the same velocity over a long-term period, and the velocity tie can be applied in TRF determination. Local ties with proper uncertainties are essential in multi-technique TRF determination, and it is the most straightforward tie to link these techniques. However, the local tie number is still far from enough, especially for VLBI–SLR co-location. The local tie uncertainty tends to be optimistic, and the performances at different co-locations vary considerably. Moreover, the LT should be updated in time, especially for the GNSS related co-locations, due to the frequent discontinuity in GNSS time series caused by instrument changes. The LT vectors are provided in the SINEX files and available from the ITRF website[34].

The LT discrepancies between local surveys and the space geodetic solutions from ITRF2014 is shown in Figure 2.7. The 3-D mean discrepancy is calculated as the root of the mean squares of differences on the three station coordinate components. As one can see, the available inter-technique LT distribution is very uneven, especially for the SLR–VLBI co-location with only 15 LTs available. As for the inter-technique discrepancies, the GPS–VLBI co-locations show the best agreement with a median value of 4.1 mm. All the intra-technique co-locations agree

[34] http://itrf.ensg.ign.fr/local_surveys.php

with each other with the median values less than 5 mm. The largest discrepancy is the GPS–DORIS co-locations, with a median value of 6.6 mm. Worth mentioning that the discrepancy in this figure is the residual after adjustment, meaning that LTs are re-weighted to fit the combined solution. Therefore, it does not necessarily indicate the real offset and accuracy.

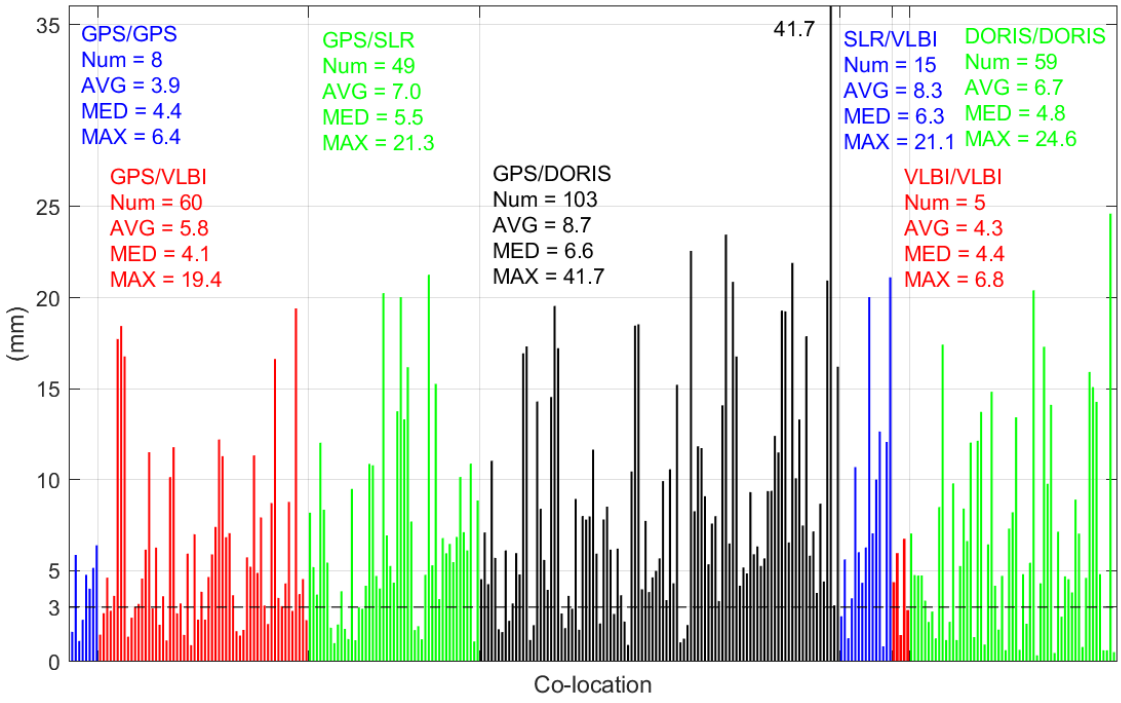

Figure 2.7 The LT discrepancies between local surveys and space geodetic solutions from ITRF2014. The 3-D mean biases of each co-location are presented.

Space tie

Space tie is defined as the coordinate difference vector between different instruments on-board one satellite, as the satellite orbit can only be described by one set of dynamic parameters. The space tie is mainly on the GNSS and LEO satellites.

- For the GNSS satellites with LRA, the GNSS and SLR techniques can be connected by the same satellite (Thaller et al., 2011; Hackel et al., 2014; Bury et al., 2020). By observing the GNSS signals from a VLBI radio telescope, the GNSS and VLBI techniques can also be integrated (Anderson et al., 2018; Klopotek et al., 2020).

- For the LEO satellites, several instruments are usually available. The GNSS receiver and DORIS payload are the two major instruments on-board the LEO satellite for orbit determination. On the other hand, most of the LEO satellites are equipped with LRA. The LEO co-location has been investigated (Männel, 2016; Koenig, 2018; Montenbruck et al., 2018a). The concept of putting a VLBI transmitter on-board LEO satellites with all the other three techniques, for instance, GRASP (Bar-Sever et al., 2009), is a perfect example of space co-location.

A useful list of the potential space co-location satellites and the corresponding instruments is given by Männel (2016), in Table A.1 and A.2.

Studies about space ties are mainly about combining the GNSS and SLR techniques to improve SLR solution, estimate GNSS antenna PCO, and determine consistent TRF from the two techniques. Pioneering studies on VLBI satellite tracking are mainly focusing on the simulation (Männel et al., 2014; Männel and Rothacher, 2015; Anderson et al., 2018; Klopotek et al., 2020).

Atmospheric tie

For co-located stations, microwave signals going through the same atmosphere should hold the same delay. Therefore, the tropospheric tie is defined as the offset of tropospheric parameters from different techniques due to the station location and instrumental effects. Assuming that the tropospheric parameter estimates are accurate and free of any instrumental effects, the tropospheric tie is simple the difference due to station location, especially the height difference.

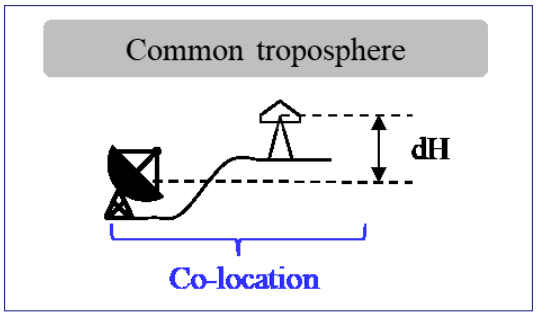

Figure 2.8 Illustration of the tropospheric ties at a GNSS and VLBI co-location site. The station height difference is presented as dH.

Another possible atmospheric tie is the ionospheric tie. The ionospheric delays for GNSS, VLBI, and DORIS are frequency-dependent and can be described as a function of the TEC and frequency. Therefore, the common ionospheric delay information can be shared by different techniques.

Nevertheless, the atmospheric tie refers to tropospheric tie in this thesis unless explicitly stated, as the ionospheric delay is not in the topics of this thesis.

Clock tie

If co-located instruments are connected to the same clock, the common clock model can be used for different techniques, which will reduce the parameter number and contribute to stabilizing the solution. However, due to the intra- and inter-system delay changes and the temperature variation, special care needs to be taken. Primary studies have been done in

GNSS–VLBI co-location (Hobiger and Otsubo, 2014) and VLBI twin-telescopes (Nilsson et al., 2015).

2.3.3 Relative weighting

The relative weighting of different techniques is always a tricky problem. First of all, it is not reasonable to directly combine the parameters from different techniques using their nominal uncertainty, nor to stack the NEQs without any modification.

Theoretically, the variance component estimation (VCE) can be used (Koch, 1999). However, it is not the case in reality. For combination on the parameter level, the mathematically or statistically VCE can hardly be used (Bähr et al., 2007; Altamimi et al., 2016). This is mainly because different observations and constraints at co-locations are used: space geodetic solutions, LTs and velocity ties; and the LTs and velocity ties have significant discrepancies, whose impact should be reduced by the weighting process.

For the ITRF2014 determination, an iterative weighting strategy is applied. In the first step, the a posteriori variance factors are derived from each technique using the long-term solutions. A primary combination is done with these values, and the LTs are applied using the corresponding variances. The discrepant ties are down-weighted to ensure that the variation of a posterior variance factor of each technique is within 10% of the unity. The reweighting of different techniques are performed again after applying the EOP ties, if the EOP estimates from different techniques do not match.

As for a combination on the NEQ level, the VCE is also not adopted. It is explained that (Seitz et al., 2012) only the EOP and co-located velocities can be combined directly and work as common parameters, while the contribution of station coordinates to the variance components is small due to the indirectly applied LTs. More importantly, the stochastic model error of each technique cannot be considered by the classical VCE, while the GNSS uncertainty is well known as over-optimistic due to the ignoring of the correlation between observations (Schön and Kutterer, 2007; Schön and Brunner, 2008). Therefore, the VC is empirically defined as the ratio of nominal uncertainty σ_{est} to the standard deviation of the coordinates σ_{TS} (Rothacher et al., 2011; Seitz et al., 2012):

$$VC = \frac{\sigma_{est}^2}{\sigma_{TS}^2}; \sigma_{TS} = \frac{RMS}{\sqrt{n}} \tag{2.30}$$

where RMS is the root mean square of the station position residual time series and n is the number of epochs.

A similar method is adopted by Thaller (2008), where a weighting factor is defined as the ratio of mean main-diagonal elements of NEQ corresponding to the station coordinates to the coordinate repeatability.

However, the relative weighting values of different techniques used by different studies disagree with each other significantly. In ITRF2014 determination, the square roots of a posteriori variance factor are 2.30, 4.80, 5.02, and 2.62 for GNSS, VLBI, SLR, and DORIS, respectively. Then the DORIS is rescaled by a factor of 3.5 after applying the local ties, and the SLR polar motion estimates are down-weighted by a factor of 2. As for DTRF2008, the VC values of VLBI, SLR, and DORIS are around 1 (1.38, 1.28, and 1.03, respectively), while that of GPS is 0.34. Therefore, the GPS NEQ is down-weighted by a factor of 3, the As for the weighting factor used by Thaller (2008), the weighting factors (not the VC values) for GPS, VLBI, and SLR are 1.0, 3.76×10^{-06}, and 0.17.

On the other hand, none of the above-mentioned methods can be applied in the integrated processing, that is, the combination on the observation level. As the epoch-wise NEQs from all the techniques are stacked at the first step, rescaling the NEQs is not an option. Therefore, weighting the observations from different techniques is critical before the integrated processing. The method used in this thesis will be described in the next chapter.

2.4 Chapter summary

The main findings in this chapter are summarized as follows.

Section 2.1 describes the concept and background of the four space geodetic techniques. The focus in this section is on the basic knowledge about how different techniques work.

Section 2.2 presents the mathematical delay models of GNSS, VLBI, and SLR. Instead of giving the model of each technique one by one, here the delay models are described more homogeneously, as the basic observables of these techniques are all time delay. The delay modeling involves deriving the instantaneous coordinates of the signal reference point from the reference frames and modeling the atmospheric effects and instrumental impact on signals transmitting time. A comparison of different techniques is summarized here.

- All three techniques can determine TRF and reach satellite orbits, while only VLBI can determine CRF. In terms of TRF, SLR contributes to the origin and scale, and VLBI can only contribute to the latter one. GNSS has huge potential to contribute to both origin and scale, but more efforts are required, including the improved orbit modeling and pre-calibrated satellite antenna phase center offset.

- Only VLBI can determine the full EOP set, while GNSS provides the best PM estimates due it the globally distributed network. Satellite techniques can contribute to the rates of the dUT1 and CPO components, if the systematic biases can be carefully calibrated.

- Both GNSS and VLBI have the same sensitivity to tropospheric and ionospheric delays, as the first delay is always estimated and the latter one is mostly eliminated by the dual-frequency observations. For SLR, the ionospheric delay is small enough to be ignored

while the tropospheric delay has to be modeled using external data, that is, meteorological observation or NWM.

Section 2.3 discusses the method of multi-technique combination, including the different levels for combination, the ties to be applied, and the handling of relative weighting.

- The three different levels for combination are described in detail, using the TRF determination as an example. The pros and cons are discussed.
    - The combination on the parameter level is convenient to be implemented and adopted by ITRF and JTRF, but loses the parameter correlation information and mixes the datums, not to mention the inconsistency from different solutions.
    - The combination on the NEQ level avoids the problems in that on the parameter level but still cannot guarantee the best consistency as different software packages are used to generate the NEQs. It is also not feasible to apply all the ties due to the potential enormous NEQ to keep the corresponding parameters, especially the clocks and atmospheric parameters.
    - The combination on the observation level provides the best consistency between different techniques and enables all the possible ties to be applied. It also allows detecting systematic bias of different techniques.
- Different types of ties can be applied in the combination, including global ties (EOP), local ties, space ties, atmospheric ties, and clock ties.
    - Only the LTs and space ties transfer the datum information between different techniques, while atmospheric ties and clock ties improve the solution robustness.
    - It is more feasible to use the pseudo-observation to apply all the ties, except for the space ties, where the method of NEQ stacking is more appropriate.
    - It is critical to investigate the systematic biases in EOP ties, space ties, atmospheric ties; while for local ties the uncertainty values can introduce a significant impact on the integrated solution
- As for the relative weighting, there is no rigorous strategy with a solid theoretical background yet. However, it is important to keep the unity of a posteriori variance factor in each single-technique solution. As the nominal uncertainty of GNSS is usually over-optimistic than that of other techniques, this has to be taken into consideration.

3 Space geodetic data processing in the PANDA software

The implementation of VLBI and SLR modules are presented in this chapter. Starting with a description of the multi-technique software packages, the PANDA software is then introduced. The data processing procedure of GNSS, VLBI, SLR, and multi-technique solutions is then presented.

3.1 Platforms for space geodetic data processing

Several software packages are capable of processing more than one technique, with different characteristics. The following listed software packages, unless explicitly stated, are all developed in the Fortran language.

- The very first one is reported as GEOSAT (Andersen and Rekkedal, 1995; Andersen, 1996) at Norwegian Mapping Authority, which can process all the four techniques. Starting from 2015, the GEOSAT was abandoned and a new software package called Where in the Python language is under development (Kirkvik, 2017; Kirkvik et al., 2018). The software aims to process all the techniques, and now has contributed to the IVS solution of ITRF2020. The software is an open-source project and available at GitHub[35].

- The GINS/DYNAMO [36] (Géodésie par Intégrations Numériques Simultanées) software developed by Groupe de Recherches de Géodésie Spatiale (GRGS) has been used for the combination of four techniques (Yaya, 2002; Bourda et al., 2007a, 2007b; Coulot et al., 2007; Gambis et al., 2009; Marty et al., 2011; Gambis et al., 2013). However, despite the capability of processing all the techniques in one software, the combination was done on the NEQ level, that is, the NEQs from different techniques are stacked.

- The Bernese[37] software is an excellent tool in processing GNSS and SLR observations (Dach et al., 2015), and several studies have been conducted combining these two techniques (Thaller et al., 2009; Thaller et al., 2011; Fritsche et al., 2014; Hackel et al., 2014; Bury et al., 2020). The VLBI module in Bernese was first implemented by Schmid (2009) and demonstrated later (Männel, 2016). However, the Bernese software

[35] https://github.com/kartverket/where
[36] https://grgs.obs-mip.fr/recherche/logiciels/gins/
[37] http://www.bernese.unibe.ch/

cannot process different techniques on the observation level simultaneously[38]. On the other hand, a powerful module to combine NEQs from different techniques are available in Bernese and was used for the combination studies (Glaser et al., 2015).

- The NAPEOS[39] (Navigation Package for Earth Observation Satellites) developed at ESOC is capable of processing GNSS, SLR, and DORIS on the observation level (Svehla et al., 2010; Springer et al., 2011; Otten et al., 2012). The VLBI module was started in 2015 (Flohrer et al., 2016), and can process single-session with high-precision EOP estimation (Flohrer et al., 2017, 2018).

- The DOGS (DGFI Orbit and Geodetic parameter estimation Software) has several components, including DOGS-RI (Radio Interferometry) for VLBI processing (Glomsda et al., 2018), DOGS-OC (Orbit Computation library) for SLR and DORIS (Bloßfeld et al., 2015; Bloßfeld et al., 2018a), and DOGS-CS (Combination and Solution library) for combination (Bloßfeld et al., 2018b).

- The GipsyX/RTGx[40] developed at JPL, is a re-designed software package using the C++ language from the old GIPSY-OASIA and REAL-Time GIPSY (RTG), with the capability of processing GNSS, SLR, and DORIS. The VLBI module is under development (Bertiger et al., 2020).

- The GEODYN[41] developed at Goddard Space Flight Center in NASA, is a set of software tools for orbit determination and geodetic parameter estimation. It was originally used to process GNSS, SLR, DORIS, and other satellite tracking techniques, while the VLBI module is also available with good OMC agreement to the VLBI-specified software: Calc/SOLVE (Lemoine et al., 2009). A study on combining VLBI and SLR has been conducted using GEODYN (MacMillan et al., 2009).

- The EPOS-OC[42] (Earth Parameter and Orbit System) software package is a collection of tools around the core of module "OC" (Orbit Computation). It is dedicated to processing satellite tracking techniques, including GPS, SLR, DORIS, Radar altimeter, accelerometer. (Zhu et al., 2004; Rudenko et al., 2011; Glaser et al., 2017). The VLBI module was newly implemented, and several simulation studies have been conducted for TRF determination on the NEQ level (Glaser et al., 2016; Glaser et al., 2017; Glaser et al., 2018; Glaser et al., 2019).

- The C5++ software[43] with the capability of handling GNSS, VLBI, and SLR (Hobiger et al., 2010; Hobiger et al., 2011) is the very first one to be demonstrated in the combination on the observation level of GNSS and VLBI (Hobiger and Otsubo, 2014; Hobiger et al., 2015), and VLBI and SLR (Hobiger et al., 2014). The software consists

[38] Männel, Personal communication
[39] http://www.esa.int/Enabling_Support/Operations/NAPEOS
[40] https://gipsy-oasis.jpl.nasa.gov/index.php?page=software
[41] https://space-geodesy.nasa.gov/techniques/tools/GEODYN/GEODYN.html
[42] https://www.gfz-potsdam.de/en/section/global-geomonitoring-and-gravity-field/topics/earth-system-parameters-and-orbit-dynamics/earth-parameter-and-orbit-system-software-epos/
[43] https://www2.nict.go.jp/sts/stmg/www3/c5++/

of a common library and the VLBI, GPS, and SLR modules, written in the C++ language. It is recently updated to process VLBI near-field objects tracking observations (Klopotek et al., 2017; Hobiger et al., 2018; Klopotek et al., 2019; Klopotek et al., 2020).

Even though so many software packages can process multi-technique observations, only the C5++ was demonstrated to process more than one technique on the observation level.

On the other hand, several single-technique software packages are also well-known and widely used.

- The GAMIT[44] (GNSS at MIT) software has a long history back to the 1980s, and is widely used in geophysical applications (Psimoulis et al., 2018; Shrivastava et al., 2019). The IGS analysis center at GFZ uses the EPOS.P8 (Uhlemann et al., 2015) software for routine processing and reprocessing. Other GNSS software packages with the focus on positioning instead of orbit determination, for instance, RTKLIB[45] and GPSTk[46] both in C++ language, usually cannot estimate the whole set of geodetic parameters, especially the orbits and EOP.

- For VLBI, several software packages dedicating to the VLBI-only solution are available, for instance, the Calc/SOLVE[47][48] software developed at NASA is used by several IVS analysis centers, including ASI CGS, BKG, NASA GSFC, Paris Observatory, and USNO. Its new version nuSolve[49] is open-sourced. The two MATLAB-based software packages: VieVS[50] and PORT are developed at Technical University of Vienna and GFZ, respectively, and are both dedicated to high-precision VLBI data analysis. The VieVS software is open-sourced at GitHub[51]. The OCCAM software is used by the IVS analysis centers at DGFI-TUM and Geoscience Australia[52] (Titov et al., 2004; Geoscience, 2010). Developed at the Institute of Geodesy and Geoinformation of the University of Bonn using C++ language, the ivg::ASCOT[53] is dedicated to VLBI analysis, scheduling, and combination.

Nevertheless, to perform the multi-technique analysis, it is optimal to use a software package with the corresponding capabilities available, or at least the critical components available. For the four space geodetic techniques, the precise orbit determination module (specifically, the numerical orbit integration) is the most important one. In this thesis the Positioning And Navigation Data Analyst is used to implement the VLBI and SLR modules and further process multi-technique observations.

---

44 http://geoweb.mit.edu/gg/
45 http://www.rtklib.com/
46 https://gitlab.com/sgl-ut/GPSTk
47 https://space-geodesy.nasa.gov/techniques/tools/calc_solve/calc_solve.html
48 http://astrogeo.org/psolve/
49 https://sourceforge.net/projects/nusolve/
50 https://vievswiki.geo.tuwien.ac.at/doku.php
51 https://github.com/TUW-VieVS
52 ftp://ftp.ga.gov.au/geodesy-outgoing/vlbi/software/
53 https://nain.oso.chalmers.se/ascotwiki/index.php?n=Main.HomePage

3.2 Introduction of the PANDA software

The PANDA software (Liu and Ge, 2003; Shi et al., 2008) is capable of processing GNSS observations, in both real-time and post-processing modes, with very high quality. The precise satellite orbits and clocks of both GNSS satellites (GPS, GLONASS, Galileo, and BDS) and LEO satellites can be precise determined with an accuracy comparable to the IGS official products and other ACs (Li et al., 2018). The POD and PCE capabilities have been demonstrated by several studies (Ge et al., 2017; Huang et al., 2020a; Huang et al., 2020b). A vast range of applications using the software have been performed (Penna et al., 2018; Wang and Liu, 2019; Wang et al., 2019; Wu et al., 2019). The PANDA software is also used by the IGS analysis centers at WHU[54], SHAO (Chen et al., 2017), and several other ACs of the iGMAS[55].

For a typical data processing procedure, the following modules in the PANDA software are usually involved (program name are presented in upper cases):

- Data conversion and preparation, including clock and orbit conversion (*sp3orb, orb2sp3, brd2clk, brd2sp3, sp3brd, brdg2n*), EOP conversion (*conveop, eopupd*), *check_rnxnav* to check the broadcast ephemeris, *atx2sat* to update the satellite parameter table, and LEO-related file format conversion (*grc2rnx, convatt, convacc*).

- Preprocessing of the observations and other auxiliary information, including cleaning the GNSS observations (*trimcor* and *turboedit*), scanning the observation files and collecting related information (*presrif*), deriving the a priori station coordinates (*spp*).

- Parameter estimation, that is, the *lsq* program to calculate the observatmio-minus-calculation (OMC) and perform the least-squares adjustment.

- Orbit integration (*oi*) and orbit fitting (*orbfit*).

- Data cleaning based on the post-fit residuals (*edtres*).

- Ambiguity fixing modules for either a network solution or a single station PPP (*ambfix*, *upd_wl*, *upd_nl*).

- Multi-day NEQ combination, that is, stacking the daily NEQs (*comb*).

- Miscellaneous functions, for instance, manipulating the clock files (*extclk*, *clkfit*, *clkdif*), retrieving the tropospheric parameters (*extztd*, *extstd*) and kinematic station coordinates (*extkin*), handling the biases (*extifsb*).

The newly implemented VLBI and SLR modules follow a similar processing procedure as above. Specifically, the following programs are implemented.

[54] http://www.igs.gnsswhu.cn/index.php/Home/Index.html?lang=en-us
[55] http://www.igmas.org/

- Data format conversion, for instance, converting the SLR CRD file to the RINEX-like observation and meteorological files (*npt2rnx*).
- Preprocessing of the observation and auxiliary information for VLBI (*prevlbi*), SLR (*preslr*), and the integrated processing (*precolc*).
- Parameter estimation. The OMC and partial derivatives of VLBI and SLR are both implemented in the existing *lsq* program.
- Outlier detection. The outlier detection of VLBI and SLR are both implemented in the existing program *edtres*.
- Miscellaneous functions, including *apl2rnx*, *aplgrd2rnx*, *check_lt*, *clk_merge*, *vmf2rnxm*, *slr2log*, *sumnpt*.

In addition to these new programs handling VLBI and SLR, the following modules are implemented within the existing programs.

- The transformation between TRS and CRS is revised carefully to rigorously follow the IERS 2010 Conventions and the latest updates.
- The station displacements, including the solid Earth tides loading, the ocean tides loading, the pole tide loading, ocean polar tide loading, the S1-S2 atmospheric pressure loading, are all revised and applied according to the IERS2010 Conventions. The non-tidal atmospheric tide loading displacement is also applied using the product from either VMF[56] or GGFC[57].
- The tropospheric delay models are updated to include the GPT2/VMF1 and GPT3/VMF3 products, and the high-order tropospheric gradients are also available.
- Other functions not related to this thesis but worth mentioning, for instance, the first order ionospheric delay correction using GIM and broadcast ephemeris.

The data processing procedures of GNSS, VLBI, SLR, and integrated-solution will be introduced in the following sections.

3.3 GNSS data processing

The basic data processing flowchart of GNSS precise orbit determination is shown in Figure 3.1. The data preprocessing is performed in the *presrif* program, where the station and satellite information is collected from the observation files, satellite and station meta-data files. The program *trimcor* handles the receiver clock jump, and the program *turboedit* performs basic data cleaning (Blewitt, 1990), including the cycle slip and outlier detection. Meanwhile, the orbit integration program *oi* generates a priori orbit file, which is then dynamically fitted to be closer

[56] https://vmf.geo.tuwien.ac.at/
[57] https://geophy.uni.lu/atmosphere-downloads/

to the broadcast ephemeris or any predicted orbits using *orbfit*. Then the orbit file is updated using these fitted dynamic parameters and further used in the parameter estimation.

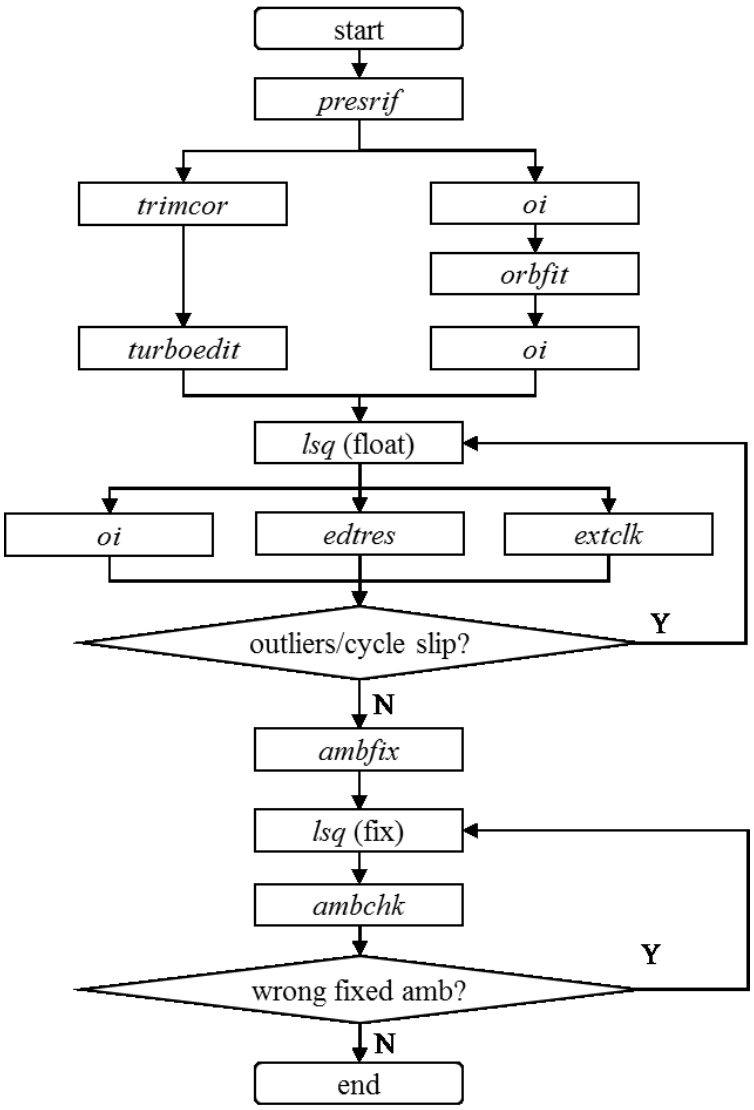

Figure 3.1 Flowchart of the GNSS data processing, taking precise orbit determination as an example. The functions are explained in Table C. 1.

The parameter estimation is performed in the major module *lsq*, where the least-squares adjustment is applied. In this program, the observation files are read in, and the epoch-wise partial derivatives and OMC are calculated and then contributed to the NEQ. At the end of the session, the NEQ is inversed to derive the estimates. The orbits and clocks are updated using *oi* and *extclk*. The program *edtres* performs quality control, that is, the detection of cycle slips and outliers. If new outliers or cycle slips are marked, this updated quality control information is used for the next iteration. It should be noted that in this parameter estimation iteration the ambiguities are estimated as float values.

If there are no more new cycle slips or outliers, the ambiguity fixing is performed in *ambfix*, where the double-differenced ambiguities are formed and the integer ambiguities are estimated. With the ambiguity fixing information available, the last round of parameter estimation can be

performed with double-differenced ambiguities constrained to integers. Depending on the observation quality and the time-consuming requirement, the ambiguity fixing can also be performed iteratively, and the program *ambchk* can be used to check if there are mis-fixed ambiguities.

If the orbit parameters are not estimated, such as in precise clock estimation or precise point positioning, then the orbit parameters are not updated and the a priori orbits, for example, from the IGS and ACs, are used. In the case of PPP, the satellite clocks are also not updated and kept fixed to the a priori precise clock.

In this section only the very basic GNSS data processing flowchart is introduced, and no more details are presented. The sophisticated GNSS modules and processing strategy are already mature. The major object of this study is the implementation of the VLBI modules and the integrated processing of GNSS and VLBI, and thus more focus will be put on the VLBI part.

3.4 VLBI data processing

3.4.1 VLBI processing flowchart

The VLBI data processing flowchart is shown in Figure 3.2. Starting with the program of *prevlbi*, the session-wise observation file in the form of NGSCARD is scanned to collect the information of the radio telescopes and AGN involved in the session. The station and AGN lists are then written into a new control-file, where the initial coordinates taken from the ITRF and ICRF file are also stored. Other related information, such as the antenna data and default user setup, are also output to the control-file. The NGSCARD is also checked for meteorological observations, cable calibrations.

In the main step of parameter estimation with the program of *lsq*, the OMC and the partial derivatives are calculated and the NEQ is formed. Then the NEQ is inversed to derive all the parameters. The parameter estimation uses the least-squares adjustment, and the epoch-wise observations in one scan are handled to form one epoch NEQ with both the global parameters (for example, the station coordinates and EOP) and temporal parameters (receiver clocks, tropospheric parameters). Those regional parameters are then eliminated to avoid an enormous NEQ, and the NEQ with only global parameters are stacked to form the global NEQ, which can be inverted for parameter estimation. Then the regional parameters can be recovered in a backward substitution. The details about this parameter elimination and recovery procedure can be found in Ge et al. (2006).

Then the receiver clocks are extracted by *extclk* and fitted using the polynomial function with the program of *clkfit*. Unlike other software packages, in PANDA the receiver clocks are estimated as random walk noises with loose constraints at the first several iterations, and thus the clock breaks can be easily detected in the clock estimates. If new clock breaks are detected, they are marked in the quality control file and handled properly in the following iterations. In

the procedure of clock break detection, the power spectral density is loosely set in the first iterations and then gets tighter.

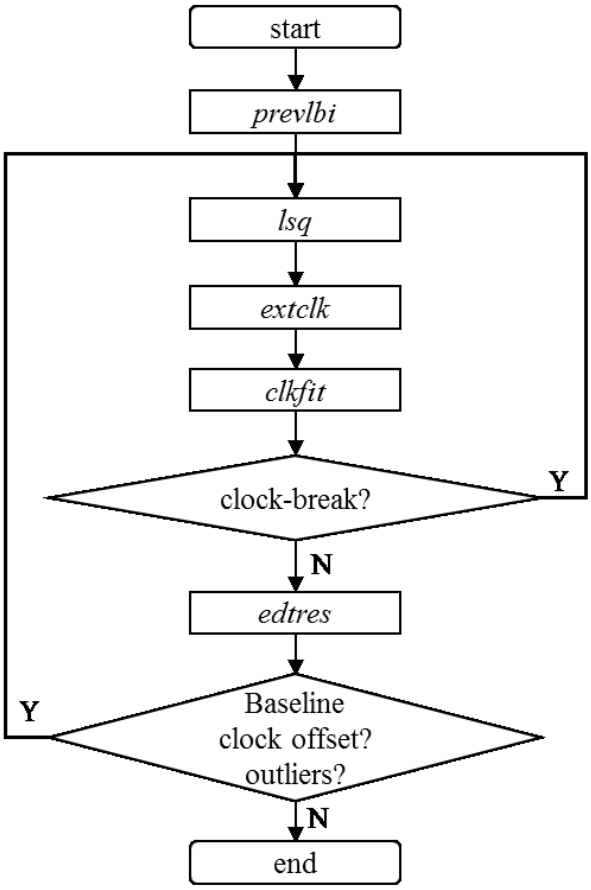

Figure 3.2 Flowchart of VLBI data processing, using the typical 24-hour session as an example. The procedure to process INT sessions is similar, but usually without clock break detection. The functions are explained in Table C. 1.

In the case of no more new clock breaks, the residual editing is performed, where the outliers and baseline dependent clock offsets are checked. If new outliers or baseline dependent clock offsets exist, the quality control file is updated with these data written, and another iteration of parameter estimation using *lsq* is performed.

The parameter estimation and the detection for clock breaks, baseline dependent clock offsets, and outliers is performed iteratively, where the criteria to determine new clock breaks, new baseline dependent clock offsets, and new outliers are updated in each iteration to avoid any improper detection. In the process of baseline dependent clock offset detection, the WMEAN and WRMS values are calculated, and an overall WRMS value ($WRMS_0$) is derived from these baseline-wise WMEAN values with the baseline-wise WRMS as weights. The baseline dependent clock offset should be set on the baselines with WMEAN larger than n times of $WRMS_0$, where n is about 3–5. In the outlier detection process, the WRMS value of all the observations are calculated, and the residuals larger than n times of this value are usually taken as outliers. These detected outliers are usually down-weighted or removed, depending on different data processing strategy.

As the clock breaks, baseline dependent clock offsets, and outliers are coupled with each other and all affect the clock estimates and residuals in a complicated way, it is not optimal to simply perform the above-mentioned procedures one by one. Therefore, the outliers, especially those with large errors, should also be checked and removed in the procedure of clock break detection. Nevertheless, the VLBI quality control is performed manually, which is quite common in the VLBI community. Currently, only the VLBI INT sessions can be processed automatically (Hobiger et al., 2011; Kareinen et al., 2015), as the necessity to detect clock breaks, baseline dependent clock offsets, and outliers is not in high demand.

The flowchart of parameter estimation, that is, the *lsq* program, is shown in Figure 3.3.

Starting with reading in the information about stations, AGN, and user setup from the control-file, the parameters are set up accordingly and the global NEQ is then established.

The scan-loop starts with reading the VLBI observations in one scan from the NGSCARD file. The planet positions and velocities from DE405 are derived, and then the matrix for the transformation between TRS and CRS is calculated with the EOP read in.

After that starts the station-loop, where the stations participating in the same scan are processed one by one. The station coordinates in TRS are first converted into CRS, and then the displacements are calculated according to the IERS2010 Conventions. Then the aberrated source vector is derived and the AGN source elevation and azimuth angles are available. The a priori tropospheric delay data, that is, ZHD, ZWD, and mapping functions are calculated. Other station-wise corrections, including axis offset and thermal deformation, are also calculated.

After all the stations are processed in the station-loop, the observation-loop starts. The theoretical time delay of each observation is calculated according to the IERS consensus model, and the OMC is derived with all the delays summed up. The partial derivatives are also calculated. The reason to use one station-loop and one observation-loop separately is to save some time. As the same station may be used in several observations in the same scan, it is not necessary to derive the same information of this station in calculating every observation.

After processing all the observations at this scan, all the observations are handled and contributed to the NEQ. As the time-flow goes, the inactive parameters (for instance, clocks and tropospheric parameters) are eliminated to keep a small NEQ.

When it comes to the end of the session, the datum constraints and other constraints (for instance, the a priori constraint of EOP if necessary) are applied to the NEQ (as pseudo-observations), which is then inverted and the parameters are derived. A backward substitution is performed to derive all the eliminated parameters, such as the receiver clocks and tropospheric parameters.

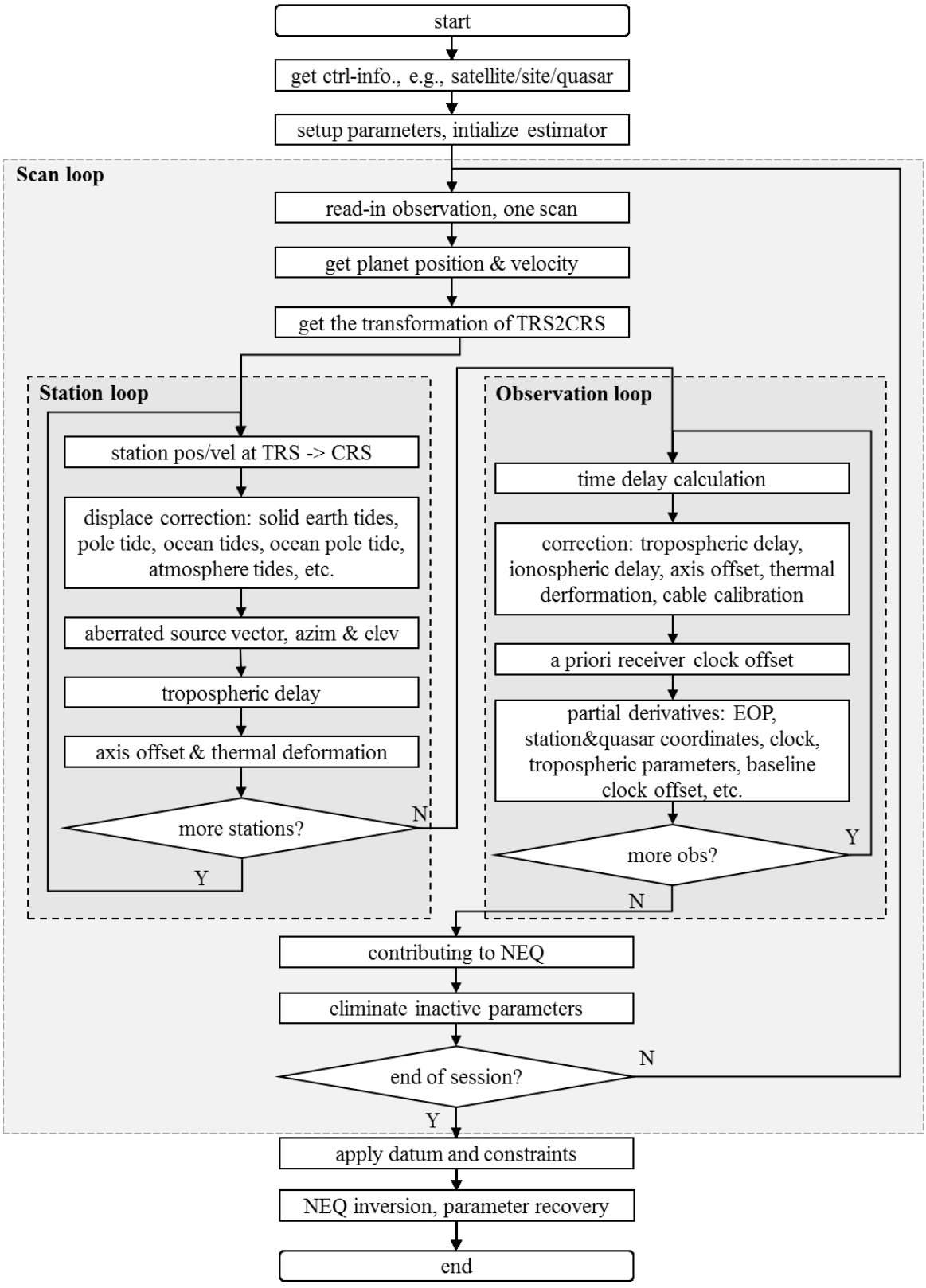

Figure 3.3 Flowchart of the VLBI modeling and parameter estimation in single-session processing. The procedure is implemented in the *lsq* program of the PANDA software.

3.4.2 VLBI telescope clock break

As the VLBI station clocks could suffer from the clock breaks, it is critical to identify these breaks and take care of them. In GNSS data processing where more than four observations are available at each epoch, the receiver and satellite clocks can be estimated as white noise, which means the clock breaks have an insignificant impact on data processing. In the case of VLBI data processing, however, it is very critical to handle the clock breaks properly. As there is usually not enough observations at one epoch (see Figure 2.4), the clock stability information has to be utilized and the constraint between epochs must be applied. In this study, the random walk process is used to handle the VLBI clock, which relies on the clock stability over time.

Taken the DOY 140 of the CONT14 campaign as an example, the clock estimates and the residuals of all the stations in the first iteration of parameter estimation are shown in Figure 3.4.

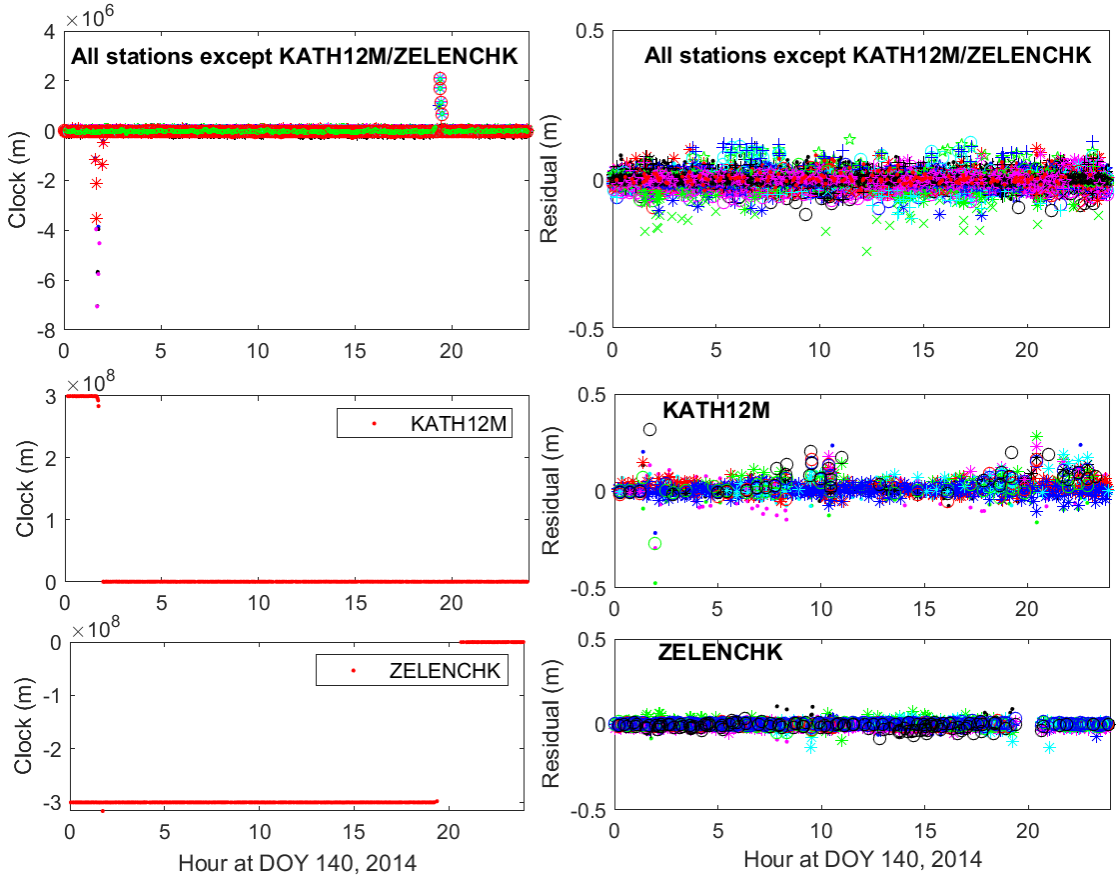

Figure 3.4 VLBI station clock estimates (left) and the observation residuals (right) in the first iteration, without the clock break detection. The stations without clock breaks are presented in the top panels, and the two stations with clock breaks are presented in the middle and bottom panels. Note that the different scales of the vertical axis in different panels. The stochastic noise is 10 m/sqrt(s).

In this round the a priori clock is zero, and neither the clock breaks nor the outliers are flagged. To allow the clock breaks to be absorbed into the clock estimates, the stochastic noise is 10

$m/\sqrt{s}$. As shown in the figure, at the stations of KATH12M and ZELENCHK one can observe significant clock breaks with a magnitude of 3×10^8 m (about 1 sec). Besides the clock breaks at these two stations, the clock estimates at other stations, that is, YARRA12M (red stars) and KOKEE (blue dot) also show large fluctuation in the same period. The reason is that the large clock breaks at KATH12M and ZELENCHK degrade the solution and affect other stations.

On the other hand, the residuals do not show any large jump or fluctuation over the whole session, meaning that the clock breaks are fully absorbed into the clock estimates.

Another test is then conducted, where the stochastic noise is set as 0.1 $mm/\sqrt{s}$, which is very tight and should not contain the large clock breaks. The clock estimates are shown in Figure 3.5, together with the observation residuals.

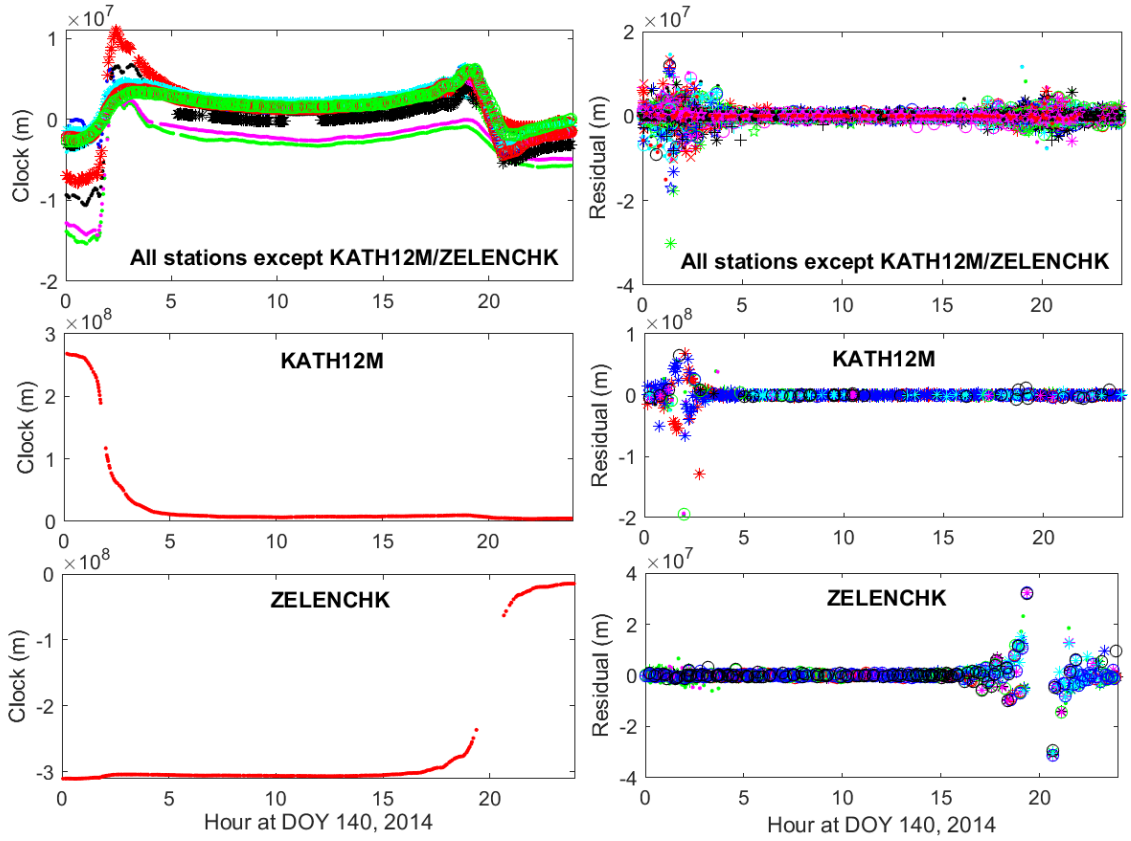

Figure 3.5 VLBI station clock estimates (left) and the observation residuals (right) in the first iteration, without the clock break detection. All the stations without clock breaks are presented in the top panels, and the two stations with visible clock breaks are presented in the middle and bottom panels. Note that the different scales of the y-axis in different panels. The stochastic noise is 0.1 mm/sqrt(s).

As shown in the left panel of Figure 3.5, due to the tight stochastic constraints, the clock estimates show a much smoother variation without any abrupt jumps during the period of the clock break, and other stations without clock breaks are also significantly affected during the whole session, as the clock estimates vary with a magnitude of 10^7 m. The residuals also show large fluctuation during the period of the clock break, and the variation could be as large as

10^7 m. Therefore, a loose constraint should be used for clock break detection if the random walk process is adopted.

The clock estimates and the a priori value in the second iteration are shown in Figure 3.6. In this iteration, the a priori clocks are used from the fitted clock estimates of the first iteration, and the clock breaks are marked in the clock fitting and the parameter estimation. The stochastic noise is 10 $mm/\sqrt{s}$.

As shown in the left panels, the clock estimates do not have any large fluctuations during the whole session, with the values varying within 10 m. This means that the clock breaks are correctly marked and the clock fit is properly performed. Also shown in the right panel, the clock breaks have been properly marked in the a priori clock. Note that the RWK constraint is not applied to the clock estimates at the break epoch.

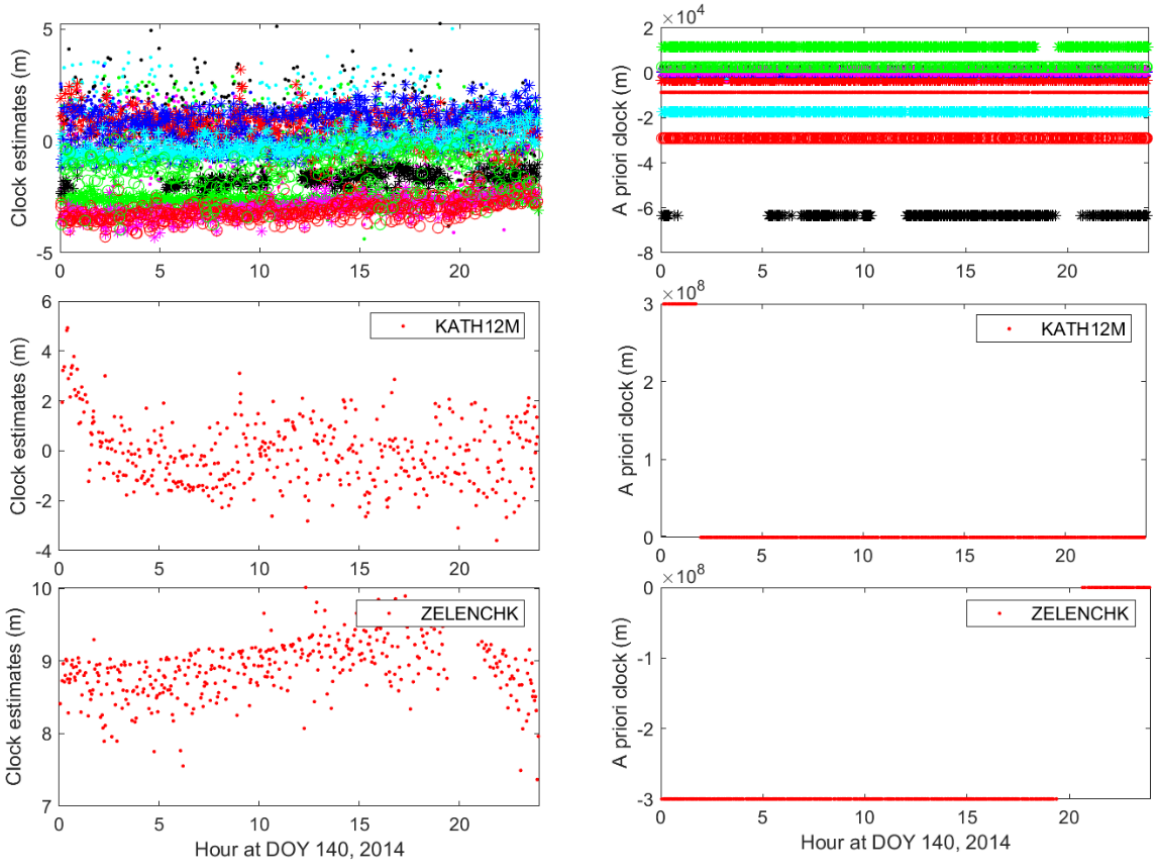

Figure 3.6 The a priori clocks (right panels) and the clock corrections (left panels) for all the stations without clock breaks (top panels) and the two stations with clock breaks: KATH12M in the middle panels and ZELENCHK in the bottom panels. The stochastic noise is 10 mm/sqrt(s).

After several more rounds of iteration and tighter constraints applied in both the clock estimation and the outlier detection, the last round is performed with no more outliers and no more baseline dependent clock offsets. In this iteration, a very tight stochastic noise of 0.3 $mm/\sqrt{s}$, is applied. Note that this is an empirical value determined from previous data processing experience, but further investigations of the clock stability and optimized stochastic

modeling of clock at each radio telescope based on real observations and the instrument performance should be done.

The clock estimates and the a priori clocks of the last iteration are shown in Figure 3.7. As shown in the left panels, the clock estimates are much smoother than those of the second iteration, and the fluctuation during the whole session (peak-to-peak) is within ±20 cm. For the two stations with clock breaks, that is, KATH12M and ZELENCHK, the clock estimates also show very stable variation within ±10 cm. Therefore, the clock break detection method works very well for this session.

On the other hand, the clock corrections (left panel) of all the stations are almost zero-mean and the maximum absolute correction is less than 0.2 m. This means that the a priori clock efficiently models the large clock offsets and drifts.

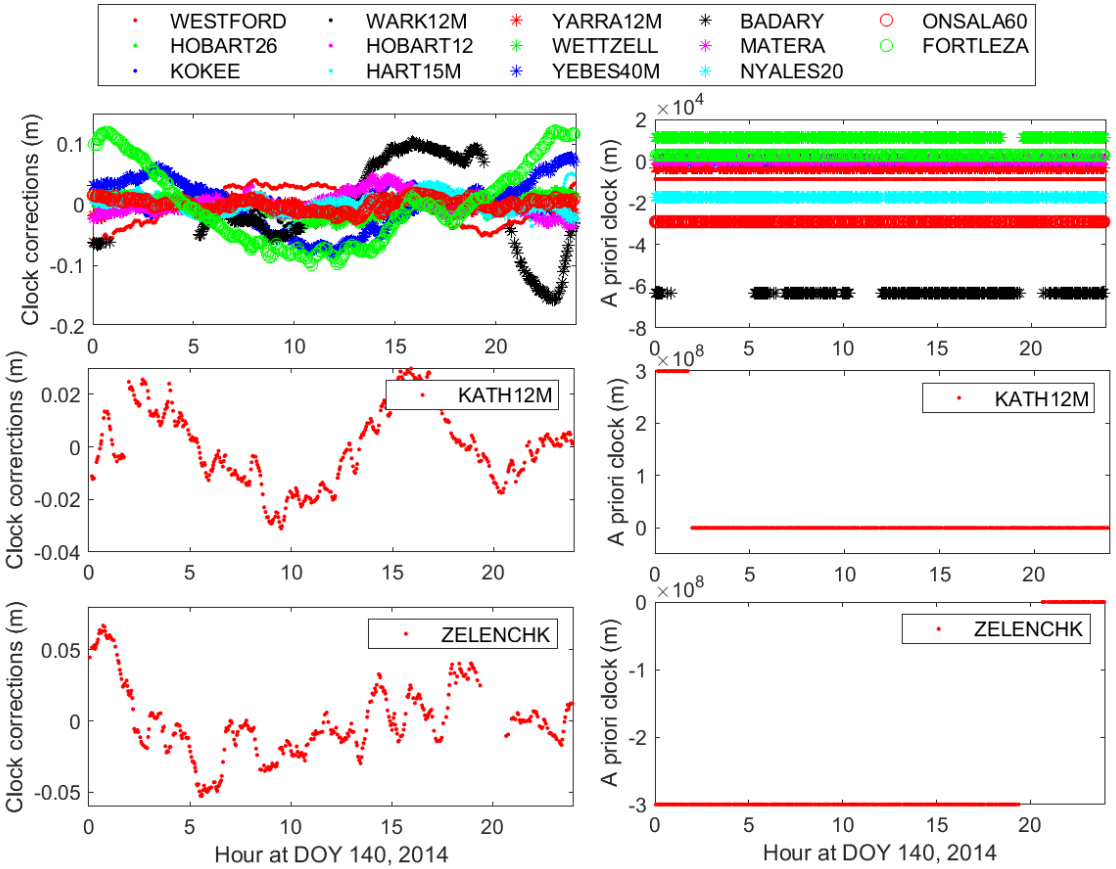

Figure 3.7 VLBI station clock estimated corrections (left panels) and the a priori clock (right panels) in the last iteration, for all the stations without clock break (top panels) and the two stations with clock break: KATH12M (middle panels) and ZELENCHK (bottom panels).

Similar other VLBI data processing software packages, in PANDA the outlier and baseline clock offset detection is conducted automatically whereas the clock break detection is performed manually. The clock estimates in the first few iterations should be screened to check the existence of clock breaks, then the outlier detection and baseline dependent clock offset detection can be performed automatically. However, it is expected to investigate the possibility

of an automatic clock break detection method. Also, the method of using the random walk process in clock estimation is more feasible for automatic clock break detection.

3.4.3 VLBI outlier elimination

A simple outlier detection method is applied based on the WRMS values of all post-residuals. The residuals larger than n times of the WRMS is taken as outliers and removed in the following iterations. As the outlier distribution is related to undiscovered clock breaks and the baseline clock offsets, the residuals should be examed cautiously. For instance, one baseline with an unmarked clock offset might lose many good observations. A more sophisticated procedure to automatically handle the outliers together with clock breaks and baseline independent clock offsets shall be the next step.

3.4.4 VLBI baseline dependent clock offset

As mentioned in section 2.2.1, the residuals of a few baselines might show constant offset, which is usually handled as the baseline dependent clock offset. Figure 3.8 shows the WMEAN and WSTD values of the residuals from different baselines at DOY 140 in CONT14. The clock breaks have been handled and large outliers are removed. The WRMS of all the WMEAN values is 6.9 mm. It is visible that some baseline residuals are biased by up to 50 mm, which is larger than 5 times of the WRMS of baseline WMEAN values. Several other baselines are also biased to about 20 mm. In this case, the baseline clock offsets should be applied iteratively.

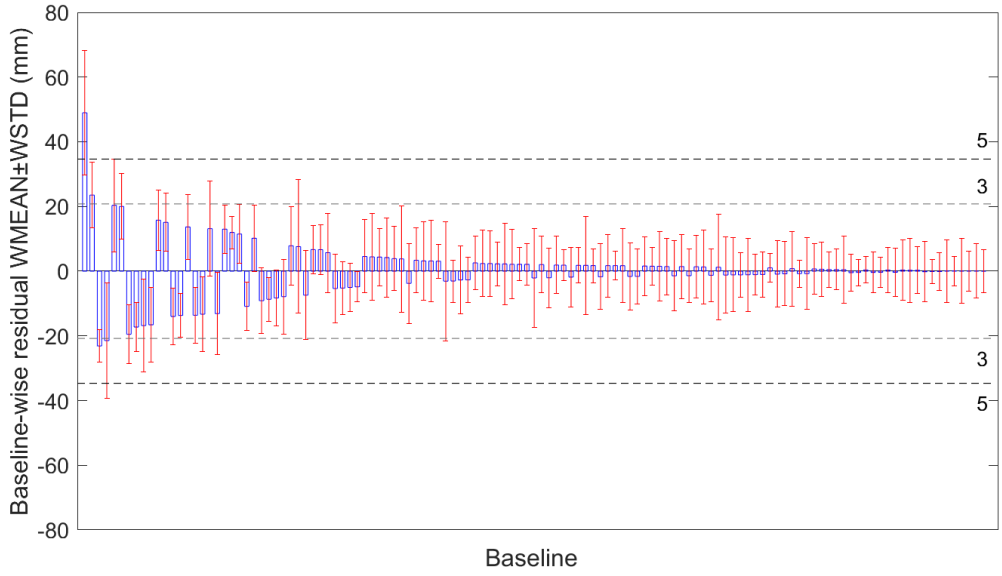

Figure 3.8 WMEAN (in blue bars) and WSTD (in red error bars) values of baseline-wise residuals without applying baseline clock offsets at DOY 140 in CONT14. The WRMS of all the WMEAN values is 6.9 mm, and on right gives the lines of three and five times of the WRMS of the WMEAN. The baselines are sorted in the order of the absolute value of WMEAN.

3.5 SLR data processing

The SLR technique is more of a GNSS-like technique with very precise range observations instead of the pseudo-range and carrier phase observations, and thus the SLR modeling and data processing strategy is more straightforward than that of GNSS.

Like GNSS, the SLR observations are also derived at each SLR station and then collected together by ILRS. The SLR observations provided by ILRS are usually available in two forms: (1) the full-rate points where the original observations with corrections are stored; (2) the normal points, which is the re-sampled observations derived from the original high-rate observations. The CRD is used by ILRS to provide flexible and extensible data to users. In this thesis, the normal points in the form of CRD files are used. The CRD file, however, covers all the SLR observations and all the meteorological, station, object, and system information. Thus, it is not easy to be adopted by the software. On the other hand, ILRS provides the observations of all the stations and all the tracked objects in hourly, daily, and monthly files, and also provides station-specific and satellite-specific files. Moreover, the data records are not rigorously chronological. All these prevent convenient observation manipulation. Therefore, it is necessary to convert the SLR CRD format to another format. Similar to the Bernese software (Dach et al., 2015), the GNSS-like RINEX format is adopted to save the SLR observations.

The SLR data processing flowchart implemented in the PANDA software is shown in Figure 3.9. In the first step: NPT2RNX, the CRD normal points are scanned and converted into the RINEX observation and meteorological files, where only the objects of interest are stored chronologically. In this study, only the tracking data to GNSS satellites, geodetic SLR spherical satellites (scuh as LAGEOS and ETALON), and interested LEO satellites (such as GRACE, SWARM, JASON) are outputted. By adopting the RINEX format, the LEO PRN code follows the IGS LEO sp3c list[58]. Note that several adjacent days CRD files should be scanned to obtain the complete observation records of one day.

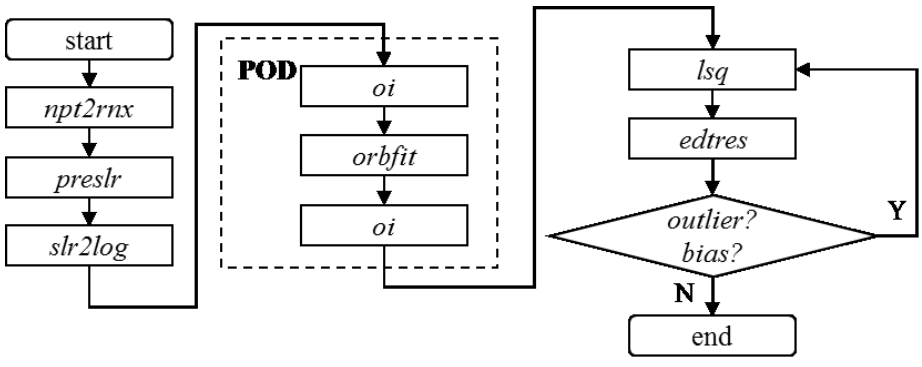

Figure 3.9 Flowchart of SLR data processing in the PANDA software. For orbit validation or SLR PPP, the OI and ORBFIT steps must not be used. The functions are explained in Table C. 1.

[58] https://cddis.nasa.gov/sp3c_satlist.html

In the second step: PRESLR, the observation files are scanned, and the satellite and station information is collected. Specifically, the station's initial coordinates are taken from the ITRF SINEX files and the eccentricity data are taken from the corresponding ILRS files. For the satellite, the center of mass and LRA information are also collected. Then a control-file with all the necessary information and other user setup is generated.

Following the PRESLR program, the program SLR2LOG reads the ILRS data handling file and convert it to the PANDA internal quality control file format. This data handling file summarizes the information on range-, time-, or meteorology biases from all SLR tracking stations, and is adopted by the ILRS analysis centers as a standard[59].

In the next step, the initial orbit data are generated by the programs of OI and ORBFIT. In the case of orbit validation or station coordinates estimation without orbit determination, the orbits are directly taken from the external product.

The major part of SLR modeling is implemented in the program of LSQ, where the OMC and the partial derivatives are calculated, and then the NEQs are stacked and finally inverted. The residuals are then checked by EDTRES to detect the outliers and other potential biases, including time bias and range bias. The SLR residuals are checked station by station and satellite by satellite to find any possible bias, and the criteria of 3 to 5 times of the sigma value is used for the outlier elimination.

The LSQ–EDTRES iteration is performed until no new outliers or biases detected. The final orbits can be derived by OI using the dynamic orbit parameters if POD is applied.

3.6 Multi-technique integrated processing on the observation level

3.6.1 Integrated processing procedure

The flowchart of integrated GNSS, SLR, and VLBI data processing is given in Figure 3.10.

Before the integrated processing, the single-technique solutions should be performed independently. The single-technique solution helps to obtain a “clean” solution, where all the information derived from the time-consuming iteration is derived, including the updated parameters, outlier information, clock breaks and baseline clock offsets in VLBI, and range biases in SLR. In the case of GNSS, the cycle slips and outliers are all detected, and the ambiguity-fixing information is derived. The orbits and clocks are updated with improved accuracy. In the case of SLR, the outliers should be removed and the time biases and range biases should be flagged. As for VLBI, the clock breaks, baseline dependent clock offsets, and

[59] https://ilrs.dgfi.tum.de/fileadmin/data_handling/ILRS_Data_Handling_File.snx

outliers are all flagged. Using this auxiliary information, the ultimate integrated processing can be performed, where different kinds of ties are applied.

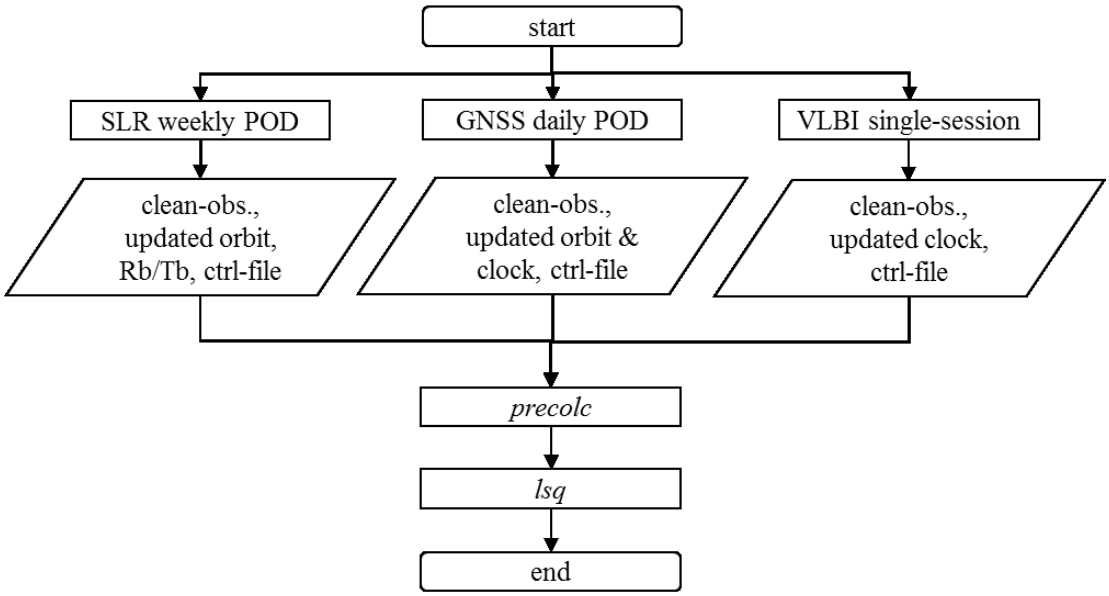

Figure 3.10 Flowchart of the multi-technique integrated processing in the PANDA software. The GNSS, VLBI, and SLR are demonstrated here.

The flowchart of the parameter estimation program LSQ in integrated processing is shown in Figure 3.11.

Starting with reading in the user setup information and the station, satellite, and AGN lists, the corresponding parameters are set up and the estimator is initialized. Then the epoch-wise observations of GNSS, SLR, and VLBI are processed one by one and contributed to the same NEQ. The tropospheric ties between GNSS and VLBI are applied to the NEQ before these tropospheric parameters are eliminated. At the end of the session without any more observations, the datum constraints and the local ties are applied, and the NEQ can be inverted. The parameter recovery is then applied to derive the residuals and eliminated parameters, typically the tropospheric delays and clocks. Worth mentioning that the delay modeling of all the techniques are performed in GCRS, as it suits both the satellite geodesy techniques and the VLBI.

One tricky issue in implementing the integrated processing is the counting of the epochs. As a classical GNSS software, the concept of regular-sampled epoch (300-sec, 30-sec, or 1-sec) is critical in handling the parameter setup and the relative constraint between consecutive epochs. The epoch number can be easily converted to time or vice versa. This is no longer the case for the uneven-sampled VLBI and SLR observations. The epoch number has to be counted one by one, and the corresponding time must be recorded. In the integrated processing, the observation time is mainly used for the time loop (or epoch-wise processing), while the epoch number works as an additional indicator.

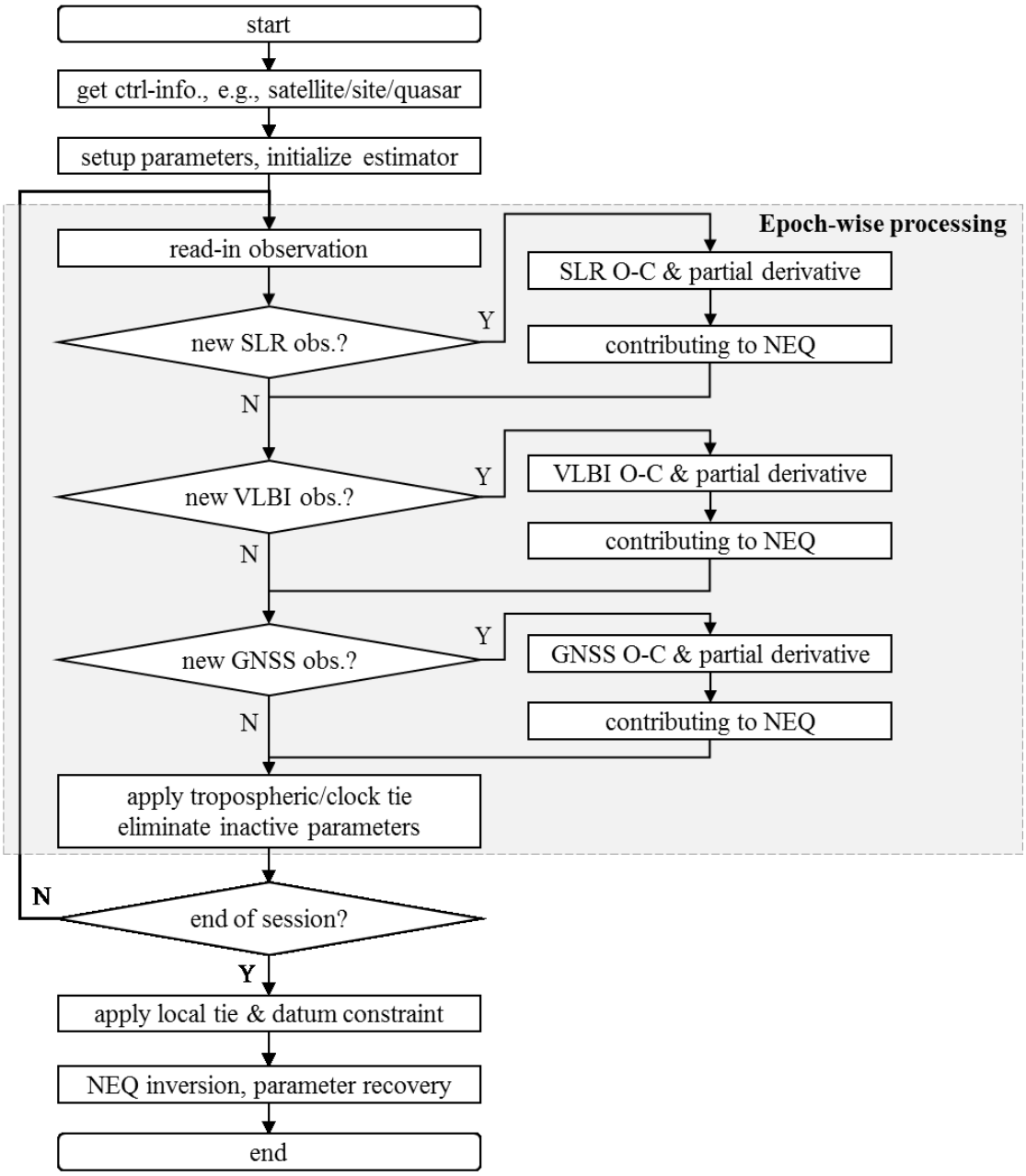

Figure 3.11 Flowchart for the parameter estimation program LSQ in multi-technique integrated processing. The GNSS, VLBI, and SLR are demonstrated.

In the integrated GNSS, SLR, and VLBI processing, several issues should be addressed. Specifically, the datum constraints should be applied, the EOP parameters should be tied together, the local tie constraints should be applied if necessary, and the tropospheric ties should also be applied. As for the space ties, the same set of dynamic orbit parameters is used for the same satellite by different techniques. The space ties are enable by the precisely pre-calibrated instrument offsets, for instance, the offset between LRA and GNSS transmitting antenna for GNSS satellite, and that between LRA and GNSS receiver on LEO satellite. These issues are discussed in the following sections.

3.6.2 Other integration levels

As the PANDA software is capable of multi-technique processing on the observation level, the combination on the parameter and NEQ levels will not be discussed in this thesis, although the module of combination on the NEQ level by NEQ stacking is available.

3.6.3 Datum definition

As different techniques have different contributions to the orientation, origin, and scale of TRF, they need different minimum conditions to obtain the solution, that is, the different datum definition conditions. However, for the integrated processing the datum conditions can be transferred by some ties, including the local ties and space ties, which means that if these ties are applied then it is not necessary to introduce the datum constraints to all the techniques, otherwise the solution will be over-constrained and potential conflicts between the datum conditions and the ties might be introduced.

In the GNSS POD the datum is defined by the coordinates of the IGS core stations. The coordinates can be either tightly constrained to the a priori TRF, or defined with the minimum conditions. As for VLBI, the minimum constraints refer to the NNR+NNT conditions. In the GNSS and VLBI integrated solution where the datum constraints are applied to the GNSS network, the VLBI datum is connected to GNSS via the LTs, and thus the NNR+NNT constraints on the VLBI network should not be applied. Another example is the GNSS and SLR integrated solution with the space ties applied. In this case, the SLR datum can be connected to GNSS via the space ties, that is, the satellite orbits, and the datum conditions should not be applied to the SLR network. On the other hand, applying the datum constraints in each technique-specific network and using the LTs (or space ties) at the same time is over constraining the solution. However, the constraints from LTs and space ties are usually not as robust as the datum constraints.

3.6.4 Automatic reweighting the ties

As the ties can be applied either as common parameters by stacking the normal equations, or as pseudo-observations with the corresponding weights, both methods are implemented in the PANDA software. To stack the normal equations of technique A and B for the common parameter x, the following observation equation is adopted:

$$\begin{bmatrix} v_A \\ v_B \end{bmatrix} = \begin{bmatrix} \cdots & \frac{\partial O_A}{\partial x} & \cdots \\ \cdots & \frac{\partial O_B}{\partial x} & \cdots \end{bmatrix} \begin{bmatrix} \cdots \\ x \\ \cdots \end{bmatrix} - \begin{bmatrix} l_A \\ l_B \end{bmatrix}, \begin{bmatrix} p_A \\ p_B \end{bmatrix} \tag{3.1}$$

where (v_A, v_B) are the residuals of the observation equation, $\left(\frac{\partial o_A}{\partial x}, \frac{\partial o_B}{\partial x}\right)$ are the corresponding partial derivatives, (l_A, l_B) are the OMC, and (p_A, p_B) are the weights. Worth mentioning that to use the common parameter, the precise relationship of the common parameter between the two technique has to be provided with high reliability.

Despite that using common parameter is more rigorous, using pseudo-observation is more flexible given the different weights. In this study the pseudo-observation is adopted as:

$$v = x_A - x_A, p_{A,B} \tag{3.2}$$

where (v_A, v_B) are the two parameters to be tied, and $p_{A,B}$ is the weighted.

As in reality the precise tie information provided from external source might not match the space geodetic observations, the pseudo-observation allows the possibility of adjusting the weight.

The normalized residual $\bar{v}_i$ reads as:

$$\bar{v}_i = \frac{v_i}{\sigma_0\sqrt{q_{vi}}} = \frac{v_i}{\sigma_{vi}} \sim N(0,1) \tag{3.3}$$

where v_i is the residual and σ_{vi} is the corresponding formal error, which is derived from the least-squares adjustment.

$$\mathbf{Q_{VV}} = \mathbf{P}^{-1} - \mathbf{A}(\mathbf{A}^{\mathrm{T}}\mathbf{P}\mathbf{A})^{-1}\mathbf{A}^{\mathrm{T}} \tag{3.4}$$

The weight of the ties is adjusted according to the normalized residual, that is, the normalized residual which follows the Student's distribution is expected to be less than a certain criteria (1.96 in this study, corresponding to 95% confidence level).

3.6.5 Global ties (EOP)

The ideal way to apply EOP ties is to consider EOP as common parameters for different techniques. However, this does not work for the LOD due to the long-term biases (see Figure 2.6). Therefore, pseudo-observation is used for the EOP ties.

For the PM offsets and rates, the weights for pseudo-observation are 0.1 μas and 0.1 μas/day, respectively. For UT1-UTC and LOD, the corresponding weights are 0.1 μs and 0.1 μs/day. Note that 1 mm surface displacement corresponds to about 30 μas rotation in angle, 0.1 μas corresponds to 0.003 mm and 0.1 μs corresponds to 0.05 mm, and thus such a constraint can effectively constrain the global ties. The LOD bias between GNSS and VLBI should be derived first using a period of single-technique solutions. In this study, the LOD bias between the GNSS and the IERS EOP 14 C04 product is first derived in each campaign and then applied as the LOD tie. This is not a perfect method, as the LOD estimates in the integrated solution will not be independent anymore. More sophisticated methods will be investigated in the future, for instance, improving the GNSS LOD bias by optimizing the satellite SRP modeling, or applying the random walk process in the long-term LOD modeling.

3.6.6 Local tie

Taking a GNSS–VLBI co-location as an example, the LTs are applied as pseudo-observation using the following equation:

$$\begin{bmatrix} X \\ Y \\ Z \end{bmatrix}_{GNSS} - \begin{bmatrix} X \\ Y \\ Z \end{bmatrix}_{GNSS} = \begin{bmatrix} \Delta X \\ \Delta Y \\ \Delta Z \end{bmatrix}, \mathbf{P} \tag{3.5}$$

where $[\Delta X \quad \Delta Y \quad \Delta Z]^{\mathrm{T}}$ is the LT vector from local surveys and $\mathbf{P}$ is the corresponding covariance matrix. In this study the diagonal elements instead of the full covariance matrix are used.

As mentioned in Section 2.3.2, the uncertainty from local surveys tends to be too optimistic. For comparison, the LT discrepancies between local surveys and space geodetic solutions are demonstrated in Figure 3.12. The LT discrepancy is calculated as:

$$\begin{bmatrix} \Delta x \\ \Delta y \\ \Delta z \end{bmatrix}_{DIF} = \begin{bmatrix} x \\ y \\ z \end{bmatrix}_{GNSS} - \begin{bmatrix} x \\ y \\ z \end{bmatrix}_{VLBI} - \begin{bmatrix} \Delta x \\ \Delta y \\ \Delta z \end{bmatrix}_{LS} \tag{3.6}$$

where $[\Delta x \quad \Delta y \quad \Delta z]^{\mathrm{T}}_{DIF}$ is the discrepancy vector in one day and $[\Delta x \quad \Delta y \quad \Delta z]^{\mathrm{T}}_{LS}$ is the LT vector from local surveys. For each campaign, the WMEAN values of the discrepancies on all three components are derived for further LT weighting.

The 3-D mean value of LT discrepancies is depicted in Figure 3.12, that is, the root of the mean squares of differences on the three coordinate components between the two co-located stations. For each campaign-wise LT discrepancy, this 3-D mean repeatability is also presented in the errorbar. In the corresponding space geodetic solutions, GNSS and VLBI observations are processed simultaneously in one estimator, and the EOP ties are applied. Therefore, there are no systematic network biases caused by EOP disagreement. In other words, the reference frames of the two techniques are aligned together. No other ties are applied in this integrated processing.

As shown in Figure 3.12, the nominal uncertainties of LTs from local surveys are clearly over optimistic, with an average value of 1.9 mm and a median value of 1.0 mm. Of all the 35 LTs shown here, only 8 are larger than 3 mm, and all except that at ZECK–ZELENCHK (10.1 mm) are below 5 mm. The discrepancies between space geodetic solutions and local surveys, however, are much larger. The average discrepancy (absolute value) of the 84 pairs over all the campaigns is 8.9 mm, and the median value is 7.2 mm. Most of the discrepancies (78 of 84) are larger than 3 mm, and around 35% (29 of 84) is larger than 10 mm. On the other hand, the average value in each campaign varies within 6 to 9 mm, except in CONT17-IVS, where the average value of all the co-locations is 12.4 mm.

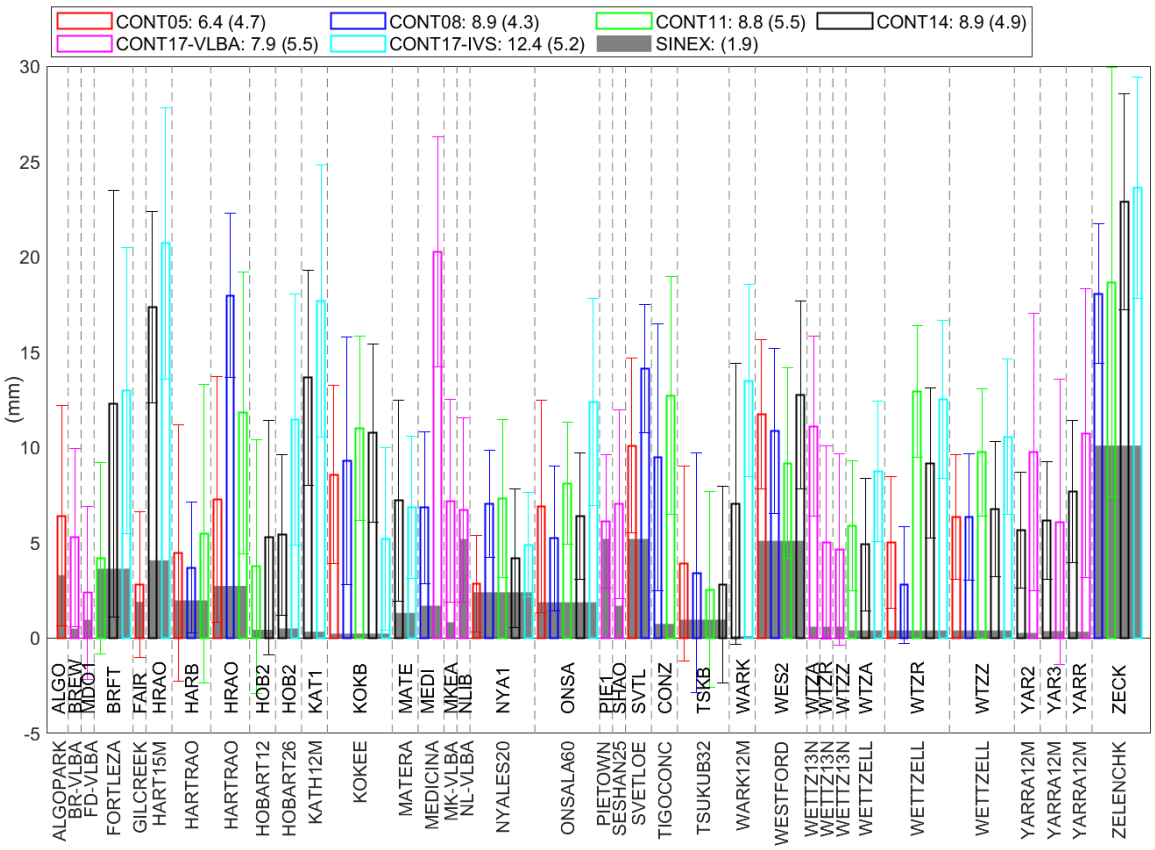

Figure 3.12 GNSS–VLBI LT differences (in hollow bars) the uncertainty (in error bars) between local surveys and space geodetic solutions in CONT05–CONT17. The 3-D mean values are shown here, and the uncertainly is the weighted repeatability of the local ties from space geodetic solutions. The nominal accuracies of local surveys given by ITRF SINEX files are shown in grey bars. The average values (mean bias and mean uncertainty) of all the co-locations in each campaign are presented in the legend.

3.6.7 Tropospheric tie

Recalling the tropospheric delay modeling in section 2.2.1, the equation 2.15 can be rewritten as:

$$L(e,a) = mf_H(e)\cdot Z_H + mf_W(e)\cdot(Z_W + dZ_W) + mf_g(e)\cdot(G_N\cos a + G_E\sin a) \quad (3.7)$$

where Z_W is the a priori value, and dZ_W is the ZWD correction. In high-precision geodetic data processing, the a priori ZHD derived from NWM should always be used, as an error of 20 mm ZHD would result in a 2.4 mm station height error (Boehm et al., 2006a). As for the wet delay, the a priori value does not matter a lot, as it is necessary to estimate ZWD. In the case of using a priori ZHD from NWM or meteorological observations, the dZ_W is also referred to as the residual zenith delay (also referred to as residual ZTD in the following text).

As for the tropospheric ties, the constraints are applied to the ZWD correction, that is, the dZ_W term, and the two gradients. The location difference induced ZHD and ZWD biases between co-located stations should be considered. In this thesis, the site-wise VMF3

(Landskron and Böhm, 2017) product is used to derive the a priori ZHD and ZWD. Therefore, the ZWD corrections can be tied up in integrated processing. Note that the site-wise VMF3 product refers to the height of the marker instead of the antenna reference point, this height bias should be considered. The empirical equation is adopted (Kouba, 2007).

For the potential systematic bias of the tropospheric tie that is not related to the site location, it can be parameterized as a constant over a certain period, for example, 24-hour in a single-session solution. However, this leads to the over-parameterizaiton issue which cannot make full used of the tropospheric ties. Therefore, the constant tropospheric tie bias parameter should be constrained to the a priori value derived from historical data processing or set as zero if no a priori information is available. In case of the conflict between the a priori constraint and the real space geodetic observations, it should be adjusted based on the statistic, that is, the normalized residual of the pseudo-observation constraining the tropospheric tie bias should be less than a certain criteria.

3.6.8 Relative weighting

As mentioned in section 2.3.3, the relative weighting is critical in integrated processing and it is not easy to apply the NEQ rescaling method when the combination is on the observation level. The reason to rescale the NEQs is to make sure that they have a comparable variance level. On the other hand, this can be done if the observations can be properly weighted. Recalling the parameter corrections as $\hat{\mathbf{x}} = (\mathbf{A^T P A})^{-1}\mathbf{A^T P L}$, scaling the weight matrix $\mathbf{P}$ is equivalent to scaling the NEQ.

The weight P of one observation considers the empirical constant σ_{const} (1 cm used in this study), the observation uncertainty σ_{obs} and the ionosphere correction uncertainty σ_{iono} from the observation file:

$$P = \frac{\sigma_0^2}{\sigma_{const}^2+\sigma_{obs}^2+\sigma_{iono}^2} \tag{3.8}$$

Further considering the elevation-dependent weighting (Gipson et al., 2008) assumes:

$$P = \frac{\sigma_0^2}{\sigma_{const}^2+\sigma_{obs}^2+\sigma_{iono}^2+\left(\frac{\sigma_{e_i}}{\sin e_i}\right)^2+\left(\frac{\sigma_{e_j}}{\sin e_j}\right)^2} \tag{3.9}$$

where e_i and e_j are the two elevation angles of the baseline, and the noise constant σ_e can be site-dependent (6 ps for all stations in this study).

It is also common to reweight different groups of observations, depending on the baselines, AGN, and stations; and the iteration can be continued until the unity of the post-fit sigma (chi-square) is obtained. This can be easily done within a few minutes and has been adopted by several IVS ACs, such as GSFC and BKG. Nevertheless, in this study, the chi-square is close to unity but not exactly equal to it.

In the case of GNSS, the empirical observation noise is used for the phase and pseudo-range observations. Different values are used on the LC and PC by different ACs, depending on whether the double-differenced or un-differenced observation is used. The elevation-dependent down weighting is usually applied. For the un-differenced mode, for instance, at EMR, ESA, JPL, the nominal sigma value is usually set as about 1 m and 10 mm for the ionosphere-free combined pseudo-range and phase observations, respectively. Due to the huge number of observations, different strategies of weighting, the processing modes (double-difference or un-difference), the weights applied to the pseudo-observations, it is extremely difficult to achieve the unity of chi-square. It is also not optimal to pursue this unity by iteration, as each iteration might take tens of minutes. It is still important to ensure that the chi-square is as close as unity, even though the exact unity cannot be achieved. On the other hand, the observation noise can be tested using several weeks' data, and then used for the following processing. In this study, the noises for ionosphere-free combined pseudo-range and phase observations are 0.9 m and 10 mm, respectively. These values are derived using 10 weeks' data covering the CONT campaigns since 2005, using several numerical tests.

As the unity of chi-square can be roughly guaranteed, another focus is on the capability of demonstrating the solution accuracy. As both GNSS and VLBI estimates have over-optimistic uncertainty, it is important to make sure that they are on the same level. Inspired by previous studies (Thaller et al., 2006; Thaller, 2008; Rothacher et al., 2011; Seitz et al., 2012), a similar method is adopted. The ratio of station coordinate repeatability to the average uncertainty in each CONT campaign is used to indicate to what extent the nominal uncertainty is over-optimistic. For each station, the ratio can be calculated as:

$$ratio = \frac{rep}{\sigma} \tag{3.10}$$

where rep is the station coordinate repeatability and σ is the formal error. The calculation of coordinate repeatability will be described in Section 4.1.2.

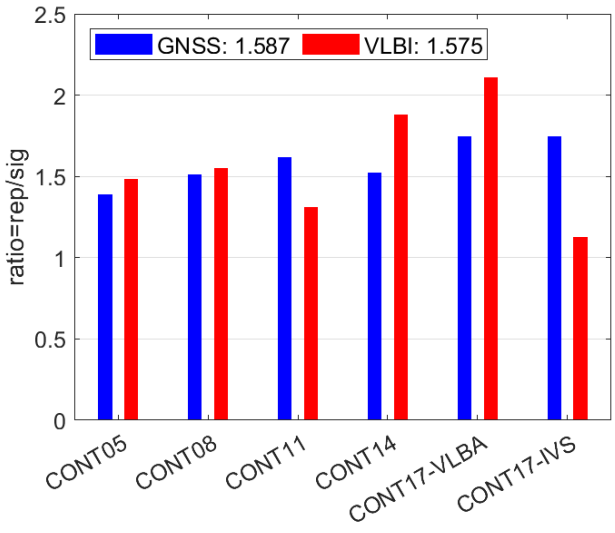

Figure 3.13 The ratio of station coordinate repeatability to nominal uncertainty for GNSS (in blue) and VLBI (in red) in CONT05–CNNT17.

The average ratio values of GNSS and VLBI stations in CONT05–CONT17 are shown in Figure 3.13. Despite the fluctuations in different campaigns, the average values in these campaigns are comparable between GNSS and VLBI. Therefore, it is safe to stick to the weighting strategy mentioned above, and no special handling is needed.

3.7 Chapter summary

The major content of this chapter is summarized as follows.

Section 3.1 introduces the current status of multi-technique software packages. Note that several of them claim to be able to process multi-technique observations, the available studies are limited. In the case of integrated processing on the observation level, NAPEOS has been demonstrated to processing GNSS, SLR, and DORIS on the LEO platform, while C5++ has been used to process GPS and VLBI, VLBI and SLR.

Section 3.2 introduces the PANDA software briefly, with both the existing and newly implemented modules presented. Basically, any data processing strategy can be performed in three steps. Note that the parameter update is usually included in the three steps.

- Data preprocessing and information collecting, including observation data cleaning.
- Computing the OMC and partial derivatives to construct the NEQ for inversion, and derives the parameter estimates.
- Residual editing, that is, scanning the residuals to find the outliers and breaks (in terms of VLBI clock), potential systematic biases such as VLBI baseline dependent clock offset, SLR range and time bias.

Section 3.3 presents the GNSS data processing procedure, using the GNSS precise orbit determination as an example. This procedure serves as a basic illustration of all other GNSS data processing, including the LEO POD and ground station PPP, with only minor modifications required.

Section 3.4 focuses on the development of the VLBI module in the PANDA software. Similar to the GNSS processing procedure, the VLBI analysis also follows the data preprocessing, parameter estimation, and outlier editing steps. The parameter estimation is applied in the same least-squares estimator as GNSS, allowing further integrated processing. A unique feature of the VLBI implementation is the random walk process for clock estimation, which makes it more feasible for clock break detection, especially for further automatic processing. The outlier elimination and baseline dependent clock offsets are also addressed.

Section 3.5 describes the newly implemented SLR module, which is able to process the SLR spherical satellites, the GNSS satellites, and the LEO satellites homogeneously.

Section 3.6 presents the procedure of multi-technique integrated processing in the PANDA software, with several issues addressed.

- The PANDA software is capable of processing multi-technique on both the NEQ level and the observation level, while the latter one is preferred.
- All the available ties can be handled as the pseudo-observation in the software, while the common parameter method can be adopted for EOP and space ties.
    - An automatic reweighting method based on the normalized residual of the pseudo-observations for the ties is developed, which is adopted to handle the local tie constraints and the tropospheric tie systematic biases.
    - The GNSS LOD bias should be derived first from the single-technique solution, and then applied in the integrated solution. There is no perfect way to cope with this bias unless the dynamic orbit modeling is improved and the GNSS processing strategy is optimized.
- As for the relative weighting, the observation noises of GNSS and VLBI are carefully selected to achieve (1) the unity of a posteriori variance factor, and (2) the comparable weight factors between the two techniques. This has been demonstrated using the 5 VLBI CONT campaigns.

4 Single-technique solutions

The major topic of this thesis is the integrated processing GNSS and VLBI observations on the observation level, however, it is necessary to analyze the single-technique solutions before coming to the integration part for the following reasons.

First, the integrated processing should start with "clean" observations for the pursue of efficiency. On the one hand, the GNSS data processing is usually time-consuming, especially for the POD, which can take hours for a daily processing. On the other hand, the GNSS data processing is a high-automatic job, where human intervention is seldom required. As for VLBI, however, one single-session processing usually costs less than one minute, whereas the manual clock break screening is necessary and can cost several minutes. It is thus strenuous to process them together from the raw observations.

Second, the VLBI and SLR modules are newly implemented in the PANDA software, and the related existing modules, for instance, the latest IERS Conventions and updates , are revised. It is therefore very necessary to validate the accuracy and robustness of these new implementations.

Moreover, the single-technique solution utilizing the information from another technique can be an efficient and proper way to provide the rapid service. For instance, in the GNSS rapid POD processing, the VLBI-only solution can provide precise UT1-UTC information. As for the VLBI intensive sessions, the tropospheric delay parameters derived from GNSS PPP solutions can help to stable the solution and improve the estimates.

Another reason is that the agreement of common parameters from different techniques should be first analyzed before any further integration. The tropospheric parameters, for example, should be analyzed in terms of both bias and scatter. In terms of EOP, it is well known that the LOD estimates from GNSS suffer long-term drift even though the short-term variation can be precisely determined, while the VLBI estimates might have lower precision in short-term signals due to uneven network. The LTs from local surveys should always be assessed before use, as it might cause network distortion. Nevertheless, any systematic inter-technique biases should be analyzed and handled properly before the integrated processing.

Finally, the pros and cons of different techniques should be identified, and the potentials of different techniques should be analyzed; and then the advantages of the integrated processing can be realized and assessed. The single-technique solutions also serve as a reference to evaluate the integrated solutions.

In this chapter, the single-technique solutions of GNSS, VLBI, and SLR are presented. For the GNSS POD solutions, the GNSS observations during the period of the five CONT campaigns (CONT05–CONT17) are used. The corresponding VLBI CONT campaigns are analyzed. Both single-technique solutions are validated by internal consistency and external

agreement. The GNSS–VLBI inter-technique agreement of ERP and tropospheric parameters are analyzed. In terms of the LT agreement between local surveys and space geodetic solutions, it is already addressed in Section 3.6.6. Moreover, the dUT1 estimates of VLBI intensive sessions in 2001–2016 are demonstrated. Last but not the least, the SLR solution is presented to demonstrate the capability of processing SLR observations tracking GNSS satellites, LEO satellites, and the SLR spherical passive satellites.

4.1 Validation criteria

One of the most critical issues in data analysis and validation is the selection of validation criteria. The product from TCs and ACs (for instance, IGS, IVS, IERS) can be an option. However, these data used in this study is also involved in the products of these TCs and ACs, and thus their product cannot serve as independent source. On the other hand, there are very few independent external data sets that can be used to assess the absolute accuracy. Nevertheless, in this study both the internal precision is evaluated mainly by the normminal uncertainty and repeatability, and the IERS, IVS, and IGS products serve for the exterinal accuracy evaluation.

4.1.1 Formal error

The very first investigation of the results is the formal error (or nominal uncertainty), which reveals the internal reliability of the estimates. As the nominal uncertainty depends only on the design matrix and the a posterior variance factor, it describes the theoretical quality. On the other hand, it is not reasonable to compare the estimates from two solutions if the a posterior variance factors are not comparable. For instance, solution (A) with only VLBI observations, and solution (B) with GNSS and VLBI observations but no ties applied, then the VLBI estimates between the two solutions should be identical whereas the formal errors can be significantly different as in solution (B) the posteri variance factor is determined by both VLBI and GNSS observations.

As for the GNSS and VLBI integrated solutions in this thesis, the a posterior is dominated by the GNSS solution, which is roughly unity as described in Section 3.6.8. Therefore, the formal error differences between two integrated solutions with different ties applied can demonstrate the theoretical improvement or deterioration introduced by the different setups, for instance, the tropospheric ties or EOP ties.

4.1.2 Repeatability

The repeatability of station coordinates is ideal to assess the stability of the reference frame from the GNSS and VLBI solution. It measures the potential to reproduce the reference frame using the observations of another day with the identical processing strategy, that is, the stability

of the reference frame solution. In this study, the weighted repeatability is measured in terms of WRMS (Nilsson et al., 2014):

$$WMEAN = \frac{\sum_{i=1}^{n}(x_i \cdot w_i)}{\sum_{i=1}^{n} w_i}$$

$$WSTD = \sqrt{\frac{\sum_{i=1}^{n}(x_i - WMEAN)^2 \cdot w_i}{\sum_{i=1}^{n} w_i}} \tag{4.1}$$

$$WRMS = \sqrt{\frac{\sum_{i=1}^{n} x_i^2 \cdot w_i}{\sum_{i=1}^{n} w_i}}$$

where the X_i is the daily coordinate or baseline length estimate, σ_i is the corresponding uncertainty; n is the number of the daily estimates, that is, 14 or 15 in the CONT campaigns. WMEAN is the weighted mean value of the coordinate estimates in a period (one campaign in this study), WSTD is used to present the repeatability, and WRMS is used to present the overall agreement. The coordinate repeatability is assessed in the north, east, and up components. Instead of the weekly repeatability that is usually used in the GNSS community, the campaign-wise repeatability is calculated for all the solutions. Therefore, for one station there is only one WSTD value in one campaign, and the statistics of all the stations in one campaign are used to present the overall repeatability.

In the case of calculating the unweighted MEAN, standard deviation (STD), and RMS values, the equal weight is applied to all the estimates in Eq. 4.1.

For the VLBI baseline repeatability, the WMEAN value of each campaign is derived and then the WRMS is available. The σ value of one baseline with two stations 1 and 2 is calculated by simply taking the uncertainty values of the two sets of coordinates $(\sigma_{X1}, \sigma_{Y1}, \sigma_{Z1})$ and $(\sigma_{X2}, \sigma_{Y2}, \sigma_{Z2})$.

$$\sigma_{BL(1,2)} = \sqrt{\sigma_{X1}^2 + \sigma_{Y1}^2 + \sigma_{Z1}^2 + \sigma_{X2}^2 + \sigma_{Y2}^2 + \sigma_{Z2}^2} \tag{4.2}$$

Note that this is a simplified method to calculate the baseline formal error, as rigorously the convarance matrix of the station coordinates from the least-squares adjustment should be adopted.

Moreover, the baseline repeatability of a set of baselines can be fitted using the function:

$$WBLR = \sqrt{A^2 + B^2 \cdot L^2} \tag{4.3}$$

where L is the baseline length, and the two coefficients A and B indicate the quality of the baseline repeatability, which are better if they are smaller, especially for the coefficient B as it is sensitive to the long baselines.

The network scale is also assessed in terms of repeatability. For one solution in a campaign, the average value over the whole campaign is used as the reference, and the seven-parameter

Helmert transformation is performed between each daily coordinate solution and the reference. Then the scale repeatability is available as the WSTD value.

It should be noted that the repeatability cannot fully represent the precision of a solution, due to (1) the possible station displacements caused by the unmodeled geophysical signals, for instance, the deficient tide models applied in the data processing, and (2) the repeatability is not sensitive to the systematic bias, for instance, the station coordinates can be biased by 1 m for all the days and the repeatability remains the same.

4.1.3 Day boundary discontinuity

In GNSS and VLBI data processing, the EOP components are usually modeled using the piece-wise linear (PWL) function. Specifically, in daily processing one offset and one rate at the noon are estimated for each EOP component, especially for the PM and UT1-UTC (note that in GNSS UT1-UTC is tightly fixed to the a priori value). Due to the fact the EOP should be continuous from day to day, the discontinuity between two consecutive days can be used to assess the internal precision. The day-boundary-discontinuity (DBD) and its uncertainty σ_{DBD} at midnight between two consecutive days i and $i+1$ can be expressed as:

$$DBD = \left(X_i + \frac{\dot{X}_i}{2}\right) - \left(X_{i-1} - \frac{\dot{X}_{i-1}}{2}\right) \tag{4.4}$$

$$\sigma_{DBD} = \sqrt{\sigma_{X_i}^2 + \frac{\sigma_{\dot{X}_i}^2}{4} + \sigma_{X_{i+1}}^2 + \frac{\sigma_{\dot{X}_{i+1}}^2}{4}} \tag{4.5}$$

where $\left(X_i, \dot{X}_i\right)$ are the offset and rate estimates of the EOP component on the first day, and $\left(X_{i+1}, \dot{X}_{i+1}\right)$ are those on the second day. Note that rigorously the DBD formal error should be derived from the covariance matrix of the least-squares adjustment. Given the time series of one EOP component in a campaign of n days, the n-1 DBDs can be derived and the WRMS value is used to assess the internal precision of this campaign from Eq. 4.1

As the satellite techniques cannot determine the UT1-UTC component, in the GNSS-only solution it is fixed to the a priori value from the IERS Bulletin A product. The celestial pole offsets are not estimated in the GNSS-only solution, whereas in VLBI-involved solutions only the offsets are estimated. Therefore, only the DBD values of PM are used in the GNSS-only solution. In the case of VLBI-involved solutions, the DBD values of the both PM and dUT1 are assessed.

The DBD is also not a flawless method to assess the internal precision, because the high-frequency EOP models (for instance, the sub-daily signals) might suffer from some errors and then propagate into the offset and rate estimates. On the other hand, systematic biases in the offset due to the network effect cannot be demonstrated in DBD statistics.

4.1.4 Inter-technique comparison

The inter-technique comparison of the parameters using the same period of data shows the agreement of different techniques, and demonstrates the accuracy of both techniques. In this thesis, the inter-technique comparison is applied to the tropospheric parameters, the EOP, and the station coordinates. In the case of coordinates, the LTs from space geodetic solution and local surveys are compared.

A good agreement of inter-techniques comparison indicates the reliability of both solutions, while bad agreements mean that at least one of the solution is not reliable, or there are systematic biases between them which stem from modeling, parameterization, and so on. For example, it is generally known that GNSS cannot determine the long-term signals of LOD. Another example is the systematic bias of the GNSS tropospheric parameters, which might be caused by the un-calibrated antenna PCV or the multi-path effect from the complicated local environment. Nevertheless, any large discrepancies in inter-technique comparison should be handled properly and an explanation is always needed.

4.1.5 Comparison with external reference

The following external data sets are used.

- The IERS EOP 14 C04 product for EOP comparison, also referred to as the C04 product in this thesis.
- The final orbits and ERP products from IGS and ACs, the second IGS reprocessed solution[60] before 2014 (referred to as IG2) and the routine solution after that.
- The submissions of IVS and ACs to the ITRF2020.

The agreement between combined solutions and different ACs in the IGS second reprocessing (IG2) is around 1 cm for the satellite orbits, 20–40 μas for polar motion offsets (100 μas rotation equals to around 3.1 mm surface displacement), and the LOD precision is about 10 μs (equivalent to 4.6 mm of equatorial displacement). However, the IGS takes the VLBI results from IERS rapid product (Bulletin A) to calibrate the LOD bias. Specifically, a 21-day sliding window is used for this calibration in the IGS operational combination before GPS week 1832 (February of 2015), after which a sliding window of 10 days is used (same as IG2). More details about the IGS routine and reprocessed product refer to the corresponding literature (Kouba, 2009; Rebischung et al., 2016).

The IVS collects the products from different ACs and regularly produces the combined product by combining datum-free normal equations (Böckmann et al., 2010). The IVS solutions also provide critical input for the ITRF realization. It is demonstrated that the WRMS

[60] http://acc.igs.org/reprocess2.html

values of EOP differences between combined and ACs' solutions are about 40 to 100 μas for the PM offsets, and about 5 to 15 μs for the dUT1 component (Bachmann and Thaller, 2016).

A summary of the agreement between TCs (IGS, IVS) and the IERS EOP 14 C04 product is shown in Table 4.1, which is taken from Bizouard et al. (2018). For the PM offsets, the WRMS values of the IVS solution are ~60 μas, about 2 times larger than that of the GNSS solution (around 30 to 40 μas). The WRMS of dUT1 is around 3.3 μs, and those of celestial pole offsets vary between 20 and 40 μas.

Table 4.1 STD values of the EOP differences between IERS EOP 14 C04 product and TC (IGS and IVS) final products. The values are taken from Table 6 of Bizouard et al. (2018).

EOP	x-pole (μas)		y-pole (μas)		dUT1 (μs)	dX (μas)	dY (μas)	LOD (μs/day)
Solution	IVS	IGS	IVS	IGS	IVS	IVS	IVS	IGS
2001–2010	68	41	66	33	3.3	34	41	18
2010–2015	58	31	56	27	3.4	21	29	10

For the EOP comparison in this thesis, the WMEAN and WSTD values are both calculated. The method follows Eq 4.1, similar to the one adopted in coordinate repeatability calculation. However, as the comparison is performed between two data sets, the weight for each difference is defined as:

$$\sigma_{A,B} = \sqrt{\sigma_A^2 + \sigma_B^2} \tag{4.6}$$

where σ_A and σ_B are the corresponding formal errors of the two data sets to be compared.

4.2 Data processing strategy

In this section the basic processing strategies of the GNSS, VLBI, and SLR solutions are given, which are followed by all the data processing through this thesis. Specific setups will be explicitly addressed in the corresponding sections. The details are listed in Table 4.2.

Several points should be clarified.

- For the GNSS solution, only the GPS constellation is used. Note that PANDA can process multi-GNSS observations, other systems are not used to be consistent with the IGS product. For the IGS processing, both the IGS second reprocessing products before 2014 and the operational products after that are based on GPS-only observations and the IERS EOP 14 C04 is based on these two products.
- The SLR processing strategy is not listed here. However, its basic setup is similar to that of the GNSS PPP solution. More details will be described in Section 4.8. Worth mentioning that the atmospheric delay modeling of SLR is different from that of GNSS, as explained in Section 2.2.1.

- For the EOP modeling, the IERS rapid product is used for the a prior value. The IERS2010 Conversions High-Frequency model is used instead of the updated HF-EOP model[61]. The linear interpolation method is applied.

Table 4.2 Description of the data processing strategies of the VLBI and GNSS solutions used in this thesis.

Mode	VLBI CONT	VLBI INT1/2	GNSS POD	GNSS PPP
Period	CONT05–CONT17	2001–2016	Same as VLBI	
Station	Most of the participating stations	KOKEE,TSUKUB32, WETTZELL	200+ stations	All the stations with VLBI co-locations
Arc-length	24-hour	1-hour	24-hour	
Sampling	All X-band		300-sec	
Observable	All X-band group delays with the quality code "0", S-band for ionospheric correction		Un-differenced ionosphere-free linear combination of GPS L1 and L2 phase and pseudo-range	
Weighting	Constant (1 cm) + Obs. & Iono. noise, elevation-dependent down-weighting		0.01 m for LC, 0.9 m for PC; elevation-dependent down-weighting	
Cut-off Elev.	No		5°	
Planet ephemeris	JPL DE405			
Space part	AGN coordinates fixed to ICRF3 (in Section 4.5–4.7, and Chapter 5), or estimated using the NNR constraints (in Section 4.4 and Chapter 6)		Orbit estimated using ECOM1 SRP model; clocks estimated as white noise	Orbits and clocks fixed to IG2/IGS products
A prior Position	ITRF2014 with velocity and PSD correction		IGS14[62] (Rebischung and Schmid, 2016) with velocity and PSD correction	
Displacement	Solid Earth tides, pole tide, ocean tides (FES2004), ocean pole tide, atmospheric pressure loading: S1&S2 (IERS2010) and non-tidal loading (VMF)			
Site Position	NNR+NNT	Fixed	NNR+NNT	Daily constant
Rcv. Clock	Linear+RWK	Linear	White noise	
Trop. model	A priori value from the 6-hour sampled VMF3-site and VMF3-grid (1°×1°) product, temporally linear interpolated, and spatially bilinear interpolated. No a priori gradient value			
ZWD Est.	1-hourly PWC			
Gradient	3-hourly PWC	None (see Table 5.1)	3-hourly PWC	
Iono.	First order correction from NGSCARD. No higher-order considered		Eliminated by ionosphere-free combination. No higher-order considered	
Antenna offset.	Telescope eccentricity from ECCDAT.ecc. Thermal deformation, axis offset corrected		Receiver and satellite PCV&PCO corrected using IGS14.atx	

[61] https://ivscc.gsfc.nasa.gov/hfeop_wg/
[62] http://acc.igs.org/igs-frames.html

- The VLBI datum is defined by NNR+NNT constraints on stations with coordinates available in ITRF2014. Therefore, the station WETTZ17N in CONT17 is not used for datum definition.

- The GNSS datum is defined by NNR+NNT constraints on a GNSS subnet. The stations are selected according to the IGS14 core station cluster file. In each daily solution, the subnet is first checked with a seven-parameter Helmert transformation to IGS14 solution, and the stations with fit residual larger than three times of the fitting RMS value are not included. The NNT is required for the geocenter motion estimation.

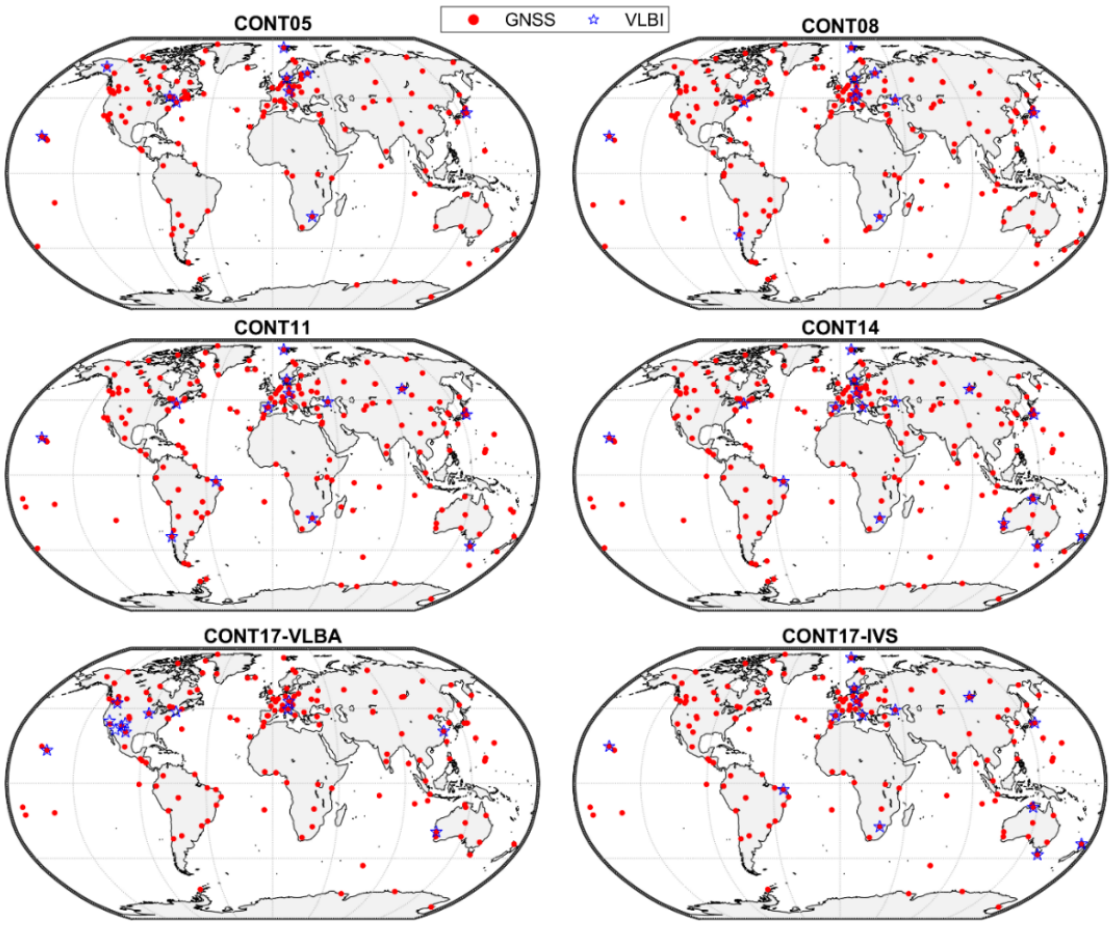

Figure 4.1 Distribution of GNSS stations (in red) for precise orbit determination in each CONT campaign. In CONT17, only one GNSS POD solution is performed. The two panels (CONT17-VLBA and CONT17-IVS) show the same GNSS network with different VLBI stations for clarity. The VLBI stations are shown in blue stars.

For the GNSS POD solution, more than 200 IGS stations are used for each campaign. The GNSS stations are selected according to the following criteria.

- The 173 IGS14 core stations are selected and grouped into 51 clusters, with one to four stations in each cluster. For the core stations, a subnet with one to two stations in each cluster is used for the GNSS datum constraints.

- All the stations with VLBI co-locations are selected. Note that one VLBI station might have more than one GNSS co-locations even though the LTs are not always available, all the co-located stations are used.
- A few more stations defined in IGS14 are selected manually to keep a global homogeneous distribution.

The distributions of GNSS stations during each CONT campaign period are provided in Figure 4.1. Despite the station clusters in North America and Europe, the global distribution is quite homogeneous.

4.3 Analysis of GNSS Precise Orbit Determination

The GNSS POD results are evaluated by comparison with the IGS solutions: the 2nd reprocessing campaign in CONT05–CONT14, and the operational products in CONT17. Then the coordinate repeatability is demonstrated, and the ERP agreement to the IERS and IGS products is presented.

4.3.1 Orbit accuracy compared to the IGS product

The orbit accuracy of the GNSS single-technique solution is first evaluated by comparison with the IGS/IG2 product, with the seven-parameter Helmert transformation. Figure 4.2 shows the daily RMS values of orbit differences, calculated as:

$$RMS_{A,C,R} = \sqrt{\frac{\sum_{i=1}^{n} res_{A,C,R}^2}{n}}$$
$$RMS_{sat} = \sqrt{\frac{\sum_{i=1}^{n} (res_A^2 + res_C^2 + res_R^2)}{3n}} \quad (4.7)$$

where res is the epoch-wise orbit residual in the along, cross, and radial directions, $RMS_{A,C,R}$ are the corresponding RMS values. RMS_{sat} gives the 1-dimension average RMS of each satellite.

As shown in Figure 4.2, the average RMS values for all satellites are less than 10 mm for all the periods except in CONT11, while the median value is smaller by 10%. Of the three components, the radial one has the best accuracy with an RMS value of 7–8 mm, and the RMS values are 10 mm and 11 mm on the cross and along components, respectively.

The relatively better precision on the radial component is rather common for GNSS, as the GNSS observation constraints are directly on the radial direction from the ground stations, whereas for the along and cross components the observation geometry is less strong. Moreover,

for the dynamic modeling of the satellite orbit, the along and cross directions are usually characterized with parameters to be estimated, which presents the issue of correlation.

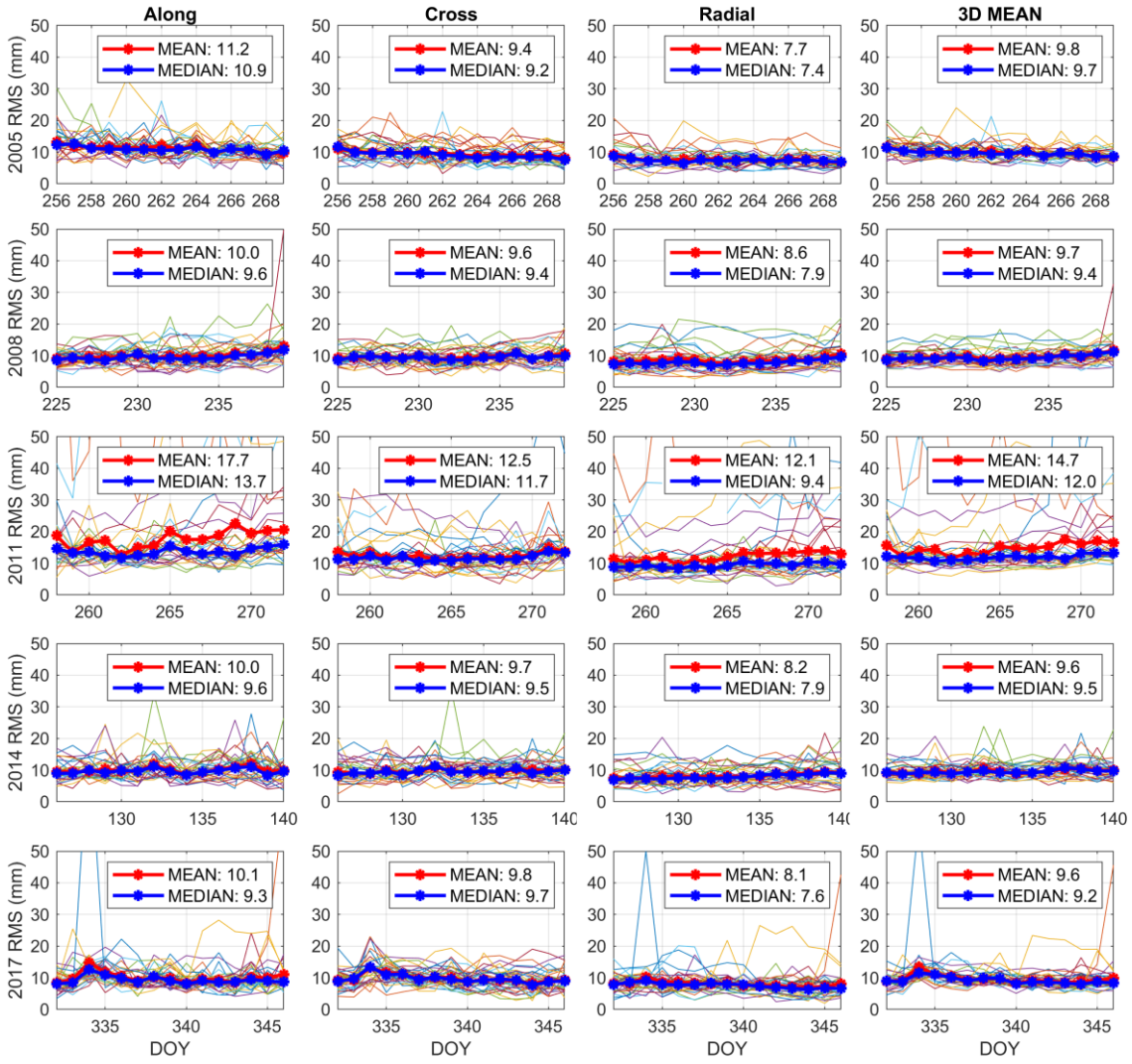

Figure 4.2 RMS values of GPS satellite orbits compared to the IGS/IG2 products. Different colors represent different satellites, and the daily mean and median values are shown in red and blue dot-lines, respectively. The average values in each CONT campaign are presented in the legend. Note that the orbit differences are calculated after the seven-parameter Helmert transformation.

The overall precision of the GPS satellite orbits in the five CONT campaigns is further summarized in Figure 4.3, which clearly shows that the radial accuracy is better than the other two components in all the CONT campaigns. On average, the GPS satellite orbit agreements to IGS/IG2 are 8.9 mm, 10.2 mm, and 11.8 mm on the radial, cross, and along components, respectively. The 3D average value is 10.7 mm. Despite the fact that in each period only 15 days observations are processed, the rather stable performance over the five periods still demonstrate that the reprocessed GPS satellite orbit accuracy is comparable to the IGS and AC products. The relatively poor orbit quality in CONT11 is caused by several GPS satellites in eclipse season, when the orbit modeling needs to be optimized.

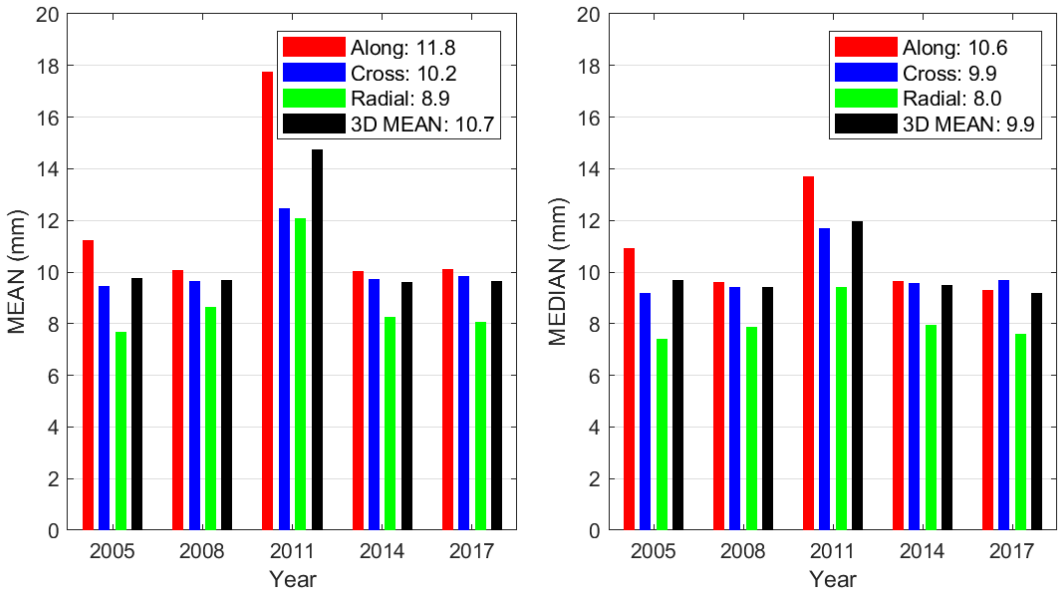

Figure 4.3 Statistics of GPS satellite orbit accuracy compared to IGS/IG2 product in different CONT campaigns. Average value of the orbit mean (left) and median (right) daily RMS.

4.3.2 Station coordinate repeatability

Repeatability in CONT05–CONT17

The median and mean WSTD of all the GNSS stations in POD processing in CONT05–CONT17 are summarized in Figure 4.4. On average, the WRMS values are 1.4 mm and 1.6 mm on the north and east components, respectively, and the vertical average WRMS is 4.2 mm. The performance in different CONT campaigns is quite stable, and no large fluctuations are observed.

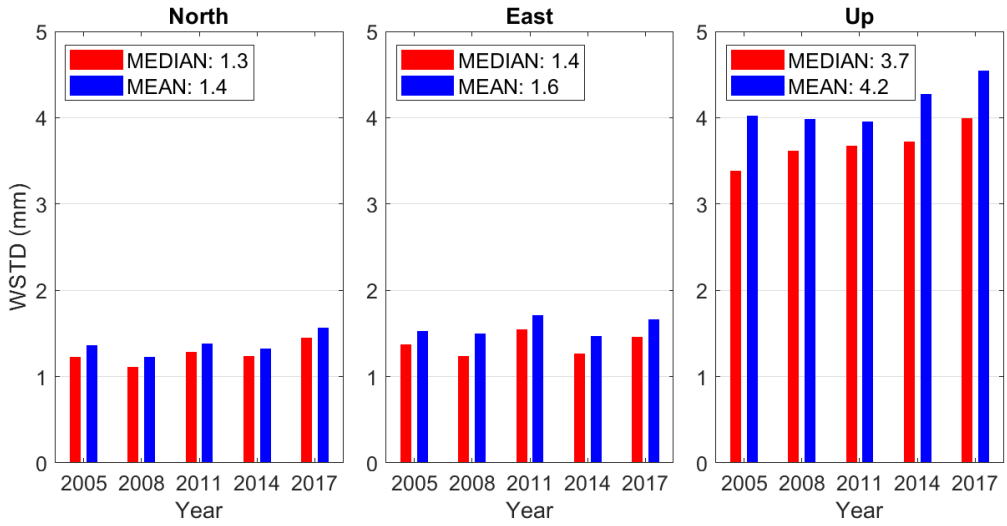

Figure 4.4 Median (in red) and MEAN (in blue) values of GNSS station coordinate weighted repeatability in CONT05–CONT17. Only stations with more than seven days' results are presented.

Station coordinate repeatability in CONT17

Taking CONT17 (DOY 332–346, 2017) as an example, Figure 4.5 shows the station-specific coordinate weighted repeatability (WSTD) on the north, east, and up components.

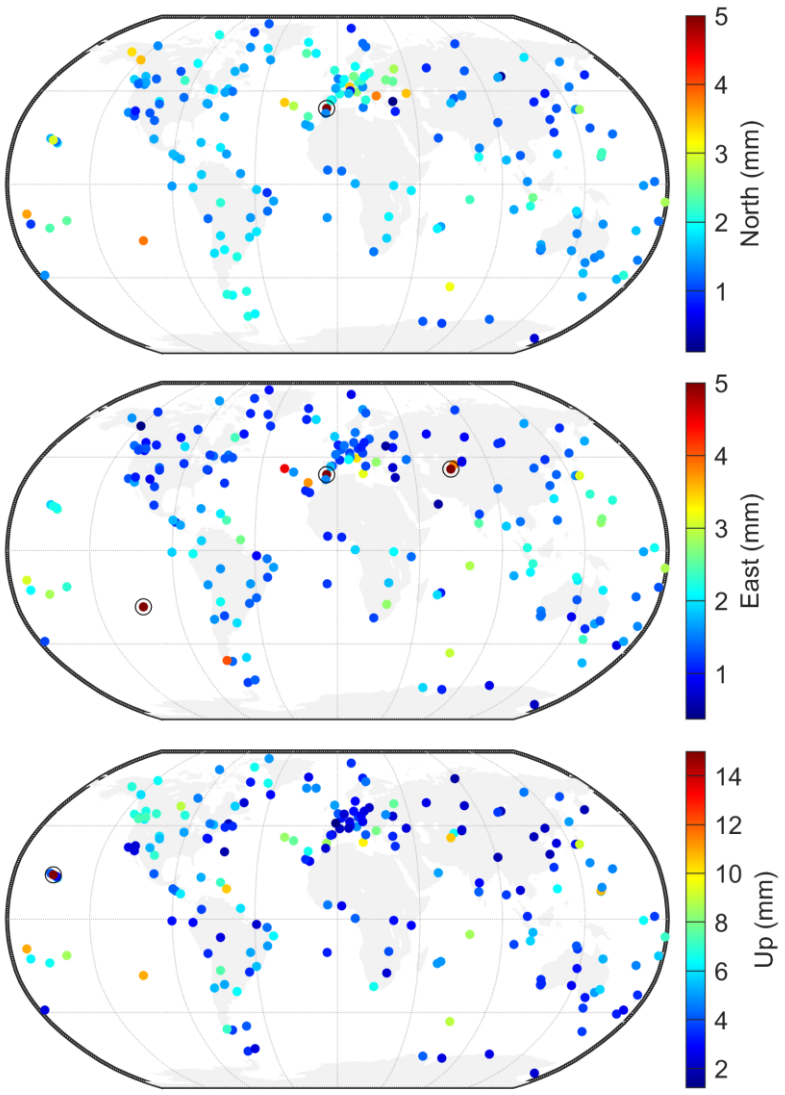

Figure 4.5 GNSS station coordinate weighted repeatability in DOY 332–345, 2017. Only stations with more than seven days' results are presented, that is, 213 of the 217 stations in total. The stations with WSTD larger than 5 mm horizontally or 10 mm vertically are shown in black circles. Note the different colormap scales between the horizontal and vertical components.

The horizontal WSTD values are below 3 mm for most of the stations, while the vertical values are below 8 mm. The numbers of stations with WSTD value larger than 5 mm horizontally or 10 mm vertically are 1, 3, and 1 on the north, east, and up components, respectively. The few stations with large WSTD values are listed in Table 4.3.

A further inspection of the WSTD values with respect to the station latitude and height is given in Figure 4.6. On the one hand, there are no obvious differences in terms of the

repeatability between stations in the Northern Hemisphere and those in the Southern Hemispheres on all the N, E, and U components. On the other hand, the east component does show slightly larger repeatability at the low latitude. As for the vertical component, large repeatability values are observed at some low-altitude stations, while the stations at different altitudes do not show any statistical differences.

Table 4.3 GNSS stations with large coordinate repeatability in CONT17.

Station	N (mm)	E (mm)	U (mm)	Location
SFER	12.9	7.9	8.3	San Fernando, Spain
ISPA	3.7	8.7	11.6	Easter Island, Chile
HNLC	2.9	2.1	15.1	Honolulu, America
KIT3	1.8	5.5	10.6	Kitab Uzbekistan

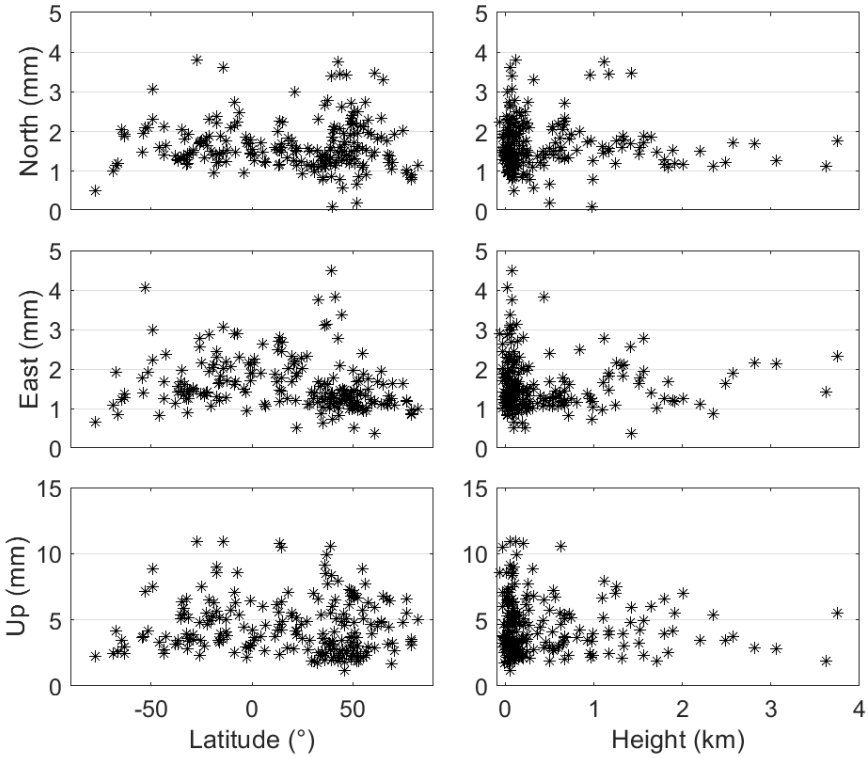

Figure 4.6 Distribution of GNSS station weighted repeatability as a function of the station latitude (left panels) and height (right panels) in the CONT17 campaign.

4.3.3 ERP precision

In this section, the precision of ERP from GNSS POD solution is analyzed. The GNSS ERP time series are shown in Appendix B (Figure B.1 to Figure B.6)

The IGS product

Besides the IERS EOP 14 C04 product, the IGS ERP products are also used. A summary of different IGS ACs used in this section is shown in Table 4.4.

Note that the IGS policy is using the 24-hour arc strictly without any between-day constraints, several ACs, however, do apply loose or tight between-day constraints.

- CODE produces both 24-hour arc (cf2 and cof) and 3-day arc (co2 and cod) products, and the latter one is derived by the rigorous stacking of the three consecutive 24-hour NEQs.
- At MIT the orbit parameters are constrained between consecutive days over 9-day time window.
- The 30-hour processing arc is adopted by JPL.

Appling between-day constraints will improve ERP estimation, especially for the rates. The LOD estimates from all the ACs are solely from the GNSS technique, while that from the IGS combination is calibrated with VLBI solution to reduce the systematic long-term bias. Note that in CONT14 the CODE operational products are used as the reprocessing product ends earlier. For details about the IGS second reprocessing it is referred to Griffiths (2018).

Table 4.4 List of IGS Analysis Centers used for the ERP comparison. The acronym of 2nd reprocessing is used in this thesis.

AC	Product acronym		Comments
	2nd reprocessing (CONT05–CONT14)	Operational (CONT17)	
IGS	ig2	igs	The IGS LOD was aligned to VLBI solution using IERS rapid product
CODE	cf2	cof	CODE 1-day solution cof product in 2017 not available
	co2	cod	CODE 3-day solution
GFZ	gf2	gfz	
ESA	es2	esa	
GRG	gr2	grg	
MIT	mi2	mit	SRP parameters constrained between consecutive days over 9-d window
JPL	jp2	jpl	30-hour data spans and orbital arcs
EMR	em2	emr	Use same software as JPL (Gipsy-OASIS)

Worth mentioning that seven ACs used six different software packages, where the processing strategy varies significantly. For instance, the un-differenced observations are used by most of the ACs, while at CODE and MIT the double-differenced observations are used. Other details, for instance, the cut-off elevation angles (3 to 10 degree), weighting strategies, observation samplings (usually 5-min, but 3-min at CODE), are also different at different ACs. Note that at EMR and JPL the same software package is used.

On the other hand, the ACs are asked by IGS to keep consistent with each other, including the conventions, reference frames, atmospheric delay modeling, dynamic orbit modeling.

ERP formal error

A first investigation of the ERP is the formal error. Figure 4.7 shows the ERP nominal uncertainties of IERS EOP 14 C04 product, the reprocessed POD solution in this study (shown as "rep") using PANDA, and those of the IGS ACs. The average values are summarized in Table 4.5.

Table 4.5 Average value of ERP formal errors of IERS EOP 14 C04 product and GNSS solutions in the CONT05–CONT17 campaigns.

EOP	C04	rep	ig2	co2	cf2	gf2	es2	gr2	mi2	jp2	em2
x-pole (μas)	46	8	3	5	6	7	10	67	12	11	30
x-pole rate (μas/day)	92	25	13	8	23	22	50	34	40	43	96
y-pole (μas)	43	8	4	5	6	7	10	67	12	13	30
y-pole rate (μas/day)	87	34	14	8	25	26	47	38	41	39	70
LOD (μs/day)	11.2	1.3	0.8	1.0	2.0	1.5	4.5	1.9	1.9	6.6	8.5

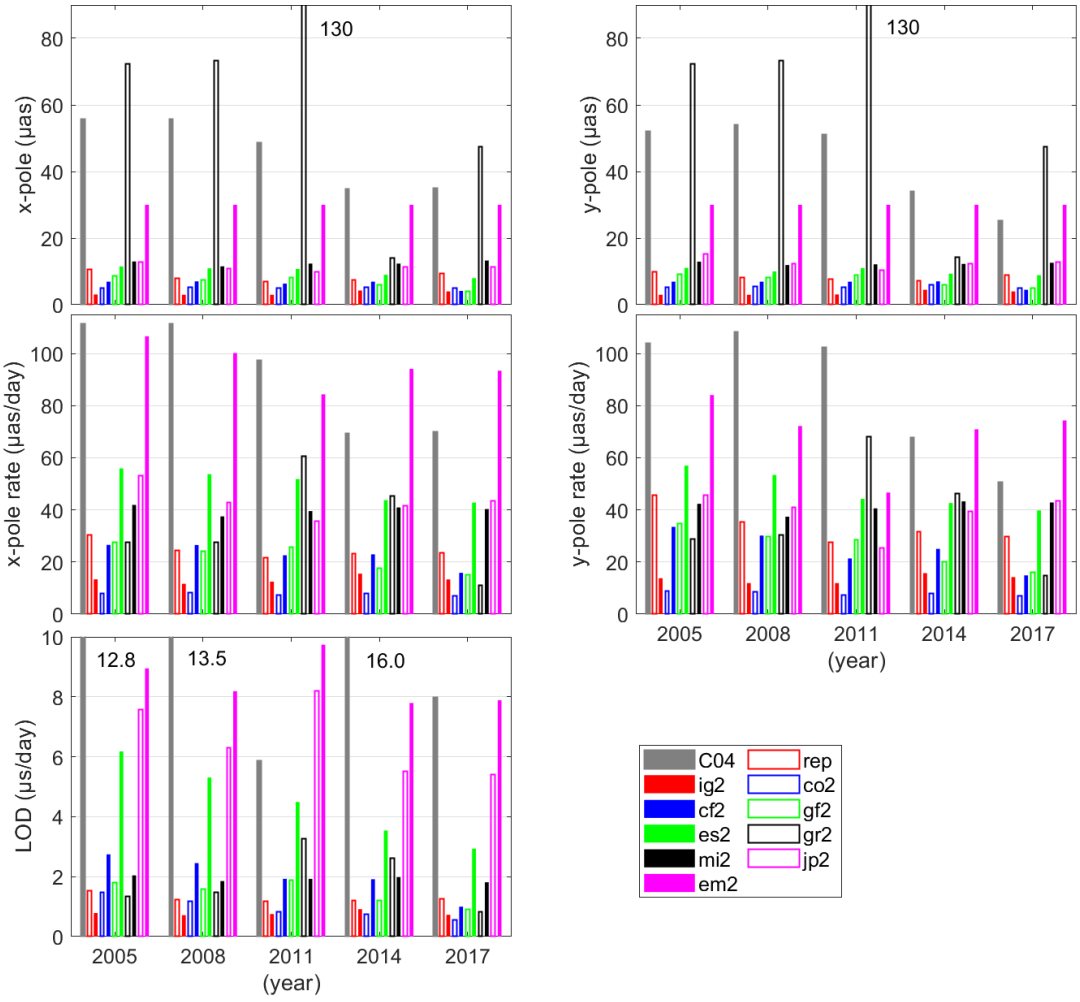

Figure 4.7 Average value of ERP formal errors during each CONT campaign. The IERS EOP 14 C04 product is shown in grey bars; the GPS POD solution using PANDA (short as "rep") is shown in empty red bars, and the IGS combined (ig2) and AC-specific products are shown in other colors. The values are given for the bars excessing the panels.

The formal error of the C04 product is around 45 μas for PM offsets and around 90 μas for PM rates. For most of the ACs, the PM offset formal errors are at the level of 10 μas or even smaller, and the PM rate uncertainties are at the level of 10–50 μas/day. The IGS and AC ERP formal errors are over-optimistic compared to the C04 product, except for GRG (gr2 and grg), which has the largest nominal accuracy of 67 μas for PM offsets, whereas the PM rate formal errors are 34 μas/day on x-pole and 38 μas/day on y-pole, which looks odd as the uncertainties of rates are usually one to four times larger than those of offsets for other ACs. The uncertainty value of gr2 at DOY 270 in 2011 is not used as the value (14358 μas for x-pole and 13992 μas for y-pole in the file of "gr216557.erp") is obviously wrong. Despite the fact of using the same software at JPL and EMR, the EMR PM offset and rate uncertainties are two to three times larger than those of JPL.

The LOD formal error of C04 is at the level of 11 μs/day, and those of most of the IGS ACs are about 1–2 μs/day. However, as the LOD estimates from satellite techniques are reliable only in the short-term signals, such a small number is certainly over-optimistic and untrustworthy. The LOD formal error at JPL (jp2 and jpl) and EMR (em2 and emr) are much larger than other ACs with an average value of 6.6 μs/day and 8.5 μs/day, respectively. The reason is still not clear but it should be repeated that these two ACs use the same software.

As shown in Figure 4.7, the formal errors of the C04 product, the PANDA reprocessed solutions, and all most of the ACs are reducing from 2005 to 2017 in general. The major reason is the improvement of the IGS network, as many more stations with better global distribution are available in the later years. However, the products from EMR (em2) and GRG (gr2) do not show steady reduction.

ERP WMEAN

The weighted mean values of ERP differences between GNSS solutions and the IERS EOP 14 C04 product are shown in Figure 4.8. Additionally, the absolute values of WMEAN over the five campaigns are averaged and shown in Table B.1, together with the average values of the WMEAN.

For most of the ACs, the WMEAN values of PM offset are within 40 μas; and those of PM rate are within 100 μs/day and 200 μs/day for the x-pole and y-pole components, respectively. The reprocessed GNSS POD solution has the comparable bias compared to other ACs, with the PM WMEAN values slightly smaller than other ACs. The COD 3-day solution (co2 and cod) has the smallest PM rate bias (6 μas/day on x-pole and 4 μas/day on y-pole), which can be attributed to the 3-day processing arc where the between-day continuity conditions are applied. The JPL product (jp2 and jpl) also has smaller PM rates (48 μas/day on x-pole and 63 μas/day on the y-pole), which might be explained by the 30-hour processing arc length. The MIT solution (mi2 and mit) which applies forced continuity conditions on between-day orbit parameters, however, does not show significant improvement compared to other ACs. This indicates that the continuity of orbit parameters solely cannot reduce the PM rate bias.

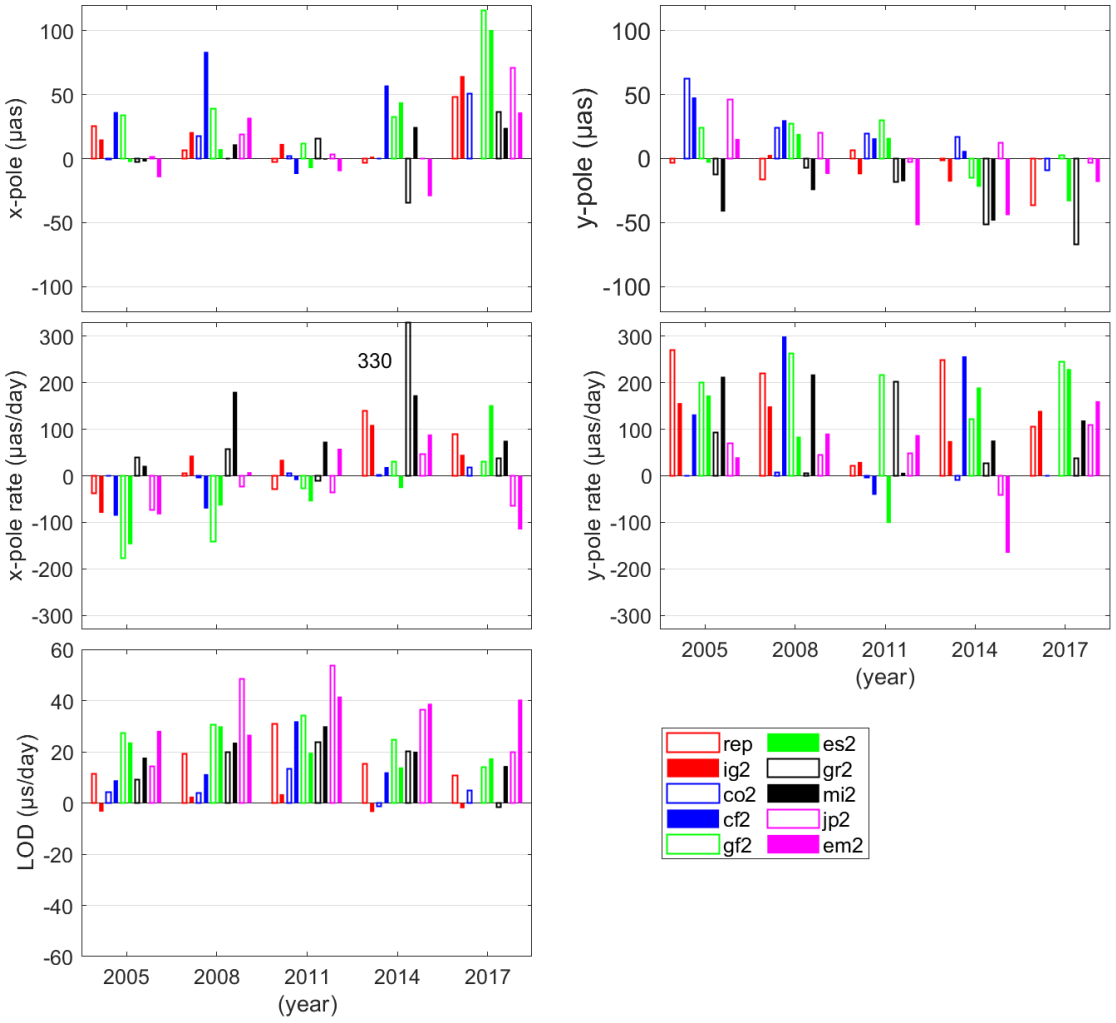

Figure 4.8 WMEAN values of ERP differences between different GNSS solutions and the IERS EOP 14 C04 product in CONT05–CONT17. Note the different vertical axis scales between different panels.

It should be mentioned here that the PM differences between the IG2/IGS and C04 products before 2014 cannot be simply explained as the AC-specific bias. The IG2 product is generated based on ITRF2008, and is further used to determine the ITRF2014. On the other hand, the C04 is a combination of the IGS second reprocessing product (together with other techniques) but with a translation to align to the ITRF2014. Therefore, systematic biases may come from the reference frame effect.

The LOD biases are within 40 μs/day for all the ACs in general, and the smallest bias (6 μs/day) is achieved by the CODE 3-day solution (co2 and cod), which can be attributed to the 3-day processing arc (Zajdel et al., 2020). The small bias of IG2/IGS LOD is simply because it has been realigned to the IERS rapid EOP product. The reprocessed GNSS POD solution has comparable performances compared to other ACs, with an average absolute WMEAN of 17.4 μs/day. The JPL and EMR LOD estimates show much larger biases compared to other ACs, which is consistent with the corresponding large uncertainties in Figure 4.7. The JPL results show that the 30-hour arc does not help in reducing the LOD bias. Nevertheless, their large bias and formal errors still need an explicit explanation from the corresponding ACs.

Furthermore, over the five campaigns, the x-pole biases are positive for most of the ACs, while the y-pole rate biases are negative. As for the LOD, the biases are positive for all the GNSS-only solutions.

ERP WSTD

The WSTD values of the detrended ERP differences between each pair of ERP comparison are given in Figure 4.9, and the average values over all the periods are summarized in Table B.2. The inter-AC PM WSTD values are all smaller than 40 μas in the five CONT campaigns, and the reprocessed GNSS POD solution ("rep") shows good agreement of 20–30 μas to other ACs' products. The C04 product has larger PM WRMS values compared to all other GNSS solutions in most of the campaigns, especially in CONT08 and CONT17.

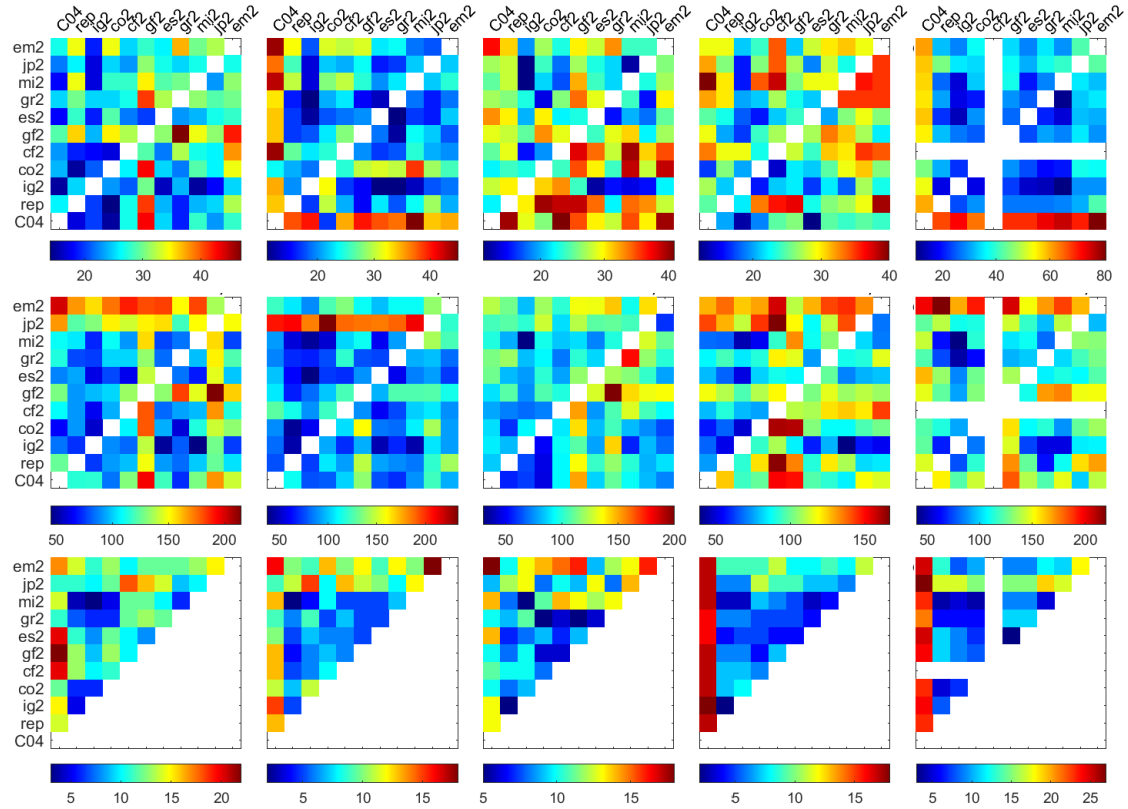

Figure 4.9 WSTD values of the ERP differences between the IERS EOP 14 C04, reprocessed GNSS POD, and the IGS and AC products in CONT05–CONT17. Top panels: PM offsets in μas for x-pole (upper triangle) and y-pole (lower triangle); middle panels: PM rate in μas/day for x-pole (upper triangle) and y-pole (lower triangle); bottom panels: LOD in μs/day. From left to right: CONT05, CONT08, CONT11, CONT14, and CONT17. Note the different colormap scales.

For PM rates, the WSTD values are less than 150 μas/day for all pairs of comparisons. The EMR solution (em2) has larger WSTD values compared to others in CONT05, CONT14, and CONT17, and the JPL product (jp2) has larger x-pole rate WSTD values in CONT08.

For LOD, the different IGS ACs agree with each other very well with the WSTD values less than 10 μs/day, but large value exists, for instance, es2, gf2, and co2 compared to the C04 product in CONT05, em2 compared to jp2 in CONT08, and em2 compared to the C04

product in CONT11. The C04 product has realatively larger WSTD values (20–25 μs/day) compared to the GNSS solutions in CONT14 and CONT17.

In general, the reprocessed POD solution ("rep") has comparable WSTD values compared to other IGS ACs in terms of both PM offsets, rates, and LOD. The WSTD values of x-pole rate and LOD for JPL and EMR (jp2 and em2) are relatively larger than those of other ACs, and it may be explained by the same software used by both ACs. Note that the GNSS POD solution in this thesis does not contributes to the IGS combination, while other ACs do.

4.4 Analysis of the VLBI CONT campaigns

In this section the VLBI single-session solutions in the CONT05–CONT17 campaigns are analyzed. The group delay residuals are first demonstrated, and then the coordinates are evaluated in terms of repeatability. The EOP accuracy is assessed using both the IERS EOP 14 C04 product and the EOP solutions from other IVS ACs. This section mainly serves as a validation and verification of the VLBI module in the PANDA software, and more focus is thus put on the inter-AC comparision. The performance of the PANDA estimates are compared to that of the products of other IVS ACs, from their ITRF2020 submission[63], which have the AGN estimates. Therefore, the AGN coordinates are also estimated using the NNR constraints. The following IVS ACs are used in this section.

Table 4.6 List of VLBI products used for the comparision of VLBI estimates. Note that all ACs except for GFZ use the Calc/SOLVE software.

AC	Softwre	Solution	Comments
ASI	Calc/Solve	asi2020a	Missing sessions: five in CONT11, one in CONT14
BKG	Calc/Solve	bkg2020a	
GFZ	PORT	gfz2020b	First day in CONT17-VLBA not used, extremely bad quality
USNO	Calc/Solve	usn2020b	The CONT17-VLBA campaign not used, extremely bad quality
IVS		ivs2020a	AGN coordinates fixed to the a priori values

As in CONT05 several ACs only process the XA series instead of the XB, whereas in this theses the XB series is processed, in this section the CONT05 results are not evaluated when comparing to other ACs. The 75 sessions from CONT08 to CONT17 can already serve as an good indicator for the software validation and verification.

4.4.1 Introduction of CONT campaigns

The continuous VLBI campaigns organized by IVS are designed to obtain state-of-the-art VLBI observations continuously over a period of 15 days, aiming to demonstrate the best performance of the VLBI system at that time (MacMillan, 2017; Behrend et al., 2020). In total

[63] https://ivscc.gsfc.nasa.gov/IVS_AC/IVS-AC_ITRF2020.htm

nine CONT campaigns have been successfully organized, with three (in 1994, 1995, and 1996) before the creation of IVS (in 1999). Six CONT campaigns were conducted since 2000, namely the CONT02, CONT05, CONT08, CONT11, CONT14, and CONT17 campaigns. These campaigns help to test and diagnose any possible station problems extensively before the experiment begins.

The successfully conducted campaigns also provide a valuable opportunity for scientific research, and plenty of studies have been conducted using the CONT campaigns, such as the investigations of the tropospheric parameters, the high-resolution EOP models, the reference frame stability (Artz et al., 2007; Heinkelmann et al., 2011; Nilsson et al., 2011; Schindelegger et al., 2011; Elgered et al., 2012; Nilsson et al., 2014; Haas et al., 2016; MacMillan, 2017; Karbon et al., 2018; Nilsson et al., 2019a; Nilsson et al., 2019b). The CONT campaigns are ideal for the inter-technique combination due to the two weeks of continuous observing scheme, and several studies have been performed (Snajdrova et al., 2005; Thaller et al., 2006; Teke et al., 2011; Haas et al., 2012; Teke et al., 2013; Hobiger and Otsubo, 2014).

Table 4.7 List of CONT campaigns since 2002. Most of the campaigns start at 00:00 UT and end at 24:00 UT.

Campaign/DBC	Code	Time	Station	Comment
CONT02/XB		DOY 289–304, 2002	8	Time window: 18:00–17:45 UT. Not used
CONT05/XB	C05	DOY 256–269, 2005	11	Time window: 18:00–17:30 UT, TIGOCONC deselected
CONT08/XA	C08	DOY 225–239, 2008	11	One day missing at ZELENCHK, three days missing at TIGOCONC
CONT11/XA	C11	DOY 258–272 2011	14	One day missing at NYALES20 and BADARY
CONT14/XA	C14	DOY 126–140, 2014	16	One day missing ZELENCHK
CONT17/XA	V17	DOY 332–346 2017	14	The Legacy-2 (VLBA) network, seven days missing at SHESHAN25, one day missing at NL-VLBA
CONT17/XB	C17	DOY 332–346 2017	14	The Legacy-1 (IVS) network, three days missing at FORTLEZA, one day missing at NYALES20
CONT17/XG		DOY 337–341 2017	6	The VGOS network, not processed

The six CONT campaigns since CONT02 are shown in Table 4.7. The participating stations are increasing due to the improving IVS network. Unlike other 24-hour VLBI sessions (for instance, R1&R4) which are usually organized in the time window of 17:00–17:00 UT, the CONT sessions are organized in the time window of 00:00–24:00 UT since 2008. For the CONT05 sessions which still use the window of 17:00–17:00 UT, a reprocessed version (the XB series) re-fringed to cover 00:00–24:00 UT is available (IVS mail[64]). This also allows a better combination with other space geodetic techniques. As for CONT17, the participating of the

[64] http://ivscc.bkg.bund.de/mhonarc/ivsmail/msg00743.html

VLBA network allows an observing program of three networks: the IVS network, the VLBA network, and the VGOS network (Behrend et al., 2020). The network effect can thus be investigated using the IVS and VLBA networks, while the five days' observations of the VGOS network serve as a demonstration of the VGOS.

The distribution of VLBI stations in CONT02–CONT17 is given in Figure 4.10. Following the GNSS data processing scheme with a time window of 00:00–24:00 UT (actually the GPST is more often used, but it makes no big difference in this case), the five CONT campaigns since CONT05 are used in this study.

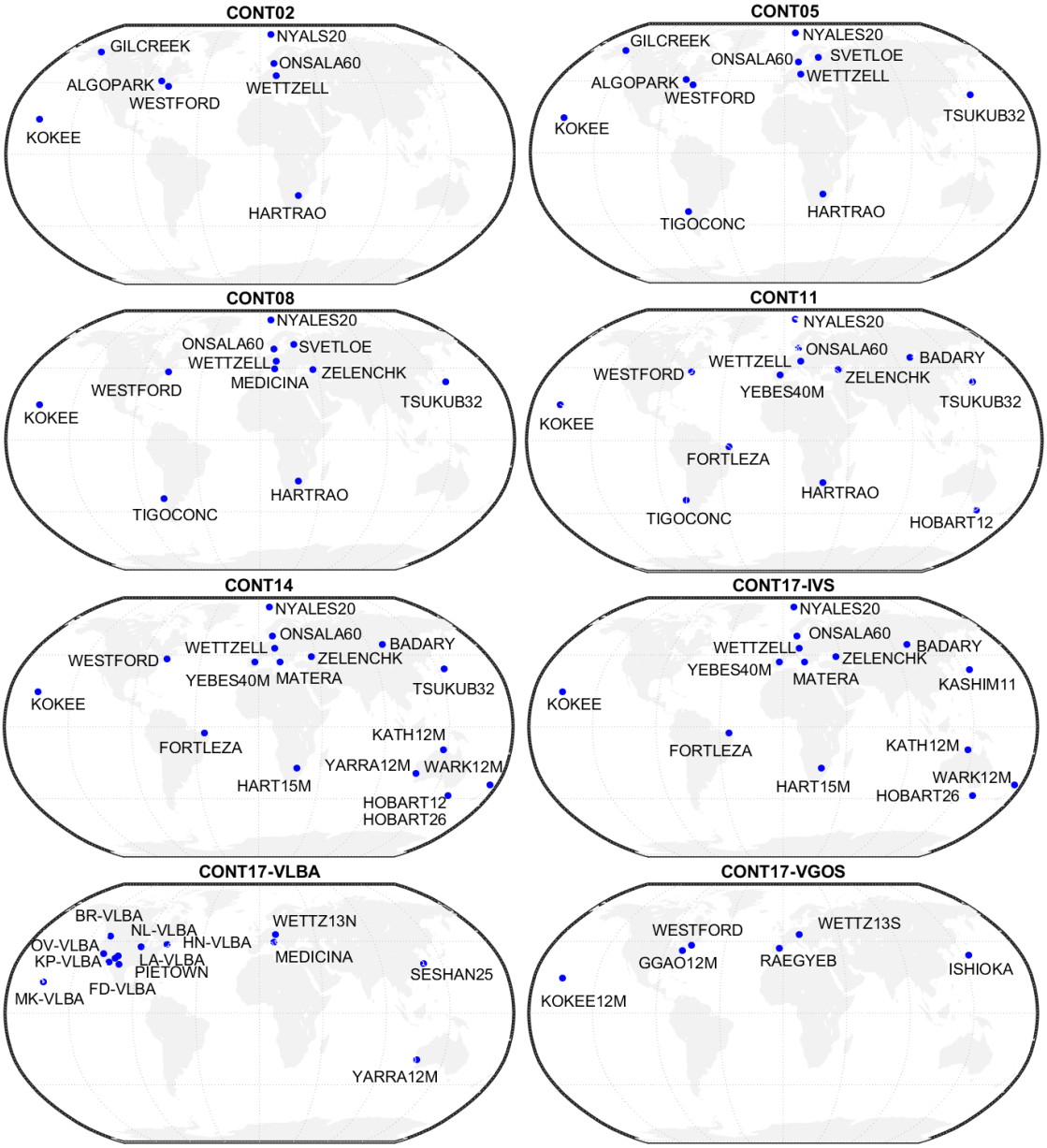

Figure 4.10 Distribution of VLBI telescopes in CONT02–CONT17. Three networks (VLBA, IVS, and VGOS) participated in CONT17.

In CONT05 the reprocessed XB series are used, while in CONT17 both the IVS and the VLBA networks are used. The CONT17-VGOS network is not used because five days results

do not have statistical significance. Therefore, in total six VLBI networks are processed. The TIGOCONC telescope is not used in both CONT05 and CONT08 due to the unstable performance, as the observation number varies a lot and might cause a negative effect on the whole network. As a consequence, the results might be biased systematically due to the uneven station distribution with only a few stations in Southern Hemisphere. However, the short-term precision should still be optimistic as the network is stable in each CONT campaign. As for the CONT17-IVS network, the station WETTZELL was de-selected in DOY 338–341 due to its bad performance. Other stations with dropped off days are shown in Table 4.7.

4.4.2 Group delay residuals

As the VLBI module is newly implemented in the PANDA software, it is necessary to investigate a bit more.

First, the group delay residuals are analyzed. The residuals in session C1415 (DOY 140 in 2014) are shown as an example in Figure 4.11. The baseline-wise residuals are shown in the left panel with different color-marker combinations, while the distribution of all the residuals is shown in the right panel. Most of the residuals (99.4%) are within 40 mm, and the mean value of all residuals is –0.2 mm. The standard deviation is 11.6 mm, and 98.6%.of the residuals are within 3σ (34.8 mm).

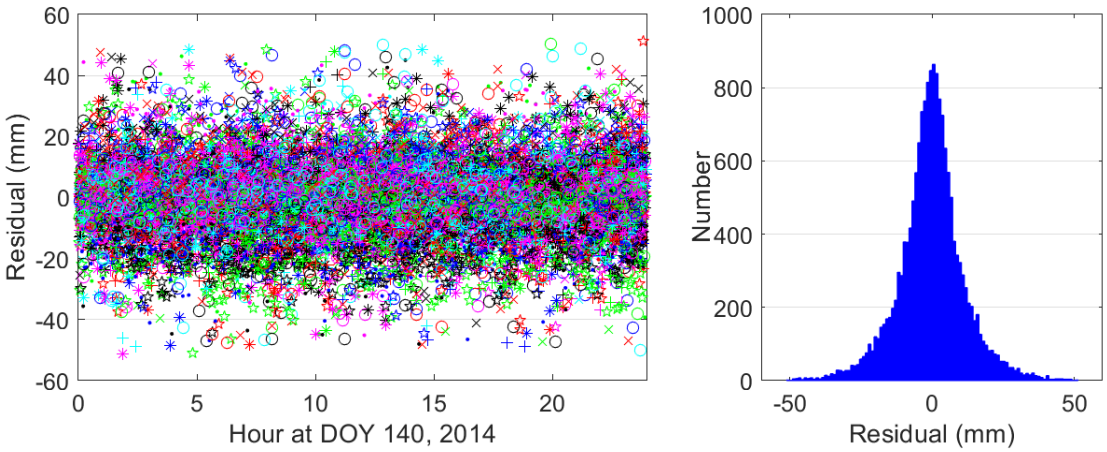

Figure 4.11 Group delay residuals of VLBI session C1415 in CONT14 (DOY 140, 2014) in the left panel, and the distribution in the right panel. In the left panel, different color-marker combinations represent different baselines.

The WRMS and RMS values of the session-wise group delay residuals in CONT05–CONT17 are given in Figure 4.12. The RMS value is calculated using the residuals, and the WRMS is calculated using the residuals and the corresponding weights.

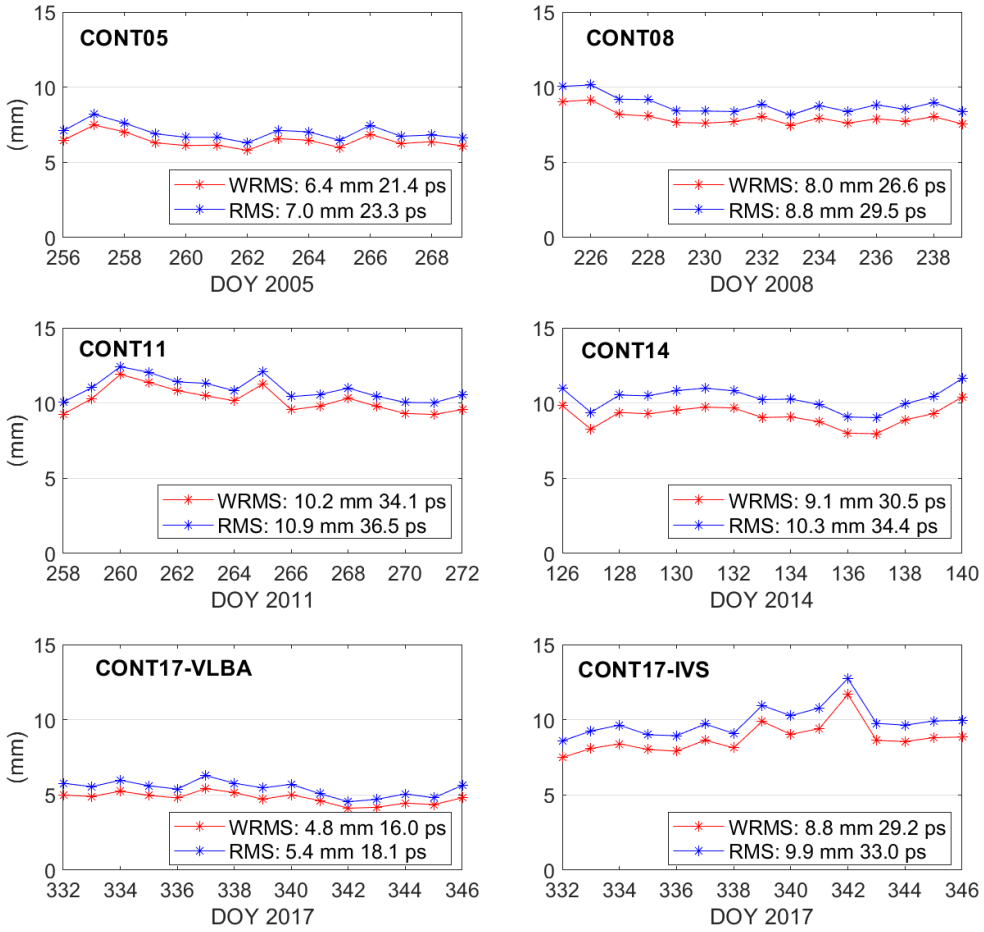

Figure 4.12 VLBI session-wise WRMS and RMS values of the group delay residuals in CONT05–CONT17. The RMS refers to the unweighted residuals, and the refers to the weighted residuals.

The session-wise WRMS values are usually less than 12 mm (40 ps), while the campaign-wise average values are less than 10 mm (34 ps), with the minimum value of 4.8 mm (16 ps) in the VLBA network of CONT17. This relatively small WRMS value can be explained by the non-even distributed network with most of the stations concentrated in North America, as most of the baselines are relatively short. In each campaign, the WRMS values between different sessions have similar magnitudes, which makes sense since there is no large network change or equipment upgrades within the campaign. Also, the radio telescope performances usually remain stable and the similar observation strategy is applied within one campaign.

4.4.3 Precision of station coordinates and baseline

Weighted repeatability of station coordinate

Figure 4.13 gives the station coordinate weighted repeatability values of the PANDA estimates and other the IVS ACs. The precision varies within 1.5–4 cm and 1.5–3 cm on the north and east components, respecticvely, and the vertical value varies between 4 and 9 mm in most cases. Dispite the various performances in different campaigns, the PANDA estimates show an

comparable precision compared to other ACs, while the IVS solution has the best precision because (1) it is a combination of 12 ACs, and (2) the AGN coordinates are fixed to the a priori values instead of estimated. The averge values for PANDA, asi2020a, bkg2020a, gfz2020b, usn2020b, and ivs2020a are 3.2, 2.8, 3.1, 3.4, 2.8, and 2.0 mm on the north component, 2.7, 2.1, 2.4, 2.7, 2.2, and 1.9 mm on the east component, and 8.4, 6.6, 7.1. 7.9, 7.3, and 5.9 mm on the up component, respectively. The PANDA performance in different CONT campaigns also agrees well with other ACs, with the best precision achieved in the CONT17-VLBA network due to the fact that most of the telescopes are located in North America, and thus the network is inhomogeneous but rather stable and most of the baselines are short. It is worth mentioning that the PANDA estimates are relatively poor in CONT08 on all the north, east, and up components, which still needs further investigation of the modeling and parameterization. Moreover, the relatively larger repeatability of PANDA solution on the up component could be attributed to the different strategies of modeling tropospheric delays and clocks, most likely about the adopted relative temporal constraints.

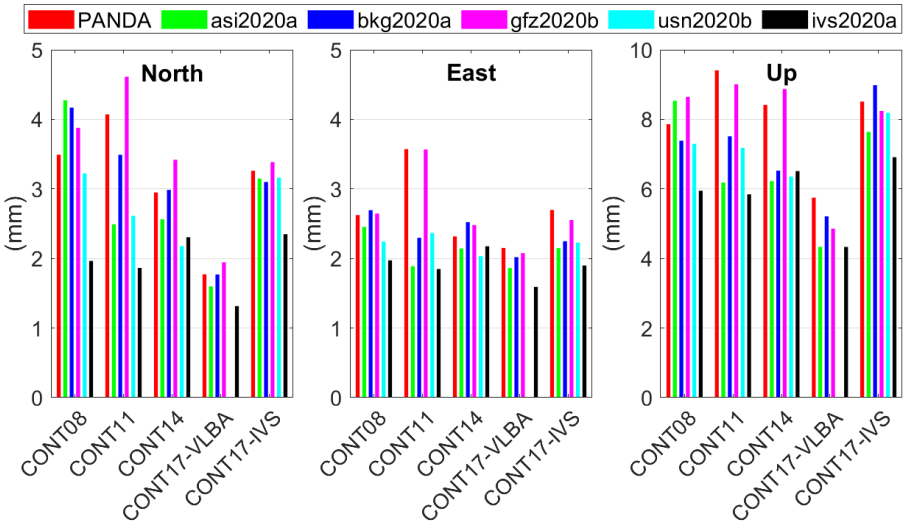

Figure 4.13 Weighted repeatability of VLBI station coordinates of the PANDA solution and other IVS ACs in CONT08–CONT17. Note the different vertical axis scales between the horizontal and vertical components.

Weighted baseline length repeatability

In addition to the coordinate repeatability, the baseline length weighted repeatability is given in Figure 4.14, and the fitting coefficients are also presented. Unlike the coordinate repeatability which might be affected by the network datum and EOP parameters, the baseline length repeatability can better demonstrate the internal precision of the VLBI modeling and coordinate estimation.

As shown in Figure 4.14, the repeatability increases at longer baselines. The repeatability is usually larger than 10 mm for the baselines longer than 10,000 km. The PANDA solution shows a comparable performance with respect to the asi2020a, bkg2020a, and usn2020b

solution, which is visibley better than the gfz2020b solution. The IVS combined solution once again demonstrates the best performance than other ACs.

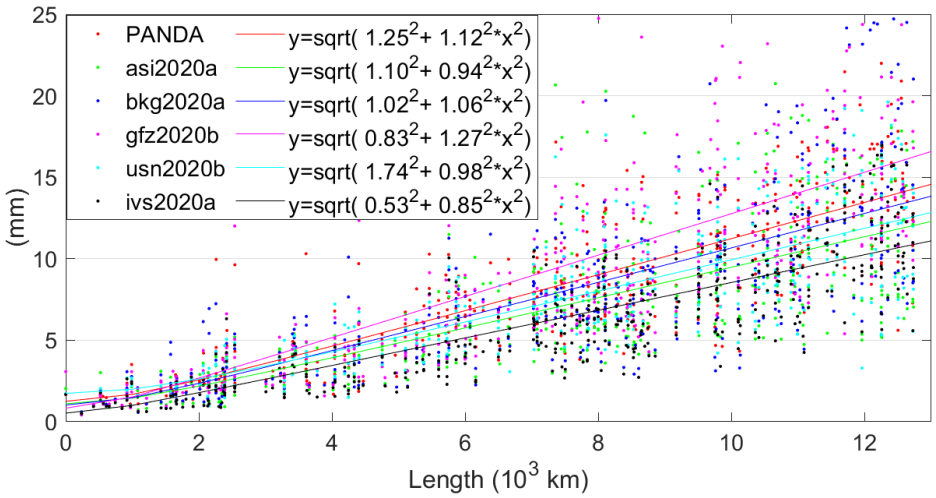

Figure 4.14 VLBI baseline length weighted repeatability (in points) and the fitted values (in line) of the PANDA solution (red) and other IVS ACs in CONT08–CONT17. The fitted coefficients in each campaign are also shown in the legend.

4.4.4 CRF precision

For the CRF precision, the coordinate repeatability of VLBI radio sources are calculated in CONT08–CONT17. The performance of the PANDA solution is comparable to those of othe ACs. The average repeatability values of right ascension are 1.5, 1.5, 1.3, 1.7, and 1.2 nanoradian for the PANDA, asi2020a, bkg2020a, gfz2020b, usn2020b solutions, respectively, and the corresponding values of declination are 1.5, 1.4, 1.4, 1.5, and 1.1 nanoradian.

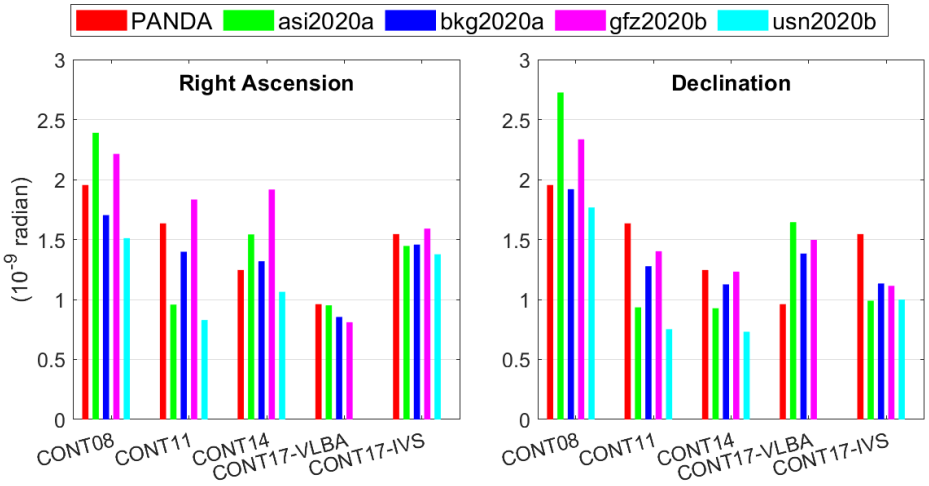

Figure 4.15 Coordinate repeatability of VLBI radio sources in the PANDA solution (red) and other IVS ACs in CONT08–CONT17.

Despite the extremely bad precision of the usn2020b solution in CONT17-VLBA which is taken as outliers and not included in this statistic, the usn2020b solution seems to have the

best performance in the rest CONT campaigns compared to other ACs, while the gfz2020b solution has relatively larger repeatability. Note that in the IVS combination solution (ivs2020a) the AGN coordinates are fixed to the a priori values, and thus the estimates are not available. Note that the difference ACs have different performances in the five networks, for instance, the asi2020a solution has larger WSTD values in CONT08, and the PANDA solution has relatively worse performance in CONT17-VLBA. Nevertheless, the overall performance is rather consistent with the statistics.

4.4.5 EOP precision

Moreover, the EOP precision of the PANDA estimates and other IVS ACs are presented in Figure 4.16, where the average values over CONT08–CONT17 are given. We can clear see that in general the precision of the PANDA estimates is comparable to other IVS ACs in both polar motion and UT1-UTC components, whereas that of the CPO comonents are relatively poorer. This might be explained by (1) in the PANDA solution no a priori constraints are applied to the EOP while all IVS ACs do apply such an a priori constraints, and (2) the IERS EOP 14 C04 product is a combination of different techniques and different ACs, where the CPO components are solely determined by VLBI, taking the contributions from the IVS ACs but not from the PANDA solution.

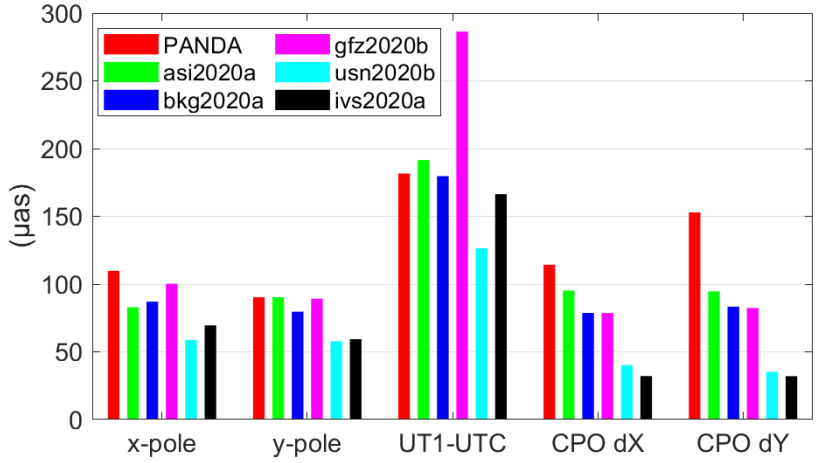

Figure 4.16 EOP precision of the PANDA solution and IVS ACs compared to the IERS EOP 14 C04 product. The average WSTD values over CONT08–CONT17 are presented here. Note that for UT1-UTC, the unit of μas is used, which is equivalent to 1/15 μs.

Moreover, the detailed statistics of each CONT campaign are given in Figure 4.17. The performance is improved from CONT08 to CONT14 due to the more homogeneous station distribution, especially the polar motion and CPO components, whereas the UT1-UTC component does not show any significant fluctuations in different campaigns as it is more related to the east-west distribution of the network, which is optimal in all the CONT campaigns. In CONT17 the two networks both show larger WSTD values compared to

CONT14, especially the y-pole component in the CONT17-VLBA network, which can be explained by the inhomogeneous network with most of the VLBI radio telescopes concentrated in North America. The gfz2020b solution has relatively larger WSTD values in all these CONT campaigns, which should be further investigated.

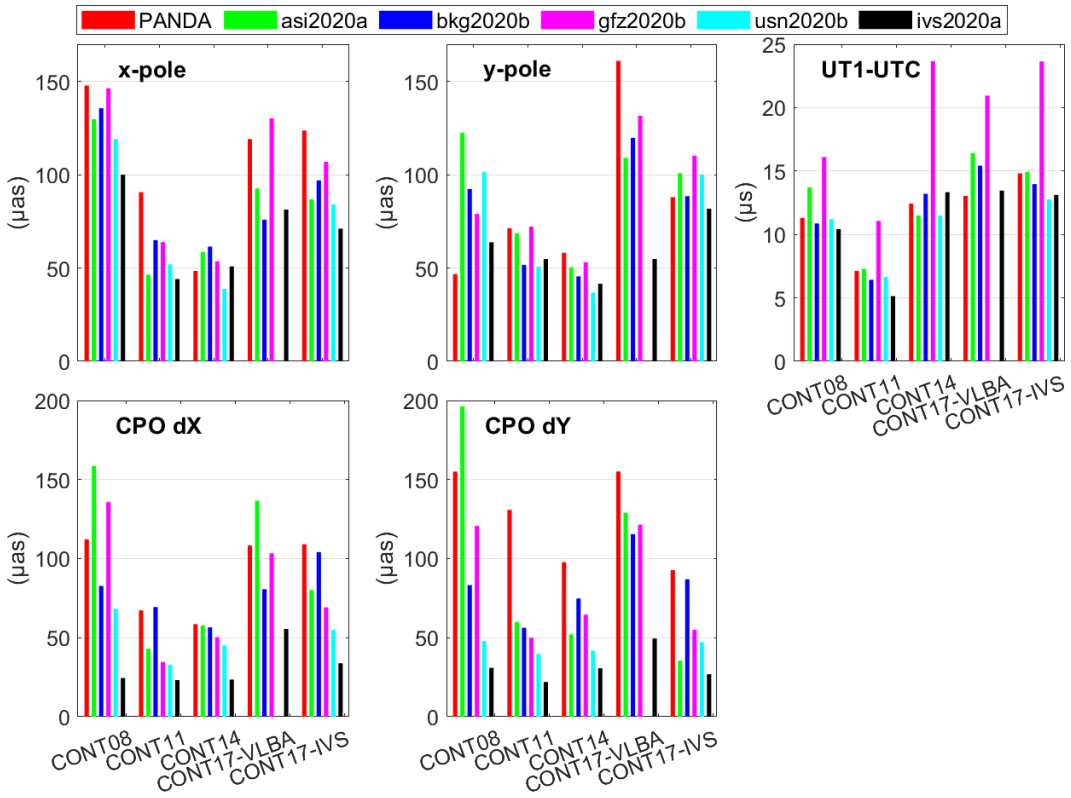

Figure 4.17 WSTD values of the EOP components compared to the IERS EOP 14 C04 product in CONT08–CONT17.

4.5 Analysis of ERP agreement between GNSS and VLBI

4.5.1 Inter-technique ERP agreement

Despite the analysis of the GNSS and VLBI solutions compared to the IERS and corresponding AC solutions, it is necessary to directly compare the GNSS daily POD solution to the VLBI single-session solution, that is, the inter-technique agreement of homogeneous reprocessed ERP estimates. The comparison between the ERP estimates from homogeneously reprocessed GNSS and VLBI solutions using the same models (the common estimator in this study) can demonstrate the inter-technique agreement and help to investigate any possible systematic biases directly and simply. As the data processing of GNSS and VLBI are performed in the same software with the same models, conventions, and parameterizations, the best consistency can be guaranteed. In this way, the comparison help to diagnose the "pure" technique-specific features.

The daily ERP differences compared to C04 and the corresponding formal errors of GNSS and VLBI solutions are shown in Figure B.1 to Figure B.6. The MEAN and STD values of the differences between GNSS and VLBI are summarized in Table 4.8. Note that in this section the AGN coordinates are fixed to the a priori values in the VLBI processing.

Table 4.8 MEAN and STD values of ERP differences between GNSS and VLBI solutions in CONT05–CONT17.

EOP	x-pole (μas)	y-pole (μas)	x-pole rate (μas/day)	y-pole rate (μas/day)	LOD (μs/day)
CONT05	–85±153	21±123	–97±241	–384±181	–6.7±14.7
CONT08	–40±156	–41±56	–33±205	–340±193	–12.0±9.4
CONT11	–24±80	21±58	–25±164	–75±220	–29±7.9
CONT14	–12±53	31±51	–84±125	–318±163	–16.8±5.0
CONT17-VLBA	135±84	–103±75	–41±213	–184±190	–14.2±8.3
CONT17-IVS	34±81	5±38	–185±164	–121±180	–13.5±13.2

As presented in Figure B.1 to Figure B.6, The PM agreement to the IERS EOP 14 C04 product of GNSS is much better than that of VLBI, and the latter one has larger biases, larger STD values, and larger uncertainties. The figures also show that the C04 product can be biased. The x-pole STD values of the differences between GNSS and VLBI are smaller than those between VLBI and C04 in the two networks of CONT17, despite the systematic biases in the CONT17-VLBA network. An obvious discrepancy between C04 and both GNSS and VLBI can be observed at DOY 337, where GNSS and VLBI agree well with each other. This can also be observed on the y-pole component in CONT08 (DOY 225–230), CONT11, and CONT17.

The x-pole agreement between GNSS and VLBI improves by time, with the values reduced from –85±153 μas in CONT05 to –12±53 μas in CONT14, and the values in CONT17 are 135±84 μas and 34±81 μas for the VLBA and the IVS networks, respectively. The STD of y-pole differences between GNSS and VLBI is 123 μas in CONT05, and is reduced to around 40–60 μas in other campaigns. The MEAN values are usually less than 50 μas, except for CONT17-VLBA with a bias of around 100 μas.

As shown in Figure B.3, the x-pole rate STD values of VLBI are larger than that of GNSS by a factor of two to three in CONT05–CONT14, and the factor is around 1.4 in CONT17. On the other hand, as the x-pole MEAN value of GNSS is usually smaller than that of VLBI, it can be larger sometimes (for instance, 139.7 μas/day for GNSS and 55.7 μas/day for VLBI in CONT14). The agreement between GNSS and VLBI in terms of STD is usually better than that between VLBI and C04, and worse than that between GNSS and C04.

As for the y-pole rate in Figure B.4, the STD value of VLBI is larger than that of GNSS in all campaigns, while the MEAN value of VLBI is smaller than that of GNSS by a factor of 1.6 (CONT08) to 3.1 (CONT14). For all campaigns, GNSS and VLBI show opposite systematic biases compared to the C04 product. Significant systematic bias between GNSS and VLBI can be observed in most campaigns, as the MEAN value of the differences between GNSS and VLBI can be as large as 300–400 μas, including CONT05, CONT08, and CONT14.

As for the LOD shown in Figure B.6, the agreement between GNSS and VLBI is usually optimal with the STD value at the level of 5–10 μs in CONT08–CONT17 (the VLBA network), despite the large GNSS LOD bias. The CONT05 and CONT17-IVS networks both show larger STD values. Nevertheless, the inter-technique agreement is usually better than the agreements to the IERS product, and obvious errors can be observed in the IERS EOP 14 C04 time series.

4.5.2 Comparison with previous studies

To further verify the VLBI module of the PANDA software, the ERP differences between GNSS and VLBI solutions from a previous study (Nilsson et al., 2014) and that from this study are shown in Table 4.9. Noted that as the global solution (derived by stacking the daily NEQs of the whole CONT campaign to one NEQ) is used by Nilsson et al., the single-session solution is also provided (Table 4 from Nilsson et al.). One may notice that the global solution is much better than the single-session solution for PM estimates. This can be attributed to: (1) the global solution uses between-day constraints, that is, the ERP parameters between consecutive days are constrained to each other, resulting in a more robust solution; and (2) only one set of coordinates is estimated in the global solution, which reduces the high correlation between daily station coordinates and EOP estimates (Artz et al., 2007).

Nevertheless, Table 4.9 demonstrates that the single-session solution in this study and that from the previous study are comparable with similar WMEAN and WRMS values. In fact, the agreement in this study are even better. The large LOD bias (–29.7 μs/day) is caused by the biased GNSS LOD, as already mentioned several times.

Table 4.9 WMEAN and WRMS values of ERP differences between VLBI and GNSS solutions from a previous study and that from this study in CONT11.

ERP	x-pole (μas)	y-pole (μas)	LOD (μs/day)
Nilsson et al.: VLBI (glob.) – IGS	–44.8±31.1	168.3±30.6	6.2±6.8
Nilsson et al.: VLBI (sing.) – IGS	–46.6±88.4	186.8±67.1	5.1±6.9
PANDA: VLBI (sing.) – GNSS POD	–24.7±73.9	59.8±57.8	–29.7±5.9

4.6 Analysis of tropospheric tie between GNSS and VLBI

In this section the agreement of tropospheric parameters between GNSS and VLBI co-located stations is analyzed. As the troposphere is non-dispersive for radio signals, these two techniques have the same sensitivity to tropospheric parameters. In the case of a VLBI telescope and a GNSS antenna co-located within tens of meters without height difference, their tropospheric parameters should be the same by nature, and can thus be tied together in integrated processing. In reality, however, both systematic bias and random noise exist. For GNSS, the tropospheric parameters can be affected by the receiver type, antenna PCV. On the

other hand, different observation geometries introduce noise to the tropospheric parameter estimates. Therefore, knowing the inter-technique agreement of the tropospheric parameters is a prerequisite for any further combination.

The inter-technique agreement of tropospheric parameters has been analyzed in previous studies using both long-term time series and the CONT campaigns. Early-stage comparison of ZTD between GPS, VLBI, DORIS, WVR, and NWM was done using the CONT02 campaign, where the ZTD agreement was reported as 3–7 mm between GPS and VLBI (Snajdrova et al., 2005). Using 11 years of observations, it is reported that the homogeneously reprocessed GNSS and VLBI tropospheric parameters show common signals with high precision, but the long-term trends agreement is not good enough to describe the climatological interpretation at that time (Steigenberger et al., 2007). The agreement between GNSS and VLBI was further investigated using the CON02–CONT11 campaigns (Teke et al., 2011; Teke et al., 2013), where an agreement of 5–6 mm for ZTD in terms of STD was demonstrated. Moreover, the tropospheric parameters from GPS, VLBI, SLR, and DORIS was also performed using the CONT08 campaign, and it concludes that the GPS technique plays a major role in the integrated tropospheric parameter estimation (Pollet et al., 2014).

In this thesis the VLBI tropospheric parameters are derived from the single-session processing using the CONT05–CONT17 campaigns. More details are presented in Section 4.2. Instead of the GNSS POD solution, the Precise Point Positioning (PPP) method is applied to derive the tropospheric parameters. The reasons to use PPP instead of POD solution are: (1) PPP is capable of deriving high-precision tropospheric parameters comparable to POD; (2) PPP is much convenient and easy to be applied; and (3) POD is a time-consuming job and can cost several hours, while PPP can be processed in parallel and processing one station only takes a few minutes. The PPP details are presented in Section 4.2. For each VLBI station, all the available co-located GNSS stations are used for a comprehensive comparison. The VLBI and GNSS co-locations are listed in Table A.1, and the receiver and antenna information of the GNSS stations are provided in Table A.2.

For a reliable comparison, the outliers should be removed first. Unlike GNSS where enough observations can be guaranteed most of the time, VLBI does suffer from the problem of limited observations, especially for the 1-hourly sampled ZTD and 3-hourly sampled gradients. Even though the constraint from the adjacent epochs can help to alleviate this problem, it is still necessary to apply the outlier detection and elimination. Therefore, the tropospheric parameter estimates with less than 10 observations are removed before the comparison. For each co-location, the MEAN and STD values of the tropospheric parameter differences over one campaign are calculated, and only those within three times of the STD are used for the further statistic.

In terms of the tropospheric parameter agreement, it should be noted that the differences caused by the horizontal distance and vertical height difference must be considered, especially the latter one due to the high sensitivity of tropospheric delay to height. Therefore, by using NWM for the a priori value, evaluating the agreement of the residual tropospheric delays,

including both residual ZWD and gradients, is the same as evaluating the tropospheric tie agreement between NWM and space geodetic solutions.

On the other hand, the tropospheric parameter differences can also act as a new source of the tropospheric ties, that is, the tropospheric ties from space geodetic solutions. The differences over a period of time can be averaged with the corresponding uncertainty derived, and this average value can be further applied in the integrated processing. It is important to ensure that the tropospheric ties from NWM and that from space geodetic solutions do not have any systematic bias, as it can cause the network distortion. This is another reason to investigate the tropospheric tie agreement between space geodetic solution and NWM.

As the focus of this section is tropospheric parameters, thus in the VLBI processing the coordinates of radio sources are fixed to the ICRF3 for a better solution.

This section is organized as follows. First, the tropospheric parameter differences from NWM (or tropospheric tie from NWM) at co-located GNSS and VLBI stations are presented. Then the intra-technique tropospheric tie agreement between space geodetic solutions and NWM is investigated for the GNSS–GNSS and the VLBI–VLBI co-locations in Section 4.6.2 and Section 4.6.3, respectively. The GNSS–VLBI inter-technique agreement of ZTD is demonstrated in Section 4.6.4, and that of gradients is demonstrated in Section 4.6.5. Moreover, as the tropospheric parameters are highly correlated with the station coordinates, the tropospheric parameter agreement also indicates the coordinate precision, as shown in Section 4.6.6. This section ends with investigating the impact of different temporal resolutions of tropospheric parameterization on the inter-technique tropospheric agreement in Section 4.6.7.

4.6.1 Tropospheric ties between GNSS and VLBI from Numerical Weather Model

The tropospheric ties from NWM, that is, the VMF3 product, are first presented. Details on handling the VMF3 product is presented in Section 4.2. As the co-located GNSS and VLBI stations are usually within a few tens of meters, and thus the tropospheric gradient differences are rather insignificant and are not presented here.

The NWM derived tropospheric ties between co-located VLBI and GNSS stations are shown in Table 4.10. At each co-location, the MEAN and STD values of the ZTD differences in the CONT campaign are computed, and the average value of several campaigns is used. For comparison, the average bias from Teke et al. (2011) is also shown in the "Teke" column. For most co-locations, the MEAN bias of the tropospheric tie is at the level of 1–5 mm with the STD value of 0.1–0.3 mm, due to the small horizontal and vertical distance. On the other hand, the large distance between co-locations introduces both large bias and large STD value at (1) FD-VLBA (GNSS: MDO1) where the height difference is 393 m, the MEAN bias is 98.3 mm with an STD value of 3.1 mm; and (2) HARTRAO and HART15M (GNSS: HARB) where

the height difference is about 150 m, the MEAN bias is up to 40 mm with a STD value of 1.5–1.8 mm. The tropospheric tie from NWM in this study and that from Teke agrees within 0.1–0.2 mm, which validates both methods.

It is worth repeating that the GNSS station height given by the VMF product does not exactly coincide with the antenna reference point (ARP) height, considering the difference between the ARP and marker and other potential biases. Nevertheless, the height of the GNSS ARP should always be used, and the empirical equation from Kouba (2007) is used to correct this height-induced bias.

Table 4.10 MEAN and STD of the NWM derived ZTD ties at co-located VLBI and GNSS stations. For stations contributing to multi-campaigns, the average value is shown here.

VLBI	GNSS	NWM (mm)	Teke	VLBI	GNSS	NWM (mm)	Teke
ALGOPARK	ALGO	–7.1±0.4		ONSALA60	ONS1	–4.7±0.2	
BADARY	BADG	–2.8±0.1			ONSA	–4.6±0.2	–4.2
BR-VLBA	BREW	–3.6±0.1		PIETOWN	PIE1	–3.9±0.1	
FD-VLBA	MDO1	98.3±3.1		SESHAN25	SHAO	–2.3±0.2	
FORTLEZA	BRFT	–0.5±0.2		SVETLOE	SVTL	–3.0±0.3	–2.9
GILCREEK	FAIR	–3.9±0.1		TIGOCONC	CONT	0.8±0.1	
HART15M	HARB	40.8±1.5			CONZ	3.0±0.2	3.1
	HRAO	1.4±0.1		TSUKUB32	TSK2	–5.0±0.4	–5.0
HARTRAO	HARB	37.4±1.8			TSKB	–5.9±0.5	–6.1
	HRAO	–0.4±0.1	–0.5	WARK12M	WARK	–5.5±0.1	
HOBART12	HOB2	0.0±0.3	0.1	WESTFORD	WES2	–0.6±0.3	–0.6
HOBART26	HOB2	–7.8±0.3		WETTZ13N	WTZA	–1.9±0.1	
KASHIM11	KSMV	–1.4±0.2			WTZR	–1.9±0.1	
KATH12M	KAT1	–1.5±0.2			WTZS	–2.7±0.1	
KOKEE	KOKB	–2.8±0.2	–2.7		WTZZ	–2.0±0.1	
	KOKV	–2.8±0.2		WETTZELL	WTZA	–0.9±0.3	–1.0
MATERA	MAT1	–2.7±0.1			WTZR	–0.9±0.3	–0.9
	MATE	–2.4±0.1			WTZS	–1.7±0.3	
MEDICINA	MEDI	–5.6±0.3	–5.5		WTZZ	–1.0±0.3	
MK-VLBA	MKEA	–1.6±0.1		YARRA12M	YAR2	–2.2±0.2	
NL-VLBA	NLIB	–4.6±0.2			YAR3	–1.7±0.2	
NYALES20	NYA1	–1.0±0.1	–1.0		YARR	–2.1±0.2	
	NYA2	–1.8±0.1		YEBES40M	YEBE	–4.4±0.1	
	NYAL	–1.1±0.1	–1.1	ZELENCHK	ZECK	–2.4±0.2	–2.4

4.6.2 GNSS–GNSS tropospheric tie from space geodetic solution

The co-located GNSS–GNSS stations share very similar satellite geometry, local environment, and atmosphere condition, and thus homogeneously reprocessed tropospheric parameters at GNSS–GNSS colocations are ideal to assess the internal consistency of the GNSS solutions.

The comparison between co-located GNSS stations also helps to identify the station-specific systematic biases from the GNSS stations, that is, potentionally related to antenna PCV.

The MEAN and STD of the residual ZTD and horizontal gradient differences in all the processed CONT campaigns are shown in Table 4.11, where the NWM based tropospheric ties have been considered. Noted that even though the observation data are available for most of the GNSS stations in all the CONT sessions, in this table only the solutions with co-located VLBI stations are presented.

For the GNSS–GNSS co-locations, the ZTD agreement in terms of STD value is usually less than 3 mm, except for the MAT1–MATE co-location in CONT14 with the value of 3.9 mm. The gradient agreement at this co-location is also worse than others, with the STD value of 0.7 mm, considering the small STD values of less than 0.3 mm at other co-locations. The MAT1–MATE ZTD biases are –3.3 mm and –1.5 mm in CONT14 and CONT17, respectively.

Despite the rough terrain of a small island (less than 50 km but height up to 1300 m) on the Pacific Ocean (22°N, 160°W), the KOKB–KOKE co-location has the best agreement, with average STD values of 0.9 mm for ZTD and 0.17 mm for gradients over three campaigns. The ZTD biases are within ±0.4 mm and those of gradients are zero. The second best agreement is observed at the NYAL–NYA1–NYA2 co-location, located on the west coast of the high-latitude island Svalbard (79°N, 12°E). The ZTD STD values vary from 0.7 to 1.4 mm, and gradient STD values are less than 0.2 mm. However, the ZTD values at both NYA1 and NYA2 are about 1–2 mm larger than that at NYAL, while the gradients (both north and east components) at NYA1 are about 0.1 mm smaller than those at NYAL.

Systematic biases can also be observed at the co-locations of HARB–HARO and YAR2–YAR3–YARR. The ZTD at HARB is about 1.2 to 2.8 mm smaller than that at HRAO, and the gradient biases are about 0.1 to 0.2 mm. The corresponding STD values at this co-location are about 2 mm and 0.4 mm for ZTD and gradients, respectively. As for the YAR2–YAR3–YARR co-location in CONT14 and CONT17, the ZTD at YAR2 is about 1 mm larger than that at YARR, while that at YAR3 is smaller than that at YARR (–1.7 mm in CONT14 and –0.4 mm CONT17). The corresponding STD values are about 1.1 mm on average. The gradient biases are usually within ±0.1 mm, with the corresponding STD values less than 0.2 mm.

The several co-located stations at Wettzell, including WTZA, WTZA, WTZZ, WTZS, agree well with each other, except for the obvious negative ZTD bias at WTZA. The ZTD at WTZA is about 1 to 3 mm smaller than that at the other co-locations. The average STD values between each pair of co-locations are about 1 to 2 mm. The other co-locations (WTZR–WTZZ–WTZS) show good agreement, as the average biases are around 0.3 mm. As for the gradients, the STD values are less than 0.2 mm for all the co-locations, while no large biases can be observed.

The CONT–CONZ co-location shows a systematic bias of –1.0 mm for ZTD and –0.3 mm for east gradient, with the STD value of of 2.4 mm for ZTD and 0.4 to 0.6 mm for gradients. As for the ONS1–ONSA co-location, the agreement is 1.2±1.2 mm for ZTD and 0.0±0.2 mm for gradients.

Table 4.11 MEAN and STD values of the residual ZTD and horizontal gradient differences between co-located GNSS stations in CONT05–CONT17.

	ZTD	G_N	G_E		ZTD	G_N	G_E
CONT–CONZ				WTZA–WTZR			
C11	–1.0±2.4	0.1±0.4	–0.3±0.6	C11	–2.2±1.6	–0.1±0.3	0.1±0.2
HARB–HRAO				C14	–1.6±1.1	–0.0±0.2	0.1±0.1
C05	–1.2±2.9	–0.0±0.5	0.2±0.7	V17	–3.0±1.1	–0.1±0.2	–0.0±0.1
C08	–2.2±1.6	–0.1±0.3	–0.0±0.3	WTZA–WTZS			
C11	–2.8±2.4	0.0±0.4	0.2±0.5	C11	–2.0±1.3	–0.0±0.2	0.1±0.2
C14	–1.7±1.6	0.1±0.2	0.1±0.3	C14	–1.4±1.1	0.0±0.2	0.1±0.2
C17	–1.4±3.4	0.1±0.5	0.1±0.5	V17	–2.7±1.0	–0.0±0.1	0.0±0.1
KOKB–KOKV				WTZA–WTZZ			
C11	–0.2±1.3	0.0±0.2	–0.0±0.2	C11	–1.1±1.3	0.0±0.2	0.1±0.2
C14	0.1±0.8	–0.0±0.2	–0.0±0.1	C14	–1.5±1.3	–0.0±0.2	0.0±0.1
C17	0.4±0.6	–0.0±0.1	–0.0±0.1	V17	–2.5±1.2	–0.1±0.2	0.1±0.1
MAT1–MATE				WTZR–WTZS			
C14	–3.3±3.9	–0.4±0.7	–0.0±0.7	C11	0.3±1.6	0.1±0.2	–0.0±0.2
C17	–1.5±2.2	–0.0±0.4	0.3±0.3	C14	0.1±0.9	0.1±0.1	0.0±0.1
NYA1–NYA2				V17	0.3±0.7	0.1±0.1	0.0±0.1
C17	0.2±1.2	–0.1±0.2	–0.0±0.2	WTZR–WTZZ			
NYA1–NYAL				C05	0.2±1.2	0.0±0.2	–0.1±0.2
C05	1.0±0.8	–0.1±0.1	–0.1±0.1	C08	–0.3±1.4	–0.0±0.1	–0.0±0.2
C08	1.2±0.7	–0.1±0.1	–0.1±0.1	C11	1.1±1.6	0.1±0.2	–0.1±0.2
C11	2.0±1.2	–0.1±0.2	–0.1±0.2	C14	0.1±1.1	0.0±0.1	–0.1±0.1
C14	0.8±1.2	–0.1±0.2	–0.0±0.2	V17	0.5±0.9	0.0±0.1	0.1±0.1
C17	1.7±1.1	–0.1±0.2	–0.1±0.2	WTZS–WTZZ			
NYA2–NYAL				C11	0.8±1.3	0.0±0.2	–0.1±0.2
C17	1.5±1.4	0.0±0.2	–0.0±0.2	C14	–0.0±1.0	–0.0±0.1	–0.1±0.1
ONS1–ONSA				V17	0.2±0.8	–0.0±0.1	0.0±0.1
C17	1.2±1.2	–0.0±0.2	–0.0±0.2	YAR2–YAR3			
TSK2–TSKB				C14	2.6±1.1	–0.2±0.2	0.0±0.2
C05	1.7±2.2	0.1±0.4	0.0±0.4	V17	1.2±1.3	0.0±0.2	0.1±0.3
C08	3.2±2.3	0.2±0.3	0.1±0.4	YAR2–YARR			
C11	2.0±2.8	–0.2±0.7	0.1±0.5	C14	1.0±1.0	–0.1±0.1	0.0±0.2
C14	0.5±2.1	–0.2±0.3	0.0±0.3	V17	0.9±0.7	–0.0±0.1	0.0±0.1
				YAR3–YARR			
				C14	–1.7±1.2	0.1±0.1	0.0±0.2
				V17	–0.4±1.3	0.0±0.2	–0.1±0.2

4.6.3 VLBI–VLBI tropospheric tie from space geodetic solution

The future VGOS network has several co-located radio telescopes, for instance, Twin Telescope Wettzell (TTW), Germany (Neidhardt et al., 2011), Onsala, Sweden (Haas, 2013), and Ny-Ålesund, Spitsbergen, Norway (Langkaas et al., 2010). If the local ties at these co-locations can be measured accurately and the atmosphere above one co-location can be assumed to be physically identical, then the tropospheric parameters at twin-telescopes can be linked in a simultaneous observing program. In this case, the observations at the co-located stations can be doubled with much better observation geometry, and the solution will be enhanced.

In practice, it is however not easy to ensure a good agreement between the tropospheric parameters at co-located stations, which is already shown in Table 4.11 in the scenario of GNSS. For the VLBI twin-telescopes, it is also necessary to first investigate the agreement.

Two co-located VLBI radio telescopes participated in the CONT14 campaign, that is, HOBART12 (CDP: 7374) and HOBART26 (CDP: 7242); while two co-located telescopes participated in the CONT17 campaign, including WETTZELL (CDP: 7224) in the IVS network and WETTZ3N (CDP: 7387) in the VLBA network. The statistic of the tropospheric tie differences between NWM and space geodetic solutions are shown in Table 4.12. Note that the height difference between the twin-telescopes at Wettzell is around 3 m, and that at Hobart is around 24 m. Nevertheless, the VMF3 product can properly model the corresponding ZTD differences.

Table 4.12 MEAN and STD values of the tropospheric parameter differences between NWM and space geodetic solutions at VLBI–VLBI co-locations. The correlation coefficients are shown in the bracket. All the correlation coefficients in this table are statistically significant with the p-value less than 0.05.

Co-location	ZTD (mm)	G_N (mm)	G_E (mm)
Hobart (HOBART12–HOBART26)	2.8±3.7 (87.8%)	0.1±0.5 (69.7%)	0.0±0.4 (69.1%)
Wettzell (WETTZELL–WETTZ3N)	–1.5±2.9 (87.4%)	0.0±0.4 (55.4%)	0.0± 0.4 (46.7%)

For the Hobart co-location, the ZTD parameters show an obvious bias of 2.8 mm in CONT14, while the gradient ties do not show any significant biases. The correlation coefficients of the north and east gradients are similar (around 69%), which are weaker than that of the ZTD (87.8%). As for the Wettzell co-location, a –1.5 mm ZTD bias is observed, and the gradients do not have any significant biases. Despite the similar RMS values of the gradients at both co-locations (0.4 mm), the correlation coefficients at Wettzell are smaller than those at Hobart on both the north and the east components.

4.6.4 GNSS–VLBI ZTD tie from space solution

ZTD estimates at Tsukuba in CONT14

A first illustration of the ZTD estimates and residual ZTD (that is, the difference between ZTD from space solution and that modeled from NWM, dZWD in Eq 3.7) is shown in Figure 4.18, where the values at the GNSS–VLBI co-location at Tsukuba in CONT14 are depicted. The Tsukuba site in Japan is about 50 km to the Pacific Ocean, and is featured with large water vapor content. In the CONT14 campaign (May 6–20 in 2014), the ZTD estimates vary from 2300 mm to 2550 mm. The large fluctuation of residual ZTD varying from –60 to 40 mm indicates that the NWM cannot model the short-term water vapor variation accurately. Nevertheless, the GNSS and VLBI estimates show good agreement in general. Several unmodeled fluctuations in NWM are detected by both GNSS and VLBI, for instance, the significant increase at DOY 128 and decrease at DOY 129, the sharp decrease at DOY 133, and the rapid change at DOY 135–136.

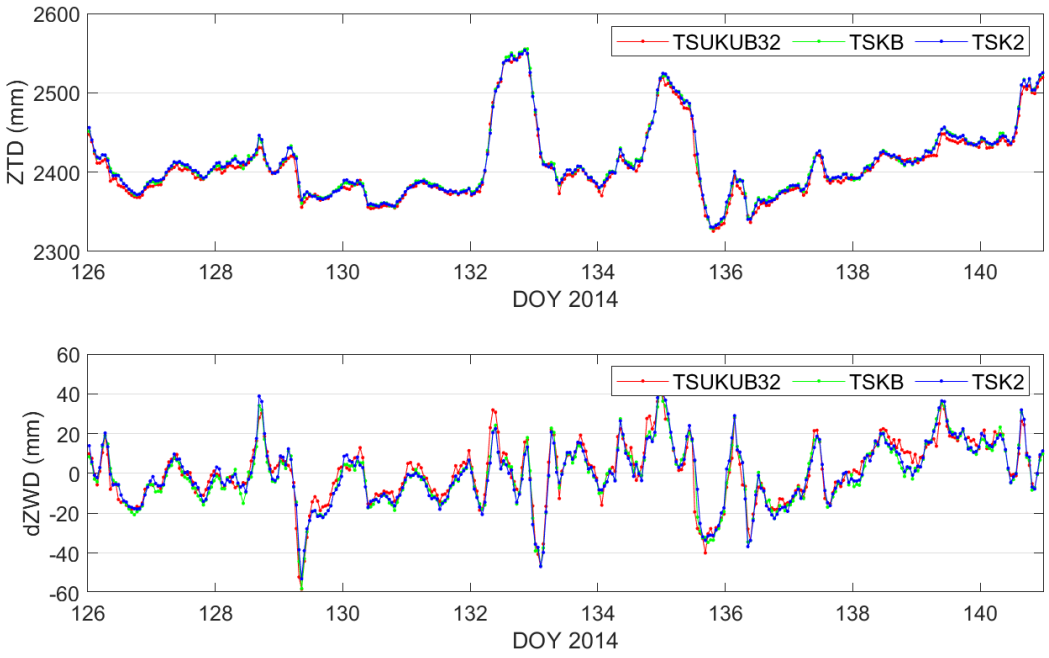

Figure 4.18 ZTD (top panel) and residual ZWD (bottom panel) at the Tsukuba co-location in CONT14. GNSS: TSKB and TSK2; VLBI: TSUKUB32.

STD values of ZTD differences between GNSS and VLBI co-locations

The STD values of ZTD differences at the GNSS–VLBI co-locations are shown in Figure 4.19. Note that these STD statistics demonstrate the agreement of the ZTD fluctuation, and is free of the systematic bias, including both the height-induced bias and the receiver-related biases. The average STD value for all the CONT campaigns is about 4 mm, but some large values up to 8 mm exists, for instance, ALGO–ALGOPARK in CONT05 (8.2 mm), BRFT–FORTLEZA in CONT14 (8.9 mm), KSMV–KASHIIM11 in CONT17-IVS (8.0 mm), and ZECK–ZELENCHK in CONT11 (9.2 mm).

Several co-locations have similar STD values in different CONT campaigns.

- The BADG–BADARY co-location has the same STD value in CONT11–CONT17, with an average value of 3.4 mm.

- The three GNSS stations co-located to NYALES20 have similar STD in CONT08–CONT17 with an average value of around 2.5 mm, while in CONT05 the STD value is smaller.

- At Onsala, the ONSA–ONSALA60 co-location has similar STD values in CONT05–CONT17 with an average value of 3.5 mm, and the ONS1–ONSALA60 STD value is similar to ONSA–ONSALA60 in the CONT17 campaign.

- At the SVTL–SVETLOE co-location, the STD values are also similar (3.5 to 4.0 mm) in CONT05–CONT08, so are the WARK–WARK12M co-location (4.5 to 5.0 mm) in CONT14 and CONT17 and the WES2–WESTFORD co-location (4.0 to 4.5 mm) in CONT05–CONT14.

- The several GNSS stations co-located to WETTZELL have very good agreement in different campaigns (around 3 mm), except for the CONT17-VLBA campaign, where the STD value is about 2 mm.

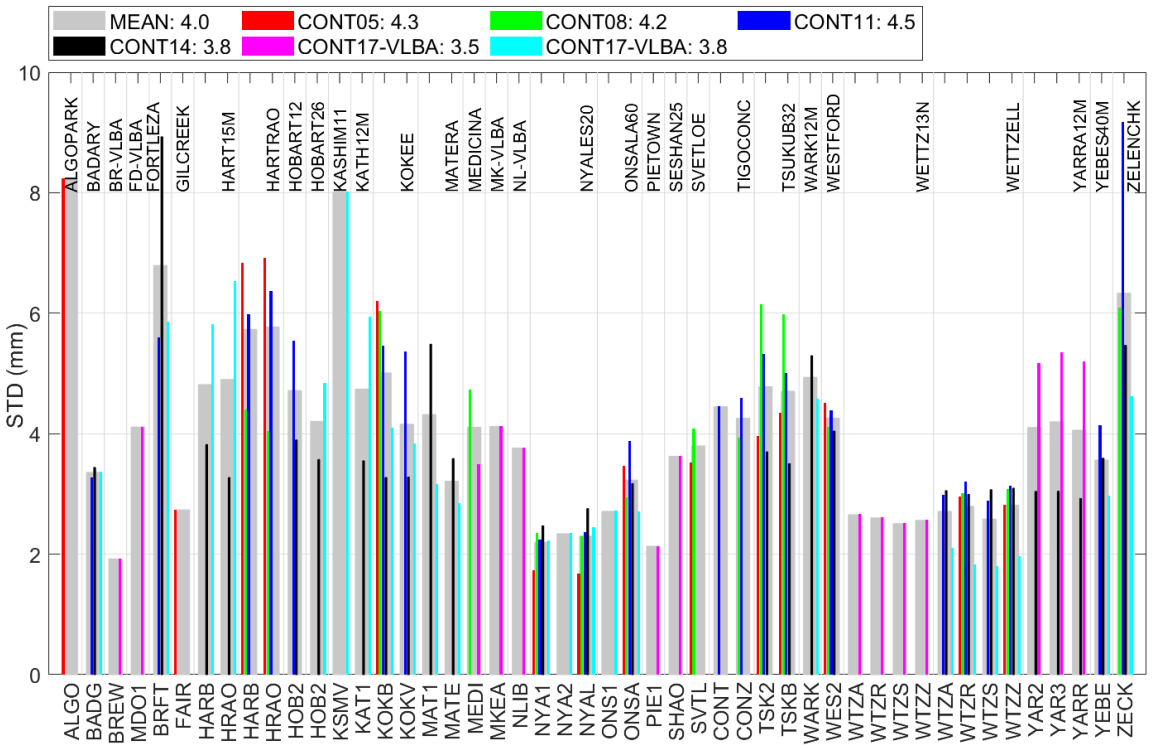

Figure 4.19 STD values of the ZTD differences between co-located GNSS and VLBI stations in CONT05–CONT17. For each co-location, the average value over all the campaigns is shown in the grey bar.

On the other hand, some co-locations have very different STD values in different campaigns.

- At the BRFT–FORTLEZA co-location, the STD values are 5.5 to 6.0 mm in CONT11 and CONT17, but extremely large in CONT14 (8.9 mm).

- At Hartrao, the STD values show good agreement between the HARB–HARTRAO and the HARB–HARTRAO co-locations, while the value has a large variation in different CONT campaigns (CONT05–CONT11). After the station upgrading, the

new station HART15M also show similar agreement with the two GNSS co-locations, and the values are quite different in CONT14 and CONT17.

- The co-locations at Hobart have larger STD values in CONT11 (HOB2–HOBART12, 5.5 mm) and CONT17 (HOB2–HOBART26, 4.8 mm), and relatively smaller values in CONT14 (3.9 mm at HOB2–HOBART12 and 3.6 mm at HOB2–HOBART26).

- At Kokee (GNSS: KOKB and KOKV, VLBI: KOKEE), the two GNSS stations have similar agreement to VLBI telescope. The values are about 5.5 to 6.0 mm in CONT05–CONT11, and reduced to 3.3 mm and 4.0 mm in CONT14 and CONT17, respectively. So are the Tsukuba co-locations. The two GNSS stations (TSKB and TSK2) have very similar performances, while the agreement between different campaigns varies from 3.5 mm to 6 mm.

- At the Matera site (MATE and MAT1 to MATERA), the two GNSS stations have similar performance in CONT17 (around 3.0 mm). In CONT05, the value at MATE–MATERA is 3.6 mm, while that at MAT1–MATERA is 5.5 mm.

- The KAT1–KATH12M co-location has very different STD values between CONT14 and CONT17, so are the MEDI–MK-VLBA co-location between CONT08 and CONT17, and the YARRA12M (GNSS: YAR2, YAR3, YARR) co-location between CONT14 and CONT17.

- The ZECK–ZELENCHK co-location show comparable variations between CONT08, CONT14, and CONT17 (5 to 6 mm), while the value is extremely large in CONT11 (9.2 mm).

Nevertheless, the general agreements at most of the GNSS–VLBI co-locations are quite optimal. Of all 114 pairs of comparisons, 29 are less than 3 mm, and 100 are less than 6 mm. The median value is 3.6 mm.

MEAN and RMS values of ZTD differences between GNSS and VLBI

Besides the STD values of the ZTD differences, the MEAN and RMS values of the residual ZTD differences are further shown in Figure 4.20. Note that the a priori ZTD is derived from NWM, and thus the height differences dependent part should have been modeled. Therefore, the residual ZTD difference should be zero-mean ideally. This is not the case in reality (as shown in the figure), and the biased differences also indicate the ZTD tie disagreement between NWM and space solutions.

As shown in Figure 4.20, the inter-technique residual ZTD biases are small in an average sense. For all 114 pairs of comparisons, the mean value is –0.1 mm and the mean absolute value is 1.6 mm. The number of co-locations with absolute mean biases larger than 3 mm is 15. The campaign-wise mean biases of all stations are within ±0.5 mm for all the campaigns.

On the other hand, large systematic biases exist at several co-locations.

- A large bias of –5 mm is observed at the WES2–WESTFORD co-location in CONT05–CONT14. Different types of receivers are used in CONT05–CONT11. There is almost no height difference at this co-location (smaller than 10 cm), so this cannot explain the bias. This bias is also reported in previous studies (Snajdrova et al., 2005; Steigenberger et al., 2007; Teke et al., 2011).

- A bias of 2 mm is observed at the TSKB – TSKUBA32 co-location in CONT05–CONT14, while the biases at TSK2–TSUKUB32 are quite small (within ±0.5 mm) in these campaigns. For both stations, the receiver was changed after CONT11.

- A bias of –1 mm is observed at WARK–WARK12M in CONT14 and CONT17, where the same receiver is used.

- Several co-locations only used in one campaign show large biases up to 3 mm.
    - In CONT05, ALGO–ALGOPARK (2 mm), FAIR–GILCREEK (2.5 mm), SVTL–SVETLOE (–2 mm).
    - In CONT17, MEKA–MK-VLBA (–4.1 mm), NLIB–NL-VLBA (–4.3 mm), SHAO–SHSHAN25 (2.7 mm), and WTZA–WETTZ13N (2.8 mm).

- Co-locations participating in several campaigns with the same receiver and antenna, but show large fluctuation.
    - The BADG–BADARY co-location shows a bias of 1.6 mm between CONT14 and CONT17
    - The BRFT–FORTZELA co-location with a bias of 4 mm between CONT11, CONT14, and CONT17.
    - The SVTL–SVETLOE co-location with a 2 mm bias between CONT05 and CONT08.

- At the Hartrao co-locations, the mean bias changes significantly between CONT05 and CONT08 (from 3.5 to –0.4 mm at HARB–HARTRAO, and from 3.0 to –1.9 mm at HARO–HARTRAO), as different types of receiver are used in these two campaigns. The same type of receiver is used in CONT08 and CONT11, and the mean biases do not show any large variations. As for the HART15M station in CONT14 and CONT17, the GNSS receiver does not change and the mean biases are all small.

- At Hobart, the same receiver is used at HOB2 in CONT11 and CONT14, and then a new receiver is used in CONT17. However, the mean biases are quite different in all the three CONT campaigns.

- At Matera, different types of receivers are used by MATE and MAT1 in CONT14 and CONT17. However, the mean biases in these two campaigns are quite similar at MAT1–MATERA, while those at MATE–MATERA show large difference (around 2 mm).

As for the Wettzell co-location, the WETZ13N telescope in CONT17-VLBA agrees with the co-located GNSS stations within ±0.3 mm, except for the WTZA station (2.8 mm). The WETTZELL station shows a negative bias compared with the GNSS stations within ±2 mm, except in CONT11 where the bias is –2.8 mm at WTZR.

The YARRA12M station has different mean biases with the three GNSS stations (YARR, YAR2, and YAR3), but the variation between CONT14 and CONT17 are less than 1 mm.

The above analysis does not cover all co-locations in all campaigns with the instrument change in consideration. Nevertheless, it is difficult to draw a general conclusion about whether the receiver change introduces biases or not, as the performances are not the same at different co-locations. As for the co-locations with more than one GNSS stations, the performances can also vary appreciably. What is certainly sure is that the NWM cannot fully model the ZTD bias, which is caused by not only the station height difference but also the instrumental effects.

The ZTD long-term agreement of GNSS and VLBI should be further investigated, where there is more opportunity to identify the discontinuity occurrence. It might also be possible to derive the magnitude of the discontinuity with the long-term time series.

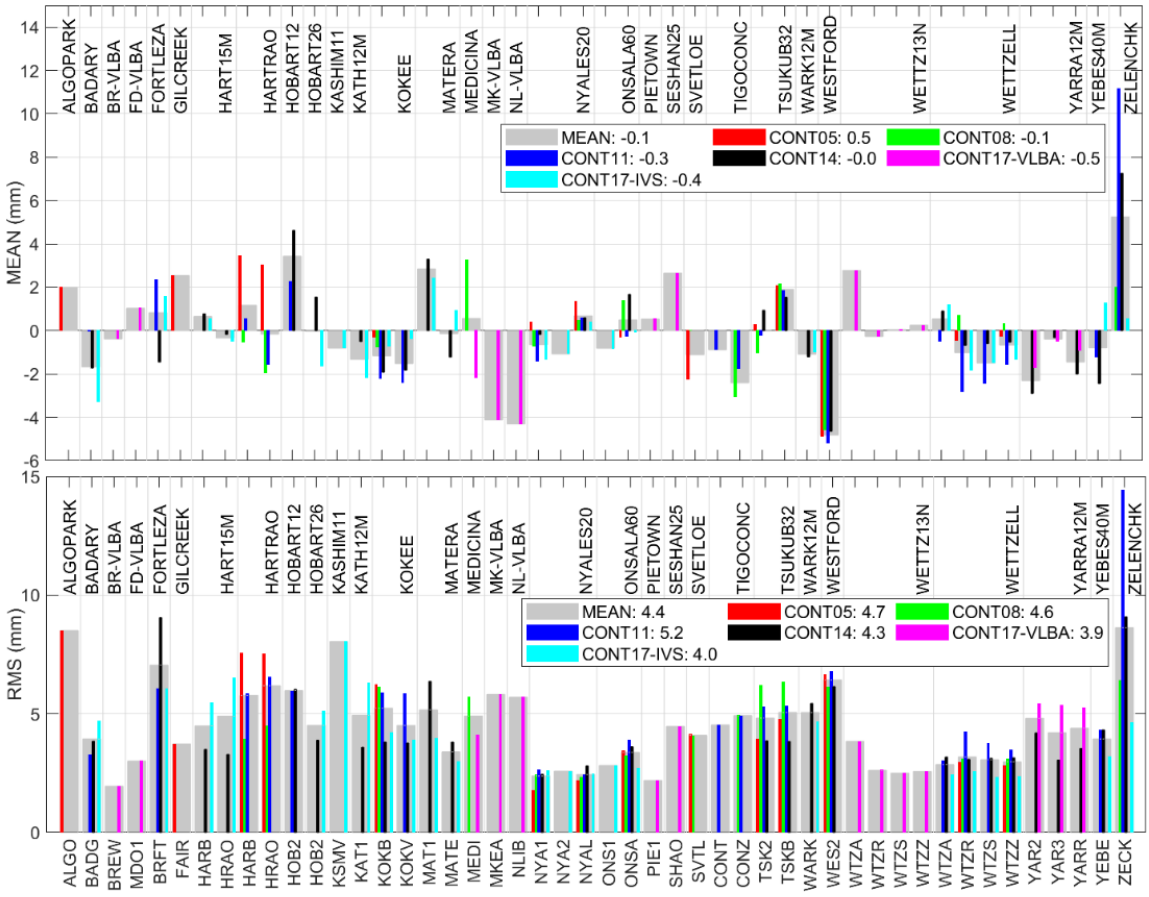

Figure 4.20 MEAN (top panel) and RMS (bottom panel) values of the residual ZTD differences between GNSS and VLBI. For each co-location, the average value over all the campaigns is shown in the grey bar.

As for the RMS values of the residual ZTD differences shown in Figure 4.20 (bottom panel), the campaign-wise average value varies from 3.9 mm (CONT17-VLBA) to 5.2 mm (CONT11)

in different campaigns, and over all the campaigns the mean value is 4.4 mm. The RMS values of all the co-locations basically follow the STD values in Figure 4.19.

The RMS value can be used for the ZTD tie constraints, if the tropospheric ties from NWM are directly applied in integrated processing. It can also be rescaled with different factors (from 0 to 1), to investigate the impact of different constraints in integrated processing. The factor of 1 is safer to apply tropospheric ties, while the value of 0 means employs the physical co-location, that is, the same tropospheric conditions for the co-locations.

Comparison with previous studies

As the inter-technique agreement of tropospheric parameters is sensitive to the data analysis software platforms, modeling, parameterization, it is necessary to compare the analysis in this thesis with previous studies. The following previous studies are used here.

- The homogeneously reprocessed GPS solution using Bernese and VLBI solution using OCCAM by Steigenberger (2009), Table 6.5. It is referred to as "A" in Table 4.13.
- The comparison between VLBI solutions and GNSS solutions in CONT08 by Teke et al. (2011), Table 6. In this comparison, several VLBI solutions are available, including the IVS product and the VieVS solution. For GNSS, the IGS and CODE products are used. The corresponding codes in Table 4.13 are: "B" for Vievs–IGS, "C" for VieVS–CODE, and "D" for IVS–CODE.
- The comparison of IGS second reprocessing and IVS solutions in CONT02–CONT11 (Teke et al., 2013), Table 8. It is referred to as solution "E" in Table 4.13.
- The GNSS–VLBI comparison of solutions processed by the Bernese software in CONT14. As the same software is used for both techniques, the best consistency is expected. In this study the height-induced ZTD differences are not considered (Männel, 2016), which will affect the MEAN value. This study is referred to as "F" in Table 4.13.
- The result in this thesis is referred to as solution "P" in Table 4.13.

The comparisons of previous studies and this thesis are shown in Table 4.13. Only the available co-locations are presented. The three campaigns which are commonly investigated in the above studies, including CONT05, CONT08, and CONT11, are focused.

The systematic biases at several co-locations are observed in these studies. For instance, 5 mm bias at WES2, 2 mm bias at TSKB in CONT05–CONT11, 3 mm bias at HRAO in CONT05, –3 mm at CONZ in CONT08–CONT11. In CONT11, the biases at most co-locations agree within 1 mm between the two studies, except for the KOKB co-location, where the bias are differed by 2 mm.

On the other hand, the STD values in this study are about 1 to 3 mm smaller than those of other studies, indicating that the homogeneously processing using one software can achieve the best consistency. Significantly reduced STD values are observed in the comparison of this

study, especially the WTZR, WES2, TSKB, and KOKB co-locations in CONT05 and CONT08.

As for the Bernese homogeneously reprocessed result in CONT14, it is unfortunately not as good as expected. The STD values from the Bernese software are larger compared to that from the PANDA software by a factor of two to three for all the co-locations listed here. One possible reason is that outlier detection is not performed, and the gradients are not estimated. The clock breaks and clock offsets are checked manually and the "misbehaving" baselines are removed[65].

Table 4.13 Comparison of ZWD differences between this study and other references at selected co-locations. The unit is mm.

	NYA1	ONSA	WTZR	WES2	TSKB	KOKB	HRAO	CONZ
CONT02								
A	0.6±3.9	2.2±4.8	0.5±4.6	–4.8±4.7	–0.1±7.8	–4.7±9.6	2.2±7.5	1.1±7.7
E	0.8±3.5	1.4±4.2	0.7±4.8	–5.1±4.9		–0.3±9.7	2.2±7.7	
CONT05								
P	0.4±1.7	0.1±3.4	–0.4±2.9	–4.9±4.5	2.1±4.3	–0.3±6.2	3.0±6.9	
E	0.3±3.0	1.7±4.9	0.2±5.0	–6.9±8.1	3.4±8.3	2.2±11.2	3.0±6.7	–0.5±6.0
CONT08								
P	–0.7±2.3	1.8±2.9	0.7±3.0	–4.6±4.1	2.1±5.9	–0.7±6.2	–1.9±4.0	–3.0±3.9
E	–0.8±3.2	2.4±4.5	0.6±4.7	–6.5±6.0	0.1±11.5	1.2±9.3	–0.6±5.2	–4.1±5.9
B	–2.0±3.9	1.0±4.5	2.2±4.1	–4.5±6.1		0.8±8.3	–0.2±4.7	–4.0±5.1
C		3.1±5.0	–2.1±4.6	–3.7±6.4	1.4±11.6	1.9±9.5	0.1±5.2	–4.5±5.0
D	1.4±2.9	3.3±4.5	–1.8±4.2	–3.7±5.5	1.5±9.7	2.0±7.3	0.9±4.0	–2.4±7.3
CONT11								
P	–1.4±2.2	0.2±3.9	–2.8±3.2	–5.2±4.4	2.0±4.9	–2.1±5.4	–1.6±6.5	–1.8±4.5
E	–1.4±4.0	1.3±5.4	–2.2±4.2	–6.2±5.5	2.9±9.0	–0.1±8.5	–1.1±7.3	–1.7±5.2
CONT14								
P	–0.2±2.4	2.1±3.2	–0.5±3.0	–4.9±3.9	1.6±3.6	–2.2±3.4		
F	–2.2±4.6	–2.4±6.3		–6.3±9.9	–5.3±9.3	–2.7±9.2	1.5±5.9	
CONT17								
P	–1.2±2.1	0.2±2.7	–1.8±1.9			–0.8±4.3		

The tropospheric parameter dependence on station height

The MEAN values of tropospheric parameter differences at GNSS–VLBI co-locations in each CONT campaign and the corresponding station height differences are shown in Figure 4.21. The ZTD difference shows a clear dependence on the height difference, while the residual ZTD difference does not show any dependence on the height difference. The large ZTD differences at both FD-VLBA–MDO1 and HARTRAO–HARB are reduced in the plot of the residual ZWD. Therefore, using the NWM-derived ZTD can effectively model the height-induced bias. The gradient differences show no dependence on the station height, indicating

[65] Benjamin Männel, personal communication

that it is not necessary to model a priori gradients to account for the gradient differences ralted to the station height differences.

On the other hand, large biases still exist on both the residual ZTD and gradients, indicating other station-dependent biases that might be related to the instrument, for instance, the GNSS receiver PCV, or small-scale local environment. For instance, the KSMV–KASHIM11 co-location shows large east gradient biases up to 2 mm in CONT17-VLBA, which is even larger than a typical gradient magnitude. More details about the gradient agreement will be demonstrated in the next section.

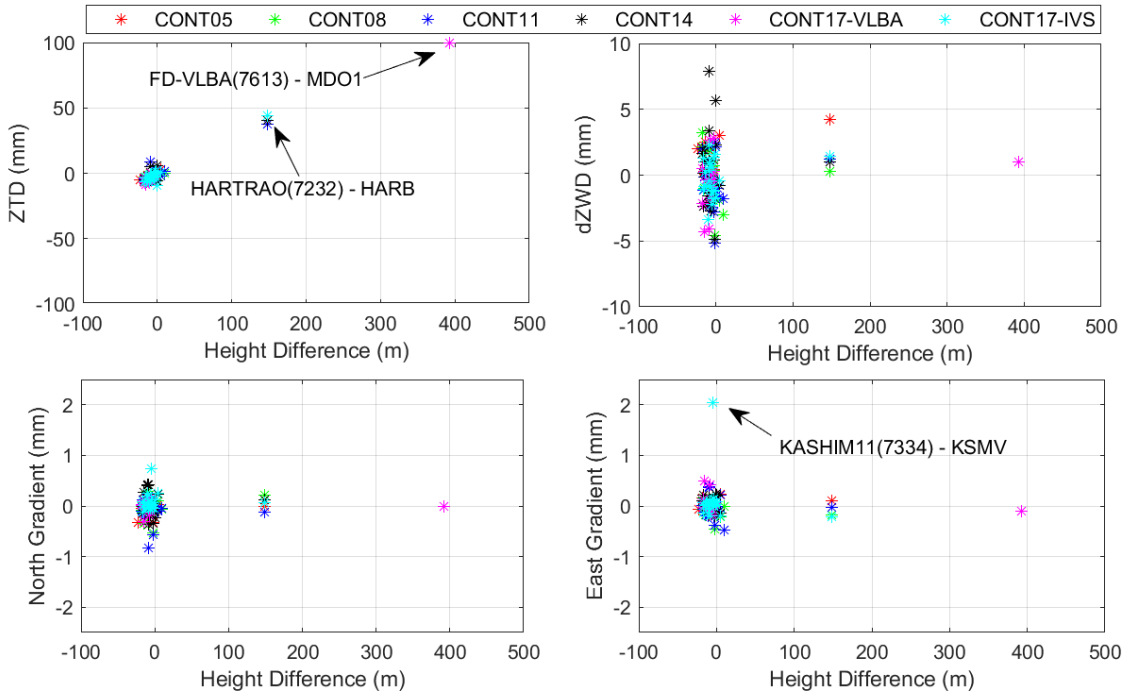

Figure 4.21 MEAN values of the GNSS–VLBI tropospheric parameter differences as a function of station height difference at co-locations in CONT05–CONT17. Top left: ZTD difference; top right: residual ZTD (dZWD) difference; bottom left: north gradient difference; bottom right: east gradient difference.

4.6.5 GNSS–VLBI gradients ties from space solutions

Gradient estimates at Tsukuba in CONT14

The gradients at the Tsukuba co-location in CONT14 (DOY 126–140, 2014) are shown in Figure 4.22. During this period, the gradients at Tsukuba vary within ±1 mm, and the estimates from GNSS and that from VLBI agree well in general, despite the fact the VLBI estimates seem more scatter.

On the other hand, the intra-technique agreement (between TSKB and TSK2) is better than the inter-technique agreement (between TSKB/TSK2 and TSUKUB32). The discrepancy between GNSS and VLBI gets larger at certain epochs. One example is the east gradient at DOY 132, where the GNSS estimates show large values up to –3 mm, while VLBI estimates show the opposite value of +2 mm. Another example is at DOY 140, where the GNSS north

gradient is observed as large as –2.5 mm, while the VLBI value is +1 mm. There are also other large discrepancies, and in most cases it is the VLBI estimate with larger scatter, for instance, the north gradient at DOY 129 and 138, and the east gradient at DOY 136. Nevertheless, the estimates at all three stations can catch most of the visible variations with good agreement, for instance, the east gradient at DOY 127–128 and 140, and the north gradient at DOY 137–139.

Figure 4.22 North (top panel) and east (bottom panel) gradients at co-located VLBI station (TSUKUB32) and GNSS stations (TSKB and TSK2) in CONT14.

MEAN values of gradient differences between GNSS and VLBI

The MEAN values of the gradient differences between co-located GNSS and VLBI stations in CONT05–CONT17 are shown in Figure 4.23, where the north and east gradients are presented in the top and bottom panels, respectively. The GNSS station name is given in the bottom of the lower panel, and the VLBI radio telescope name is given in the top of both panels for better clarity.

The average value of all co-located stations over all campaigns is 0.0 mm on both the north and the east components, indicating that no significant systematic bias in an average sense. The mean values in all campaigns are within ±0.1 mm. The RMS values of all the mean biases are 0.19 mm and 0.24 mm for the north and east components, respectively. On the other hand, the median values of the absolute mean biases are 0.1 mm on both components. Therefore, the overall agreement of gradients between GNSS and VLBI networks is optimal in the CONT campaigns, and systematic biases are not significant in terms of the average values of the whole network.

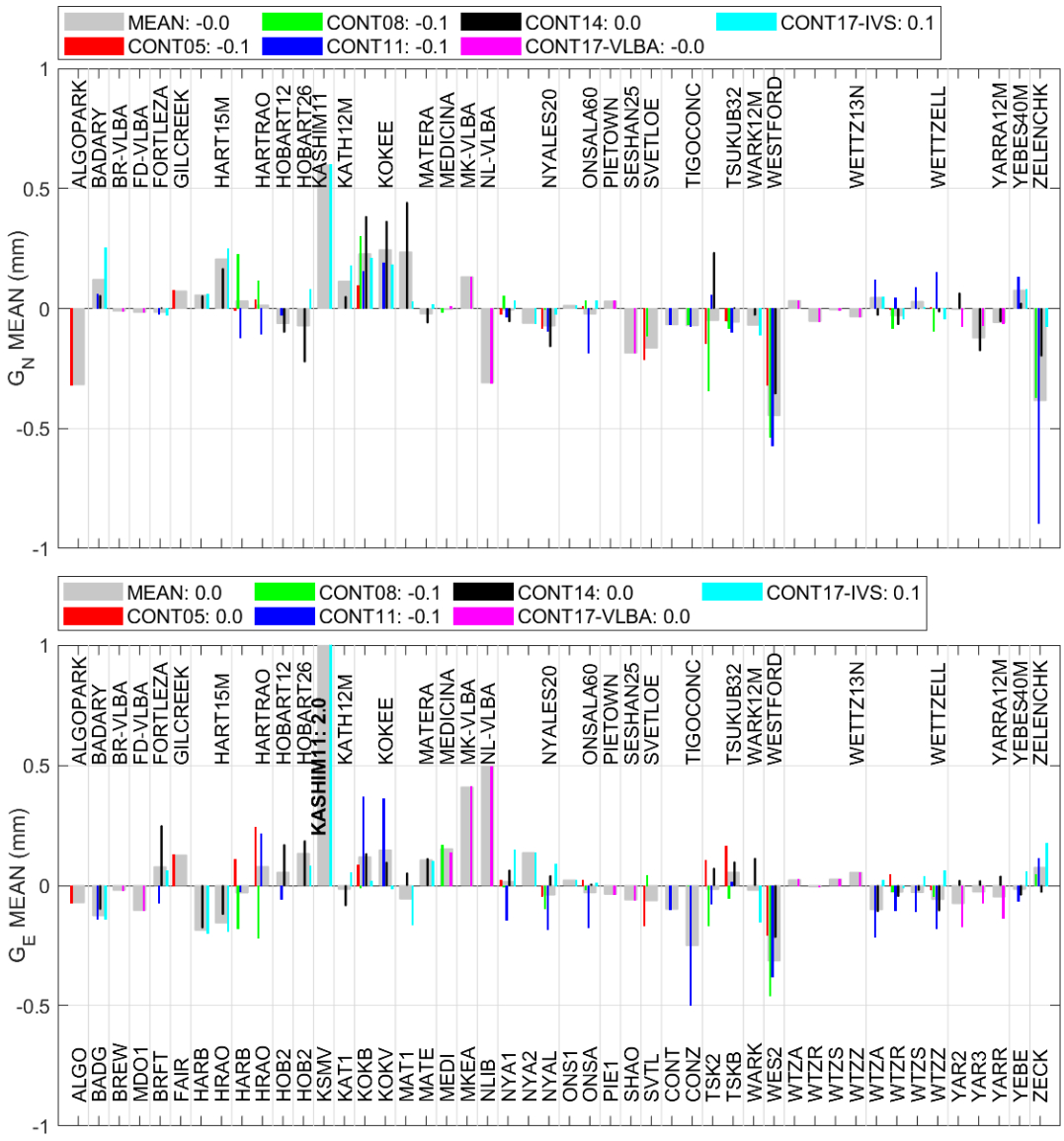

Figure 4.23 MEAN values of the gradient differences between co-located GNSS and VLBI stations in CONT05–CONT17. Top panel for the north gradient and the bottom panel for the east gradient. For each co-location, the average value over all campaigns is shown in the grey bar. The average value of all co-locations in each campaign is shown in the legend.

However, some co-location show extremely large gradient biases.

- The largest bias is observed at the KSMV–KASHIM11 co-location, located on the east coast of Japan (36°N, about 3 km to the Pacific Ocean). The north gradient bias is 0.6 mm and the east one is 2.0 mm. The corresponding RMS values are about 2.5 mm, much larger than the other co-locations.

- The second-largest bias is observed at ZECK–ZELENCHK in CONT11, with a north gradient bias of –0.9 mm and an RMS value of 2.3 mm. The corresponding east gradient bias, however, is quite small (less than 0.1 mm, RMS of 2.1 mm).

- Several co-locations also show large biases on one of the gradient components.
    - On the north component: ALGO–ALGOPARK in CONT05 (–0.3 mm), BADG–BAGARY in CONT17 (0.3 mm), TSK2–TSUKUB32 in CONT08 (–0.3 mm) and CONT14 (0.2 mm), MAT1–MATERA in CONT14 (0.4 mm).
    - On the east component: BRFT–FORTLEZA in CONT14 (0.2 mm), HARO–HARTRAO in CONT05–CONT11, CONZ–TIGOCONC in CONT11 (–0.5 mm).
- Several co-locations show large biases on both the north and east components. For instance, the KOKEE co-location in CONT08 and CONT11, the MEDI–MK-VLBA and NLIB–NL-VLBA co-locations in CONT17.
- Systematic biases are observed at the WES2–WESTFORD co-location in CONT05–CONT14, with an average value of –0.4 mm on the north component and –0.3 mm on the east component.
- Systematic north gradient biases at KOKB/KOKV–KOKEE in CONT08–CONT17, around –0.2 mm.
- Systematic east gradient biases at HARB/HARO–HART15M in CONT14 and CONT17, around –0.1 mm.

Unlike the residual ZTD biases which can be explained by the GNSS instrument type (receiver and/or antenna), the gradient biases are more plausible to be caused by the local environment (some stations located near the coast with complex terrain), the observation geometry (some stations in Southern Hemisphere have more observations in the north direction), and potentially the antenna PCV. Nevertheless, the systematic biases should always be double-checked with long-term gradients time series, where the seasonal variation can also be investigated.

RMS values of gradient differences between GNSS and VLBI

The RMS values of the gradient differences between GNSS and VLBI are given in Figure 4.24. In general, the inter-technique agreement of tropospheric gradients are not optimal as that of the ZTD, considering the small magnitude of the gradients, which is usually only a few millimeters. The average RMS value of each campaign varies between 0.6 mm and 0.9 mm for the north gradient, and between 0.5 mm and 0.8 mm for the east gradient. The mean RMS values of all co-locations over all campaigns are 0.7 mm and 0.6 mm on the north and east components, respectively. The median values are 0.4 mm and 0.5 mm, correspondingly. Some co-locations with large RMS can be explained by the corresponding large mean biases, for example, at ALGO–ALGOPARK, KSMV–KASHIM11, ZECK–ZELENCHK, MKEA–MK-VLBA.

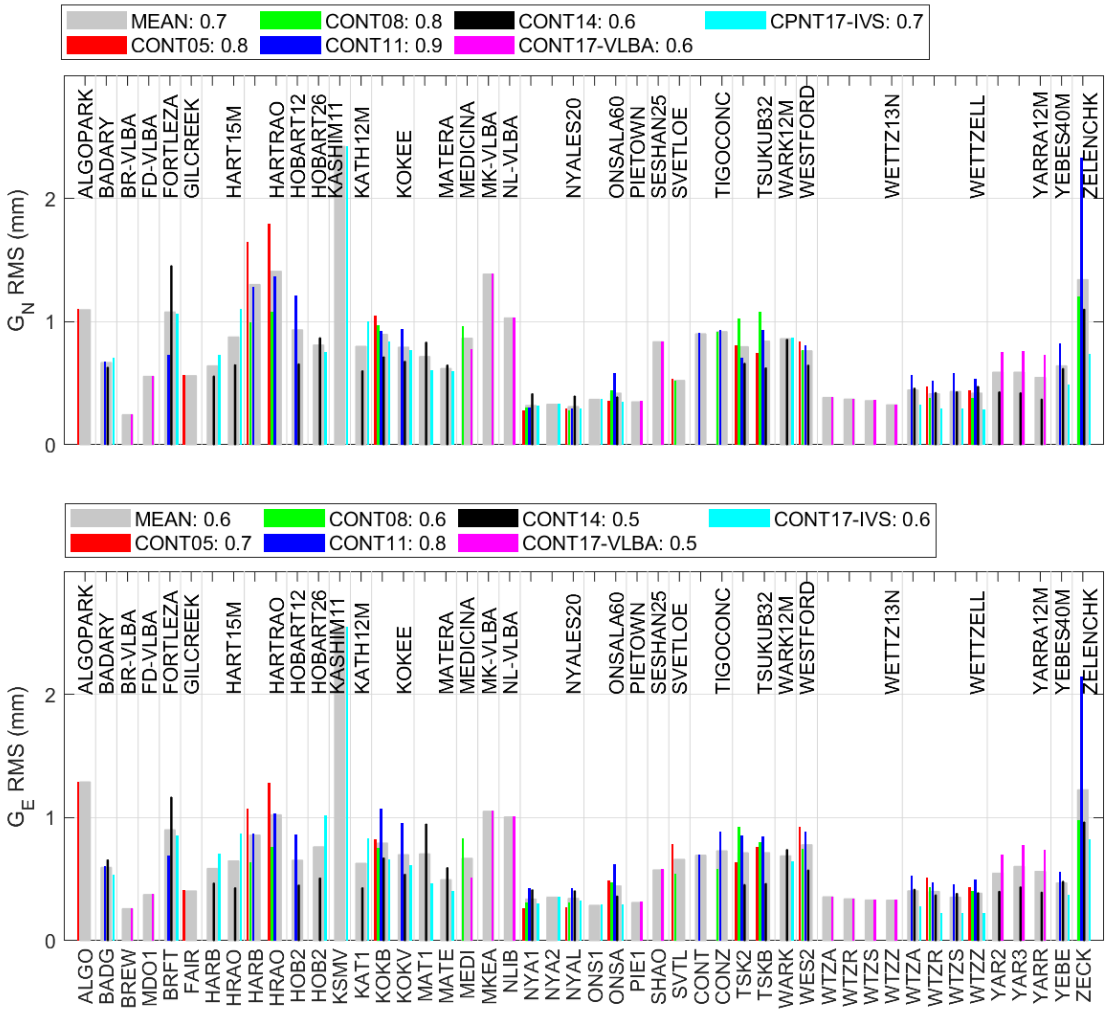

Figure 4.24 RMS values of the north gradient (top panel) and east gradient (bottom panel) differences at co-located GNSS and VLBI stations in CONT05–CONT17. For each co-location, the average value over all the campaigns is shown in the grey bar. The average RMS of all the co-locations in each campaign is shown in the legend.

On the other hand, some large RMS at co-locations with small mean bias are attributed to the large STD values, for instance, BRFT–FORTLEZA, HARB/HARO–HARTRAO, and the Tsukuba co-locations. Some co-locations show good agreements, as listed below.

- All the co-locations at Wettzell have good agreement with the RMS values around 0.5 mm in all campaigns.
- All the co-locations at Onsala agrees well with the RMS values around 0.4 mm.
- All the co-locations at Ny-Alesund (NYA1–NYA2–NYAL–NYALES20) have good agreement with the RMS values around 0.3 mm.

Several co-locations show relatively large but comparable agreements in different campaigns.

- The RMS values at Kokee co-locations are around 0.8 to 1.0 mm in CONT05–CONT17.
- The RMS values at Tsukuba co-locations are around 0.6 to 1.0 mm in CONT05–CONT14.
- The RMS values at the WES2–WESTFORD co-location are around 0.8 mm in CONT05–CONT14.

Comparison with previous studies

The MEAN and STD values of GNSS–VLBI east gradient differences in this thesis, and those from previous studies are given in Table 4.14. See Section 4.6.4 for the previous studies. The comparison of the north gradients are not provided in the previous studies, and thus not presented here.

Table 4.14 MEAN and STD values of tropospheric east gradient differences at GNSS–VLBI co-locations: comparison between the result in this thesis and those from previous studies. The unit is mm.

	NYA1	ONSA	WTZR	WES2	TSKB	KOKB	HRAO	CONZ
CONT02								
E	0.1±0.3	0.1±0.4	0.1±0.4	–0.4±0.4		0.5±0.9	0.5±0.8	
CONT05								
P	0.0±0.3	0.0±0.5	0.0±0.5	–0.2±0.9	0.2±0.7	0.1±0.8	0.2±1.3	
E	0.0±0.2	0.1±0.4	0.1±0.4	–0.5±1.0	0.3±1.0	0.1±0.9	0.2±0.6	0.1±0.6
CONT08								
P	0.0±0.3	0.0±0.5	0.0±0.4	–0.5±0.6	–0.1±0.8	0.0±0.8	–0.2±0.7	0.0±0.6
E	0.0±0.3	–0.1±0.4	0.0±0.5	–0.6±0.5	–0.2±1.1	0.1±0.9	–0.1±0.5	0.1±0.5
C	0.2±0.5	–0.1±0.5	–0.3±0.6	–0.4±0.8	0.2±1.1	0.1±0.7	0.0±0.5	0.1±0.8
CONT11								
P	–0.1±0.4	–0.2±0.6	–0.1±0.5	–0.4±0.8	0.0±0.9	0.4±1.0	0.2±1.0	–0.5±0.8
E	–0.1±0.3	–0.2±0.4	–0.1±0.4	–0.5±0.5	–0.4±0.8	0.4±0.6	–0.2±0.7	–0.4±0.5
CONT14								
P	0.0±0.4	0.0±0.4	–0.1±0.4	–0.2±0.5	0.1±0.5	0.2±0.6		
CONT17-IVS								
P	0.1±0.3	0.0±0.3	0.0±0.2			0.0±0.7		

For most co-locations, the statistic in this thesis agrees well with previous studies, as the mean value differences are usually within 0.1 mm. The two exceptions are the TSKB–TSUKUB32 and the HRAO–HARTRAO co-locations in CONT11, where the mean value is biased by 0.4 mm. The corresponding STD values are both large from the two studies (0.7 to 1.0 mm).

Most of the systematic biases can be observed in both studies. For instance, the systematic bias varying from –0.6 to –0.4 mm in CONT05–CONT11 is observed at the WES2–WESTFORD co-location. In CONT11, the 0.4 mm bias at KOKB–KOKEE and the –0.4 mm bias at CONT–TIGOCONC are both observed in the two studies.

As for the STD of the east gradient, the values in this thesis are slightly larger than those from previous studies. The reason is that in this study the temporal resolution of gradients is 3-hour, while in the previous study it is 6-hour. Gradient estimation with higher temporal resolution might cause less robustness due to the limited observation number and weak observation geometry, especially for VLBI. However, lower-resolution might miss catching some short-term gradient signals. A more detailed analysis of the temporal resolution impact on tropospheric parameter agreement will be presented in Section 4.6.7.

4.6.6 Analysis of tropospheric parameter agreement and the station coordinate precision

Due to the correlation between the vertical coordinate and the ZTD parameter, as well as that between the horizontal coordinates and the gradients, the precision of the tropospheric parameters can be used to assess the coordinate solution.

Figure 4.25 shows the station coordinate repeatability of the north, east, and vertical components in the left, middle, and right panels, respectively. A visible correlation between the tropospheric parameters and the coordinates can be observed, as a larger STD value usually comes with larger coordinate repeatability, especially for the VLBI solution on the north and vertical components. This makes sense as the tropospheric parameter agreement is usually dominated by the worse solution between VLBI and GNSS, and a larger STD value of the tropospheric parameters means that the relatively worse solution (usually VLBI instead of GNSS) has a bad performance. The fact that the tropospheric parameter agreement is highly correlated with the coordinate precision indicates that by applying the tropospheric ties at GNSS–VLBI co-locations, an improved solution can be expected, expecially for the relatively weak solution, that is, VLBI in this scenario. Noted that only the VLBI stations with co-located GNSS are shown here.

The tropospheric parameter agreement between GNSS and VLBI is also known as highly correlated to the local weather condition (not shown here), for instance, the water vapor content (Teke et al., 2013). The reason is that high fluctuation of the water vapor causes relatively larger noise and lower precision in the tropospheric estimates of each space geodetic technique, resulting in poorer inter-technique agreement.

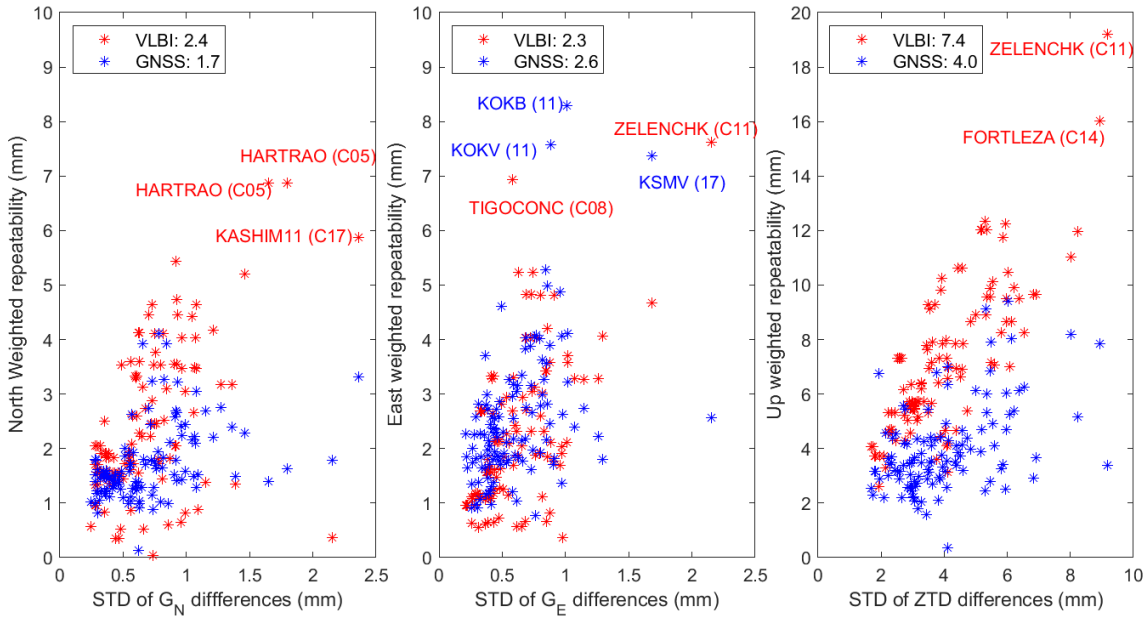

Figure 4.25 Campaign-wise coordinate repeatability of VLBI (red) and GNSS (blue) solutions as a function of the STD values of the tropospheric parameter differences. Left panel: north gradient; middle panel: east gradient; right panel: ZTD. The mean coordinate repeatability of GNSS and VLBI stations are shown in the legend.

4.6.7 Impact of temporal resolution on tropospheric parameter agreement

As mentioned above (see Table 4.14), the gradient STD values are slightly larger than those from previous studies, which is attributed to the 3-hourly gradient resolution. The impact of temporal resolution on tropospheric parameter agreement is thus investigated in this section. As the gradient fluctuation is usually slow but could be dramatic during severe weather conditions, there is no "common rule" about the gradient modeling. Higher-resolution estimates are usually less robust due to the weak observation geometry and the limited number of observations over the short-period, especially for VLBI which has fewer observations than GNSS; on the other hand, lower-resolution estimates might fail to catch the short-term rapid weather changes.

In addition to the 1-hourly resolution for ZTD and 3-hourly resolution for gradients used in this study, other temporal resolutions, including 30-min, 1-hour, and 2-hour for ZTD, and 1-hour, 2-hour, 6-hour, 12-hour, and 24-hour for gradients, are also investigated. For each ZTD resolution, different gradient resolutions are tested. An example of the gradient estimates using different gradient resolutions at the Tsukuba co-location in CONT14 are given in Figure 4.26.

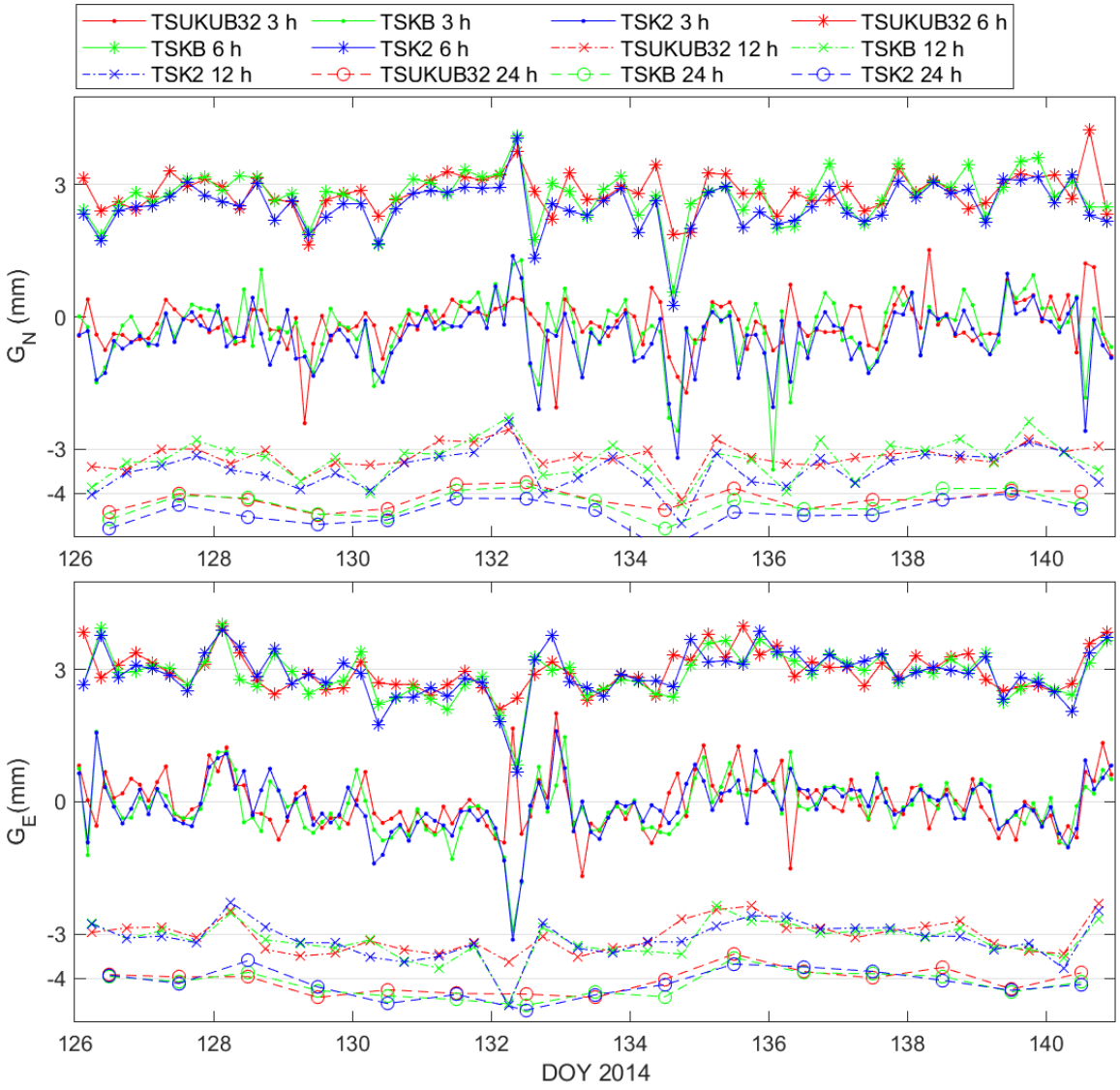

Figure 4.26 North (top panel) and east (bottom panel) gradients at co-located VLBI station (TSUKUB32) and GNSS stations (TSKB and TSK2) using different tropospheric gradient temporal resolutions. The solution of 6-hour, 12-hour, and 24-hour are offset by 3 mm, –3 mm, and –4 mm for better readability.

As expected, the estimates of low-resolution are much smoother than those of high-resolution, but short-term variation might be lost. For instance, at DOY 140, the east gradient increase is captured by both GNSS and VLBI when the resolution is no more than 12-hour, but the estimates of the 24-hourly resolution miss this signal. On the other hand, contradictory signals are observed in the 3-hourly resolution estimates at DOY 132, where the east gradients from GNSS and VLBI show the opposite variations. Another example is the 3-hourly sampled north gradients at DOY 140, where the VLBI estimates strike up while the GNSS estimates go down. This visible disagreement is alleviated when the resolution is extended to 12-hour.

The statistics of the residual ZTD and gradient differences at GNSS–VLBI co-locations using different tropospheric parameter resolutions are shown in Figure 4.27. For the ZTD agreement, the best one is achieved with the ZTD resolution of 30-min and gradient resolution of 6-hour.

The agreement decreases with the ZTD resolution increases. On the other hand, the agreement increases when the gradient resolution gets larger than 6-hour or smaller than this value. The discrepancy using 1-hourly gradients is visibly larger, while the difference between other gradient resolutions is insignificant (less than 0.2 mm).

For the gradient agreement, however, the RMS values of GNSS–VLBI differences decrease significantly as the gradient resolution increases. The RMS values of gradient differences are around 10 mm using 1-hourly resolution, and the value decreases to around 0.3 mm using 24-hourly resolution. The impact of ZTD resolution on the GNSS–VLBI gradient differences is insignificant (less than 0.1 mm). The reduced RMS values of GNSS–VLBI gradient differences are caused by both the smaller gradient fluctuation (see Figure 4.26) and the more robust estimates from better observation geometry at lower gradient resolution. However, this reduced value does not necessarily mean that the gradient agreement gets better, because the gradient correlation may get weaker if the gradient magnitude gets smaller.

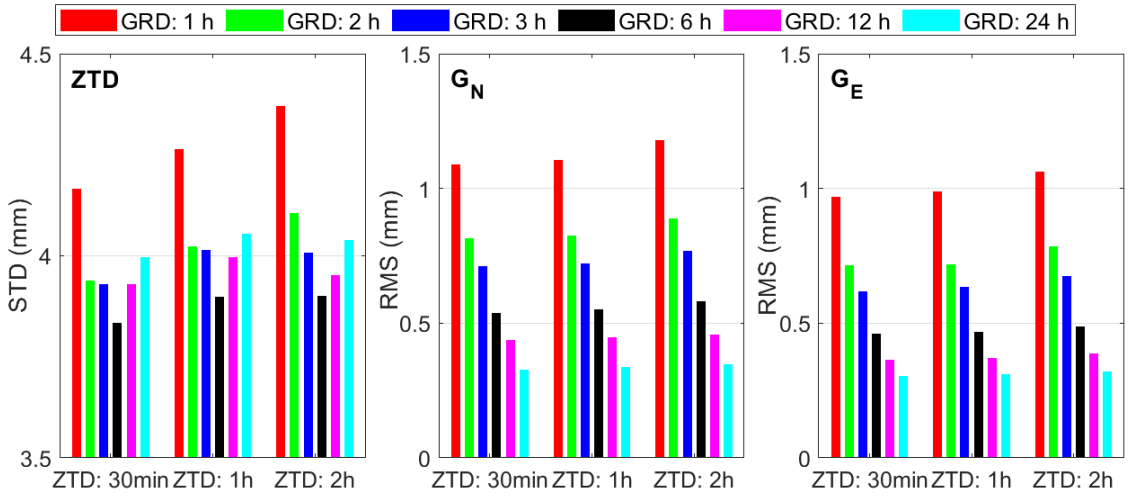

Figure 4.27 STD and RMS values of ZTD (left panel) and gradients (middle and right panels) at GNSS–VLBI co-locations in CONT05–CONT17 using different temporal resolutions. Please note that the vertical axis of the left panel starts with 3.5 mm for better visibility.

For a further illustration of the GNSS–VLBI gradient agreement using different gradient resolutions, the correlation coefficients between VLBI gradients and GNSS gradients are shown in

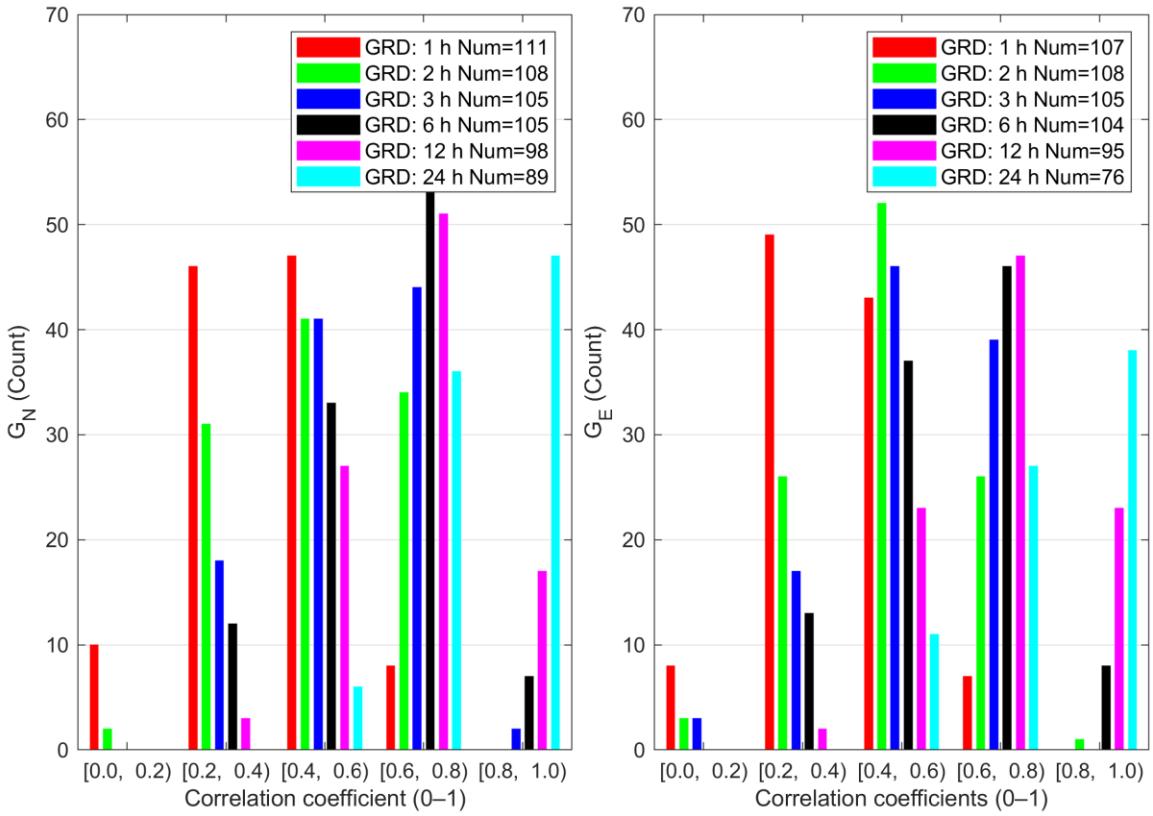

Figure 4.28. For each co-location, the gradient estimates in one campaign are correlated to get one correlation coefficient. Only the correlation coefficients that are statistically significant with a p-value smaller than 0.05 are used, and the total number of correlated pairs (p-value smaller than 0.05) in each solution is also counted. As one can see, the number of correlation coefficients that are statistically significant decreases as the gradient resolution increases, meaning that there are fewer samples that have a valid correlation coefficient. For the 1-hourly resolution, there are 111 samples and 107 samples that are statistically significant on the north and east gradients, respectively; but the correlation coefficients mainly vary between 0.2 and 0.6. On the other hand, the numbers of samples that are statistically significant are 89 on the north gradient and 76 on the east gradient with the 24-hourly resolution, while the correlation coefficient mainly varies from 0.6 to 1.0.

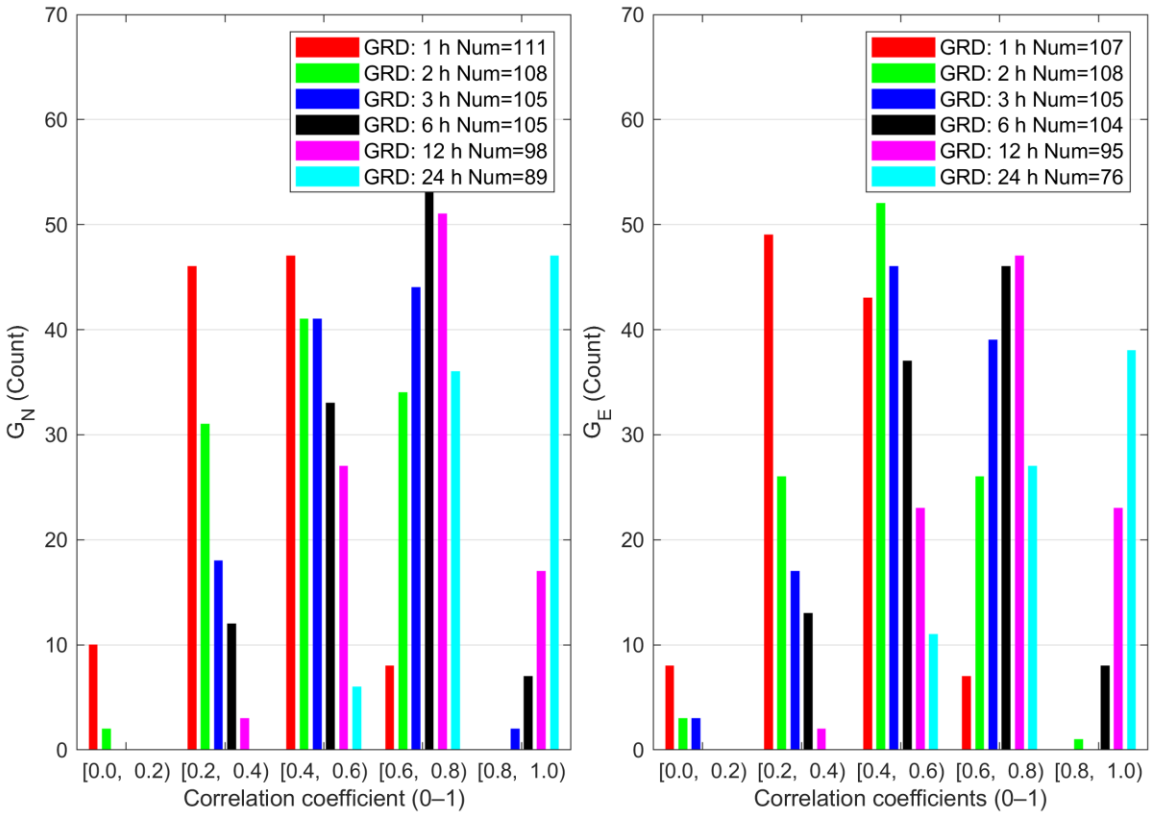

Figure 4.28 Correlation coefficients of GNSS–VLBI north gradient (left panel) and east gradient (right panel) using different gradient resolutions in CONT05–CONT17. The ZTD temporal resolution is 1-hour. Only the statistically significant correlation coefficients (p-value smaller than 0.05) are used.

4.7 UT1-UTC estimates from VLBI Intensive sessions

The UT1-UTC estimates from 16 years of VLBI intensive sessions are presented in this section. The VLBI intensive sessions are first introduced, followed by the residuals analysis, and then the UT1-UTC comparison to the IERS EOP 14 C04 product.

4.7.1 The VLBI INT sessions

For the purpose of rapid UT1 estimation and prediction, the VLBI intensive sessions are conducted, which usually contains two (occasionally three or four) radio telescopes with 1-hour observations. Therefore, the observation number is limited to 20 to 50 and the observation geometry is also relatively weak. The processing strategy of these short-period sessions is quite different compared to the "normal" sessions with globally distributed stations and 24-hour observations. Specifically, the station coordinates cannot be estimated and are fixed to the a priori TRF solution, so are the AGN coordinates. The EOP values are fixed to the a priori values except for UT1-UTC. The station clocks are usually estimated using the linear function over the whole period (1-hour). As for the tropospheric delay, only one zenith wet delay per station is estimated, and the gradients cannot be estimated due to the biased

observation geometry. Other sophisticated procedures, that is, the detection of clock breaks, baseline dependent clock offsets, and outliers, are usually not performed.

Three different types of intensive sessions are usually available. The INT1 sessions observed on weekdays from 18:30 to 19:30 UT with the baseline from WETTZELL to KOKEE, the INT2 sessions observed on weekend from 07:30 to 08:30 UT with the baseline from WETTZELL to TSUKUB32, and the INT3 sessions observed on Monday from 07:00 to 08:00 UT with three stations: WETTZELL, TSUKUB32, and NYALES20. Occasionally, other baselines are also observed in case of the maintenance of these typical INT stations. The INT1 and INT2 baselines are shown in Figure 4.29.

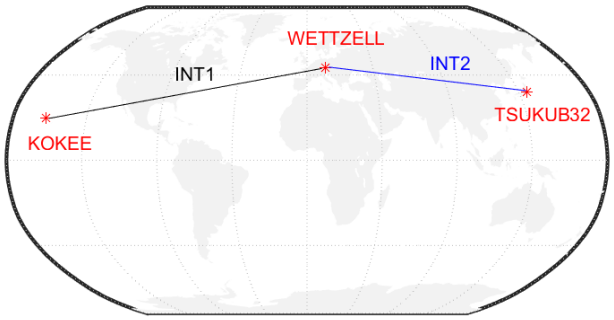

Figure 4.29 The radio telescopes of VLBI intensive sessions: INT1 between WETTZELL and KOKEE in black, and INT2 between WETTZELL and TSUKUB32 in blue.

The observation skyplots in the INT1 and INT2 session are shown in Figure 4.30. The observations in INT1 and INT2 are mainly distributed in the north direction, and mostly below 60°. As for the INT2 session, the observations are mainly distributed in the north-west direction at TSUKUB32, and in the north-east direction at WETTZELL. Nevertheless, none of the stations has a good observation geometry in the INT sessions. As a consequence, the tropospheric parameter modeling might be biased systematically. It is also not optimal to estimate the gradients, as the observations are concentrated in one direction and the tropospheric parameters will be highly correlated with each other. However, neglecting the gradients will certainly introduce systematic biases in the UT1-UYC estimates.

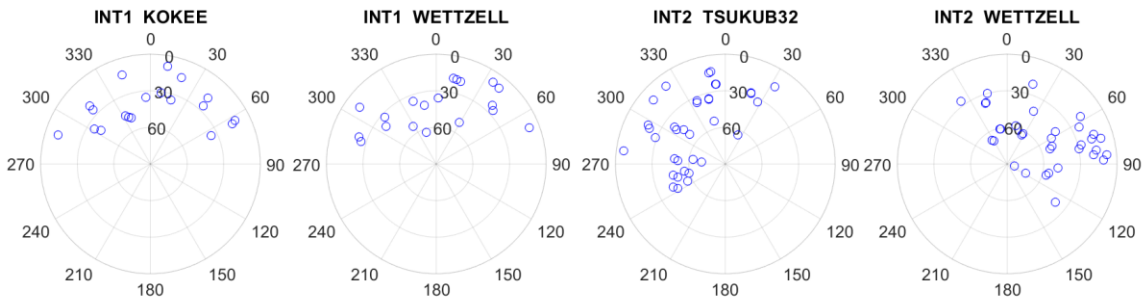

Figure 4.30 Observation skyplots of the VLBI telescopes in INT1 (session IN114-002, NGCARD: 14JAN02XU_N004) shown in the left two panels, and in INT2 (session IN214-004, NGS card: 14JAN04XK_N003) shown in the right two panels.

In this study, the VLBI Intensive sessions from 2001 to 2016 are processed, including both the INT1 and INT2. Here only the "standard" INT1 sessions from WETTZELL to KOKEE and INT2 sessions from WETTZELL to TSUKUB32 are analyzed. The analysis follows the standard processing strategy, that is, only one UT1-UTC, one clock offset and drift at the non-reference station, and two ZWD parameters (one per station) are estimated.

4.7.2 Group delay residuals

A first illustration of the residuals of all the INT1 and INT2 sessions in 2008 is provided in Figure 4.31. It can be seen that most of the residuals are within ±40 mm (98.3%). Indeed, 95% of the residuals are within ±25 mm. The mean and median values of the absolute residuals are 11.6 mm and 6.2 mm for all INT1 and INT2 sessions, respectively. The WRMS values of daily residuals are also calculated and the median and mean values over the whole year are also given in the panel. The median values are 13.8 mm (46 ps) and 9.5 mm (32 ps) for INT1 and INT2 sessions, respectively; while the corresponding mean values are 14.7 mm and 15.4 mm. The significantly larger MEAN value than the median value for INT2 sessions can be explained by some large residuals in INT2 sessions, which might be caused by the severe weather conditions in the INT2 station TSUKUBA32.

Also worth mentioning, the outlier detection is not performed in these INT sessions, which can explain the relatively larger mean value than the median value. Around 0.9% of the residuals are beyond ±100 mm. and some large residuals up to 1 meter exist and increase the MEAN statistic. The outlier detection procedure in INT sessions should be investigated in further analysis. Nevertheless, Figure 4.31 shows that there are no visible systematic biases in the residuals.

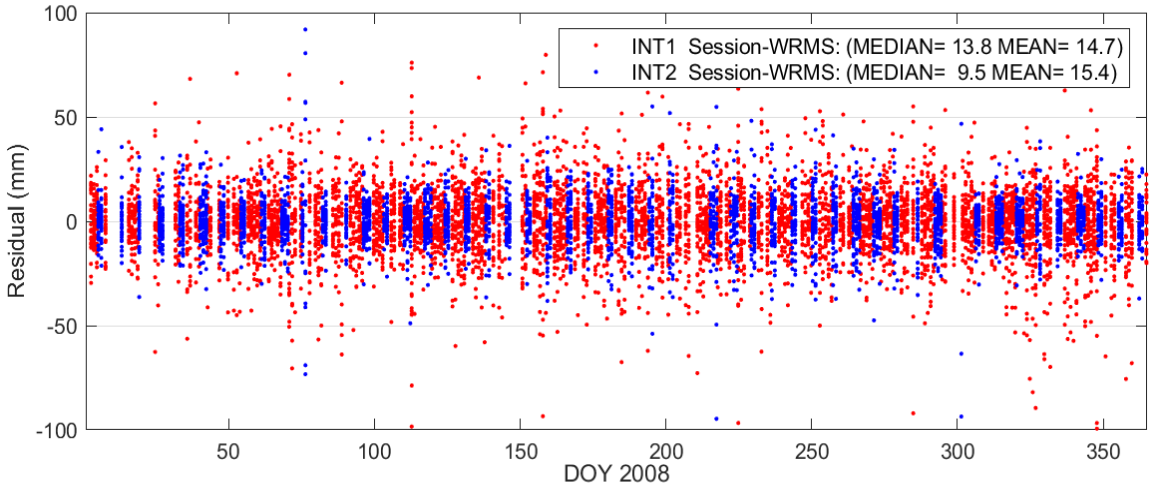

Figure 4.31 Residuals of the VLBI INT1 (red dot) and INT2 (blue dot) sessions in 2008. The average and median values of the daily WRMS are presented in the legend. The outlier elimination is not applied.

The daily residual WRMS values of all the INT1 and INT2 sessions are shown in Figure 4.31. Despite the very few days where the WRMS values are larger than 100 mm, which only counts to 0.33% of INT1 and 0.82% of INT2 sessions, the overall residual WRMS values are quite optimal. The median values are 12.2 mm and 9.9 mm for INT1 and INT2 sessions, respectively, with the corresponding mean values of 14.5 mm and 15.5 mm. The WRMS values of around 95% of INT1 sessions are less than 22 mm, and those in around 95% of the INT2 sessions are less than 17 mm.

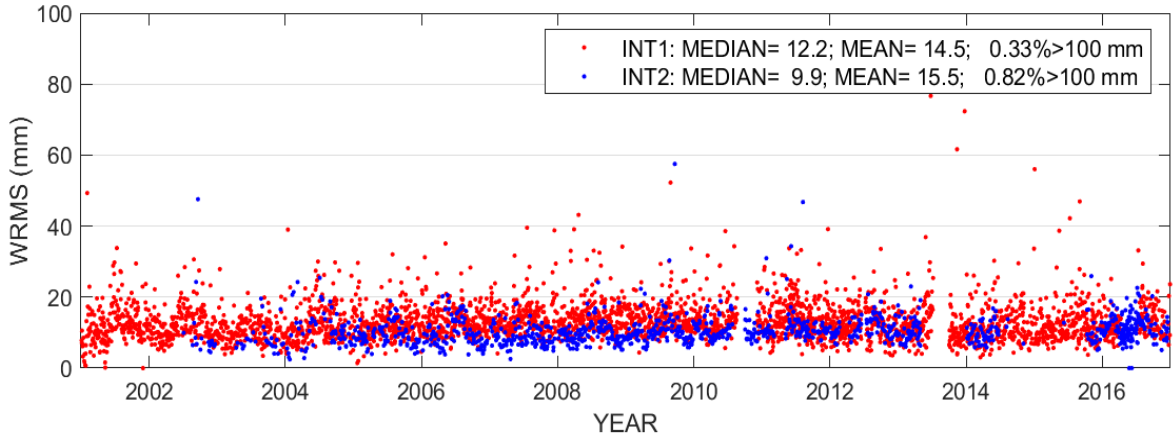

Figure 4.32 WRMS of the session-wise residuals for the INT1 (red dot) and INT2 (blue dot) sessions in 2001–2016. The median and mean values and the percent of sessions with WRMS larger than 100 mm are presented in the legend. No data editing is applied.

4.7.3 UT1-UTC estimates

Figure 4.33 shows the UT1-UTC estimates in 2001–2016 for both INT1 and INT2. Note that only those within ±100 μs are shown in this figure and further used in the statistics, accounting for around 99.5% and 99.8% of all the sessions for INT1 and INT2, respectively. The WSTD values compared to the IERS EOP 14 C04 product are 26.7 μs and 22.5 μs, respectively. This precision is comparable to previous studies, for instance, 25 μs and 22 μs in the period of 2010–2018 (Hellmers et al., 2019). The corresponding WMEAN values are 5 μs and 13 μs, and visible positive systematic biases can be observed for the period before 2010, especially for the INT2 sessions. The reasons are still under investigation. Around 95% of the INT1 biases are within ±59 μs and 95% of the INT2 biases are within ±53 μs.

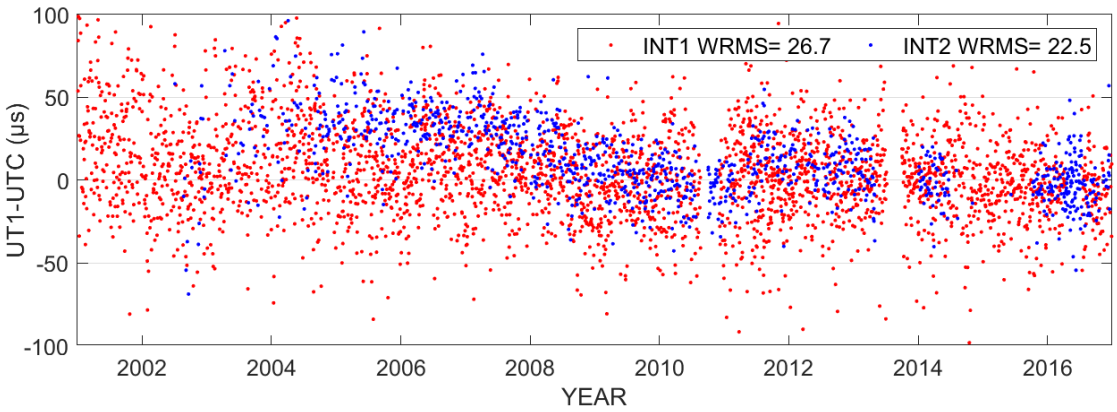

Figure 4.33 UT1-UTC estimates of VLBI INT1 (red dot) and INT2 (blue dot) sessions compared to the IERS EOP 14 C04 product. Only those within ±100 μs are shown.

4.8 SLR solution

As the focus of this thesis is the integration of GNSS and VLBI, SLR does not contribute to a large extend. Therefore, the newly implemented SLR module is validated using SLR residuals to precise orbits of the LEO and GNSS satellites where the station coordinates are fixed to the ITRF2014 solution; and the concept of SLR Precise Point Positioning (SLR PPP) where the station coordinates are estimated using SLR observations with the satellite orbits fixed.

The SLR solution is performed using the SLR observations to (1) four SLR spherical passive satellites: LAGEOS-1/LAGEOS-2 and ETALON-1/ETALON-2, (2) the whole GLONASS constellation, and (3) the GRACE-A/GRACE-B satellites. The normal points in the period of DOY 001–150 in 2017 are used. Details about the SLR data processing procedure are already shown in Figure 3.9, and the basic models are similar to the GNSS PPP as presented in Section 4.2. The following models are used specifically for SLR solutions.

- The tropospheric delay is modeled using the in situ meteorological observations with the Mendes (2004) model and Mendes et al. (2002) mapping function.
- No clocks are estimated in SLR, while the range and time biases are corrected using the ILRS data handling file. No additional time- or range- bias detection is performed.
- The observation weight is 40 mm for GNSS satellites, and 10 mm for both spehrical and LEO satellites.

It is generally known that the SLR observations are highly station-dependent, and can be grouped into the core and non-core ILRS stations, and the first group has more stable performance and more observations than the latter one. Nevertheless, in this section all the SLR stations are used. As the SLR observations are processed on a daily basis, the outlier detection is applied with a simple criteria of three to five times of the sigma.

The ILRS-A combined orbit product is used for LAGEOS and ETALON satellites. The GLONASS satellite orbits are from the GFZ final product, and the GRACE satellite orbits are retrieved from the ISDC at GFZ[66].

4.8.1 SLR residuals for orbit evaluation

The SLR observation residuals to different types of satellite orbits are shown in Figure 4.34. In this period, the observation number is more than 48,000 for the LAGEOS satellites and 4,515 for the ETALON satellites. Most of the residuals are within ±50 mm with only a few exceptions, while the STD values are 12.7 mm and 16.4 mm for LAGEOS and ETALON satellites, respectively. The observation number to the GLONASS satellites is about 35,000, and the STD value is 38.3 mm. As for the GRACE satellites, in total 15,199 normal points are available, and the STD value is 13.2 mm. The reason of a relatively larger noise of the GLONASS orbit residuals is because (1) the LAGEOS and ETALON satellites have very simple geometry and the dynamic modeling is straightforward; (2) the GRACE satellite orbits are determined from the GPS observations with good accuracy; (3) the GLONASS POD result is usually not good due to the FDMA-induced ambiguity issue, that is, the phase ambiguity cannot be fixed.

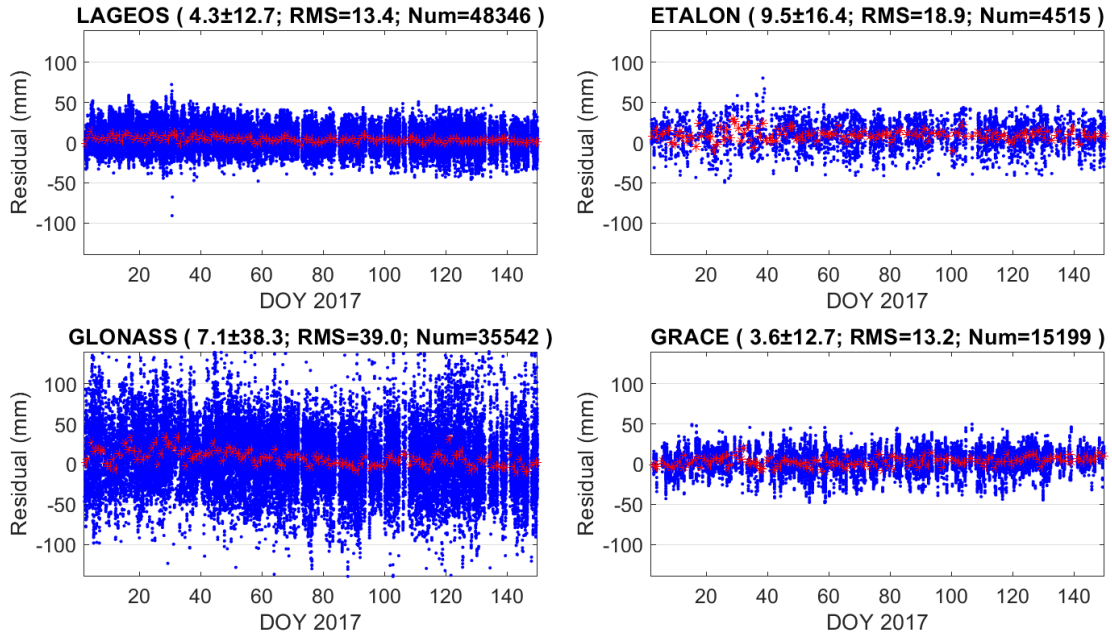

Figure 4.34 SLR residuals of different types of satellites in DOY 001–150, 2017. For each type of satellite the MEAN, STD, and RMS values are shown in bracket with the observation number. The daily average values of the residuals are shown in red dots.

The analysis of the GLONASS satellites is consistent with previous studies, for instance, around 33 mm on average of the 3-day arc orbits (Fritsche et al., 2014), 31 to 42 mm of the CODE product (Sośnica et al., 2015b), 4 cm of the MGEX product (Steigenberger and

[66] ftp://isdcftp.gfz-potsdam.de/grace/

Montenbruck, 2020). For the GRACE satellites, the RMS value in this thesis is also comparable to previous studies, which is around 1 to 2 cm (Männel and Rothacher, 2017; Arnold et al., 2018; Sušnik et al., 2020; Xia et al., 2020).

4.8.2 SLR PPP

In addition to the SLR observation residuals to precise orbits, the SLR PPP solution is also conducted. The concept of SLR Precise Point Positioning is to use precise satellite orbits to determine the daily (or weekly) static coordinates of the SLR stations. The SLR daily station coordinates are determined in the period of DOY 001–150 in 2017. It is well known that the weekly arc is more widely used in SLR data processing as there are not enough observations to have a robust daily solution. However, in this thesis, the daily solution is used to demonstrate the prototype of the SLR solution with not only the SLR satellites (LAGEOS and ETALON), but also the LEO and GNSS satellites. Moreover, the weekly solution will have the high-frequency (daily) station deformation signals smoothed over a week and is only a product of the compromise.

Due to the limited observation number, the station coordinates are loosely constrained to the ITRF2014 solution with a priori sigma value of 1 m. For each station, only the estimates with more than 15 observations are used. Moreover, only the stations with more than 14 daily solutions are used for the statistics. In total 16 stations are used, and on average each station has around 56 days of solution. The station coordinate RMS value is calculated as the root mean square of the coordinate differences compared to the ITRF2014 solution over the three components, so is the uncertainty.

The SLR PPP solutions are shown in Figure 4.35, where the daily observation number, the coordinate mean RMS compared to the ITRF2014 solution, and the formal error are shown in the top, middle, and bottom panels, respectively. With the LAGEOS and ETALON constellation, the average daily observation number is 45.9, and the 1-D average coordinate accuracy is 17.2 mm with an uncertainty of 3.7 mm. If the additional GLONASS constellation is used, the daily observation number is increased by 44%, and the coordinate RMS value is improved by 24%. The GRACE satellites can further increase 11 observations each day on average, and improve the coordinate RMS value by 0.8 mm. The significant improvement from GLONASS comes from the large satellite number (24) of the GLONASS constellation, as there are only two GRACE satellites. However, it should be noted that other LEO satellites, for instance, JASON, SWARM, SENTINEL, all have much more observations than the GRACE satellites (as shown in Figure 2.2). Therefore, a much larger improvement is expected if more LEO satellites are used.

If a minimum observation number of 10 is used instead of 15, in total 17 stations are available with an average solution of 61 days. The average RMS value of coordinate differences compared to ITRF2014 using LAGEOS+ETALON constellation is 32.2 mm, and can be reduced to 19.8 mm with additional GLONASS satellites, and further reduced to 18.8 mm

with additional GRACE satellites. The corresponding daily observation numbers are 40.6, 61.4, and 71.2, respectively.

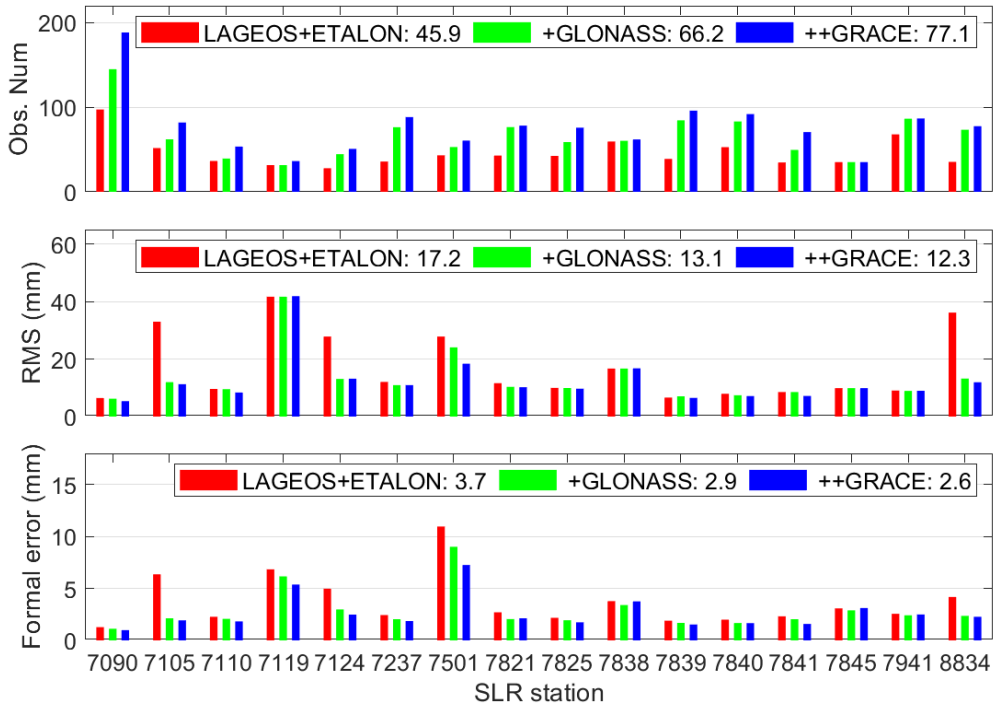

Figure 4.35 SLR daily average observation number (top panel), coordinate 1-D mean RMS (middle panel), and formal error (bottom panel), in DOY 001–150, 2017.The LAGEOS and ETALON satellies in red, with additional GLONASS satellites in green, with additional GLONASS and GRACE satellites in blue.

4.9 Chapter summary

The single-technique solutions are summarized as follows.

Section 4.1 introduces the criteria to evaluate the solutions, which are used for both the single-technique solutions and the integrated solutions in the following chapters. Principally, the solutions are evaluated in the following two aspects.

- The internal precision is assessed in terms of formal error, repeatability (including station coordinate, network scale, baseline length, and AGN coordinate), and day-boundary-discontinuity of EOP components (mainly polar motion and UT1-UTC).
- The external accuracy is assessed by comparing with other solutions, including the IGS, IVS, and IERS products for EOP and the IGS product for satellite orbits.

Section 4.2 describes the basic data processing strategy, including the conventions, models, and parameterization. The IERS Conventions 2010 are followed strictly, and the data processing adopts the standards from TCs, including but not limited to applying atmospheric pressure

loading corrections, modeling the tropospheric delays from NWM. The strategy applies to all the following solutions unless the special setup is explicitly stated.

Section 4.3 demonstrates the GNSS solution in the period of the five CONT campaigns since 2005. The station coordinate weighted repeatability of the GPS-only POD solution is 1.5 mm and around 4 mm on the horizontal and vertical components, respectively. The orbit agreement to the IGS product is about 1 cm, which is comparable to other IGS ACs. As for the ERP components, the PM offsets are about 35 μas in terms of WSTD compared to the IERS EOP 14 C04 product, and the corresponding LOD WSTD value is 17 μas/day. On the other hand, the reprocessed solution shows a comparable agreement with most of the GNSS solutions, with the WSTD value varying between 20 and 30 μas for the PM offsets, and that varying around 5 to 10 μs/day for the LOD component. As most of the GNSS solutions agree well with each other, the products of JPL and EMR both show relatively larger discrepancies in the PM rate and LOD components.

Section 4.4 concisely presents the VLBI single-session solution, using the four CONT campaigns (five networks). The group delay residuals are first analyzed, and the WRMS values of the residuals are around 5 to 10 mm in these campaigns. The campaign-wise station coordinate weighted repeatability values are about 2 to 4 mm horizontally, and 6 to 8 mm vertically, which are comparable to other IVS ACs. The baseline length repeatability also show similar precision compared to other ACs, so are the AGN coordinates. The EOP are evaluated by comparing them to the IERS EOP 14 C04 product. In general, the EOP estimates of the PANDA solution have a comparable precision with respect to those of other IVS ACs, despite the relatively larger CPO WSTD values.

Section 4.5 presents the ERP agreement between the homogeneously reprocessed GNSS and VLBI solutions. The STD values of the inter-technique differences are 90 μas and 67 μas for the x-pole and y-pole components, respectively. The value is around 10 μs/day for LOD. The inter-technique agreement is better than the agreement of each technique to the IERS EOP 14 C04 product, indicating that the IERS product still needs to be improved. Also demonstrated in this section, the ERP inter-technique agreement in this thesis is comparable with the previous study.

Section 4.6 presents the agreement of tropospheric parameters from GNSS and VLBI solutions. The a priori delay is modeled with NWM, and the focus lies on the agreement of the residual delay. In general, a good agreement of both intra-technique and inter-technique tropospheric parameters is demonstrated.

- The STD values at GNSS–GNSS co-locations are less than 3 mm for ZTD, and around 0.1 to 0.2 mm for the horizontal gradients.
- For the VLBI co-locations, the STD values at Hobart in CONT14 are 3.7 mm and 0.4 to 0.5 mm for ZTD and gradients, respectively. As for the Wettzell co-location in CON17, the corresponding values are 2.9 mm and 0.4 mm.

- The ZTD agreement at the GNSS–VLBI co-locations is around 4 mm in the five CONT campaigns in terms of STD values. However, systematic biases still exist after the NWM is used, for example, the WES2–WESTFORD co-location with a bias of 4 mm, the TSKB–TSUKUB32 co-location with a bias of 2 mm. Nevertheless, the agreement of the homogeneously reprocessed solutions in this study is much better than those from previous studies.

- The gradient agreement at the GNSS–VLBI co-locations is around 0.6 to 0.7 mm in terms of the RMS value. Systematic bias can be observed at several co-locations, for example, the WES2–WESTFORD co-location with a bias of 0.3 to 0.5 mm in different campaigns. The gradient agreement in this study is comparable to that of previous ones.

- The tropospheric parameter agreement between GNSS and VLBI shows a strong correlation with the station coordinate repeatability, especially on the VLBI stations.

- The GNSS–VLBI tropospheric parameter agreement is dependent on the parameter temporal resolution. For the ZTD agreement, the STD value gets larger with the resolution increases, and the best agreement is achieved if the gradient resolution is 6-hour. As for gradients, the agreement improves with larger gradient resolution, which is attributed to the improved geometry and smaller gradient magnitude.

Section 4.7 presents the UT1-UTC estimates of the VLBI intensive sessions in 2001–2016. The INT1 and INT2 sessions are first described. The average WRMS values of the residuals are 14.5 mm and 15.5 mm for INT1 and IN2 sessions, respectively. As for UT1-UTC estimates, the WSTD values compared to the IERS EOP 14 C04 product is 26.7 μs and 22.5 μs for INT1 and INT2, respectively.

Section 4.8 demonstrates the SLR capability by SLR residuals to precise orbits and the SLR PPP solutions, both in the period of DOY 001–150 in 2017. For the SLR residuals, the RMS values are 13.4 mm, 18.9 mm, 39.0 mm, and 13.2 mm for the LAGEOS, ETALON, GLONASS, and GRACE satellites, respectively. As for the SLR PPP solution, an accuracy of 17.2 mm is achieved using the LAGEOS and ETALON satellites in terms of 1-D mean RMS value, and the accuracy is improved to 13.1 mm by using additional GLONASS satellites, and further to 12.3 mm by using additional GRACE satellites.

5 Improving VLBI solution by the tropospheric ties from GNSS

The multi-technique combination is nothing new and the studies involving the VLBI technique on the observation level have been performed (Hobiger and Otsubo, 2014; Hobiger et al., 2014; Hobiger et al., 2015). In terms of integrated GNSS and VLBI processing, one unique focus is the tropospheric ties, as it is expected that the superior tropospheric parameters from the GNSS technique will improve the VLBI solution. However, the previous studies are mainly limited to the positioning domain where the station coordinates are improved by tropospheric ties, and a comprehensive investigation of the VLBI solution including the EOP is still necessary, which is underlined in this chapter.

Several studies have investigated the impact of applying the GNSS tropospheric parameters on the UT1-UTC estimates in the VLBI intensive sessions, where different software packages are used for GNSS and VLBI (Teke et al., 2015; Nilsson et al., 2017). As shown in Section 4.6, a much better agreement of tropospheric parameters is available from the homogeneously processed GNSS and VLBI solutions in the same software. It is thus necessary to investigate the impact of tropospheric ties on the UT1-UTC estimates in INT sessions, especially in the integrated solution.

5.1 Improving the UT1 estimates in the VLBI INTensive sessions

As mentioned in Section 4.7, the 1-hour VLBI INT sessions with two stations have imperfect geometry and simplified processing strategies, that is, the tropospheric horizontal gradients are ignored, the clock breaks and baseline are usually not considered either. Therefore, the INT sessions suffer from some systematic biases and noises. By applying the tropospheric ties between GNSS and VLBI, the estimation of the gradients is also available for VLBI. Several studies have been conducted to improve the VLBI INT sessions by optimizing the tropospheric parameter estimation, using both GNSS and NWM products (Nafisi et al., 2012; Teke et al., 2015; Nilsson et al., 2017; Landskron and Böhm, 2019).

5.1.1 Data processing

The VLBI INT1 and INT2 sessions from 2001 to 2016 are processed using the strategy mentioned in Section 4.7. The daily PPP is performed using the strategy described in Section

4.2. For the INT1 sessions, the co-located GNSS stations KOKB and WTZR are processed, while for INT2 sessions, the co-located TSKB and WTZR stations are processed. The temporal resolutions for ZWD and gradients are 1-hour and 3-hour, respectively. Instead of a strict 24-hour length, the GNSS daily PPP starting time is delayed by 30-min to have the ZWD parameters exactly overlapping with the VLBI session, and gradient parameters covering the VLBI sessions in the middle.

To evaluate the UT1-UTC accuracy, the IERS EOP 14 C04 product is used as the reference. However, it should be noted that the INT sessions also contribute to the generation of the IERS product, especially for the days when the 24-hour VLBI sessions such as R1&R4 are not available. As this product is not an independent source for evaluation, the LOD is further derived from the UT1-UTC estimates, and then compared with the IGS LOD product. As mentioned in Section 2.3.2 (see Figure 2.6), the IGS LOD is a combined product with the long-term signals from VLBI and short-term signals from GNSS. Despite these limits, there are no perfect options to evaluate the UT1-UTC and LOD from INT sessions.

The details about tropospheric delay modeling in processing INT sessions are shown in Table 5.1. For the ZWD-free solutions, the ZWD parameters are estimated separately for GNSS and VLBI, while for the ZWD-tied solutions, the ZWD parameters are tightly tied together. The gradients in VLBI solutions are treated in three ways: (1) without gradients ("w/ Grd") where gradients are not estimated; (2) with gradients ("w/ Grd") where gradients are estimated as 3-hourly piece-wise-constant (PWC); and (3) with gradient ties ("w/ Grd_{tie}") where gradients estimated as 3-hourly PWC and tied to GNSS.

Table 5.1 Description of the tropospheric delay modeling strategies in VLBI INT session processing.

Solution		ZWD		Gradients	
		VLBI	GNSS	VLBI	GNSS
ZWD-free	w/o Grd	1-hourly PWC, no ZTD ties		None	3-hourly PWC
	w/ Grd			3-hourly PWC, no gradient ties	
	w/ Grd_{tie}			3-hourly PWC, gradient ties applied	
ZWD-tied	w/o Grd	1-hourly PWC, ZTD ties applied		None	3-hour PWC
	w/ Grd			3-hourly PWC, no gradient ties	
	w/ Grd_{tie}			3-hour PWC, gradient ties applied	

To ensure that the posteriori variance factors are comparable between different solutions, the GNSS and VLBI observations are always processed in the same least-squares estimator whether the tropospheric ties are applied or not.

5.1.2 Analysis of UT1-UTC and LOD

The statistics of the UT1-UTC differences compared to the IERS EOP 14 C04 product and those of the LOD differences compared to the IGS final product are shown in Figure 5.1. The IG2 products are used for the period before 2014, and the IGS operational products are used after that. Three statistics are given, including (1) the weighted root mean square of the

errors (or differences) WRMS; (2) the weighted mean of the differences WMEAN; and (3) the weighted standard deviation WSTD.

For UT1-UTC, estimating gradients in VLBI solutions independently causes large noise, that is, an increased WSTD value for both INT1 (increased from 25 μs to 37 μs) and INT2 (increased from 22 μs to 25 μs). The average bias (WMEAN), however, is reduced, especially for the INT2 sessions with the bias reduced from 13 μs to 11.5 μs. By applying the gradient ties, the WMEAN values are further reduced, that is, from 5 μs to around 3 μs for INT1 and from 11.5 μs to 10 μs for INT2. The noise (WSTD) is reduced compared to the solution without gradient ties, but still larger than the solution without gradients. As for WRMS, it is significantly increased with gradient estimation, but reduced to be comparable with the solution without gradients when the gradient ties are applied. The same conclusions stand in the solutions where the ZWD ties are applied, while all the statistics (WMEAN, WSTD, and WRMS) are slightly reduced.

As for the LOD estimates shown in Figure 5.1, one can see a significant increase for INT1 (from 27 μs to 44 μs), and a slight increase for INT2 (around 0.5 μs) in terms of both WSTD and WRMS if the VLBI gradients are estimated independently. On the other hand, applying gradient ties improves the LOD of INT2 sessions significantly, with the WSTD value reduced from 23 μs to 20 μs, which applies to solutions with or without ZWD ties. For the INT1 solutions with ZWD ties, the gradient ties introduce a reduction of around 1 μs in terms of WSTD and WRMS. The LOD WMEAN values of both INT1 and INT2 are within ±1 μs.

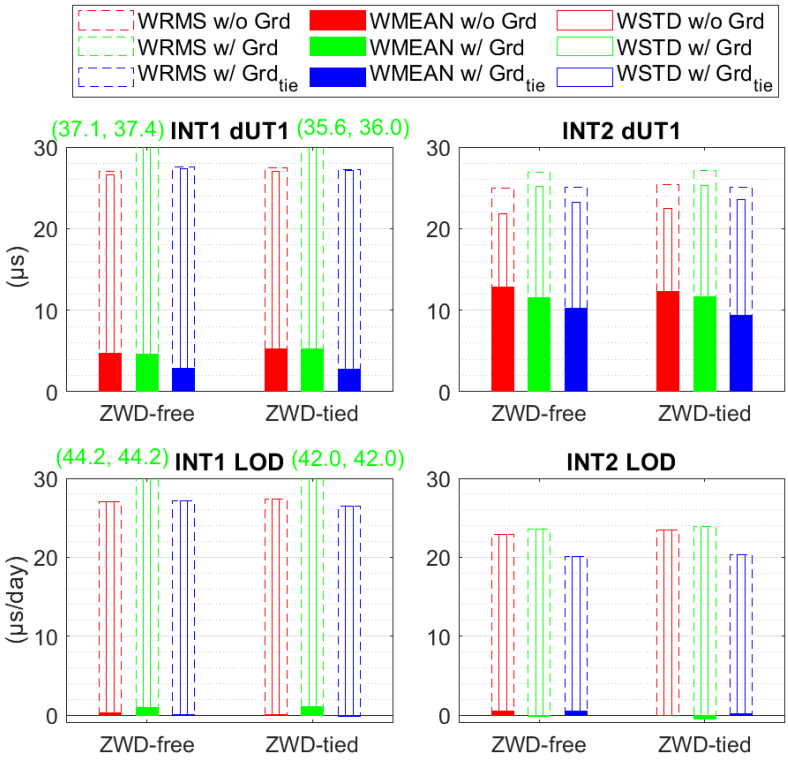

Figure 5.1 Statistics of the UT1-UTC differences compared to the IERS EOP 14 C04 product and LOD differences compared to the IGS product. The WSTD and WRMS values of INT1 exceeding the panels are given in the parentheses.

To summarize the results, it is clear that systematic bias exists in the UT1-UTC estimates with the traditional processing strategy, and it can be reduced by estimating gradients, and further reduced by applying GNSS–VLBI gradient ties. As for the LOD, the estimates can be improved in INT2 when gradient ties are applied, and can be improved in INT1 only if both the ZWD and gradient ties are applied.

The UT1-UTC differences between the solutions with and without ZWD ties are shown in Figure 5.2. Here the VLBI gradients are not estimated. Even though the UT1-UTC WSTD value does not show significant differences when comparing to the IERS EOP product (as shown in Figure 5.1), applying ZWD ties does make a difference in terms of the UT1-UTC scatter. The median values of the absolute differences are 4 μs and 3 μs for INT1 and INT2, respectively, and the corresponding STD values are 13 μs and 9 μs. The average value of the differences is zero, indicating that no systematic bias is caused by ZWD ties.

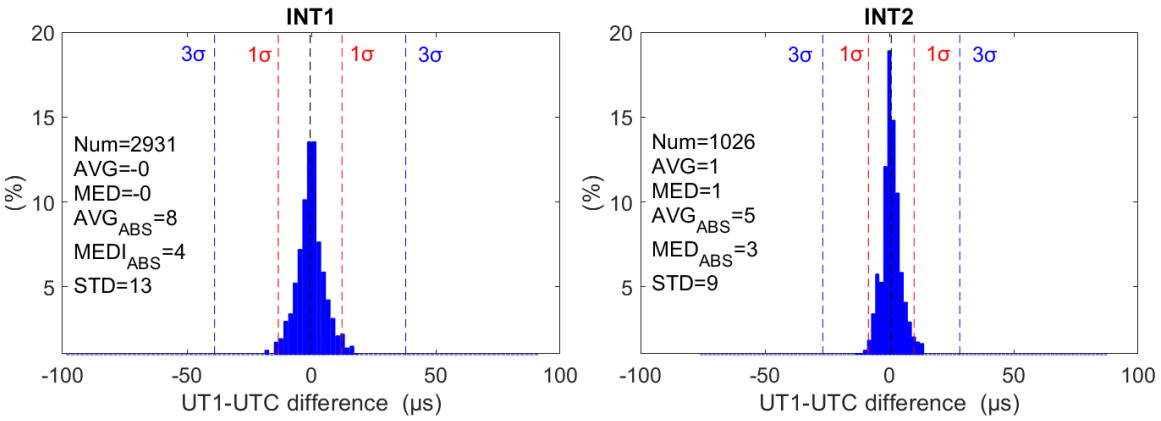

Figure 5.2 UT1-UTC differences between solutions with and without ZWD ties for INT1 (left) and INT2 (right). In each panel, the 1σ (68.3%) and 3σ (99.7%) regions are also presented in dash lines, and the statistics (AVG for average, MED for median, AVG_{ABS} for average absolute, MED_{ABS} for median absolute, and STD for standard deviation values) are presented within the panels.

The UT1-UTC differences between solutions with and without gradients are shown in Figure 5.3. For the solution with gradients, the gradient ties are applied; for both solutions, the ZWD ties are not applied. The average values of UT1-UTC differences are 2 μs for INT1 and 3 μs for INT2, and the median values of absolute differences are 8 μs and 7 μs, correspondingly. As for the STD, the value in INT1 (17 μs) is larger than that in INT2 (13 μs).

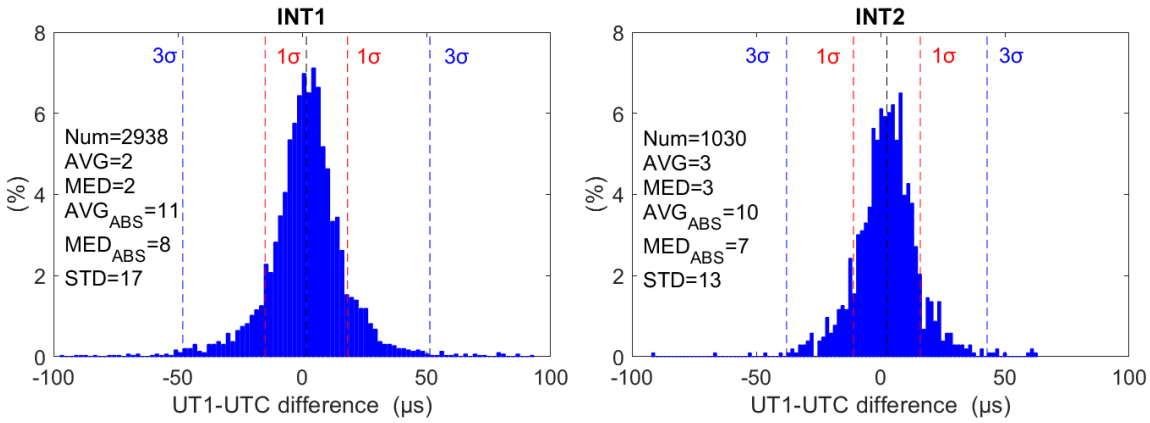

Figure 5.3 UT1-UTC differences between solutions with gradient ties and those without gradients for INT1 (left) and INT2 (right). In each panel, the 1σ (68.3%) and 3σ (99.7%) regions are also presented in dash lines, and the statistics (AVG for average, MED for median, AVG_{ABS} for average absolute, MED_{ABS} for median absolute, and STD for standard deviation values) are presented within the panels.

As shown in Figure 5.2 and Figure 5.3, the UT1-UTC differences caused by ZWD ties in INT1 are larger than those in INT2, so are the differences caused by gradient ties.

A further inspection of the UT1-UTC differences and gradients is shown in Figure 5.4 and Figure 5.5 for INT1 and INT2, respectively. The UT1-UTC differences are linearly fitted as a function of the horizontal gradients and the coefficient of determination R^2 is presented to analyze how the UT1-UTC differences can be explained by the gradients. The coefficient of determination is defined as:

$$R^2 = 1 - \frac{\Sigma_{i=1}^{n}(y_i - y_{i,fit})^2}{\Sigma_{i=1}^{n}\left(y_i - \frac{1}{n}\Sigma_{i=1}^{n} y_i\right)^2} \tag{5.1}$$

where y_i and $y_{i,fit}$ are the UT1-UTC difference and the fitted value, respectively. This coefficient describes to what extend the fitting function can explain the differences, and can roughly indicate the squares of the correlation coefficient between the original and the fitted time series.

For the INT1 sessions (WETTZELL–KOKEE), the UT1-UTC differences are highly dependent on the sum of east gradients at the two stations. The coefficient of determination (R^2) is 0.68, indicating a correlation coefficient of 82% between the raw observations and the fitted line. The fitting slope of –11.7 μs/mm indicates that a sum of 1 mm east gradient at the two stations introduces a negative dUT1 bias of about 11.7 μs. Moreover, it seems that the KOKEE station that plays a much more important role in this gradient related UT1-UTC bias, as the coefficient of determination at KOKEE (0.52) is much larger than that at WETTZELL (0.17). This can be attributed to the location of the two stations, as KOKEE is located on the tropical island of Kauai (35 km north-south, 45 km east-west) in the Pacific Ocean (22.1°N, –159.5°E, Hawaii, America) with drastic terrain variation (from the sea surface to 1300 m), while WETTZELL is located in central Europe (49.1°N, 12.9°E) with relatively plain terrain. The UT1-UTC differences do not shown any dependence on the north gradient component at all.

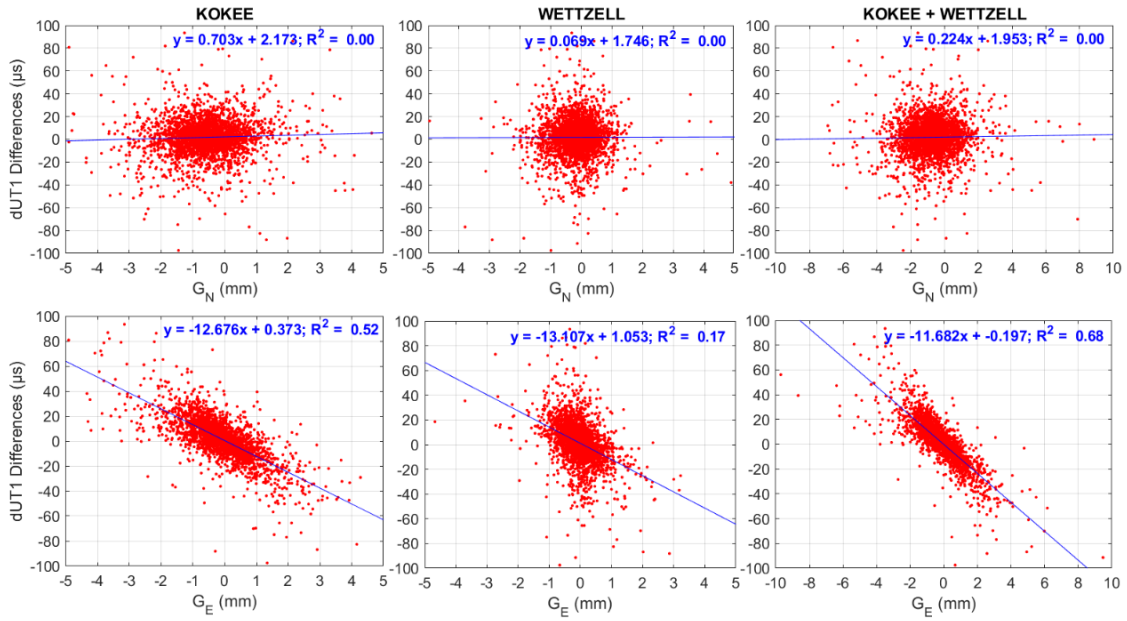

Figure 5.4 Correlation between UT1-UTC differences and gradients for INT1 sessions. The station-wise gradients are shown in the left and middle panels, and the sum of gradients at the two stations is shown in the right panels. The linear fit coefficients and the coefficient of determination (R^2) are shown in the panels.

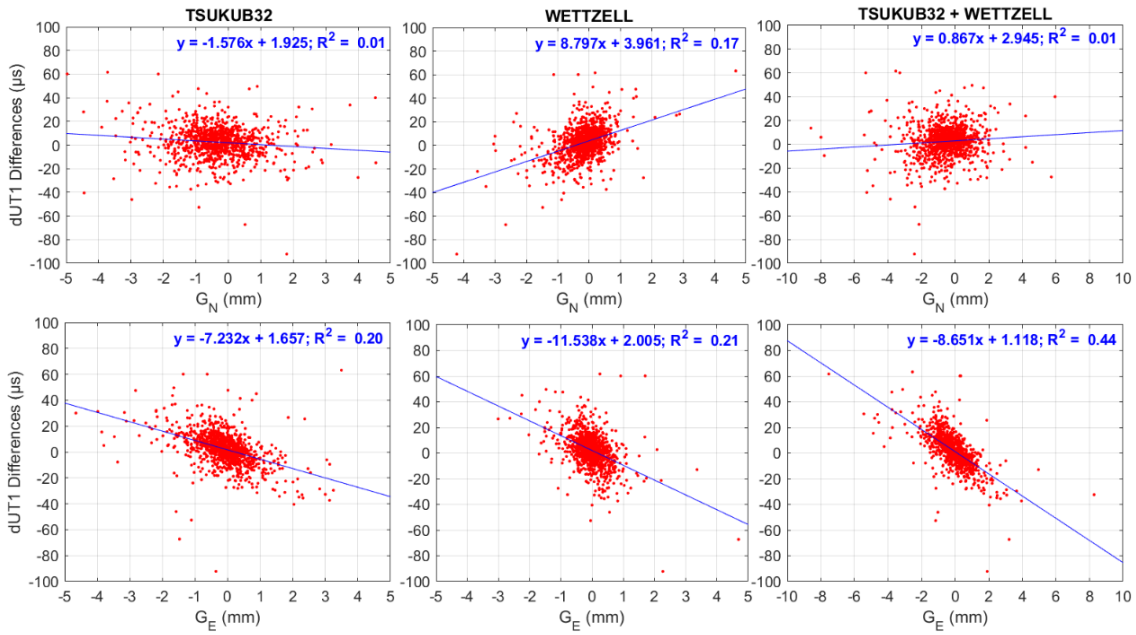

Figure 5.5 Correlation between UT1-UTC differences and gradients for INT2 sessions. Vertical axis: UT1-UTC differences between solutions without gradients and those with gradient ties. The station-wise gradients are shown in the left and middle panels, and the sum of gradients at the two stations is shown in the right panels. The linear fit coefficients and the coefficient of determination (R^2) are shown in the panels.

As for the INT2 sessions, the correlation between UT1-UTC differences and the east gradient is weaker than that in the INT1 sessions. A sum of 1 mm east gradient component causes a negative UT1-UTC bias of about 9 μs. The two stations seem to have comparable impacts on the UT1-UTC bias. Unlike INT1 where the north gradients make not impact on the UT1-UTC estimates, in INT2 the north gradient at WETTZELL also show a visible correlation with the UT1-UTC differences, with the coefficient of determination of 0.17.

As shown in Figure 5.3, the UT1-UTC differences caused by gradients in INT1 are larger than those in INT2 sessions. A further investigation of the gradients at the INT stations is conducted. The statistics of gradients from PPP solution, IGS product, and NWM (the VMF3 site-wise product) in 2001–2016 are given in Table 5.2.

Table 5.2 MEAN and STD values of the tropospheric gradients at three GNSS stations from PPP, IGS product, and NWM during the period of 2011–2016.

Station	G_N (mm)			G_E (mm)		
	PPP	IGS	NWM	PPP	IGS	NWM
KOKB	–0.5±1.0	–0.6±0.8	–0.1±0.2	–0.1±0.9	–0.1±0.7	+0.0±0.2
TSKB	–0.5±1.0	–0.3±1.2	–0.4±0.5	–0.1±0.8	–0.1±0.8	–0.1±0.4
WTZR	–0.2±0.6	+0.0±0.6	–0.3±0.3	+0.0±0.5	+0.1±0.5	+0.0±0.3

As one can see in Table 5.2, the gradient variations are underestimated by NWM, especially for the station KOKB. NWM shows that the gradient fluctuations at KOKB (around 0.2 mm) are smaller than that at WTZR (0.3 mm), while the two GNSS solutions (PPP and IGS) both show the opposite: the fluctuation at KOKEE is larger (0.8 to 1.0 mm) than that at WETTZELL (0.5 to 0.6 mm). The underestimated fluctuation of NWM at these three stations are partly caused by the lower temporal resolution of NWM (6-hour), while for KOKB there is another reason: the spatial resolution of NWM (1°×1° in VMF3 product) is not good enough to describe the complex terrain at KOKB, where the gradient variation can be caught by both GNSS and VLBI, but can hardly be modeled by NWM.

To further quantify the impact of tropospheric delay on the dUT1 estimates, the linear regression is performed using the following equation:

$$\Delta_{dUT1} = \Delta_{ZTD,1} + \Delta_{ZTD,2} + \Delta_{GN,1} + \Delta_{GN,2} + \Delta_{GE,1} + \Delta_{GE,2} \tag{5.2}$$

where Δ_{dUT1} is the UT1-UTC differences before and after the tropospheric ties, $\Delta_{ZTD,1}$ $\Delta_{ZTD,2}$ are the ZTD differences at the two VLBI stations, $(\Delta_{GN,1}, \Delta_{GN,2})$ and $(\Delta_{GE,1}, \Delta_{GE,2})$ are the corresponding differences of the north and east gradients, respectively. The regression coefficients and the uncertainties are given in Table 5.3.

Table 5.3 confirms with conclusions from Figure 5.4 and Figure 5.5. For INT1, the UT1-UTC differences are mainly associated to the east gradients at both KOKEE and WETTZELL, and the two stations have similar impact. As for INT2, the impacts of east gradient at TSUKUBA and WETTZELL are comparable, and both are smaller than the INT1 sessions. Moreover, The north gradients also have significant impact on the UT1-UTC estimates, that is, a north

gradient bias of +1 mm at TSUKUBA causes −4.42 μs UT1-UTC bias, and that at WETTZELL causes +9.88 μs UT1-UTC bias.

Table 5.3 Regression coefficients of the UT1-UTC differences caused by tropospheric zenith delay and gradient ties in the INT1 and INT2 sessions from 2001 to 2016.

INT type	Station	ZTD (μs/mm)	North gradient (μs/mm)	East gradient (μs/mm)
INT1	KOKEE	−0.03 ± 0.01	+1.33 ± 0.20	−12.84 ± 0.25
	WETTZELL	+0.07 ± 0.04	−2.37 ± 0.41	−11.15 ± 0.40
INT2	TSUKUBA	+0.31 ± 0.05	−4.42 ± 0.34	−7.82 ± 0.34
	WETTZELL	−0.65 ± 0.07	+9.88 ± 0.56	−8.29 ± 0.58

5.2 Impact of tropospheric ties in VLBI CONT sessions

The INT sessions can certainly benefit from the tropospheric ties due to its own deficiency of limited observation number and weak observation geometry in a short period. The CONT sessions representing state-of-the-art VLBI technique at that time with much stronger observation geometry, can also benefit from the tropospheric ties. To demonstrate this effect, in this section the CONT 05–CONT17 campaigns are investigated, and the impact of applying tropospheric ties at co-locations is analyzed.

5.2.1 Data processing

The CONT sessions from CONT05 to CONT17 are used, and the VLBI stations are shown in Figure 4.10. The co-locations are provided in Table A.1. All the VLBI stations have at least one GNSS co-location in all the campaigns, except for the VLBA network in CONT17, where five co-locations are missing: OV-VLBA, HN-VLBA, LA-VLBA, KP-VLBA, and FD-VLBA. More details about the GNSS–VLBI tropospheric ties at co-locations can be found in Section 4.6.

The VLBI observations are processed in the single-session mode, where the details can be found in Section 4.2. The GNSS observations are processed in the PPP mode on a daily basis, see Table 4.2 for details. In addition, the tropospheric ties, that is, the ZWD and gradients, are then applied one by one to investigate their impacts. The tropospheric tie handling strategy is shown in Table 5.4.

Table 5.4 Description of the tropospheric parameter handling strategy in integrated GNSS and VLBI solutions of CONT campaigns.

Solution	A priori ZHD and ZWD	ZWD tie	Gradient tie
NO	A priori value from the site-wise VMF3 product, residual ZWD	No	No
ZTD	estimated as 1-hourly PWC, gradients estimated as 3-hourly PWC.	Yes	No
GRD	Mapping function: VMF3 for zenith delays, Chen and Herring	No	Yes
TRP	(1997) for gradients	Yes	Yes

As the VMF3 products derived from NWM are used to derive the a priori zenith hydrostatic and wet delays and the mapping functions, the tropospheric delay difference caused by the different statin heights can be properly handled. For the potential remaining tropospheric tie biases which are more likely related to the instrument (see Figure 4.20 for zenith delay and Figure 4.23 for gradients), they are parameterized as daily constant and estimated as unknowns, and constrained to the a priori value derived in each campaign (that is, the values in Figure 4.20 and Figure 4.23). The constraints are adjusted according to the normalized residuals, with a criteria of 1.96.

For the stations with more than one GNSS co-locations, the tropospheric tie constraints are applied between the VLBI station and every one of the GNSS co-locations, while constraints are not applied between the co-located GNSS stations. This is performed to avoid the over-constraint of tropospheric ties. The solutions are evaluated in terms of TRF stability (repeatability of station coordinates and VLBI network daily scales) and EOF precision. The statistics of station coordinate weighted repeatability, network scale repeatability, and EOP accuracies are described in Section 4.1.

Note that in this section the coordinates of AGN are fixed to the a priori values, that is, the ICRF3. As the focus is on the impact of tropospheric ties on TRF and EOP in this section, the discussion about CRF with be presented in next chapter, together with the global and local ties.

5.2.2 Station coordinates and network scale

Weighted repeatability of the station coordinates

The coordinate repeatability for VLBI and GNSS stations are shown in Figure 5.6. The VLBI horizontal components are improved by applying both ZTD and gradients ties, with the repeatability reduced by 12% (from 2.6 mm to 2.3 mm) on the north component, and by 12% (from 2.4 mm to 2.1 mm) on the east component. As for the up component, the major improvement of 29% (from 7.2 mm to 5.1 mm) is introduced by the ZTD ties, while the gradient ties only reduce the WSTD by 6%. The overall vertical improvement is 28% with all the tropospheric ties. For the GNSS solutions, applying tropospheric ties has an insignificant impact on both the horizontal (1 to 2%) and vertical (6%) components.

Also shown clearly in this figure, the coordinate precision of GNSS stations is better than that of VLBI, especially on the up and north components, due to the better geometry of GNSS with always more than four satellites continuously tracked at most of the stations.

It should be noted that while VLBI has comparable repeatability on the north and east components, this is not the case for GNSS. The phenomenon of a worse precision on the east component than the north one in GNSS is well-known. Despite the fact of larger east repeatability in GNSS solutions without or with any kind of tropospheric ties, the VLBI east component is improved from 2.4 mm to 2.1 mm by the tropospheric ties.

Further inspecting Figure 5.6, the tropospheric ties (both ZTD and gradient ties) improve VLBI solution in all campaigns on all the north, east, and up components. However, applying only ZTD or gradient ties can degrade the performance. The WSTD value on the north component is increased when only ZTD or gradient ties are applied in CONT17. As for the east component, the WSTD value is increased in CONT17-VLBA if only gradient ties are applied. As for the GNSS stations, there are no significant differences between different campaigns.

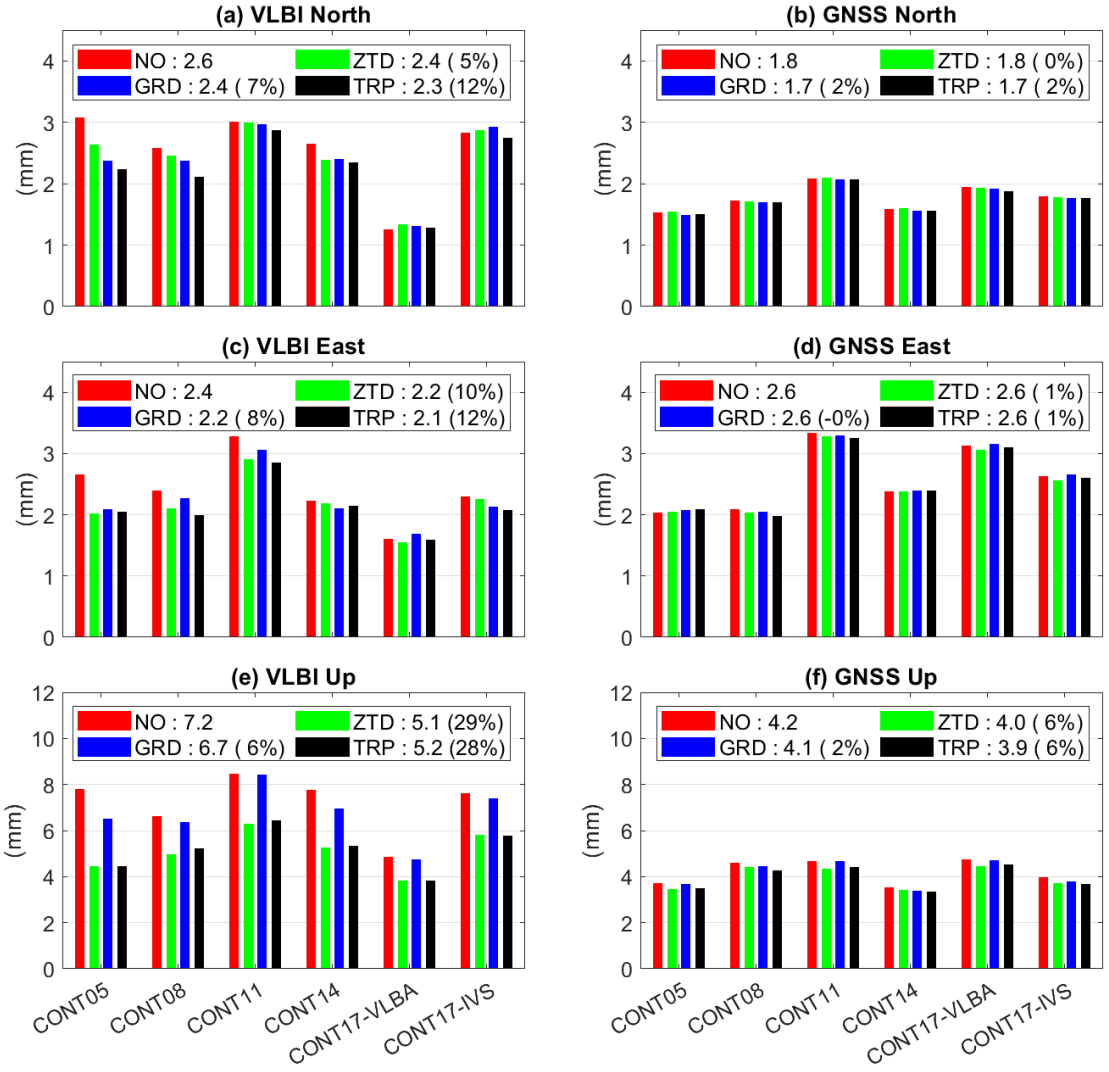

Figure 5.6 Weighted repeatability of station coordinates for VLBI (left panels) and GNSS (right panels) on the north (upper), east (middle) , and up (lower) components.

VLBI weighted baseline length repeatability

In addition to the station coordinate repeatability, the VLBI baseline length repeatability (BLR) in weighted standard deviation (WBLR) is shown in Figure 5.7. The WBLR is more independent of any external systematic effects, for instance, the TRF stability, and can better represent to VLBI internal precision. The WBLR values of solutions with different tropospheric ties are shown in the left panel, and the WBLR differences between solutions

with tropospheric ties and those without tropospheric ties are shown in the right panel. The repeatability is further fitted with Eq. 4.3 and the repeatability differences are fitted using a second-order polynomial function:

$$WBLR = a_0 + a_1 \cdot L + a_2 \cdot L^2 \tag{5.3}$$

where $WBLR$ is the weighted baseline length repeatability, L is the baseline length, and (a_0, a_1, a_2) are the fitted coefficients. As shown in Figure 5.7, both ZTD and gradient ties improve the WBLR, and the improvement from the first one is more significant than that from the latter one. The WBLR improvement is more significant for the longer baselines than the shorter ones. On average, the WBLR improvements are 1.1 mm by applying ZTD ties, 0.5 mm by applying gradient ties, and 1.2 mm by applying tropospheric ties.

As shown in the right panel of Figure 5.7, the WBLR values are reduced for most of the baselines when the zenith delay ties are applied, but they can also increase in some baselines when only the gradient ties are applied, especially for the long baselines. As shown in the fitted results, the overall improvement with zenith delay ties is around 1 mm for the baseline with the length of 10, 000 km and 2 mm for the baseline with the length of 12, 000 km. The largest improvement can be up to 5 mm.

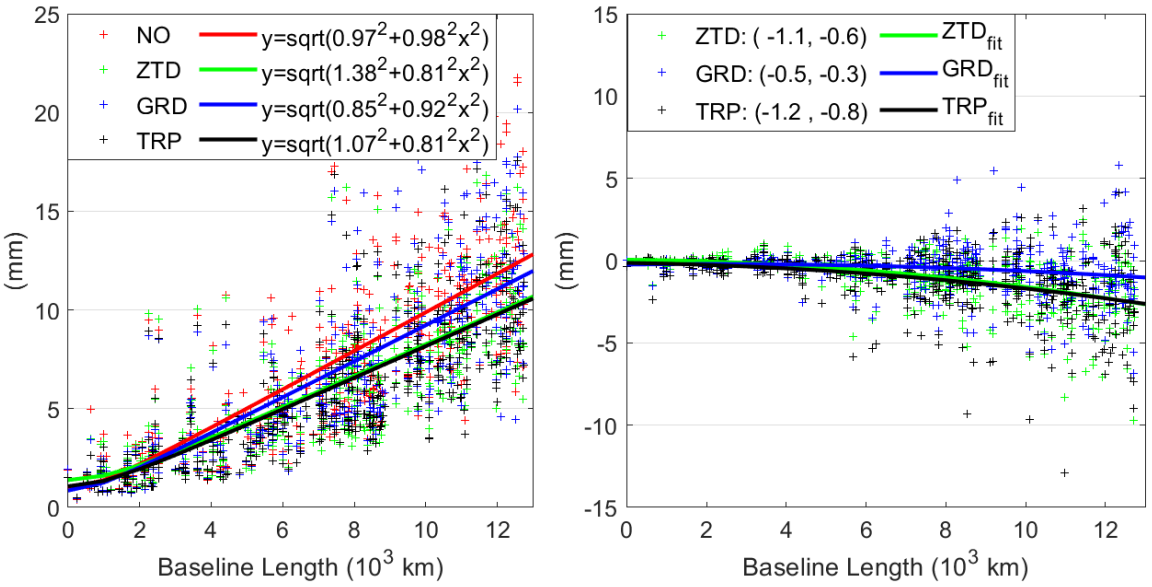

Figure 5.7 The VLBI weighted baseline length repeatability in CONT05–CONT17 using different tropospheric ties (left panel); and the WBLR differences between solutions with tropospheric ties and solution without tropospheric ties (right panel). In the right panel a negative value means that the solution is improved after applying the tropospheric ties.

VLBI network scale

The VLBI daily network scale estimates using different tropospheric ties in CONT05–CONT17 are shown in Figure 5.8. Each daily scale is calculated by the seven-parameter Helmert transformation between the daily station coordinate estimates and the values from ITRF2014. In each campaign, the average scale value of the solution without tropospheric ties

is used as a reference, and the daily scale offsets of other solutions are calculated with respect to this average scale.

The average network scale weighted repeatability of VLBI solution without tropospheric ties is around 0.60 ppb over all the campaigns, with the maximum value of 0.82 ppb in CONT11 and the minimum one of 0.45 ppb in CONT14. The network scale is improved significantly if the ZTD ties are applied, where the repeatability varies between 0.2 and 0.7 ppb with an average value of 0.42 ppb, indicating an average improvement of 31% (minimum improvement of 16% in CONT17-VLBA and maximum improvement of 47% in CONT05). The gradient ties generally introduce slight scale repeatability improvement in most of the campaigns except for CONT11, where the repeatability is increased by 0.06 ppb (around 7%). By applying ZTD and gradient ties together, the best repeatability is achieved with an average value of 0.40 ppb, which is about 33% improvement compared to the solution without tropospheric ties, that is, 0.60 ppb.

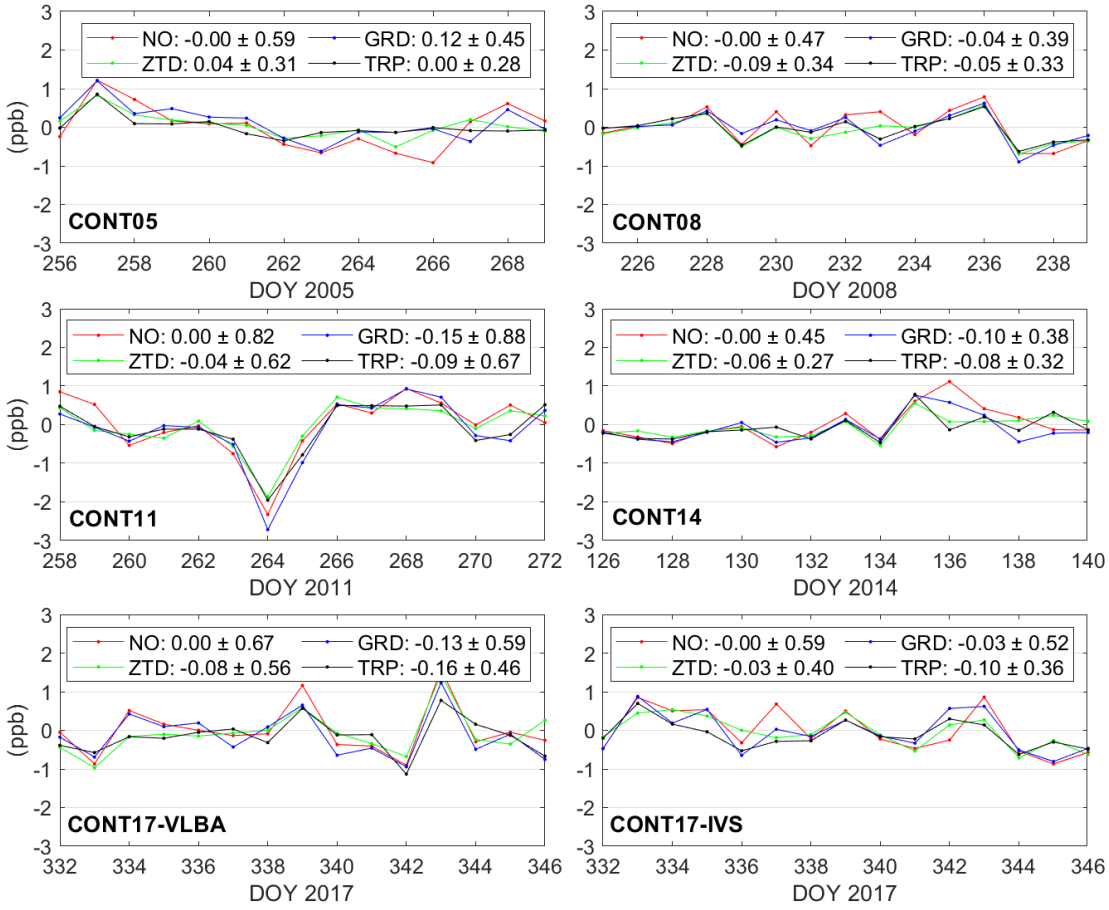

Figure 5.8 Daily estimates of VLBI network scale in CONT05–CONT17 using different tropospheric ties. The average bias with respect to the solution without tropospheric ties ("NO" shown in red) and the network scale weighted repeatability of each solution are shown in the legend.

On the other hand, it should be noted that the tropospheric ties can introduce systematic network scale offsets up to –0.16 ppb (CONT17-VLBA). In the absolute sense, the ZTD ties induced bias varies within 0.03 to 0.09 ppb, while the gradient ties induced bias varies within

0.03 to 0.15 ppb. This network scale bias is caused by the tropospheric tie biases between the space solutions and NWM in both the ZTD and the gradient parameters, as shown in Section 4.6. However, this statistic does not necessarily mean any significant improvement or deterioration of the VLBI network scale estimates, as (1) the magnitude is rather insigficiant with respect to the uncertainty, and (2) the investigation and comparison with other techniques (for instance, SLR) using long-term observations are essential for any conclusions.

5.2.3 EOP estimates

In addition to the TRF improvement from tropospheric ties, it is also expected to have better EOP estimates correspondingly. The EOP formal errors are first analyzed, followed by the EOP comparison with the IERS EOP 14 C04 product, and the ERP comparison with GNSS solutions.

Formal error analysis

The EOP formal error improvement by applying tropospheric ties is shown in Figure 5.9, where the solution without tropospheric ties is used as a reference. The tropospheric ties reduce the PM offset formal errors by 33% and 30% on the x-pole and y-pole components, respectively. The improvements of PM rate formal errors are around 22% for both the x-pole and y-pole components. As for UT1-UTC and its first time derivative (LOD), the tropospheric ties improve the formal errors by 23% and 17%, respectively. Moreover, the CPO components are also improved by 20% on both components.

The impact of ZTD ties and gradients are different for different EOP components. As the ZTD ties contribute more on the improvement of PM offsets, it is obvious that the gradient ties contribute more on the improvement of PM rate, LOD, and CPO components, which is larger than the contribution of ZTD ties by a factor by two to three.

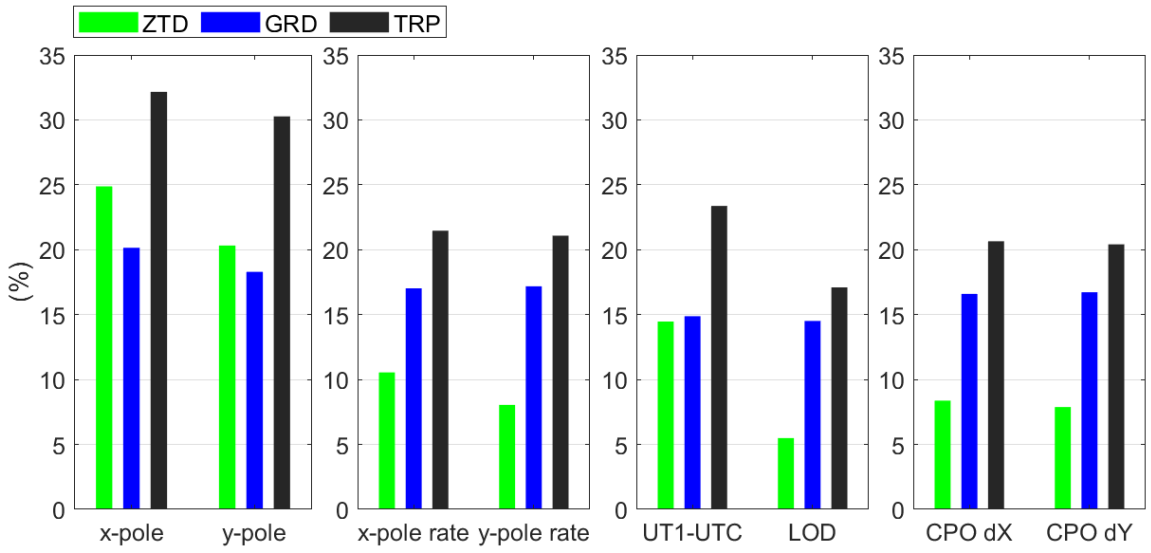

Figure 5.9 EOP formal error improvement of solutions with tropospheric ties compared to that without tropospheric ties. The average improvement over CONT05–CONT17 is presented.

As the EOP uncertainty reduction reveals the theoretical improvement introduced by the tropospheric ties in the integrated solution. This improvement is caused by the stabilized network, as the tropospheric ties de-correlate the tropospheric parameters and station coordinates.

Analysis of the correlation coefficients

Note the different contributions of ZTD and gradient ties to the different EOP comoponents, Figure 5.10 presents the correlation coefficients between EOP and tropospheric parameters, taking the session C1415 (20th of May in 2014, CONT14) as an example. For the solution of 1-hourly ZTD and 3-hourly gradient resolution (upper left panel), which is used in the data processing of this study, it is clearly that the PM offsets and UT1-UTC have larger correlation with ZTD than with gradients, whereas for the PM rates, LOD, and CPO, the correlations to gradients are larger than those to ZTD. Further inspecting the solutions of 1-hourly ZTD and 1-hourly gradients, or 3-hourly ZTD and 3-hourly gradients, they both agree with this conclusion. As for solution of 24-hourly ZTD and 24-hourly gradients, it is worth mentioning that the north gradient has slightly larger correlation to x-pole offset that ZTD, and the east gradient has larger correlation to UT1-UTC than ZTD.

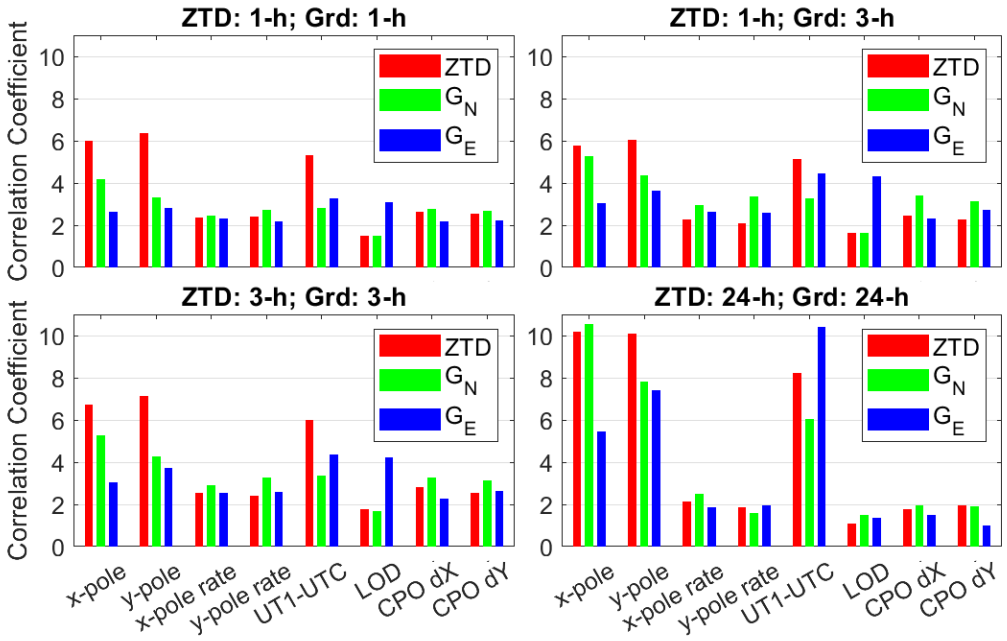

Figure 5.10 Correlation coefficients (in percentage) between different EOP components and the tropospheric parameters. The average absolute values of all pairs in the session C1415 (20th of May, 2014) are used. Different temporal resolutions are used in different subplots.

WSTD of EOP estimates

As the EOP formal error can be improved by tropospheric ties, it is expected to observe similar behavior in the WSTD statistic when comparing to the IERS EOP 14 C04 product.

The WSTD values of the EOP differences comparing to the C04 product are shown Figure 5.11. Apparently, the PM offsets are improved by the tropospheric ties, with the average WSTD reduced by 18% (from 97 μas to 79 μas) on x-pole and 13% (from 78 μas to 68 μas) on y-pole. The PM rates are also improved by 12% to 14%. The LOD WSTD value is reduced by 10% (reduced from 17.2 μs/day to 15.4 μs/day). On the other hand, the UT1-UTC component does not show significant improvements after applying tropospheric ties, as the WSTD reduction is only 2% on average. As for CPO, the dX component is improved by 13% on average while and improvement of the dY component is only 4%. One possible explanation is that the UT1-UTC and CPO from the C04 product are solely dependent on the VLBI techniques, whereas the PM and LOD are derived from both GNSS and VLBI where GNSS contributes more.

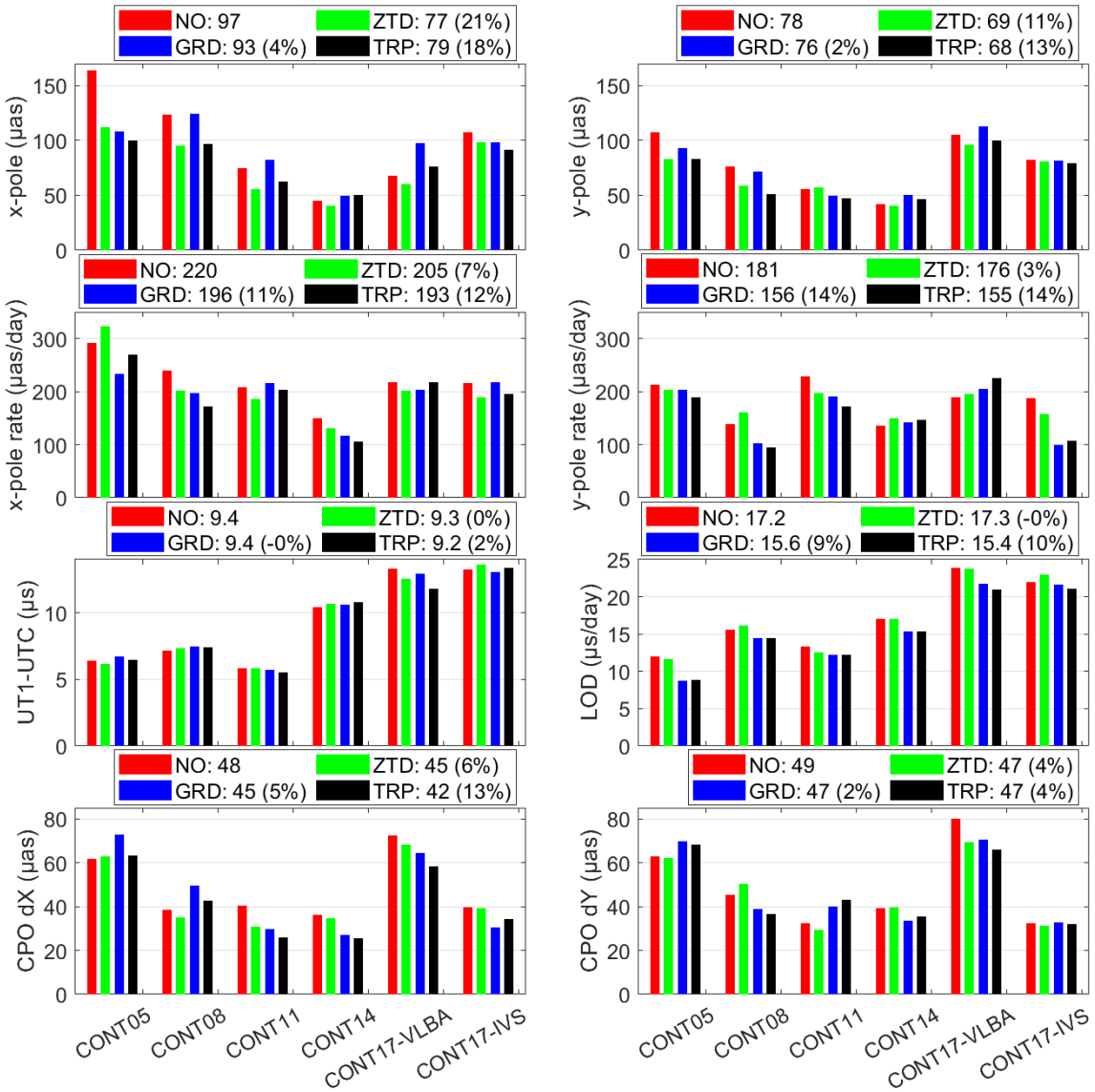

Figure 5.11 WSTD of the EOP differences with respect to the IERS EOP 14 C04 product using different tropospheric ties in CONT05–CONT17. Please note the different vertical axis scales. The average values over CONT05–CONT17 are given in the legend, and the improvements of the solutions with tropospheric ties compared to the solution without tropospheric ties are given in the bracket.

The impact of ZTD ties and gradient ties on EOP WSTD values corresponds to the analysis of the formal errors, as the PM offsets are mainly improved by the ZTD ties and the rates are mainly improved by the gradients ties. The LOD improvement is also mainly attributed to the gradient ties, which is consistent with the formal error analysis. As for the UT1-UTC and CPO, the variations of WSTD values do not fully agree with those of the uncertainties, which might be caused by the problematic C04 reference. Nevertheless, all the EOP components are improved by tropospheric ties.

Inspecting campaign by campaign, one can clearly see that the statistics vary in different campaigns. For the PM offsets, the WSTD values are reduced by tropospheric ties significantly in the early-stage campaigns from CONT05 to CONT11. In CONT14 and CONT17, however, the tropospheric ties do not necessarily reduce the WSTD values, especially when only the gradient ties are applied in CONT17-VLBA. For LOD, the WSTD values are reduced in all the campaigns when gradient ties are applied, but are slightly increased in some campaigns when only ZTD ties are applied, for instance, CONT8 (0.5 μs/day) and CONT17-IVS (1 μs/day). The UT1-UTC and CPO performances vary in different campaigns. The WSTD values of UT1-UTC with tropospheric ties are slightly increased (less than 0.3 μs/day) in CONT08 and CONT14, while those of CPO are increased in various campaigns, including the dX component in CONT05 and CONT08, and the dY component in CONT05 and CONT11.

WRMS of ERP DBD

In addition to the comparison with the IERS EOP product, the DBD is of polar motion and UT1-UTC is further investigated to indicate the internal precision. The WRMS values of DBD in different campaigns are shown in Figure 5.12. For the PM components, a larger improvement is introduced by ZTD ties while the impact of gradient ties is relatively insignificant. On average, the x-pole DBD is improved by 7% (reduced from 214 μas to 199 μas) and 0% (to 215 μas) by ZTD ties and gradient ties, respectively; and the combined impact is 5% (reduced to 203 μas). Correspondingly, the y-pole component is improved by 11% (reduced from 199 μas to 178 μas), 3% (to 193 μas), and 10% (to 179 μas). As for UT1-UTC, the DBD WRMS values are improved by 7% (reduced from 10.5 μs to 9.8 μs) with ZTD ties applied and 12% (reduced from 10.5 μs to 9.2 μs) with gradient ties applied, while the improvement is 17% (to 8.7 μs) when both ZTD and gradient ties are applied.

On the other hand, the ZTD or gradient ties do not always introduce the improvement to the DBD statistics. For the PM components, the ZTD ties usually reduce the DBD WRMS, except for the y-pole component in CONT14. The gradient ties reduce the x-pole DBD WRMS values in two of the six campaigns (CONT05 and CONT14), and increase the y-pole values in two campaigns (CONT14 and CONT17-VLBA). As for UT1-UTC, the gradient ties usually bring a smaller DBD WRMS value except for the CONT17-VLBA network. Nevertheless, the overall DBD improvement of both PM and UT1-UTC introduced by the tropospheric ties are visible, except x-pole in CONT11 and CONT17, y-pole in CONT14.

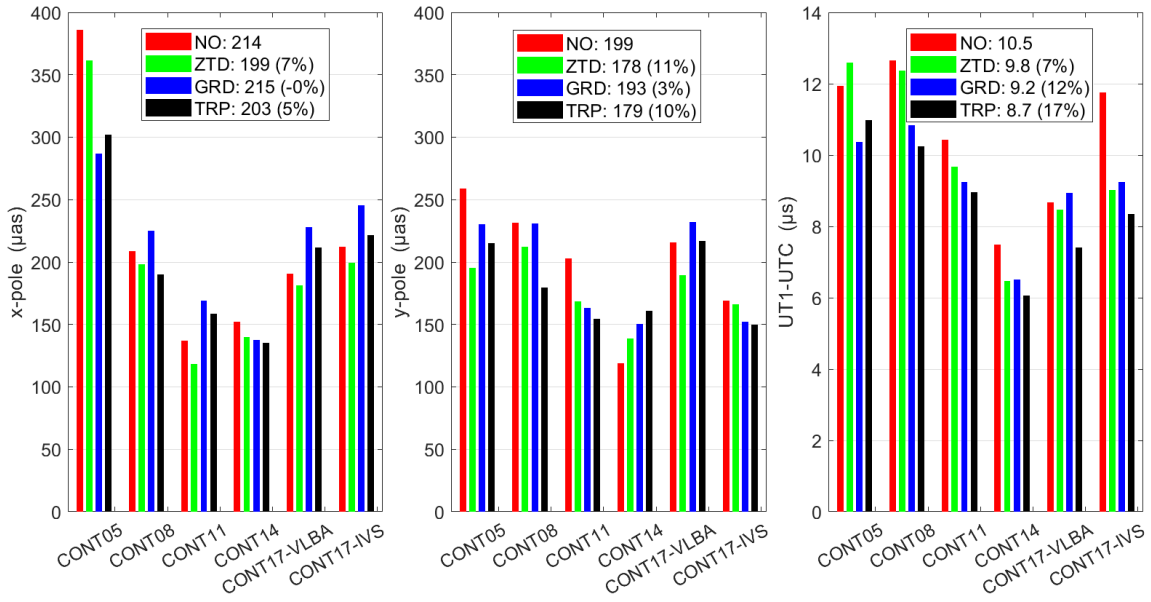

Figure 5.12 WRMS of the day-boundary-discontinuity values for polar motion and UT1-UTC using different tropospheric ties in CONT05–CONT17. The average value of all the campaigns are shown in the legend, and the reduction compared to the solution without tropospheric ties is shown in the parentheses.

Intra-technique agreement of the CONT17 campaign

The WSTD values of the EOP differences between the two networks in CONT17 are given in Figure 5.12.

For polar motion, the intra-technique agreement tends to degrade when the tropospheric ties are applied, except for the y-pole rate, which is consistent with the analyses of Figure 5.11 and Figure 5.12 where the CONT17 campaign does not present a significant improvement with tropospheric ties applied.

On the other hand, the parameters that relies more on the VLBI technique, that is, UT1-UTC, LOD, and CPO components, all show visible improvement introduced by the tropospheric ties. The UT1-UTC agreement is improvd by 11% (reduced from 3.2 μs to 2.8 μs) and 6% (reduced from 3.2 μs to 3.0 μs) by gradients ties only and by ZTD and gradient ties together, respectively, whereas degraded by 4% (increased to 3.3 μs) by ZTD ties only. As for LOD, the improvement is much more significant, as the values are reduced from 9.0 μs/day in solution "NO" to 6.2 μs/day in solution "ZTD" (31% improvement) and 6.8 μs/day in solution "GRD" (24% improvement), and the solution "TRP" presents an improvement of 20% with the WSTD value of 7.2 μs/day. For the two CPO components, the benefit from tropospheric ties is larger on the dY component (13%, 22%, and 29% improvement by ZTD ties only, gradient ties only, and ZTD and gradients ties together, respectively) than on the dX component (corresponding improvement of 2%, 5%, and 10%).

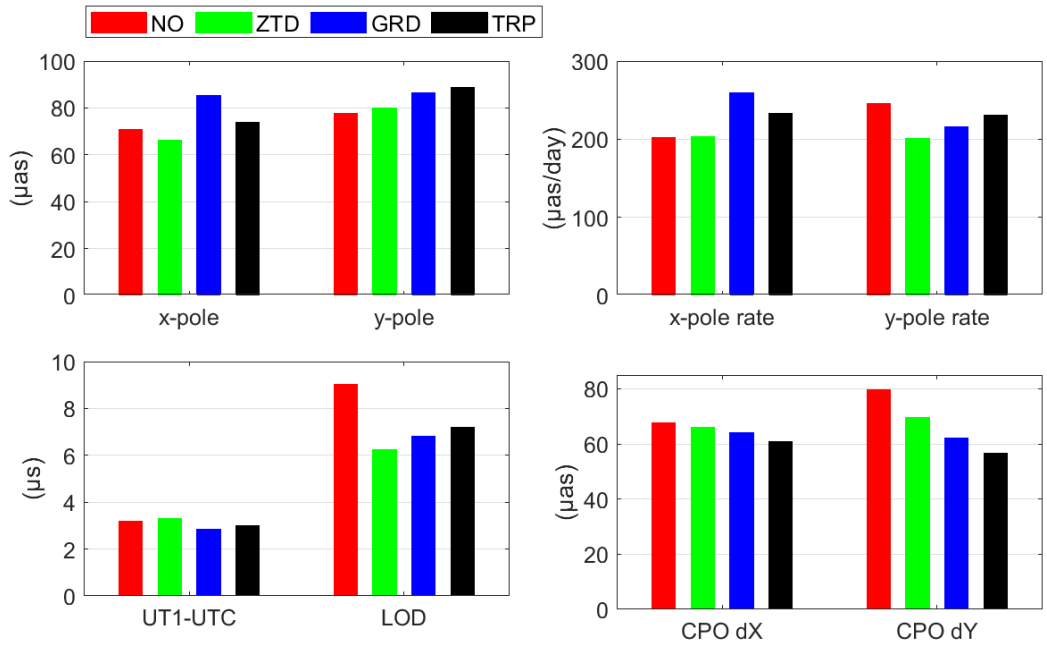

Figure 5.13 WSTD values of the EOP differences between the two VLBI networks in CONT17 (that is, IVS and VLBA) using different tropospheric ties.

Comparison with GNSS solutions

Note that the IERS EOP product is a combination of several techniques including VLBI, the homogeneously reprocessed GNSS solution is further used as an external reference. The GNSS ERP is derived from the daily POD solution, and the details are described in Section 4.2 and 4.3.

As shown in Figure 5.14, when comparing with the independent GNSS solution, applying tropospheric ties improves the PM offset WSTD values by 26% and 12% on the x-pole and y-pole components, respectively. The PM rate WSTD values are improved by 14% on the x-pole and 10% on the y-pole. The PM offset changes are more influenced by the ZTD ties, while the rate changes are more dominated by the gradient ties, which is consistent with the above analyses of formal errors and the agreement to the IERS EOP product.

The LOD agreement is also slightly improved by 5%, while the improvements are 4% and 6% by ZTD and gradient ties, respectively.

Nevertheless, the comparison to independent GNSS estimates agrees well with that to the IERS EOP 14 C04 product.

On the other hand, the performance in each campaign varies a lot. The PM offset and rate WSTD values are generally reduced by tropospheric ties (ZTD and gradient ties together) for most of the campaigns. However, there are a few exceptions.

- The y-pole component in CONT14 (caused by the gradient ties) and CONT17-IVS (caused by both ZTD and gradient ties).

- The x-pole rate component in CONT11 and CONT7-VLBA (both caused by the gradient ties).
- The y-pole rate component in CONT17-VLBA (caused by both ZTD and gradient ties).

As for the LOD component, despite the overall improvement of all the campaigns on average, the performance varies in different campaigns. The WSTD values are reduced in campaigns where the GNSS–VLBI inter-technique LOD agreement are relatively large, including CONT05, CONT08, and CONT17-IVS (all larger than 8 μs/day), but increased in the campaigns where inter-technique agreement are relatively small, including CONT11, CONT14, and CONT17-VLBA (all around 4 to 6 μs/day).

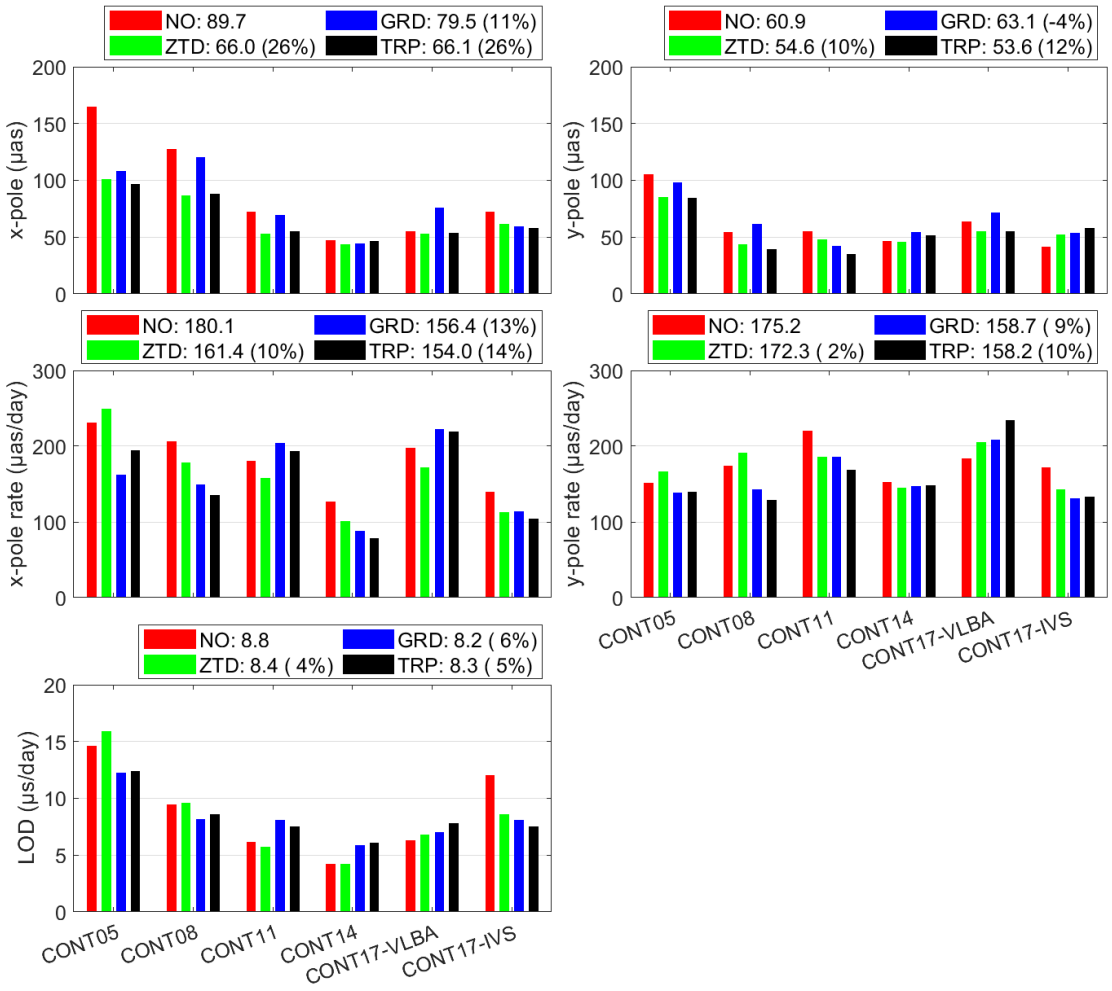

Figure 5.14 WSTD values of the ERP differences between VLBI and GNSS solutions in CONT05–CONT17. The average values are presented in the legend.

5.3 Chapter summary

The impact of applying tropospheric ties in GNSS and VLBI integrated solutions are investigated in this chapter, with the focus on the VLBI estimates. The results are summarized as follows.

Section 5.1 gives the results of the VLBI intensive sessions, where the gradient and ZTD ties are investigated separately.

- The gradient ties reduce the UT1-UTC bias from 5 μs to 3 μs for the INT1 sessions, and from 13 μs to 10 μs for the INT2 sessions. As for LOD, the WSTD values are reduced from 23 μs/day to 20 μs/day for the INT2 sessions, while the improvement for INT1 sessions is not significant.

- Generally, ZTD ties do not introduce significant differences in UT1-UTC and LOD components. However, there are slight differences in the LOD statistics of the INT1 sessions. The accuracies (both WRMS and WSTD values) are comparable with or without gradient ties if the ZTD ties are not applied, but a slight improvement is observed by applying gradient ties in the case of ZTD ties applied.

- The UT1-UTC biases are mainly caused by the east gradientat of both stations. For INT1 sessions, 1 mm bias in the east gradient of KOKEE introduces a negative UT1-UTC bias of 12.8 μs, for the WETTZELL station the corresponding bias is 11.1 μs. For the INT2 sessions, the factor is –8 μs/mm for the east gradients, at both TSUKUBA and WETTZELL. As the north gradients have almost neglectable impact on the KOKEE–WETTZELL sessions, the impact on the INT2 sessions are rather significant, that is, –4.4 μs/mm at TSUKUBA and 9.9 μs/mm at WETTZELL.

Section 5.2 gives the results of applying tropospheric ties in the five VLBI CONT campaigns, in terms of both station coordinates and EOP.

- The VLBI station coordinate estimates benefit significantly from the tropospheric ties.
    - The VLBI coordinate repeatability can be improved by tropospheric ties by 12%, 12%, and 28% on the north, east, and up components, respectively. The vertical improvement is mainly from the ZTD ties.
    - The VLBI baseline length repeatability is also improved. On average, an improvement of 1.1 mm, 0.5 mm, and 1.2 mm is introduced by ZTD ties, gradient ties, and them together.
    - The VLBI network scale repeatability is reduced by 33% on average over all the campaigns.
- The impact on GNSS station coordinate repeatability is insignificant, as the most significant improvement of 6% is observed on the up component.

- The EOP formal errors are reduced by up to 30%, and different EOP components have different sensitivities to the tropospheric ties.
    - The formal errors of PM offsets are improved by 30% to 35%, where the ZTD ties have slightly larger impact than gradient ties. The improvement is about 20% for PM rates, where the impact of gradient ties (17%) is about twice larger than that of ZTD ties (8% to 10%).
    - The formal error of UT1-UTC is reduced by 24%, where ZTD and gradient ties both contribute about 15%. As for LOD, the improvement is 17%, where the contribution of gradient ties (14%) triples that of the ZTD ties (5%).
    - The formal errors of CPO are reduced by 20%, where ZTD ties contribute 7–8% and gradient ties contribute 16%.
- The WSTD values of the EOP differences compared to the IERS EOP 14 C04 product are reduced in most of the campaigns. The average numbers over all the campaigns are listed as follows.
    - The PM offsets WSTD values are improved by 18% on the x-pole and 12% on the y-pole component, and the corresponding improvements on rates are 13% and 14%.
    - The improvement of UT1-UTC is 2%, and that of LOD is 10%.
    - The CPO WSTD values are improved by 13% on dX and 4% on dY component.
- The DBD valuues of x-pole, y-pole, and UT1-UTC are improved by 5%, 10%, and 17%, respectively.
- In CONT17, the EOP agreement between the two networks is improved on the dUT1 and LOD (18–19%), and CPO (dX: 7%, dY: 30%) components, while deteriorated on the y-pole component by –26%.
- Comparing with homogeneously reprocessed GNSS solution, the improvement introduced by tropospheric ties are consistent with the analysis of the comparision to the IERS EOP product.

6 Integrated GNSS and VLBI solution

In this chapter the analysis of integrated GNSS POD and VLBI solutions is presented. The data processing strategy is first introduced, where the handling of local ties, tropospheric ties, and global ties (EOP) is explained. The impact of applying global ties, local ties, tropospheric ties is investigated one by one in terms of the precision of ground station coordinates, network scale, AGN coordinates, and EOP estimates.

6.1 Data processing

The data processing strategy in this chapter is similar to that in the single-technique solutions, as shown in Table 4.2. For VLBI, the daily single-session observations are processed in CONT05–CONT17, while for GNSS, the daily POD is performed during the same periods. The global ties, local ties, and tropospheric ties are handled using different ways in different solutions, which is briefly summarized in Table 6.1. Note that the coordinates VLBI radio sources are estimated as daily constant parameters, constrained by the NNR conditions to the a priori CRF, that is, ICRF3 in this study. The details of these solutions are shown below.

- For the single-technique solution ("NONE" in the table), there are no common parameters between GNSS and VLBI, and no ties are applied. GNSS and VLBI use their own datum constraints.

- For solution "PM", GNSS and VLBI share the same PM set; while for the solution of "ERP", the additional LOD tie is shared. The reason to have two solutions handling the PM and LOD separately is that the GNSS LOD estimate is usually biased over long-term signals (see Figure 2.6 and Figure 4.8). Note that for the large LOD biases of GNSS previously shown in Figure 4.8, the LOD tie is applied in the following way: $LOD_{GNSS} = LOD_{VLBI} + \Delta LOD$, where ΔLOD is the campaign-average LOD bias of GNSS using the IERS EOP 14 C04 product as reference.

- Besides the common ERP set, the LTs and tropospheric ties are applied separately in the solution of "ERP+LT" and "ERP+AT", where AT is short for the atmospheric tie, that is, tropospheric tie in this scenario. The tropospheric ties are derived from NWM, as mentioned in Section 3.6.7. At each co-location one constant tropospheric tie bias is set up for ZTD, north gradient, and east gradient, and the bias is constrained to the a priori value (zero in this chapter) with the weight automatically adjusted according to the normalized residual. The LTs from IERS local survey SINEX files are used, where the nominal accuracy of these LTs are used as the a priori constraint. Nevertheless, the LT constraints are always adjusted automatically, based on the normalized residuals.

- In the last integrated solution "ERP+LT+AT", the global ties, LTs, and tropospheric ties are applied.

Table 6.1 Integrated processing solutions of VLBI and GNSS. For all the solutions the GNSS and VLBI observations are processed simultaneously in the common least-squares estimator.

Solution	EOP	Local tie	Trop. tie	Datum
NONE	One set for GNSS	No	No	GNSS: NNR+NNT
	One set for VLBI			VLBI: NNR+NNT
PM	Same PM set	No	No	Same as above
ERP	Same ERP set	No	No	Same as above
ERP+LT	Same ERP set	Applied	No	GNSS: NNR+NNT
ERP+AT	Same ERP set	No	Applied	GNSS: NNR+NNT
				VLBI: NNR+NNT
ERP+LT+AT	Same ERP set	Applied	Applied	GNSS: NNR+NNT

Note that in the solution with LTs applied, the datum of VLBI is realized by the GNSS network and transfered via LTs, and thus no additional datum constraints for the VLBI network are applied. Therefore, the corresponding VLBI solution might not as good as the one without LTs where the datum constraints of the VLBI network are also applied. However, it is no longer a minimum constrained solution to apply the datum conditions on the two networks in addition to the LTs at the same time. The reason to define the datum via the GNSS network instead of the VLBI network is that the GNSS stations have a much better global distribution (see Figure 4.1).

6.2 Ground station coordinates, network scale, and baseline length

6.2.1 Coordinate repeatability

The campaign-wise average coordinate weighted repeatability of VLBI stations are shown in Figure 6.1. As for GNSS stations, there are no significant differences between the singl-technique and the integrated solutions due to (1) the statistics of more than 200 stations do not change as only around 20 co-located GNSS stations are affected by the LTs and ATs, and (2) the GNSS stations usually have a much stronger observation geometry with more observatiosn than VLBI, meaning that the GNSS estimates can hardly be affected by the VLBI, which has already been demonstrated in Figure 5.6. The average repeatability for GNSS stations over CONT05–CONT17 is 1.4 mm, 1.6 mm, and 4.2 mm on the North, East, and Up components, respectively.

For the horizontal coordinates of VLBI stations, applying PM ties reduces the repeatability by 0.2 mm on both the north and the east components. The reason is that with more precise PM

estimates provided by GNSS, the VLBI network is stabilized and the between-day rotation effect is allieviated, which leads the reduced horizontal repeatability. The additional LOD tie does not make any significant difference (less than 0.01 mm). In addition to the ERP ties, the tropospheric ties (solution "ERP+AT") further reduce the horizontal repeatability, by 0.1 mm and 0.3 mm on the north and east components, respectively. This can be attributed to the more precise tropospheric gradients from GNSS observations. The solutions with LTs applied, however, do not always have optimal repeatability. The solution with LTs (solution "ERP+LT") usually has smaller north repeatability in CONT05–CONT14 campaigns but larger ones in CONT17. The last solution with all the ties applied (solution "ERP+LT+AT") shows the best repeatability of all solutions in the north component, but not in the east component.

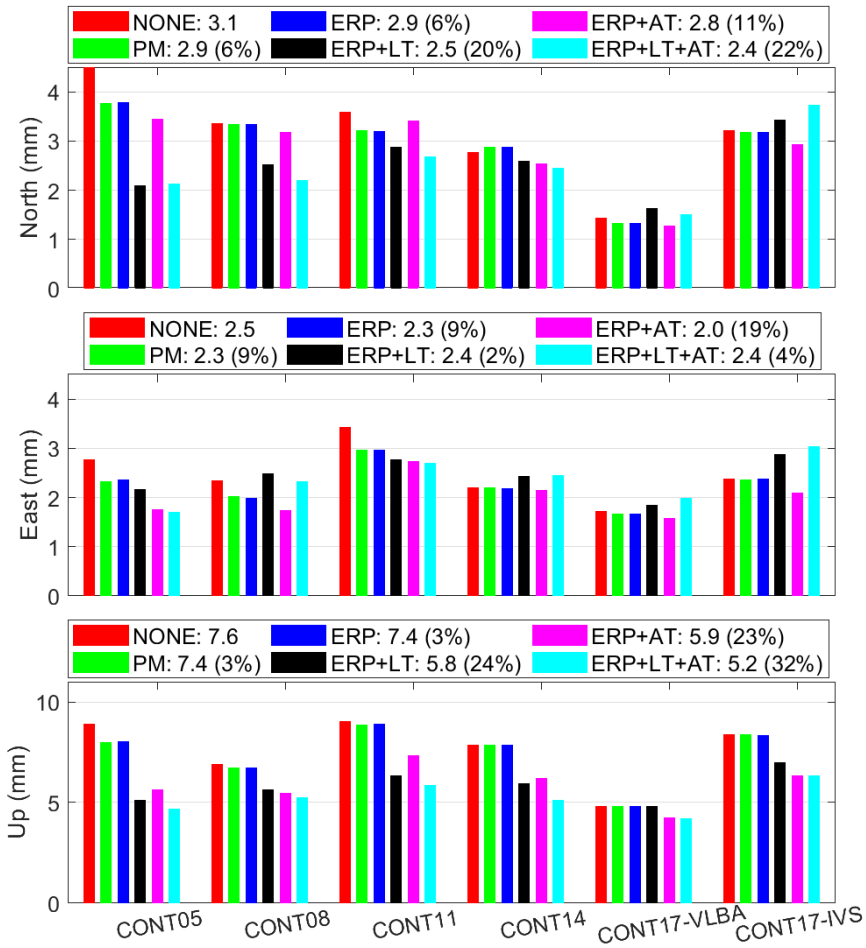

Figure 6.1 VLBI station coordinate repeatability during CONT05–CONT17 with different tie configurations applied. The average value of each solution over CONT05–CONT17 is presented in the legend, and the improvement of solutions with ties applied compared to the solution without ties is also given in the bracket. Note the different vertical axis scales.

The larger repeatability on the east component in the solutions with LTs applied is caused by the loose constraints of the VLBI network, as only the local ties are applied and the VLBI is connected by them. These local ties, however, are not accurate enough to provide an improved solution. This is more severe for the CONT17-IVS network, as the LT discrepancy (12 mm)

is much larger than that during other campaigns (6 to 7 mm), as shown in Figure 3.12. Moreover, the NNR and NNT conditions are applied to the GNSS datum network which has a global distribution, whereas the VLBI network datum is realized by the less than 20 co-located station, linked to a subset of the GNSS datum network. As a result, despite that the GNSS datum network satisfies the NNR conditions, its subnet of stations co-located to VLBI may most likely not satisfy the conditions, causing the VLBI network rotate to some extent, which further causes larger repeatability in the east component and degraded UT1-UTC precision potentional (see section 6.3).

For the vertical component of the VLBI stations, applying ERP ties slightly improves the repeatability (reduced from 7.6 mm to 7.40 mm, 3% improvement). The reason is that the vertical coordinate is much lesser correlated with the ERP. Applying tropospheric ties or LTs reduces the vertical repeatability to 5.9 mm (23% improvement) and 5.8 mm (24% improvement), respectively. The last solution of "ERP+LT+AT" shows the best repeatability of 5.2 mm, that is, an improvement of 32%. Note that for the vertical components, all the campaigns show improved repeatability in the integrated solutions than in the single-technique solution, that is, solution "NONE" with no ties applied.

6.2.2 Network scale

The network scale estimates are further shown in Figure 6.2, where the daily scales in CONT14 are presented in the top panels, and the scale weighted repeatability of each campaign is shown in the bottom panels. The network scale performances of different solutions are consistent with the vertical station coordinate repeatability in Figure 6.1. Applying the tropospheric ties introduces an improvement of 15% (reduced from 0.51 ppb to 0.44 ppb), and applying the LTs introduces an improvement of 34% (reduced from 0.51 ppb to 0.34 ppb). The last solution ("ERP+AT+LT") has the best repeatability with the average value of 0.33 ppb over all the CONT campaigns.

As for the GNSS network scale, the repeatability is much better than that of VLBI, and the impact of various ties is insignificant. The repeatability during all the campaigns is less than 0.1 ppb, with an average value of 0.08 ppb. Note that here the GNSS network scale is not an absolute scale, but rather a relative. As generally known, the GNSS technique cannot determine the absolute scale of TRF due to the high-correlation between satellite antenna PCO-Z and the station height, and the precise satellite antenna PCO values are not available from the manufactor, but calibrated based on the TRF scale, which is determined from other techniques including VLBI and SLR. However, the GNSS technique is capable of monitoring the scale time-evolution, that is, the relative scale with respect to a reference value. Therefore, here the GNSS scale is based on the ITRF2014 scale, as the satellite antenna PCO product derived from ITRF2014 is used.

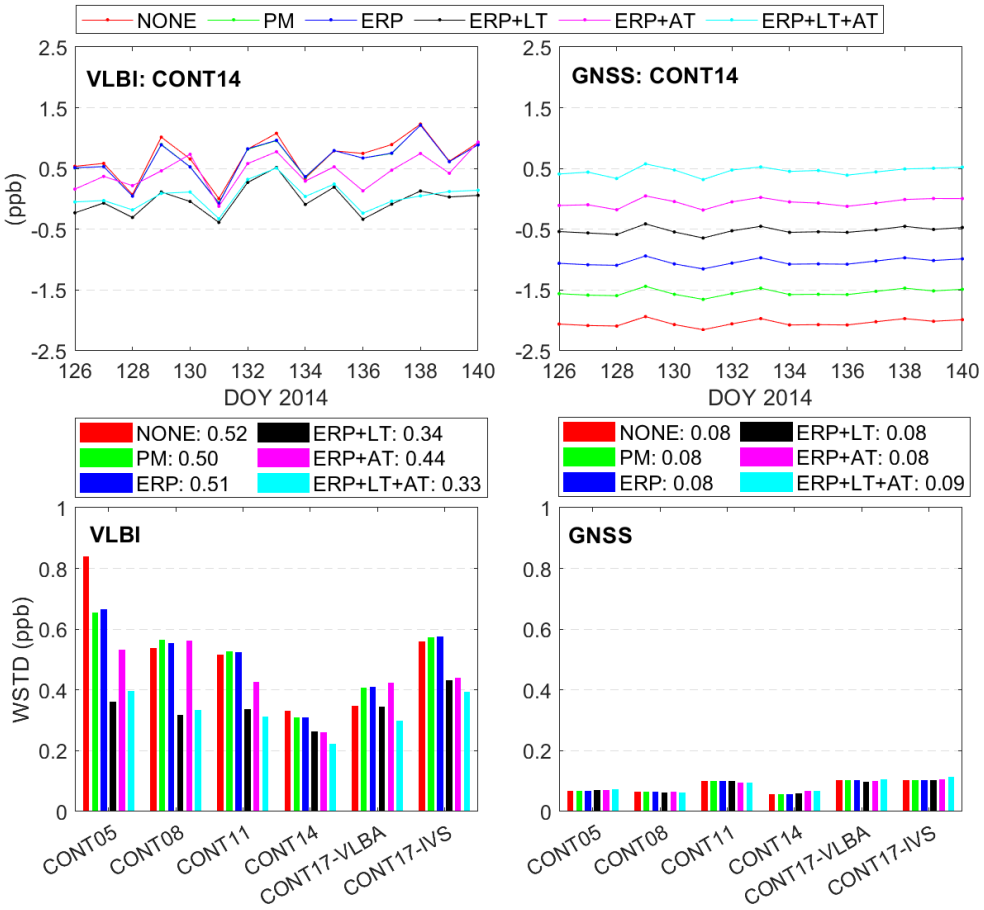

Figure 6.2 Daily estimates of network scale for VLBI (left) and GNSS (right) in CONT14 (top panels), and the weighted repeatability values of each campaign (bottom panels) with the average values given in the legend. The GNSS daily scale in CONT14 is offset by multiples of 0.5 ppb for clarity, and the scale has no bias with respect to the a priori value.

Further inspecting the daily estimates of network scale in CONT14, which are shown in the upper panels of Figure 6.2, the conclusions are consistent with the repeatability statistic. The GNSS daily scale is obviously stable and there are no visible differences between different solutions. As for VLBI, despite the fluctuation differences between different solutions, it is clear that the solutions with LTs applied show large systematic differences compared to the solutions without LTs. For the latter cases, the VLBI scale estimates present systematic biases with respect to the a priori TRF, that is, the ITRF2014. This is caused by the already-known scale discrepancy between SLR and VLBI in the ITRF2014, which results in the different scales between VLBI (positive systematic bias with respect to ITRF2014), SLR (negative systematic bias with respect to ITRF2014), and GNSS (consistent with ITRF2014 as the GNSS antenna PCO is re-aligned to it) (Altamimi et al., 2016). As a result, the GNSS scale estimates in CONT14 (left upper panel) agree very well with the a priori TRF, that is, ITRF2014, whereas the VLBI scale estimates show an obvious positive systematic bias. After applying the LTs, the VLBI scale systematic bias is significantly reduced to be consistent with ITRF2014 due to the strong constraints from GNSS and LTs. Nevertheless, this VLBI scale is not independent

anymore, but it can be fixed by estimating the GNSS antenna PCO in the integrated solution, in which case the GNSS PCO values will be aligned to the VLBI TRF scale.

6.2.3 VLBI baseline length repeatability

The weighted repeatability of the VLBI baseline lengths is presented in Figure 6.3, where the different solutions are presented in dots of different colors, and the fitted functions are also given. The improvement from global ties (PM and LOD) is rather insignificant, as the average WBLR is reduced by only 0.2 mm. This further supports the analyses of the VLBI station coordinate repeatability shown in Figure 6.1, that is, the global ties improves the VLBI solution by introducing more precise polar motion estimates thanks to the GNSS technique, and thus the VLBI horizontal coordinate repeatability is improved as the the between-day rotation of the VLBI network is reduced. The baseline length, however, is not associated with the network rotation effect and can hardly get influenced from that, resulting in the slight change shown in Figure 6.1.

The impact of LTs and tropospheric ties is obvious, and the solutions "ERP+LT" and "ERP+AT" are both much better than those without them. The average improvement with additional LTs and ATs are 2.3 mm and 1.6 mm, respectively. Unlike the statistic of station coordinate repeatability where the solutions with LTs shown comparable improvement with those with ATs on the vertical component, but have deteriorated impact on the east component due to the datum issue, the statistic of WBLR does not follow this. The larger improvement introduced by LTs than by ATs once again confirms that the relatively worse coordinate repeatability of the east component is attributed to the datum issue, and as a direct constraint on the station coordinate, LT works more effectly in improving the baseline length repeatability than tropospheric tie (AT), as the latter contributes indirectly, through the correlation between tropospheric parameters and station coordinates.

For the solution "ERP+LT+AT" with global, local, and tropospheric ties simultaneously applied, the WBLR is much better than other solutions, and the average improvement over all baselines is 2.9 mm. Moreover, it is worth mentioning that the longer baselines improve more than the shorter ones, which is also illsurated in fitted coefficient B of the fitted function $WBLR = \sqrt{A^2 + B^2 \cdot L^2}$ as it keeps getting reduced. The coefficient A varies between different solutions and might get rather large, that is, 1.16 in the solution without ties ("NONE") compared to 1.94 in the solution with all ties ("ERP+LT+AT"). This variation comes from the numerical issue of the fitting function, as A only presents the baseline with the length of zero. Nevertheless, by inspecting the figure carefully, the short baselines do not deteriorate after applying the various ties.

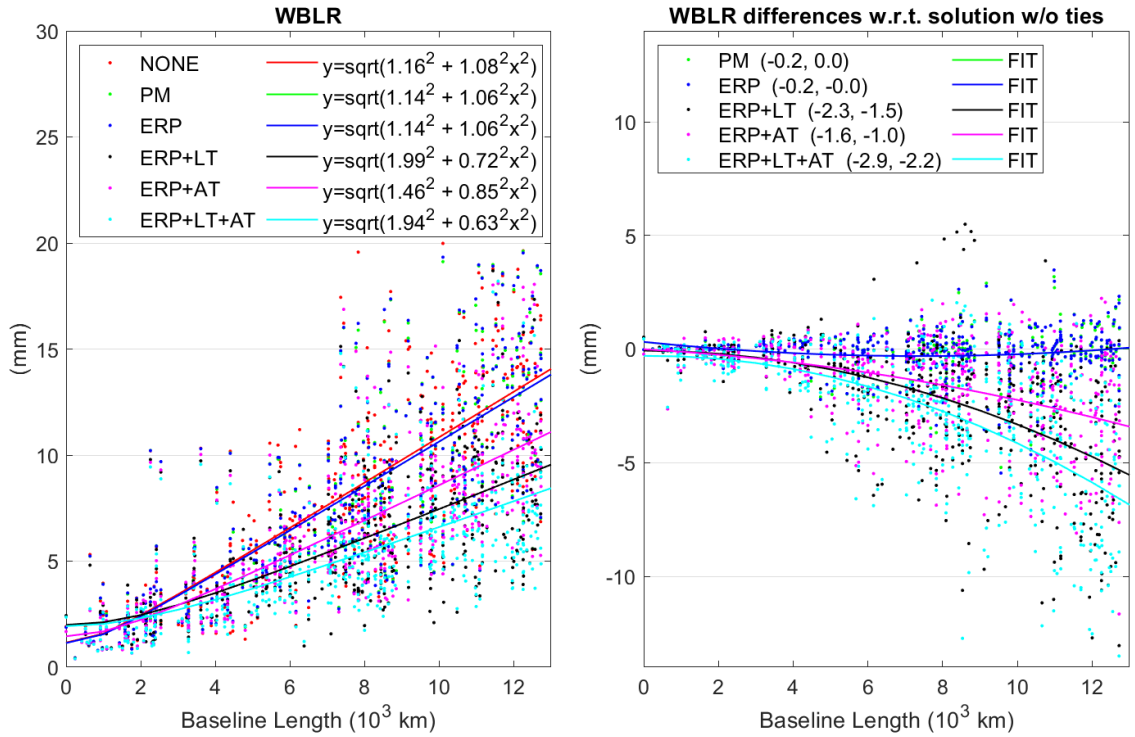

Figure 6.3 Left: VLBI weighted baseline length repeatability (WBLR) values of different solutions in CONT05–CONT17 (given in the dots), and the fitted functions (given in the solid lines). Right: VLBI WBLR improvement of solutions with ties applied compared to the solution without ties in dots, and the polynomial fitting lines; the negative value means that the solutions are improved.

6.3 EOP estimates from integrated processing

6.3.1 EOP formal error

The average formal errors of the EOP components over CONT05–CONT17 are shown in Figure 6.4. For both the offsets and rates of PM, the formal errors of the integrated solutions are dominated by the GNSS technique, which is much better than those of the VLBI technique. This can be obviously attributed to the global distribution of more than 200 GNSS stations compared to fewer than 20 VLBI stations concentrated in the Northern Hemisphere. In the integrated solutions, the PM formal errors are around 8 μas for the offsets, while the values are around 23 μas/day for x-pole rate and 31 μas/day for y-pole rate. Applying additional tropospheric ties and local ties does not have a visible impact on the PM formal errors.

For UT1-UTC, the formal error is reduced slightly by PM ties from 3.2 μs to 3.0 μs, and further reduced to 2.6 μs by tropospheric ties. The solution with LTs shows relatively larger uncertainty (3.5 μs), due to the above mentioned issue of LTs constraints and VLBI datum constraints. The LOD uncertainties in integrated solutions are dominated by the GNSS technique, and the

contribution from additional local ties or tropospheric ties is insignificant. As for the celestial pole offsets, the formal errors are reduced by PM ties, and the LTs and tropospheric ties both improve the formal errors, especially the latter one with the improvement of 10% to 15%.

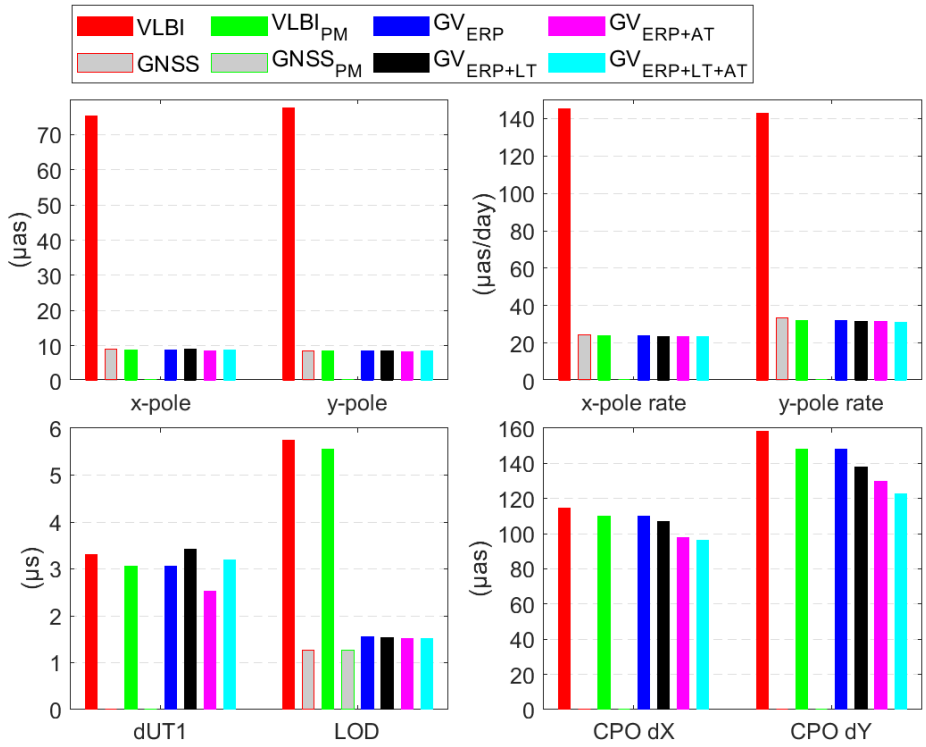

Figure 6.4 Average values of the EOP formal errors over CONT05–CONT17. The "VLBI" and "GNSS" columns show the VLBI and GNSS estimates in the solution "NONE" with no ties applied, and the "$VLBI_{PM}$" and "$GNSS_{PM}$" solutions show the VLBI and GNSS estimates in the integrated solution "PM", with only PM ties applied. For the solution "GV_{SOLU}", it refers to the integrated solution where "SOLU" refers to the ties applied. More details are illustrated in Table 6.1. The following EOP analyses also follow this naming convention.

6.3.2 EOP WSTD

The EOP precision in terms of the WSTD values is presented in Figure 6.5, where the average values over CONT05–CONT17 are given. The performances of of different solutions agrees well with the analyses of the formal errors. The PM offsets and rates in the integrated solutions are dominated by the huge amount of GNSS observations, and are much better than the VLBI estimates. The UT1-UTC is slightly improved by PM ties and tropospheric ties, but degraded by when local ties are applied. The LOD WSTD values are rather comparable in the several integrated solutions. As for the celestial pole offsets, slight improvements can be observed for the dX component when the PM ties are applied, and a relatively larger improvement is introduced by the LTs. The dY component is not improved by either PM ties or LTs, but with the tropospheric ties the improvement is significant, that is, around 10%.

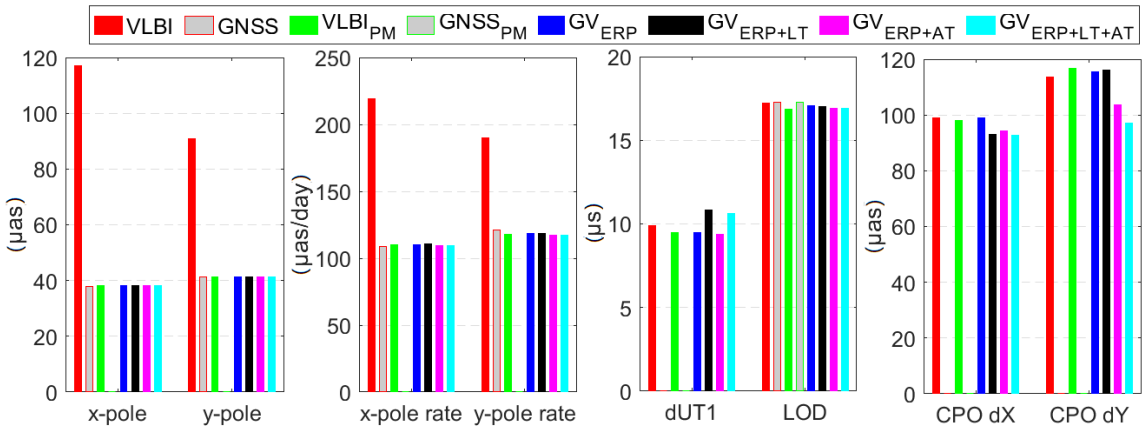

Figure 6.5 WSTD values of the EOP estimates compared to the IERS EOP 14 C04 product. The average values over CONT05–CONT17 are presented.

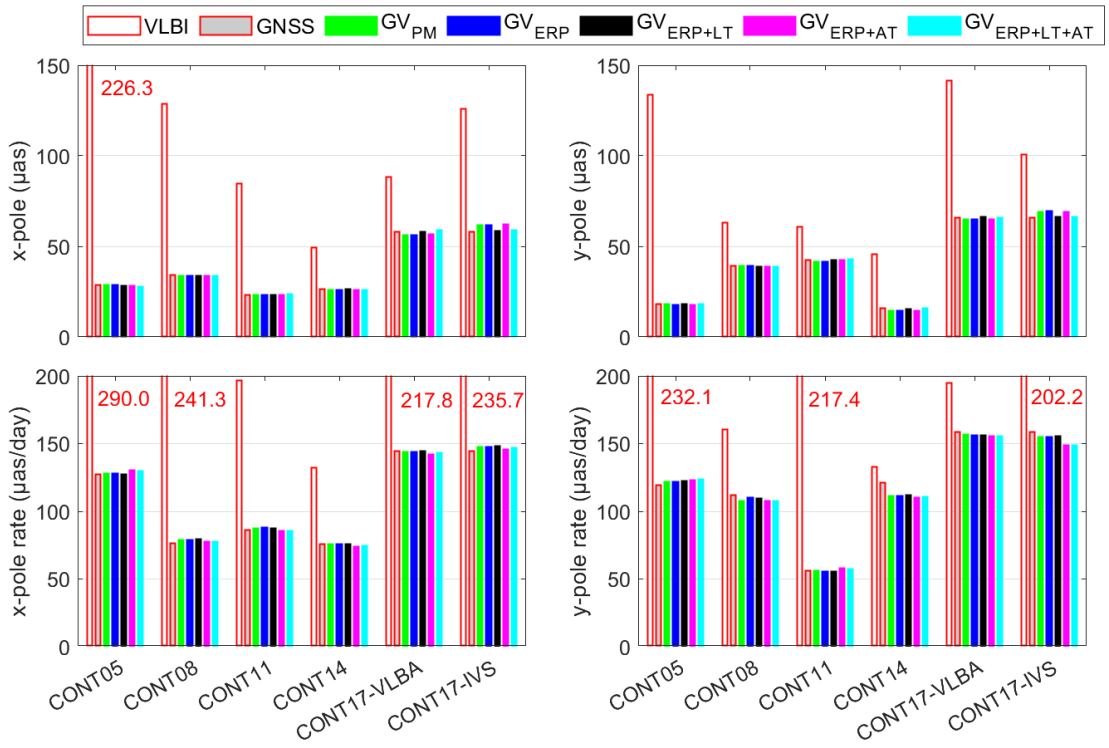

Figure 6.6 WSTD values of the PM estimates compared to the IERS EOP 14 C04 product in CONT05–CONT17. The values excessing the panels are given in the text.

The WSTD value of PM estimates in each campaign is shown in Figure 6.6. The performance of different solutions in different sessions agrees well with that of the average statistic shown in Figure 6.5. It is quite clear that the PM offset and rate estimates in the integrated solutions are usually dominated by the GNSS observations, as discussed before, and are much better than the VLBI estimates. On the other hand, it is worth metioning that a slight improvement can also be observed after applying the various ties in several campaigns, such as the x-pole offset in CONT17-IVS (reduced from 62 µas in solution "ERP" to 58 µas in solution

"ERP+LT"), the y-pole rate in CONT14 (reduced from 120 μas in GNSS-only solution to 111 μas in solution "PM") and CONT17-IVS (reduced from 159 μas in the GNSS-only solution to 155 μas in solution "PM", and further to 149 μas in solution "ERP+AT").

The WSTD values of UT1-UTC, LOD, and CPO estimates in each campaign are also shown in Figure 6.7.

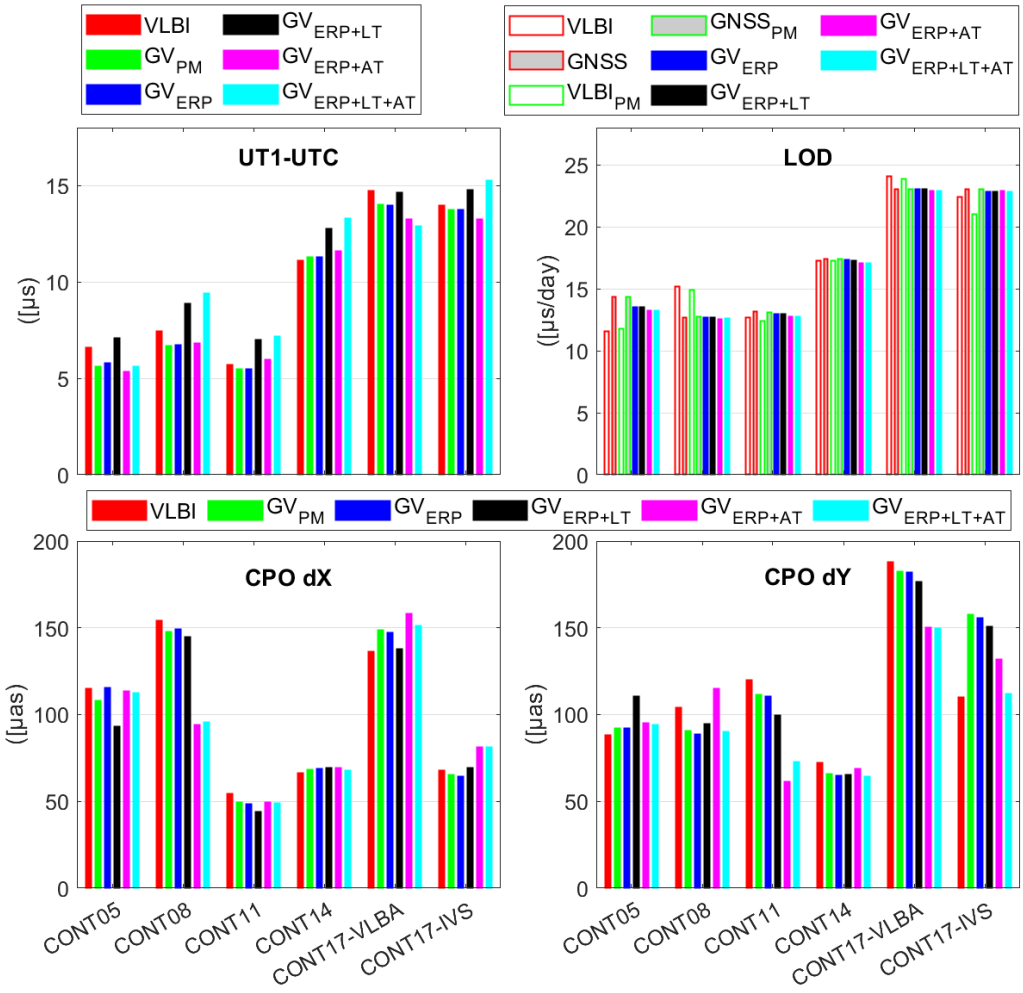

Figure 6.7 WSTD values of the UT1-UTC, LOD, and CPO components compared to the IERS EOP 14 C04 product in CONT05–CONT17.

For UT1-UTC, the precision is usually improved by PM ties (that is, the "GV_{PM}" column compared to the "VLBI" column) due to the stabilized VLBI network introduced by the more precise PM estimates from GNSS. The solutions with LTs ("GV_{ERP+LT}" and "$GV_{ERP+LT+AT}$") are usually deteriorated due to the issue of VLBI network datum and LTs, as discussed in Section 6.3.1. The impact of tropospheric ties (the solution "GV_{ERP+AT}") varies in different campaigns, including a positive effect in CONT05 and CONT17 but a negative one in CONT11 and CONT14. Despite the various performances of different solutions in different campaigns, the UT1-UTC precision are rather comparable in the integrated solutions, as presented in Figure 6.5, except for the issue with LTs mentioned above. As for LOD, the GNSS estimates have poorer agreement with the IERS EOP 14 C04 product than the VLBI estimates

in CON05 but better one in CONT08, and the integrated solutions are usually dominated by the GNSS observations. The overall conclusion is, however, the LOD agreement to the IERS EOP product can hardly be influenced by the different ties.

As for the two CPO components, the precision is usually improved by the PM ties, such as the dX component in CONT05–CONT11 and the dY component in CONT08–CONT14 and CONT17-IVS. The LTs also improves the CPO precision, except for the dY component in CONT05, which show a visible larger WSTD value after applying the LTs. Applying tropospheric ties significantly improves the dX components in CONT08, the dY component in CONT11 and CONT17; whereas the impact is negative for the dX component in CONT05 and CONT17-VLBA, and the dY component in CONT08.

Despite the general positive (at least non-negative) impact of tropospheric ties on the EOP precision when averaging all campaigns, the deteriorated EOP precision caused by tropospheric ties in several CONT campaigns can be explained by (1) in this chapter the a priori tropospheric tie bias related to the instrument is not applied, and (2) the agreement of tropospheric parameters are usually around 3 to 5 mm in terms of ZTD (see Section 4.6 for detailed information), which might cause problems in the integrated solution as GNSS and VLBI might observe in totally different directions.

6.3.3 EOP day-boundary-discontinuity

A further investigation of the internal precision of polar motion and UT1-UTC using the DBD is shown in Figure 6.8, where the WRMS values of DBD in each campaign are presented.

For x-pole, the DBD WRMS values in integrated solutions are comparable with those of the GNSS-only solution (102 μas on average), which are all much smaller than the VLBI-only solution (241 μas on average). The integrated solutions are significantly better than the VLBI-only solution in all the campaigns except for the CONT14, due to the large x-pole rate bias of the GNSS solution (see Figure 4.8).

For y-pole, GNSS and VLBI have different performances in different campaigns. The y-pole DBD of VLBI is smaller than that of GNSS in CONT05, CONT08, and CONT14, but larger in CONT11 and CONT17-VLBA. The average DBD WRMS values over all the campaigns are 200 μas and 195 μas for VLBI and GNSS single-technique solutions, respectively. The values in the integrated solutions, on the other hand, are reduced to around 180 μas (that is, 10% improvement) when PM ties are applied, and further reduced to 173 μas (around 14% improvement) with the tropospheric ties applied. Applying local ties has no impact in terms of the PM DBD statistics.

As for UT1-UTC, on average the DBD is improved by 8% when the PM ties are applied, that is, reduced from 11.0 to 10.1 μs, and larger improvement is observed in CONT05 (18% improvement) and CONT17-IVS (21% improvement). Further applying the LOD ties increases the improvement to 15%, and with additional tropospheric ties the improvement is

around 22%. Applying LTs have a negative impact on the DBD statistics, as the average value is increased from 9.3 to 10.0 µs. For the last solution with global, local, and tropospheric ties together, the UT1-UTC DBD (9.7 µs) is still better than that of the VLBI solution (10.0 µs), but worse than the solution with only global and tropospheric ties (8.6 µs).

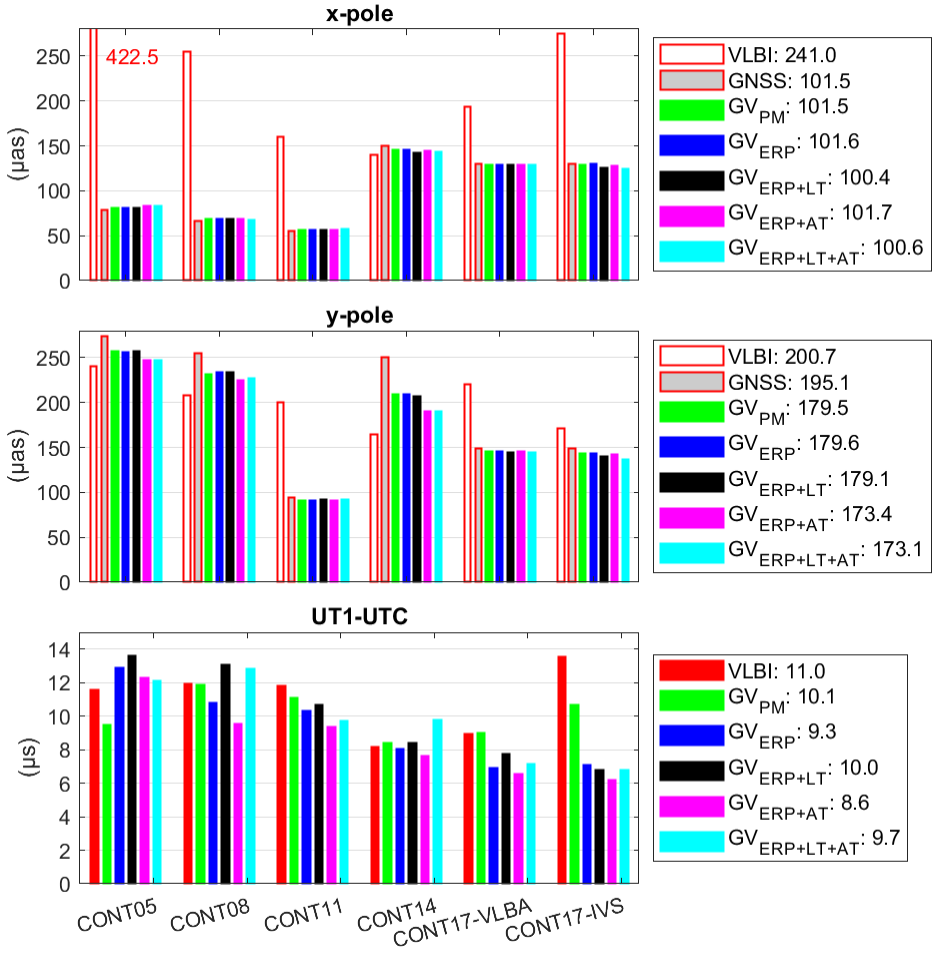

Figure 6.8 WRMS values of the day-boundary-discontinuities for polar motion and UT1-UTC in CONT05–CONT17. For UT1-UTC, the VLBI estimates are used in the solution GV_{PM}. The average values over CONT05–CONT17 are presented in the legend.

6.3.4 EOP WMEAN

The WSTD values investigated in Section 6.3.2 indicate the agreement to the IERS EOP 14 C04 product, where the systematic differences are ignored. Therefore, the WMEAN values of the EOP differences are shown in Figure 6.9 and Figure 6.10, which can help further identifying the systematic biases and explaining the DBD statistics.

Generally speaking, the PM WMEAN values in integrated solutions agree well with the values of the GNSS solution, demonstrating again that the integrated solution is dominated by the huge amount of GNSS observations (to repeat, more than 200 stations compared to the less

than 20 VLBI stations). The values of the GNSS solution are significantly smaller than those of the VLBI solution in terms of the offsets, thanks to the homogeneously distributed GNSS stations. For the PM rates, however, the estimates of GNSS are not as good as those of VLBI. The x-pole rate of GNSS is much larger than that of VLBI in CONT14 and CONT17-VLBA, but smaller in CONT05–CONT11 and CONT17-IVS. It is clear that GNSS provides poor y-pole rate estimates in most of the CONT campaigns except for CONT11, as the systematic bias varies between 100 μas/day and 250 μas/day. It is also demonstrated that the GNSS and VLBI estimates usually show the opposite sign in terms of the y-pole rate in most campaigns. Nevertheless, the systematic polar motion rate bias is nothing new (see Figure 4.8 for other IGS ACs) and might be attributed to the dynamic modeling of the GNSS satellite orbit, which needs further optimization.

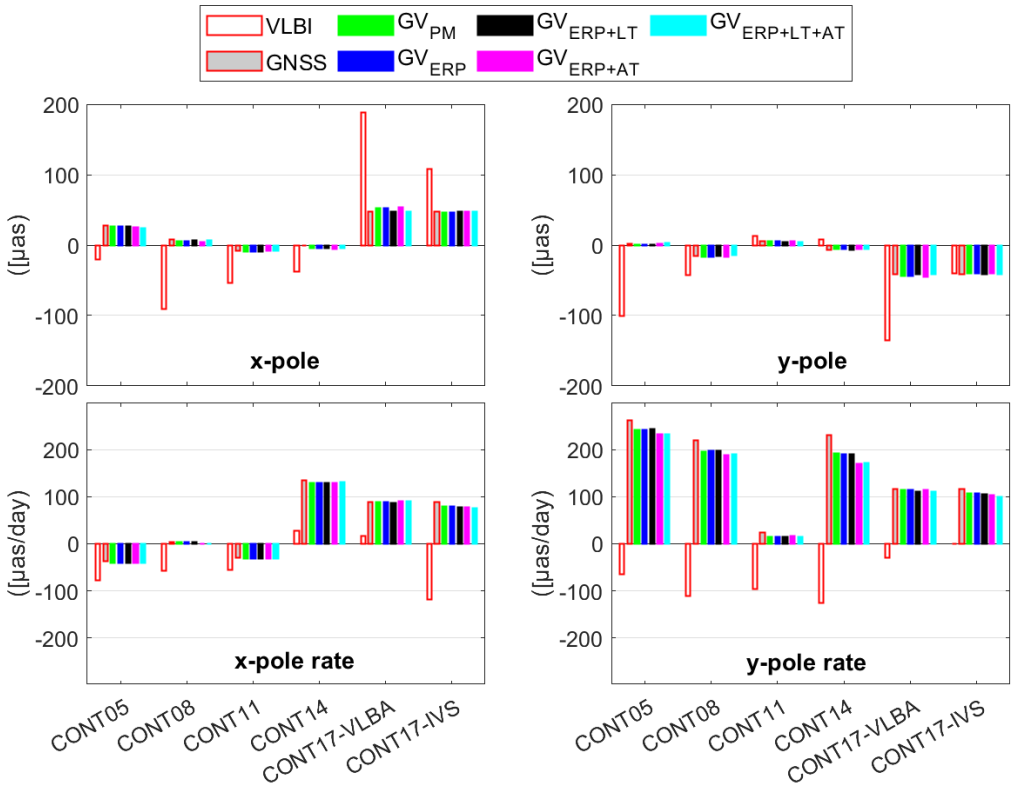

Figure 6.9 WMEAN values of polar motion offset and rate estimates compared to the IERS EOP 14 C04 product in CONT05–CONT17.

For the WMEAN values of UT1-UTC and LOD shown in Figure 6.10, it is clear that for UT1-UTC, (1) PM ties have insignificant impact on the systematic bias; (2) LTs can introduce visible systematic bias ; and (3) tropospheric ties have relatively small impact. As for LOD, the GNSS estimates show large bias, whereas the WMEAN values of the VLBI estimates are usually within 5 μs/day. In the integrated solutions the LOD WMEAN values are close to zero due to the strong constraints, as explained in Section 6.1.

The celestial pole offsets in the integrated solutions are noticeably impacted by the various ties in terms of WMEAN values. The PM ties can introduce large bias up to 50 to 100 μas, such as the dX component in CONT05 and CONT08, and the dY component in CONT17-VLBA.

Applying LTs can have similar large impact, such as CONT05 (both components), CONT08 (the dY component), and CONT17-VLBA (the dY component). As for the tropospheric ties, the systematic effects are relatively small.

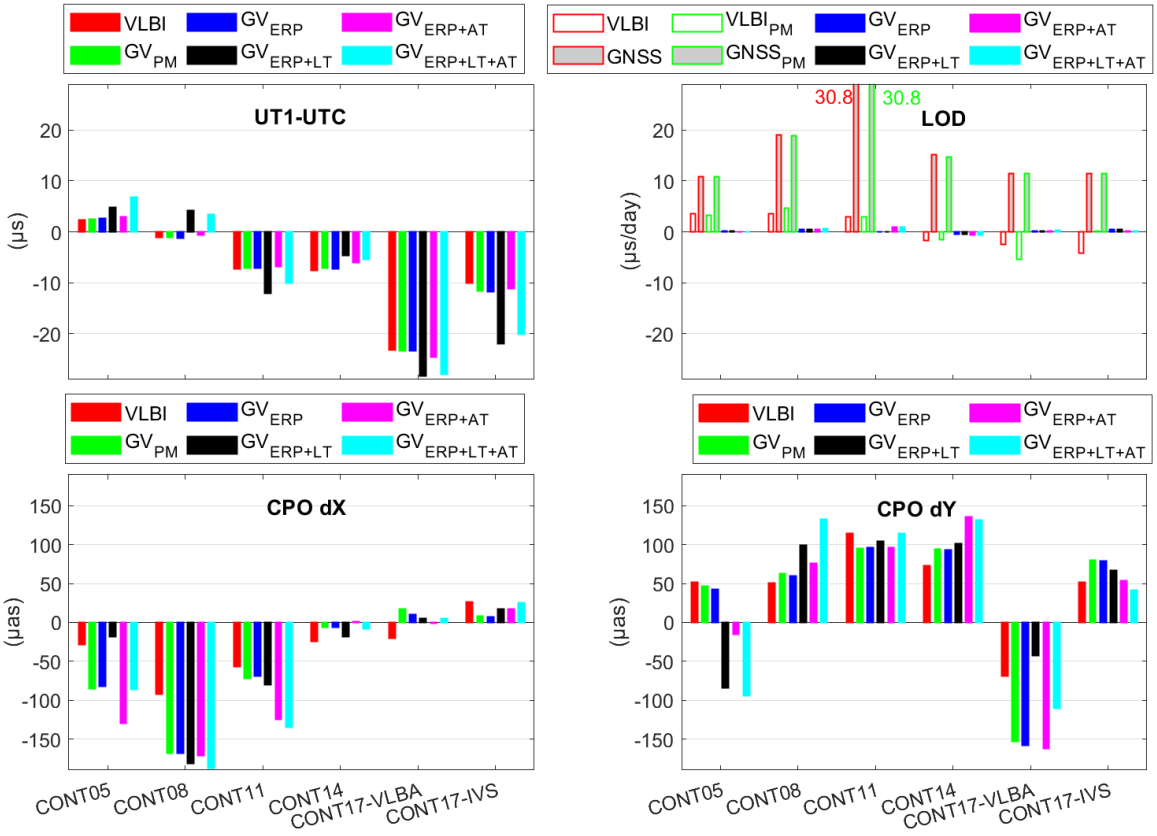

Figure 6.10 WMEAN values of the UT1-UTC, LOD, and CPO estimates compared to IERS EOP 14 C04 in CONT05–CONT17.

6.4 CRF precision

The precision of the VLBI AGN coordinates is investigated in this section, using both the weighted repeatability and the formal errors.

First, the weighted repeatability of the right ascension $\alpha \cos\delta$ and declination δ in each campaign is given in Figure 6.11. For the right ascension, there are no significant differences between the different solutions in all the campaigns, and on average the differnces are within 2%. As for the declination, however, the impact of the ties are rather noticeable. The PM ties introduces large improvement of the declination in CONT05 (around 30%), but not in other campaigns. Applying LTs usually introduce visible improvement in all campaigns, and on average the declination repeatability is enhanced by 12% (from 18.7 μas to 16.5 μas). The impact of tropospheric ties, however, varies between different campaings, as the CONT11 campaign is improved by around 17% but the CONT17-VLBA campaign is deteriorated by around 15%. The reason is that (1) the a priori value of the tropospheric tie bias is zero, and

(2) the tropospheric parameter agreement between GNSS and VLBI in terms of standard deviations are not optimal due to the potential different sky coverage. Nevertheless, the last solution ("ERP+LT+AT") shows an improvement of 14% compared to the VLBI-only solution.

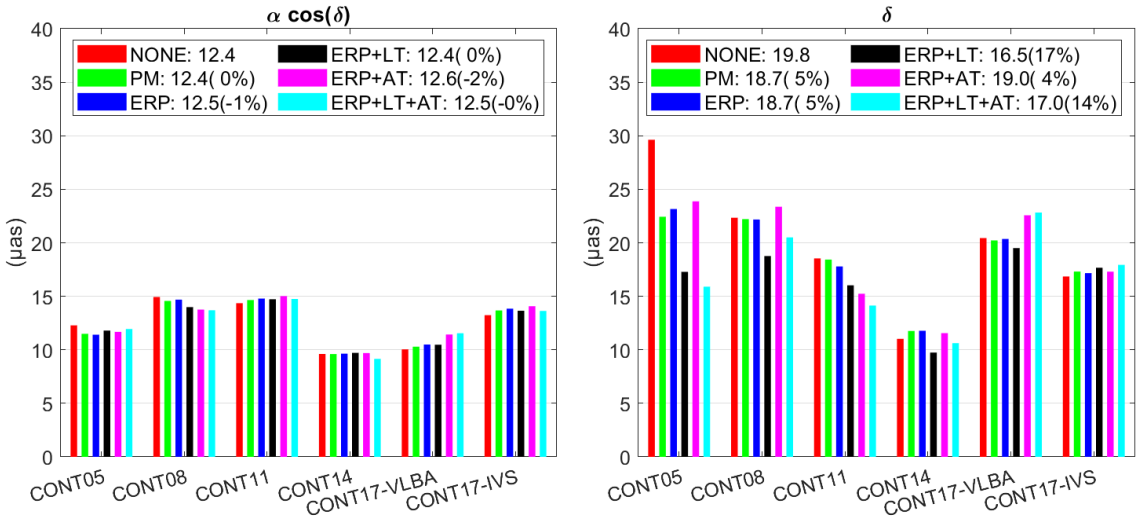

Figure 6.11 Weighted repeatability of AGN coordinates in CONT05–CONT17. The average values over CONT05–CONT17 are given in the legend.

Second, the formal errors of the AGN coordinates are investigated, and the improvement of the integrated solutions with different ties applied compared to the solution with not ties applied (solution "NONE") are given in Figure 6.12.

For the right ascension, the improvement varies up to 10 μas, mainly due to the tropospheric ties, which introduce 10% improvement on average (solution "ERP+AT" compared to solution "ERP"). Moreover, the linear fitting also shows that the southern AGN get more improvements than the northern ones, as the southern ones are less observed due to the relatively less VLBI radio telescopes in the Sourthern Hemisphere. On the other hand, both global and local ties have insignificant impact on the formal error of right ascension.

The declination of the AGN shows larger improvement than the right ascension thanks to the ties. The average improvement from global ties is 4%, and the from additional LTs and tropospheric ties is 13% and 16%, respectively. In total all the ties together bring an improvement of 21%, which is quite significant. Once again, it is the southern AGN that improve more, especially from the LTs and tropospheric ties. The maximum improvement up to 40 μas is observed for the AGN between 0° and –40°.

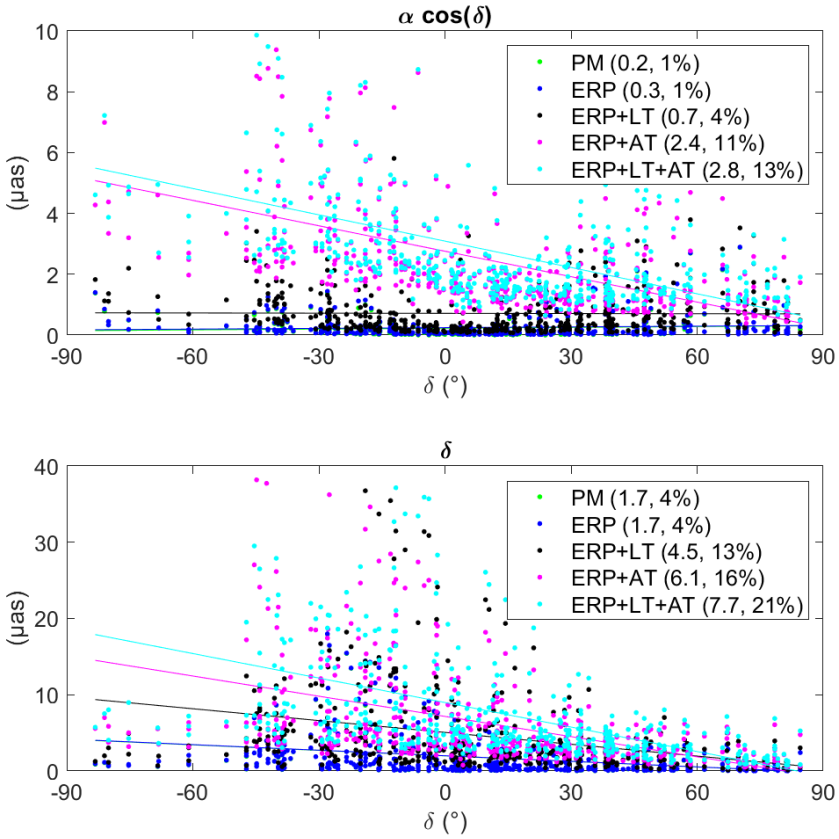

Figure 6.12 Improvement of the AGN coordinate formal errors of the solutions with different ties applied compared to the solution without ties applied (solution "NONE"), as a function of the declination. All the AGN in CONT05–CONT17 are depicted, and the average value of each solution is presented in the legend, together with the relative improvement in percentage. The linear fit results of the improvement as a function of the declination are also presented. Note the different vertical axis scales.

6.5 Chapter Summary

This chapter presents the consistent determination of TRF, CRF, and EOP from the GNSS and VLBI integrated processing on the observations.

Section 6.1 describes the data processing strategy, with several issues addressed.

- Different ties are applied one by one, to demonstrate the impacts separately.
    - All the ties are applied as pseudo-observations.
    - The PM ties are applied tightly. The GNSS LOD bias in each campaign is first derived as constant and then applied in the daily solutions.

  - The tropospheric ties from NWM are applied to all the GNSS–VLBI co-locations, and the weights are adjusted automatically according to the normalized residuals.
  - The LT vectors and formal errors from local surveys are applied, and the constraints are adjusted according to the normalized residuals.

- For solutions without LTs applied, both GNSS and VLBI apply the minimal constraints (NNR+NNT); for solutions with LTs applied, the network datum is defined by the GNSS minimal constraints.

Section 6.2 gives the station coordinate repeatability in the integrated solution. In principle, the GNSS stations have insignificant changes (less than 1%), while the VLBI stations are improved significantly. The specific analyses of VLBI stations are listed as follows.

- Applying global ties (mainly polar motion) improves the horizontal coordinates as the network is stabilized and the between-day rotation effect is reduced.
- Applying additional tropospheric ties improves both the horizontal and vertical coordinates significantly.
- Applying additional local ties improves the north and up components, whereas the repeatability of the east component is deteriorated due to the weak datum conditions realized through the LTs.
- The VLBI network scale is stabilized in the integrated solution, especially by the local and tropospheric ties. However, due to the strong constraints from GNSS, the VLBI scale is biased, which can be fixed by estimating the GNSS satellite antenna PCO in the futher study.
- The VLBI baseline length repeatability is mainly improved by the local and tropospheric ties, and is not affected by the datum issue in the solutions with local ties.

Section 6.3 presents the EOP precision in different integrated solutions. The ERP estimates are dominated by the GNSS technique, while the UT1-UTC and CPO components are solely determined by VLBI.

- The PM formal errors in the integrated solutions are comparable to those of the GNSS estimates, and much better than those of the VLBI estimates.
- The UT1-UTC formal errors are mainly improved by global ties (polar motion) and tropospheric ties, whereas the solutions with local ties have deteriorated UT1-UTC formal error due to the datum issue.
- The CPO formal errors are improved by global, local, and tropospheric ties.

Section 6.3 further gives the EOP precision comparing to the IERS EOP 14 C04 product, and the statistics are summarized as bellows.

- The analysis of WSTD values is consistent with that of the formal errors in general, while the performances of different campaigns vary a lot, with a few campaigns degraded by the ties.

- The DBD statistic of polar motion and UT1-UTC shows that the integrated solutions outperform the GNSS or VLBI single-technique solutions in the y-pole and UT1-UTC components, by up to 15%.

- The WMEAN statistic of the EOP estimates with respect to the IERS EOP product shows that only the local ties introduce visible systematic differences to UT1-UTC, while for the CPO both global and local ties have significant systematic impact.

Section 6.4 presents the precision of the VLBI AGN in the integrated solutions.

- For the coordinate repeatability, the different ties have insignificant impact on the right ascension, but introduce visible improvement on the declination, especially the local ties.

- For the formal error analysis, the global ties have marginal impact, while local and tropospheric ties improve 4% and 11%, respectively. On the other hand, the declination was improved by global ties (4%), local ties (9%), and tropospheric ties (12%), and in total improved by 21%. Moreover, the southern AGN are improved more than the northern ones due to the relatively less radio telescopes located in the Sourthern Hemisphere.

7 Conclusions and outlook

7.1 Conclusions and recommendations

The combination of space geodetic techniques contributes comprehensively to the core of geodesy: reference frames, and one of the three pillars: Earth rotation. With the pursue of highly accurate (1 mm) and stable (0.1 mm/year) TRF required by GGOS (Gross et al., 2009), the multi-technique combination has been developed and conducted for decades. It has been demonstrated that the combined solutions can exploit the advantages of each technique, and provide more reliable estimates of both TRF and EOP. The previous combinations, however, are mostly performed either on the parameter level or on the normal equation level. As applying the ties and ensuring the consistency are critical in the combination, these cannot be fully achieved unless the combination is conducted on the observation level, referred to as the integrated processing of multi-technique on the observation level in this thesis.

The integrated processing can only be performed in one software package, which naturally guarantees the best consistency. It also allows all the potential ties to be applied, especially the atmospheric ties and clock ties, which can hardly be handled in the NEQs and are usually pre-eliminated. Therefore, such an integrated solution enables the possibility to fully exploit the features of different techniques free of the influences from inconsistent models and conventions. It allows inter-technique outlier detection, which leads to a more robust solution, especially for the SLR and VLBI techniques. The estimates from integrated solution describe the geokinematics and explain geophysical processes more homogeneously.

Having the integrated processing of the four space geodetic techniques as the ultimate goal, the very first fundamental achievement of this thesis is the software package capable of processing multi-technique observations. Based on the Positioning And Navigation Data Analyst software with high-quality GNSS modules, the VLBI and SLR modules are implemented in a common least-squares estimator. The VLBI delay modeling strictly follows the IERS consensus model, which is consistent with most of other software packages. The VLBI module can handle the commonly used parameters, including TRF, CRF, EOP, atmospheric parameters, and clocks. As for the SLR module, the adopted one-way delay model allows a more general handling of the observations and is compatible with the GNSS processing. All the SLR tracking satellites, including GNSS, LEO, and spherical satellites can be handled. Worth mentioning that the VLBI and SLR residual editing modules are also applied in a common program with GNSS, which opens the window for further common outlier detection and optimized observation weighting. The residual editing modules can handle not only the outliers but also the VLBI clock breaks and baseline clock offsets, and the SLR time and range biases. The integrated processing of multi-technique is also realized, where all the possible ties can be applied, and the datum can be flexibly defined. Moreover, the existing modules of the software are thoroughly revised with state-of-the-art models according

to the IERS Conventions 2010 and updates, especially the station displacement and the transformation between TRS and CRS parts. The modeling of tropospheric delay is updated with different NWM inputs; the function to use GIM TEC for ionospheric delay correction is implemented; several options of the tidal and non-tidal atmospheric pressure loading displacement are now available.

The achieved high accuracy and robustness of the software are demonstrated using single-technique solutions. High-precision station coordinates of the GNSS POD solution are shown with the repeatability of 1.5 mm and 4 mm on the horizontal and vertical components, respectively. A good agreement with the IGS products is demonstrated (1 cm orbit, 20 to 30 μas PM offsets, and 5 to 10 μs/day LOD). As for the VLBI single-session solution in the CONT campaigns, the station coordinate precisions are about 2 to 3 mm horizontally and 6 to 8 mm vertically. The EOP accuracies are comparable to previous studies, that is, 70 to 90 μas PM offsets and 10 μs/day LOD comparing to GNSS solutions, 40 μas CPO comparing to the IERS product. As demonstrated in the SLR PPP solutions, the station coordinate accuracy can be improved by 20% to 30% with additional GLONASS and GRACE satellites contributing to the typical LAGEOS and ETALON constellation. Therefore, the GNSS and LEO constellation should be included in the future SLR operational processing and the SLR TRF determination.

The features of different techniques are demonstrated in the single-technique solutions. The GNSS technique has better performance in determining the PM components than VLBI by a factor of 2 to 3, due to the globally distributed network. This can be compensated in the VGOS era, with more VLBI radio telescopes available. On the other hand, the GNSS LOD estimates show high short-term precision but have long-term biases due to the flaws in processing strategy and orbit modeling, indicating that the corresponding optimization must be performed. The co-located GNSS–VLBI tropospheric parameters agree at the level of 4 mm on ZTD and 0.4 to 0.7 mm on gradients. However, the tropospheric ties from NWM cannot fully explain the systematic biases at some co-locations, which can be up to several millimeters in ZTD (for instance, 4 mm at Westford). These systematic tropospheric biases are more related to the instruments and local terrains and must be identified before any further integrated processing. As for the local ties, the discrepancies between local surveys and space solutions show that the current LT accuracy still needs to be improved, and the nominal uncertainty of local surveys is certainly over-optimistic. It is required that the local surveys should be conducted as frequent as possible, and the follow-up updates are always necessary especially there are instrument changes.

In terms of the integrated processing strategy, several raised issues are addressed. As shown in this thesis, using the pseudo-observations to apply the ties works perfectly for the LTs, global ties (EOP), and tropospheric ties. It should also work for space tie, but using the common parameter method is more recommend. The discrepancy of the ties must be handled properly, otherwise, systematic bias will be introduced. For the LTs, the uncertainties from local surveys can hardly be used, as large ERP bias will be introduced. In this thesis an automacit reweighting method is developed, which is based on the normalized residual of the pseudo-observations

of the ties. This method is adopted for the LTs and tropospheric ties, and can efficiently mitigate the systematic biases without loosing the too much constraint information of the ties. The LOD parameter in the integrated solution is handled as LOD tie, that is, the campaign-wise LOD bias is derived and used as a pseudo-observation. This keeps the short-term precision from GNSS and avoids systematic biases. Last but not the least, the relative weighting between GNSS and VLBI in this thesis is handled with two criteria, including (1) comparable chi-squares, and (2) comparable levels of the nominal uncertainty. The contributions of both techniques are preserved in this way.

The VLBI solutions certainly benefit from applying tropospheric ties in integrated processing. For the VLBI INT sessions, the UT1-UTC bias can be reduced by 2 to 3 μs for both INT1 and INT2, while the LOD estimates can be improved by 3 μs/day. The major contribution is from the east gradients at both INT stations. Applying tropospheric ties also improves the 24-hour CONT sessions in both TRF stability and EOP precision. The station coordinate repeatability is improved by 12% horizontally and 28% vertically, and the network scale repeatability is improved by 33%. For the EOP, the formal error can be improved by around 30% on the PM offsets, and up to 20% on the other EOP components. The PM rates, LOD, and CPO components mainly benefit from the gradient ties, while the ERP offsets benefits from both ZTD and gradient ties. Comparing to the IERS product, the PM precision are improved by 18% and 13% on the x-pole and y-pole components, respectively. The improvement of UT1-UTC is less significant, whereas that of LOD is 10%. The CPO components are also enhanced, especially the dX component with an improvement of 13%. For further VLBI processing, it is highly recommended to apply the tropospheric ties to GNSS co-locations. Even though the impact on long-term TRF has not been demonstrated, the VLBI scale stability and instantaneously TRF (weekly or daily) determination will certainly benefit a lot. On the other hand, since the NWM cannot fully model the tropospheric ties, the VLBI network and ERP parameters can be biased significantly. The inter-technique agreement of tropospheric parameters still needs further investigation using long-term observations.

The superiorities of each technique are exploited in the integrated GNSS POD and VLBI solution, in which the consistent TRF, CRF, and EOP are achieved. Both techniques contribute to TRF and EOP estimation. As a result, the integrated solution achieves better precision and robustness than any single-technique solutions. The VLBI TRF is improved significantly in terms of the repeatability of station coordinates and network scale, which is attributed to the global ties (ERP), the tropospheric ties, and the local ties. The PM and LOD estimates are dominated by the GNSS techniques, which are much better than the VLBI estimates due to the globally distributed GNSS stations. Moreover, the y-pole estimates are even better than the GNSS-only solution by up to 10% in terms of the DBD statistic. The UT1-UTC and CPO estimates show smaller formal error by applying PM ties, and the values are further reduced by applying additional tropospheric ties. In terms of the agreement to the IERS product, the UT1-UTC and CPO components are also improved by the global, local, and tropospheric ties. As for the CRF, the AGN coordinates are enhanced by the various ties, especially the declination of the southern radio sources, which are improved more in the integrated solutions due to the fact that there less VLBI radio telescopes in the Sourthern Hemisphere. To cut it

short, the integrated solution preserves the advantages of both technique with improved TRF, CRF, and EOP estimates. The additional tropospheric ties provide further improvements.

7.2 Future work

Towards the ultimate goal of realizing consistent TRF, CRF, and EOP on the observation level, the following studies will be performed following the outcomes of this thesis.

A very first step is to optimize the VLBI data processing strategy, especially the automatic processing capability. As the INT sessions can be easily processed without manual intervention, it is not the case for the 24-hour sessions, where manual screening is mandatory for the clock break detection. However, automation will improve the processing efficiency and solution robustness significantly, for both the reprocessing and the operational processing. According to the IVS Development Plan 2030 (Nothnagel et al., 2020), there will be continuous daily 24-h observing programs with 16 VGOS stations for TRF and EOP determination. In this case, it would be a huge burden to manually process all the daily observations. Nevertheless, the random walk process used for clock modeling in the PANDA software is feasible and almost ready for automation. As shown in this thesis, the clock breaks will show up in the clock estimates given the proper stochastic noise, and some basic change point detection algorithm can be applied to detect the breaks. On the other hand, it is critical to use the proper clock stochastic noise. In this case, the clock characteristic at each station should be analyzed using long-term observations, and the station-wise stochastic noise should be then determined for further use.

As demonstrated in this thesis, the NWM cannot accurately model the tropospheric ties at co-located GNSS–VLBI stations, as some systematic biases still exist. Therefore, the tropospheric ties from space solutions should be investigated using long-term observations. Very detailed information about the instrument changes and the local terrain must be taken into consideration. Moreover, the seasonal and drift signals, if exist, should also be investigated. The VLBI 24-hour sessions should be processed homogeneously together with the co-located GNSS stations in PPP mode. As a byproduct, the tropospheric estimates from both techniques can be used for homogeneous water vapor monitoring and climate change applications.

Due to the limited observation number and imperfect geometry, the VLBI tropospheric parameters have relatively larger noise than those from GNSS. Therefore, applying the tropospheric ties between GNSS and VLBI can certainly improve the VLBI network stability, especially for the scale. A further investigation of the VLBI instantaneous (monthly, weekly, or even daily) TRF determination shall be performed, and the tropospheric ties from the GNSS solution will contribute to improving the stability.

The GNSS POD strategy and orbit dynamic modeling will be investigated to mitigate the LOD biases. One preliminary idea is to utilize the multi-GNSS constellation and extend the 24-hour POD arc to a multi-day arc, for instance, 3-day arc. The concept of a continuous GNSS

solution, that is, stacking the long-term NEQs together to determine instantaneous GNSS TRF with optimized EOP will be further developed. The CPO rates can also be determined in the continuous GNSS solution. Another possibility is to first derive the LOD time series, calibrate the bias, and fix the calibrated LOD in the POD solution. The dynamic orbit parameters can then be investigated and optimized. With the improved orbit modeling, the LOD bias should be mitigated. Other options include incorporating the LEO constellations, which have much better global geometry due to the rapid moving and the precisely measured and calibrated metadata available to the public, making them an optimal enhancement for the current space geodetic tools in determining EOP and TRF.

The current SLR processing in TRF determination only involves the LAGEOS and ETALON satellites. However, a huge number of SLR observations to the LEO and GNSS satellites are unexploited. It has been shown that the available observations can be increased by a factor of 10 if all the available satellites are utilized. Using all these additional observations can not only improve the SLR TRF stability significantly but also contribute to a more consistent TRF between GNSS and SLR, as now the combination relies solely on the LTs. Another benefit is that such a space co-location with accurately calibrated LRA offset and LEO PCO as well as possible GNSS PCO of newly launched satellites, for instance, Galileo satellites, connects the scales of the two techniques, and provides an alternative method to calibrate the local ties.

The realization of TRF, CRF, and EOP from integrated processed GNSS, VLBI, and SLR observations will be carried out as the ultimate output. From the GNSS perspective, the multi-GNSS observations on both ground stations and LEO platforms must be utilized. The SLR processing will include all the tracking satellites, including all the passive spherical satellites, all the tracking LEO and GNSS satellites. Unlike current TRF determination, in the integrated processing all the parameters will be handled homogeneously and estimated simultaneously, including the station and AGN coordinates, satellite antenna PCO (if not precisely calibrated), EOP, atmospheric parameters. All the possible ties will be applied according to the corresponding weights. Of course the parameter pre-elimination after applying the ties has to be performed to avoid an enormous normal equation.

Last but not the least, the last patch of space geodetic techniques (in terms of TRF determination) in the PANDA software, that is, the DORIS technique, is also expected to be available. The DORIS community is under the transition from the old DORIS conventions to the new GNSS-like conventions, including using the GNSS RINEX observation format and applying the GNSS phase-like observation modeling. Therefore, it is relatively more feasible to be applied in a GNSS-based software package than before. On the other hand, the DORIS POD accuracy is still limited due to several issues, such as the atmospheric delay and clock modeling. For instance, due to the fast movement of the LEO satellites, the tropospheric parameter accuracy of DORIS is not as good as that of GNSS. One simple optimization is to process several LEO satellites at the same time to improve the tropospheric parameter geometry. Applying the tropospheric ties between DORIS and GNSS is also an available option. The DORIS and GNSS instruments onboard the same LEO platform usually share the same clock, and thus the clock tie can also be investigated. Nevertheless, integrated

processing of GNSS, SLR, and DORIS observations offers a more robust solution for satellite orbit, and further contributed to the realization of TRF and EOP.

Bibliography

Abbondanza C, Chin TM, Gross RS, Heflin MB, Parker JW, Soja BS, van Dam T, Wu X. (2017). JTRF2014, the JPL Kalman filter and smoother realization of the International Terrestrial Reference System. Journal of Geophysical Research: Solid Earth, 122, 8474-8510. doi: 10.1002/2017jb014360.

Altamimi Z, Rebischung P, Métivier L, Collilieux X. (2016). ITRF2014: A new release of the International Terrestrial Reference Frame modeling nonlinear station motions. Journal of Geophysical Research: Solid Earth, 121, 6109-6131. doi: 10.1002/2016jb013098.

Altamimi Z, Sillard P, Boucher C. (2002). ITRF2000: A new release of the International Terrestrial Reference Frame for earth science applications. Journal of Geophysical Research: Solid Earth, 107, ETG 2-1-ETG 2-19. doi: 10.1029/2001jb000561.

Andersen PH. (1996). Status of the GEOSAT software after ten years of development and testing. 115, 310-314. doi: 10.1007/978-3-642-80133-4_51.

Andersen PH, Rekkedal S. (1995). VLBI data analysis with the GEOSAT software. Bulletin géodésique, 69, 125-134. doi: 10.1007/bf00815481.

Anderson JM, Beyerle G, Glaser S, Liu L, Männel B, Nilsson T, Heinkelmann R, Schuh H. (2018). Simulations of VLBI observations of a geodetic satellite providing co-location in space. Journal of Geodesy. doi: 10.1007/s00190-018-1115-5.

Anderson JM, Xu MH. (2018). Source Structure and Measurement Noise Are as Important as All Other Residual Sources in Geodetic VLBI Combined. Journal of Geophysical Research: Solid Earth, 123, 10,162-110,190. doi: 10.1029/2018jb015550.

Arnold D, Montenbruck O, Hackel S, Sośnica K. (2018). Satellite laser ranging to low Earth orbiters: orbit and network validation. Journal of Geodesy. doi: 10.1007/s00190-018-1140-4.

Artz T, Böckmann S, Nothnagel A, Tesmer V. (2007). ERP time series with daily and sub-daily resolution determined from CONT05. In: Boehm J, Pany A, Schuh H (eds), Proceedings of the 18th European VLBI for Geodesy and Astrometry Working Meeting, Technische Universität Wien, pp. 69-74.

Bachmann S, Thaller D. (2016). Adding source positions to the IVS combination—First results. Journal of Geodesy, 91, 743-753. doi: 10.1007/s00190-016-0979-5.

Bähr H, Altamimi Z, Heck B. (2007). Variance Component Estimation for Combination of Terrestrial Reference Frames. Karlsruher Institut für Technologie.

Balidakis K, Nilsson T, Zus F, Glaser S, Heinkelmann R, Deng Z, Schuh H. (2018). Estimating Integrated Water Vapor Trends From VLBI, GPS, and Numerical Weather Models: Sensitivity to Tropospheric Parameterization. Journal of Geophysical Research: Atmospheres, 123, 6356-6372. doi: 10.1029/2017jd028049.

Banville S, Sieradzki R, Hoque M, Wezka K, Hadas T. (2017). On the estimation of higher-order ionospheric effects in precise point positioning. GPS Solutions, 21, 1817-1828. doi: 10.1007/s10291-017-0655-0.

Bar-Sever Y, Haines B, Bertiger W, Desai S, Wu S. (2009). Geodetic Reference Antenna in

Space (GRASP) - A Mission to Enhance Space-based Geodesy. In.

Behrend D, Thomas C, Gipson J, Himwich E, Le Bail K. (2020). On the organization of CONT17. Journal of Geodesy, 94. doi: 10.1007/s00190-020-01436-x.

Bertiger W, Bar-Sever Y, Dorsey A, Haines B, Harvey N, Hemberger D, Heflin M, Lu W, Miller M, Moore AW, Murphy D, Ries P, Romans L, Sibois A, Sibthorpe A, Szilagyi B, Vallisneri M, Willis P. (2020). GipsyX/RTGx, a new tool set for space geodetic operations and research. Advances in Space Research, 66, 469-489. doi: 10.1016/j.asr.2020.04.015.

Bizouard C, Lambert S, Gattano C, Becker O, Richard J-Y. (2018). The IERS EOP 14C04 solution for Earth orientation parameters consistent with ITRF 2014. Journal of Geodesy, 93, 621-633. doi: 10.1007/s00190-018-1186-3.

Blewitt G. (1990). An Automatic Editing Algorithm for GPS data. Geophysical Research Letters, 17, 199-202. doi: 10.1029/GL017i003p00199.

Bloßfeld M, Müller H, Gerstl M, Štefka V, Bouman J, Göttl F, Horwath M. (2015). Second-degree Stokes coefficients from multi-satellite SLR. Journal of Geodesy, 89, 857-871. doi: 10.1007/s00190-015-0819-z.

Bloßfeld M, Rudenko S, Kehm A, Panafidina N, Müller H, Angermann D, Hugentobler U, Seitz M. (2018a). Consistent estimation of geodetic parameters from SLR satellite constellation measurements. Journal of Geodesy, 92, 1003-1021. doi: 10.1007/s00190-018-1166-7.

Bloßfeld M, Rudenko S, Lemoine FG. (2018b). Status of the IDS data processing at DGFI-TUM. In: DORIS Analysis Working Group (AWG) meeting of the International DORIS Service, Toulouse, France.

Böckmann S, Artz T, Nothnagel A, Tesmer V. (2010). International VLBI Service for Geodesy and Astrometry: Earth orientation parameter combination methodology and quality of the combined products. Journal of Geophysical Research, 115. doi: 10.1029/2009jb006465.

Boehm J, Heinkelmann R, Mendes Cerveira PJ, Pany A, Schuh H. (2009). Atmospheric loading corrections at the observation level in VLBI analysis. Journal of Geodesy, 83, 1107-1113. doi: 10.1007/s00190-009-0329-y.

Boehm J, Niell A, Tregoning P, Schuh H. (2006a). Global Mapping Function (GMF): A new empirical mapping function based on numerical weather model data. Geophysical Research Letters, 33. doi: 10.1029/2005gl025546.

Boehm J, Werl B, Schuh H. (2006b). Troposphere mapping functions for GPS and very long baseline interferometry from European Centre for Medium-Range Weather Forecasts operational analysis data. Journal of Geophysical Research-Solid Earth, 111, n/a-n/a. doi: 10.1029/2005jb003629.

Böhm J, Möller G, Schindelegger M, Pain G, Weber R. (2015). Development of an improved empirical model for slant delays in the troposphere (GPT2w). GPS Solutions, 19, 433-441. doi: 10.1007/s10291-014-0403-7.

Böhm J, Schuh H. (2013). Atmospheric Effects in Space Geodesy. Springer-Verlag Berlin Heidelberg.

Bourda G, Charlot P, Biancale R. (2007a). GINS: a new tool for VLBI Geodesy and Astrometry. In: Dans Proceedings of the 18th European VLBI for Geodesy and Astrometry (EVGA)

Working Meeting - 18th European VLBI for Geodesy and Astrometry (EVGA) Working Meeting, Vienna.

Bourda G, Charlot P, Biancale R. (2007b). VLBI Analyses with the GINS Software for Multi-technique COmbination at the Observation Level. In: Bouvier J, Chalabaev A, Charbonnel C (eds), Soci´et´e Francaise d'Astronomie et d'Astrophysique (SF2A) 2007.

Bury G, Sosnica K, Zajdel R. (2019). Impact of the Atmospheric Non-tidal Pressure Loading on Global Geodetic Parameters Based on Satellite Laser Ranging to GNSS. IEEE Transactions on Geoscience and Remote Sensing, 57, 3574-3590. doi: 10.1109/tgrs.2018.2885845.

Bury G, Sośnica K, Zajdel R. (2018). Multi-GNSS orbit determination using satellite laser ranging. Journal of Geodesy. doi: 10.1007/s00190-018-1143-1.

Bury G, Sośnica K, Zajdel R, Strugarek D, Hugentobler U. (2020). Determination of precise Galileo orbits using combined GNSS and SLR observations. GPS Solutions, 25. doi: 10.1007/s10291-020-01045-3.

Chen G, Herring TA. (1997). Effects of atmospheric azimuthal asymmetry on the analysis of space geodetic data. Journal of Geophysical Research: Solid Earth, 102, 20489-20502. doi: 10.1029/97jb01739.

Chen Q, Song S, Zhou W, Huang C, Zhu W, Cheng Z. (2017). Hourly Updated GNSS Orbit and Clock Correction. In: IGS Workshop 2017, Paris.

Chen X, Ge M, Marques HA, Schuh H. (2019). Evaluating the impact of higher-order ionospheric corrections on multi-GNSS ultra-rapid orbit determination. Journal of Geodesy, 93, 1347-1365. doi: 10.1007/s00190-019-01249-7.

Chen X, Lu C, Guo B, Guo F, Ge M, Li X, Schuh H. (2018). GPS/GLONASS Combined Precise Point Positioning With the Modeling of Highly Stable Receiver Clock in the Application of Monitoring Active Seismic Deformation. Journal of Geophysical Research: Solid Earth, 123, 4025-4040. doi: 10.1029/2017jb015060.

Couhert A, Mercier F, Moyard J, Biancale R. (2018). Systematic Error Mitigation in DORIS-Derived Geocenter Motion. Journal of Geophysical Research: Solid Earth, 123, 10,142-110,161. doi: 10.1029/2018jb015453.

Coulot D, Berio P, Biancale R, Loyer S, Soudarin L, Gontier AM. (2007). Toward a direct combination of space-geodetic techniques at the measurement level: Methodology and main issues. Journal of Geophysical Research, 112. doi: 10.1029/2006jb004336.

Dach R, Böhm J, Lutz S, Steigenberger P, Beutler G. (2010). Evaluation of the impact of atmospheric pressure loading modeling on GNSS data analysis. Journal of Geodesy, 85, 75-91. doi: 10.1007/s00190-010-0417-z.

Dach R, Lutz S, Walser P, Fridez P. (2015). Bernese GNSS Software Version 5.2. In. Astronomical Institute, Universtiy of Bern, Bern.

Drewes H. (2008). Reference Systems, Reference Frames, and the Geodetic Datum. 133, 3-9. doi: 10.1007/978-3-540-85426-5_1.

Drożdżewski M, Sośnica K, Zus F, Balidakis K. (2019). Troposphere delay modeling with horizontal gradients for satellite laser ranging. Journal of Geodesy, 93, 1853-1866. doi: 10.1007/s00190-019-01287-1.

Duev DA, Molera Calvés G, Pogrebenko SV, Gurvits LI, Cimó G, Bocanegra Bahamon T. (2012). Spacecraft VLBI and Doppler tracking: algorithms and implementation. Astronomy & Astrophysics, 541, A43. doi: 10.1051/0004-6361/201218885.

Elgered G, Haas R, Wahlbom J, Ning T. (2012). Assessing the Quality of Water Vapor Radiometer Data from Onsala during the CONT11 Geodetic VLBI Campaign. In: Seventh General Meeting (GM2012) of the international VLBI Service for Geodesy and Astrometry (IVS), Madrid, Spain, pp. 410-414.

Flohrer C, Schönemann E, Springer T, Zandbergen R, Enderle W. (2016). VLBI processing at ESOC. In: 9th IVS General Meeting Johannesburg, South Africa.

Flohrer C, Schönemann E, Springer T, Zandbergen R, Enderle W. (2017). Update on VLBI Data Analysis at ESA/ESOC. In: 23rd European VLBI Group for Geodesy and Astrometry Working Meeting.

Flohrer C, Schönemann E, Springer T, Zandbergen R, Enderle W. (2018). VLBI-derived Earth Orientation parameters generated at ESOC. In: 10th IVS General Meeting (GM2018), Longyearbyen, Svalbard.

Fritsche M, Dietrich R, Knöfel C, Rülke A, Vey S, Rothacher M, Steigenberger P. (2005). Impact of higher-order ionospheric terms on GPS estimates. Geophysical Research Letters, 32. doi: 10.1029/2005gl024342.

Fritsche M, Sośnica K, Rodríguez-Solano CJ, Steigenberger P, Wang K, Dietrich R, Dach R, Hugentobler U, Rothacher M. (2014). Homogeneous reprocessing of GPS, GLONASS and SLR observations. Journal of Geodesy, 88, 625-642. doi: 10.1007/s00190-014-0710-3.

Gambis D, Biancale R, Carlucci T, Lemoine JL, Marty J, Bourda G, Charlot P, Loyer S, Lalanne T, Soudarin L, Deleflie F. (2009). Combination of Earth Orientation Parameters and Terrestrial Frame at the observation level. In: Drewes H (ed), Geodetic Reference Frames. International Association of Geodesy Symposia. Springer, Berlin, Heidelberg.

Gambis D, Richard JY, Biancale R, Bizouard C. (2013). Why Combining at the Observation Level? In: Altamimi Z, Collilieux X (eds), Reference Frames for Applications in Geosciences. International Association of Geodesy Symposia. Springer, Berlin, Heidelberg.

Ge H, Li B, Ge M, Shen Y, Schuh H. (2017). Improving BeiDou precise orbit determination using observations of onboard MEO satellite receivers. Journal of Geodesy, 91, 1447-1460. doi: 10.1007/s00190-017-1035-9.

Ge M, Gendt G, Dick G, Zhang FP. (2005a). Improving carrier-phase ambiguity resolution in global GPS network solutions. Journal of Geodesy, 79, 103-110. doi: 10.1007/s00190-005-0447-0.

Ge M, Gendt G, Dick G, Zhang FP, Reigber C. (2005b). Impact of GPS satellite antenna offsets on scale changes in global network solutions. Geophysical Research Letters, 32. doi: 10.1029/2004gl022224.

Ge M, Gendt G, Dick G, Zhang FP, Rothacher M. (2006). A New Data Processing Strategy for Huge GNSS Global Networks. Journal of Geodesy, 80, 199-203. doi: 10.1007/s00190-006-0044-x.

Ge M, Gendt G, Rothacher M, Shi C, Liu J. (2007). Resolution of GPS carrier-phase ambiguities in Precise Point Positioning (PPP) with daily observations. Journal of Geodesy,

82, 389-399. doi: 10.1007/s00190-007-0187-4.

Geoscience A. (2010). OCCAM VLBI Processing Software FTP site. In.

Gipson J. (2015). vgosDB format.

Gipson J, MacMillan D, Petrov L. (2008). Improved estimation in VLBI through better modeling and analysis. In: Proceedings of the Fifth IVS General Meeting "Measuring the Future, pp. 3-6.

Glaser S, Ampatzidis D, König R, Nilsson T, Heinkelmann R, Flechtner F, Schuh H. (2016). Simulation of VLBI Observations to Determine a Global TRF for GGOS. 147, 3-9. doi: 10.1007/1345_2016_256.

Glaser S, Fritsche M, Sośnica K, Rodríguez-Solano CJ, Wang K, Dach R, Hugentobler U, Rothacher M, Dietrich R. (2015). A consistent combination of GNSS and SLR with minimum constraints. Journal of Geodesy, 89, 1165-1180. doi: 10.1007/s00190-015-0842-0.

Glaser S, König R, Ampatzidis D, Nilsson T, Heinkelmann R, Flechtner F, Schuh H. (2017). A Global Terrestrial Reference Frame from simulated VLBI and SLR data in view of GGOS. Journal of Geodesy, 91, 723-733. doi: 10.1007/s00190-017-1021-2.

Glaser S, König R, Neumayer KH, Balidakis K, Schuh H. (2019). Future SLR station networks in the framework of simulated multi-technique terrestrial reference frames. Journal of Geodesy, 93, 2275-2291. doi: 10.1007/s00190-019-01256-8.

Glaser S, König R, Neumayer KH, Nilsson T, Heinkelmann R, Flechtner F, Schuh H. (2018). On the impact of local ties on the datum realization of global terrestrial reference frames. Journal of Geodesy, 93, 655-667. doi: 10.1007/s00190-018-1189-0.

Glomsda M, Bloßfeld M, Seitz M, Seitz F. (2020). Benefits of non-tidal loading applied at distinct levels in VLBI analysis. Journal of Geodesy, 94. doi: 10.1007/s00190-020-01418-z.

Glomsda M, Kwak Y, Gerstl M, Angermann D, Seitz F. (2018). VLBI Analysis with DOGS-RI at DGFI-TUM. In: Geodätische Woche at INTERGEO 2018, Frankfurt a.M., Germany.

Gordon D. (2010). Use of GPS TEC Maps for Calibrating Single Band VLBI Sessions. In: Proceedings of the Sixth General Meeting of the International VLBI Service for Geodesy and Astrometry.

Griffiths J. (2018). Combined orbits and clocks from IGS second reprocessing. Journal of Geodesy. doi: 10.1007/s00190-018-1149-8.

Gross R, Beutler G, Plag HP. (2009). Integrated scientific and societal user requirements and functional specifications for the GGOS. In: Plag H, Pearlman M (eds), Global Geodetic Observing System. Springer, Berlin, Heidelberg., pp. 209-224.

Haas R. (2013). The Onsala Twin Telescope Project. In: Poutanen NZaM (ed), Proceedings of the 21st Meeting of the European VLBI Group for Geodesy and Astronomy, Espoo, Finland, pp. 61-65.

Haas R, Hobiger T, Kurihara S, Hara T. (2016). Ultra-rapid earth rotation determination with VLBI during CONT11 and CONT14. Journal of Geodesy, 91, 831-837. doi: 10.1007/s00190-016-0974-x.

Haas R, Rieck C, Jarlemark P. (2012). VLBI and GNSS Frequency Link Instabilities during

CONT Campaigns. In: IVS 2012 General Meeting Proceedings.

Hackel S, Steigenberger P, Hugentobler U, Uhlemann M, Montenbruck O. (2014). Galileo orbit determination using combined GNSS and SLR observations. GPS Solutions, 19, 15-25. doi: 10.1007/s10291-013-0361-5.

Hadas T, Krypiak-Gregorczyk A, Hernández-Pajares M, Kaplon J, Paziewski J, Wielgosz P, Garcia-Rigo A, Kazmierski K, Sosnica K, Kwasniak D, Sierny J, Bosy J, Pucilowski M, Szyszko R, Portasiak K, Olivares-Pulido G, Gulyaeva T, Orus-Perez R. (2017). Impact and Implementation of Higher-Order Ionospheric Effects on Precise GNSS Applications. Journal of Geophysical Research: Solid Earth, 122, 9420-9436. doi: 10.1002/2017jb014750.

Hawarey M. (2005). Effects of the 2nd order ionospheric terms on VLBI measurements. Geophysical Research Letters, 32. doi: 10.1029/2005gl022729.

Heinkelmann R, Böhm J, Bolotin S, Engelhardt G, Haas R, Lanotte R, MacMillan DS, Negusini M, Skurikhina E, Titov O, Schuh H. (2011). VLBI-derived troposphere parameters during CONT08. Journal of Geodesy, 85, 377-393. doi: 10.1007/s00190-011-0459-x.

Hellmers H, Thaller D, Bloßfeld M, Kehm A, Girdiuk A. (2019). Combination of VLBI Intensive Sessions with GNSS for generating Low latency Earth Rotation Parameters. Advances in Geosciences, 50, 49-56. doi: 10.5194/adgeo-50-49-2019.

Hernández-Pajares M, Juan JM, Sanz J, Orús R. (2007). Second-order ionospheric term in GPS: Implementation and impact on geodetic estimates. Journal of Geophysical Research, 112. doi: 10.1029/2006jb004707.

Hernández-Pajares M, Juan JM, Sanz J, Orus R, Garcia-Rigo A, Feltens J, Komjathy A, Schaer SC, Krankowski A. (2009). The IGS VTEC maps: a reliable source of ionospheric information since 1998. Journal of Geodesy, 83, 263-275. doi: 10.1007/s00190-008-0266-1.

Hobiger T. (2005). VLBI as a tool to probe the ionosphere.

Hobiger T, Gotoh T, Otsubo T, Kubooka T, Sekido M, Takiguchi H, Takeuchi H. (2010). c5++ - Multi-technique Analysis Software for Next Generation Geodetic Instruments. In: IVS 2010 General Meeting Proceedings, pp. 212–216.

Hobiger T, Klopotek G, Diamantidis P, Haas R. (2018). Update on c5++. In: IVS Analysis Workshop 2018.

Hobiger T, Kondo T, Schuh H. (2006). Very long baseline interferometry as a tool to probe the ionosphere. Radio Science, 41, n/a-n/a. doi: 10.1029/2005rs003297.

Hobiger T, Otsubo T. (2014). Combination of GPS and VLBI on the observation level during CONT11—common parameters, ties and inter-technique biases. Journal of Geodesy, 88, 1017-1028. doi: 10.1007/s00190-014-0740-x.

Hobiger T, Otsubo T, Sekido M. (2014). Observation level combination of SLR and VLBI with c5++: A case study for TIGO. Advances in Space Research, 53, 119-129. doi: 10.1016/j.asr.2013.10.004.

Hobiger T, Otsubo T, Sekido M, Gotoh T, Kubooka T, Takiguchi H. (2011). Fully automated VLBI analysis with c5++ for ultra-rapid determination of UT1. Earth, Planets and Space, 62, 933-937. doi: 10.5047/eps.2010.11.008.

Hobiger T, Rieck C, Haas R, Koyama Y. (2015). Combining GPS and VLBI for inter-

continental frequency transfer. Metrologia, 52, 251-261. doi: 10.1088/0026-1394/52/2/251.

Hoque MM, Jakowski N. (2008). Estimate of higher order ionospheric errors in GNSS positioning. Radio Science, 43, n/a-n/a. doi: 10.1029/2007rs003817.

Hoque MM, Jakowski N, Berdermann J. (2017). Ionospheric correction using NTCM driven by GPS Klobuchar coefficients for GNSS applications. GPS Solutions, 21, 1563-1572. doi: 10.1007/s10291-017-0632-7.

Huang W, Männel B, Brack A, Schuh H. (2020a). Two methods to determine scale-independent GPS PCOs and GNSS-based terrestrial scale: comparison and cross-check. GPS Solutions, 25. doi: 10.1007/s10291-020-01035-5.

Huang W, Männel B, Sakic P, Ge M, Schuh H. (2020b). Integrated processing of ground- and space-based GPS observations: improving GPS satellite orbits observed with sparse ground networks. Journal of Geodesy, 94. doi: 10.1007/s00190-020-01424-1.

Jayles C, Chauveau JP, Rozo F. (2010). DORIS/Jason-2: Better than 10cm on-board orbits available for Near-Real-Time Altimetry. Advances in Space Research, 46, 1497-1512. doi: 10.1016/j.asr.2010.04.030.

Karbon M, Belda S, Ferrándiz JM, Nothnagel A. (2018). CONT17: Impact of the different network realizations on the key products of VLBI. In: European Geoscience Union General Assembly 2018, Vienna.

Kareinen N, Hobiger T, Haas R. (2015). Automated analysis of Kokee–Wettzell Intensive VLBI sessions—algorithms, results, and recommendations. Earth, Planets and Space, 67. doi: 10.1186/s40623-015-0340-x.

Kikuchi F, Liu Q, Hanada H, Kawano N, Matsumoto K, Iwata T, Goossens S, Asari K, Ishihara Y, Tsuruta S, Ishikawa T, Noda H, Namiki N, Petrova N, Harada Y, Ping J, Sasaki S. (2009). Picosecond accuracy VLBI of the two subsatellites of SELENE (KAGUYA) using multifrequency and same beam methods. Radio Science, 44, n/a-n/a. doi: 10.1029/2008rs003997.

Kirkvik A-S. (2017). Norwegian mapping authority analysis center IVS biennial report 2015–2016. In: Baver KD, Behrend D, Armstrong KL (eds), International VLBI Service for Geodesy and Astrometry 2015+2016 Biennial Report.

Kirkvik A-S, Hjelle GA, Skjæveland A, Dahnn M, Fausk I. (2018). NMA Analysis Center - Progress Report. In: Armstrong KL, Baver KD, Behrend D (eds), IVS 2018 General Meeting Proceedings, pp. 237-241.

Klioner SA. (2003). A Practical Relativistic Model for Microarcsecond Astrometry in Space. The Astronomical Journal, 125, 1580-1597. doi: 10.1086/367593.

Klopotek G. (2020). Observations of artificial radio sources within the framework of geodetic Very Long Baseline Interferometry. Chalmers University of Technology.

Klopotek G, Hobiger T, Haas R. (2017). Geodetic VLBI with an artificial radio source on the Moon: a simulation study. Journal of Geodesy, 92, 457-469. doi: 10.1007/s00190-017-1072-4.

Klopotek G, Hobiger T, Haas R, Jaron F, La Porta L, Nothnagel A, Zhang Z, Han S, Neidhardt A, Plötz C. (2019). Position determination of the Chang'e 3 lander with geodetic VLBI. Earth, Planets and Space, 71. doi: 10.1186/s40623-019-1001-2.

Klopotek G, Hobiger T, Haas R, Otsubo T. (2020). Geodetic VLBI for precise orbit determination of Earth satellites: a simulation study. Journal of Geodesy, 94. doi: 10.1007/s00190-020-01381-9.

Koch K-R. (1999). Parameter Estimation and Hypothesis Testing in Linear Models. Springer-Verlag Berlin Heidelberg, Berlin.

Koenig D. (2018). A Terrestrial Reference Frame realised on the observation level using a GPS-LEO satellite constellation. Journal of Geodesy. doi: 10.1007/s00190-018-1121-7.

Kotsakis C. (2018). Datum Definition and Minimal Constraints. 1-6. doi: 10.1007/978-3-319-02370-0_157-1.

Kouba J. (2007). Implementation and testing of the gridded Vienna Mapping Function 1 (VMF1). Journal of Geodesy, 82, 193-205. doi: 10.1007/s00190-007-0170-0.

Kouba J. (2009). A Guide to using International GNSS Service (IGS) Products.

Krawinkel T, Schön S. (2015). Benefits of receiver clock modeling in code-based GNSS navigation. GPS Solutions, 20, 687-701. doi: 10.1007/s10291-015-0480-2.

Landskron D, Böhm J. (2017). VMF3/GPT3: refined discrete and empirical troposphere mapping functions. Journal of Geodesy, 92, 349-360. doi: 10.1007/s00190-017-1066-2.

Landskron D, Böhm J. (2019). Improving dUT1 from VLBI intensive sessions with GRAD gradients and ray-traced delays. Advances in Space Research, 63, 3429-3435. doi: 10.1016/j.asr.2019.03.041.

Langkaas L, Dahlen T, Opseth PE. (2010). New fundamental station in Ny-Ålesund. In: D B, KD B (eds), 6th IVS general meeting, Hobart, Tasmania, Australia, pp. 111-112.

Leick A, Rapoport L, Tatarnikov D. (2015). GPS Satellite Surveying. John Wiley & Sons, Inc.

Lemoine FG, Rowlands DD, Pavlis DE, Luthcke SB, McCarthy JJ, Zelensky NP, Chinn DS, Macmillan DS, Bail KL. (2009). GEODYN & Multitechnique Processing for the Reference Frame.

Lemoine J-M, Capdeville H, Soudarin L. (2016). Precise orbit determination and station position estimation using DORIS RINEX data. Advances in Space Research, 58, 2677-2690. doi: 10.1016/j.asr.2016.06.024.

Li X, Chen X, Ge M, Schuh H. (2018). Improving multi-GNSS ultra-rapid orbit determination for real-time precise point positioning. Journal of Geodesy. doi: 10.1007/s00190-018-1138-y.

Liu J, Ge M. (2003). PANDA software and its preliminary result of positioning and orbit determination. Wuhan University Journal of Natural Sciences, 8, 603-609. doi: 10.1007/BF02899825.

Lou Y, Zheng F, Gu S, Wang C, Guo H, Feng Y. (2015). Multi-GNSS precise point positioning with raw single-frequency and dual-frequency measurement models. GPS Solutions, 20, 849-862. doi: 10.1007/s10291-015-0495-8.

Luceri V, Pirri M, Rodríguez J, Appleby G, Pavlis EC, Müller H. (2019). Systematic errors in SLR data and their impact on the ILRS products. Journal of Geodesy, 93, 2357-2366. doi: 10.1007/s00190-019-01319-w.

MacMillan DS. (2017). EOP and scale from continuous VLBI observing: CONT campaigns to future VGOS networks. Journal of Geodesy, 91, 819-829. doi: 10.1007/s00190-017-

1003-4.

MacMillan DS, Lemoine FG, Chinn DS, Pavlis EC, Rowlands DD. (2009). VLBI-SLR Combination Solution Using GEODYN. In: AGU Fall Meeting.

Männel B. (2016). Co-location of Geodetic Observation Techniques in Space.

Männel B, Dobslaw H, Dill R, Glaser S, Balidakis K, Thomas M, Schuh H. (2019). Correcting surface loading at the observation level: impact on global GNSS and VLBI station networks. Journal of Geodesy, 93, 2003-2017. doi: 10.1007/s00190-019-01298-y.

Männel B, Rothacher M. (2015). Ionospheric corrections for single-frequency tracking of GNSS satellites by VLBI based on co-located GNSS. Journal of Geodesy, 90, 189-203. doi: 10.1007/s00190-015-0865-6.

Männel B, Rothacher M. (2017). Geocenter variations derived from a combined processing of LEO- and ground-based GPS observations. Journal of Geodesy, 91, 933-944. doi: 10.1007/s00190-017-0997-y.

Männel B, Rothacher M, Kodet J, Ulrich S, Schmid R. (2014). GLONASS Satellites Simultaneously Observed by VLBI, GNSS and SLR. In: Behrend D, Baver KD, Armstrong KL (eds), International VLBI Service for Geodesy and Astrometry 2014 General Meeting Proceedings: "VGOS: The New VLBI Network". Science Press, Beijing, China, pp. 461-465.

Marini J, Murray C. (1973). Correction of laser range tracking data for atmospheric refraction at elevations above 10 degrees.

Marty J, Loyer S, Perosanz F, Mercier F, Bracher G, Legresy B, Portier L, Capdeville H, Fund F, Lemoine J. (2011). GINS: the CNES/GRGS GNSS scientific software. In: 3rd international colloquium scientific and fundamental aspects of the Galileo programme, ESA proceedings WPP326, Copenhagen, Denmark, pp. 8-10.

Meindl M, Beutler G, Thaller D, Dach R, Jäggi A. (2013). Geocenter coordinates estimated from GNSS data as viewed by perturbation theory. Advances in Space Research, 51, 1047-1064. doi: 10.1016/j.asr.2012.10.026.

Mémin A, Boy J-P, Santamaría-Gómez A. (2020). Correcting GPS measurements for non-tidal loading. GPS Solutions, 24. doi: 10.1007/s10291-020-0959-3.

Mendes VB. (2004). High-accuracy zenith delay prediction at optical wavelengths. Geophysical Research Letters, 31. doi: 10.1029/2004gl020308.

Mendes VB, Prates G, Pavlis EC, Pavlis DE, Langley RB. (2002). Improved mapping functions for atmospheric refraction correction in SLR. Geophysical Research Letters, 29, 53-51-53-54. doi: 10.1029/2001gl014394.

Mercier F, Cerri L, Berthias J-P. (2010). Jason-2 DORIS phase measurement processing. Advances in Space Research, 45, 1441-1454. doi: 10.1016/j.asr.2009.12.002.

Montenbruck O, Arnold D, Sosnica K, Jäggi A, Hackel S. (2018a). Improving the SLR network calibration through GPS-based precise orbit determination of LEO satellites. In: EGU General Assembly 2018.

Montenbruck O, Schmid R, Mercier F, Steigenberger P, Noll C, Fatkulin R, Kogure S, Ganeshan AS. (2015). GNSS satellite geometry and attitude models. Advances in Space Research, 56, 1015-1029. doi: 10.1016/j.asr.2015.06.019.

Montenbruck O, Steigenberger P, Hauschild A. (2018b). Multi-GNSS signal-in-space range error assessment – Methodology and results. Advances in Space Research, 61, 3020-3038. doi: 10.1016/j.asr.2018.03.041.

Montenbruck O, Steigenberger P, Prange L, Deng Z, Zhao Q, Perosanz F, Romero I, Noll C, Stürze A, Weber G, Schmid R, MacLeod K, Schaer S. (2017). The Multi-GNSS Experiment (MGEX) of the International GNSS Service (IGS) – Achievements, prospects and challenges. Advances in Space Research, 59, 1671-1697. doi: 10.1016/j.asr.2017.01.011.

Müller J, Biskupek L, Oberst J, Schreiber U. (2009). Contribution of Lunar Laser Ranging to Realise Geodetic Reference Systems. 134, 55-59. doi: 10.1007/978-3-642-00860-3_8.

Müller J, Murphy TW, Schreiber U, Shelus PJ, Torre J-M, Williams JG, Boggs DH, Bouquillon S, Bourgoin A, Hofmann F. (2019). Lunar Laser Ranging: a tool for general relativity, lunar geophysics and Earth science. Journal of Geodesy, 93, 2195-2210. doi: 10.1007/s00190-019-01296-0.

Müller J, Nordtvedt K. (1998). Lunar laser ranging and the equivalence principle signal. Physical Review D, 58. doi: 10.1103/PhysRevD.58.062001.

Nafisi V, Madzak M, Böhm J, Ardalan AA, Schuh H. (2012). Ray-traced tropospheric delays in VLBI analysis. Radio Science, 47, n/a-n/a. doi: 10.1029/2011rs004918.

Neidhardt A, Kronschnabl G, Klügel T, Hase H, Pausch K, Göldi W. (2011). VLBI2010—current status of the TWIN radio telescope project at Wettzell, Germany. In: Alef W, Bernhart S, Nothnagal A (eds), Proceedings 20th European VLBI for geodesy and astrometry (EVGA) working meeting, Bonn, Germany, pp. 67-70.

Nilsson T, Balidakis K, Heinkelmann R, Schuh H. (2019a). Earth Orientation Parameters from the CONT17 Campaign. Geophysica, 54, 19-25.

Nilsson T, Balidakis K, Ning T. (2019b). An assessment of the tropospheric parameters estimated from the CONT17 campaign. In: 24th Meeting of the European VLBI Group for Geodesy and Astrometry, Las Palmas, Gran Canaria, Spain.

Nilsson T, Böhm J, Schuh H. (2011). Universal time from VLBI single-baseline observations during CONT08. Journal of Geodesy, 85, 415-423. doi: 10.1007/s00190-010-0436-9.

Nilsson T, Heinkelmann R, Karbon M, Raposo-Pulido V, Soja B, Schuh H. (2014). Earth orientation parameters estimated from VLBI during the CONT11 campaign. Journal of Geodesy, 88, 491-502. doi: 10.1007/s00190-014-0700-5.

Nilsson T, Karbon M, Soja B, Heinkelmann R, Lu C, Schuh H. (2015). Atmospheric modeling for co-located VLBI antennas and twin telescopes. Journal of Geodesy, 89, 655-665. doi: 10.1007/s00190-015-0804-6.

Nilsson T, Soja B, Balidakis K, Karbon M, Heinkelmann R, Deng Z, Schuh H. (2017). Improving the modeling of the atmospheric delay in the data analysis of the Intensive VLBI sessions and the impact on the UT1 estimates. Journal of Geodesy, 91, 857-866. doi: 10.1007/s00190-016-0985-7.

Nothnagel A, Anderson J, Behrend D, Böhm J, Charlot P, Colomer F, Witt Ad, Gipson J, Haas R, Hall D, Hase H, Himwich E, Kotary NW, Li J, Nosov E, Ruszczyk C, Tuccari G. (2020). IVS Infrastructure Development Plan 2030.

Otten M, Flohrer C, Springer T, Enderle W. (2012). Multi-technique combination at

observation level with NAPEOS: combining GPS, GLONASS and LEO satellites. In: EGU General Assembly 2012.

Pazamickas K, Clark T, Hambly R. (2015). High-accuracy Time and Frequency in VLBI. In: The eighth biennial IVS Technical Operations Workshop, MIT Haystack Observatory, Westford, MA, USA.

Penna NT, Morales Maqueda MA, Martin I, Guo J, Foden PR. (2018). Sea Surface Height Measurement Using a GNSS Wave Glider. Geophysical Research Letters, 45, 5609-5616. doi: 10.1029/2018gl077950.

Petit G, Luzum B. (2010). IERS Conventions (2010) (IERS Technical Note No. 36). In, Frankfurt am Main.

Petrachenko WT, Niell AE, Corey BE, Behrend D, Schuh H, Wresnik J. (2012). VLBI2010: Next Generation VLBI System for Geodesy and Astrometry. 136, 999-1005. doi: 10.1007/978-3-642-20338-1_125.

Petrov L. (2000). Instrumental Errors of Geodetic VLBI. In: Vandenberg NR, Baver KD (eds), International VLBI Service for Geodesy and Astrometry 2000 General Meeting Proceedings, pp. 230-235.

Petrov L, Gordon D, Gipson J, MacMillan D, Ma C, Fomalont E, Walker RC, Carabajal C. (2009). Precise geodesy with the Very Long Baseline Array. Journal of Geodesy, 83, 859-876. doi: 10.1007/s00190-009-0304-7.

Plank L. (2013). VLBI satellite tracking for the realization of frame ties. TU Wien.

Pollet A, Coulot D, Bock O, Nahmani S. (2014). Comparison of individual and combined zenith tropospheric delay estimations during CONT08 campaign. Journal of Geodesy, 88, 1095-1112. doi: 10.1007/s00190-014-0745-5.

Prange L, Orliac E, Dach R, Arnold D, Beutler G, Schaer S, Jäggi A. (2016). CODE's five-system orbit and clock solution—the challenges of multi-GNSS data analysis. Journal of Geodesy, 91, 345-360. doi: 10.1007/s00190-016-0968-8.

Psimoulis PA, Houlié N, Behr Y. (2018). Real-Time Magnitude Characterization of Large Earthquakes Using the Predominant Period Derived From 1 Hz GPS Data. Geophysical Research Letters, 45, 517-526. doi: 10.1002/2017gl075816.

Qing Y, Lou Y, Dai X, Liu Y. (2017). Benefits of satellite clock modeling in BDS and Galileo orbit determination. Advances in Space Research, 60, 2550-2560. doi: 10.1016/j.asr.2017.03.040.

Ray J, Altamimi Z. (2005). Evaluation of co-location ties relating the VLBI and GPS reference frames. Journal of Geodesy, 79, 189-195. doi: 10.1007/s00190-005-0456-z.

Ray J, Kouba J, Altamimi Z. (2005). Is there utility in rigorous combinations of VLBI and GPS Earth orientation parameters? Journal of Geodesy, 79, 505-511. doi: 10.1007/s00190-005-0007-7.

Ray JR. (1996). Measurements of length of day using the Global Positioning System. Journal of Geophysical Research: Solid Earth, 101, 20141-20149. doi: 10.1029/96jb01889.

Rebischung P, Altamimi Z, Ray J, Garayt B. (2016). The IGS contribution to ITRF2014. Journal of Geodesy, 90, 611-630. doi: 10.1007/s00190-016-0897-6.

Rebischung P, Schmid R. (2016). IGS14/igs14. atx: a new framework for the IGS products. In:

AGU Fall Meeting 2016.

Ricklefs RL. (2009). Consolidated Laser Ranging Data Format (CRD) v101. In. The University of Texas at Austin / Center for Space Research.

Robertson DS. (1991). Geophysical applications of very-long-baseline interferometry. Reviews of Modern Physics, 63, 899-918. doi: 10.1103/RevModPhys.63.899.

Rothacher M, Angermann D, Artz T, Bosch W, Drewes H, Gerstl M, Kelm R, König D, König R, Meisel B, Müller H, Nothnagel A, Panafidina N, Richter B, Rudenko S, Schwegmann W, Seitz M, Steigenberger P, Tesmer S, Tesmer V, Thaller D. (2011). GGOS-D: homogeneous reprocessing and rigorous combination of space geodetic observations. Journal of Geodesy, 85, 679-705. doi: 10.1007/s00190-011-0475-x.

Rothacher M, Beutler G, Herring TA, Weber R. (1999). Estimation of nutation using the Global Positioning System. Journal of Geophysical Research: Solid Earth, 104, 4835-4859. doi: 10.1029/1998jb900078.

Rudenko S, Blossfeld M, Muller H, Dettmering D, Angermann D, Seitz M. (2018). Evaluation of DTRF2014, ITRF2014, and JTRF2014 by Precise Orbit Determination of SLR Satellites. IEEE Transactions on Geoscience and Remote Sensing, 56, 3148-3158. doi: 10.1109/Tgrs.2018.2793358.

Rudenko S, König R, Neumayer K-H, Raimondo J-C, Flechtner F. (2011). Earth Parameter and Orbit System - Orbit Computation (EPOS-OC) software - a tool for space geodesy research at GFZ. In: DORIS Analysis Working Group meeting (AWG) of the International DORIS Service, Paris, France.

Saastamoinen J. (1972). Atmospheric Correction for the Troposphere and Stratosphere in Radio Ranging Satellites. In: The Use of Artificial Satellites for Geodesy (eds S. W. Henriksen, A. Mancini and B. H. Chovitz). 247-251. doi: 10.1029/GM015P0247.

Schartner M, Bohm J. (2020). Optimizing schedules for the VLBI global observing system. J Geod, 94, 12. doi: 10.1007/s00190-019-01340-z.

Schartner M, Böhm J. (2019). VieSched++: A New VLBI Scheduling Software for Geodesy and Astrometry. Publications of the Astronomical Society of the Pacific, 131, 084501. doi: 10.1088/1538-3873/ab1820.

Schindelegger M, Böhm J, Salstein D, Schuh H. (2011). High-resolution atmospheric angular momentum functions related to Earth rotation parameters during CONT08. Journal of Geodesy, 85, 425-433. doi: 10.1007/s00190-011-0458-y.

Schmid R. (2009). Combination of VLBI and GNSS. Technical University of Munich.

Schmid R, Steigenberger P, Gendt G, Ge M, Rothacher M. (2007). Generation of a consistent absolute phase-center correction model for GPS receiver and satellite antennas. Journal of Geodesy, 81, 781-798. doi: 10.1007/s00190-007-0148-y.

Schön S, Brunner FK. (2008). A proposal for modelling physical correlations of GPS phase observations. Journal of Geodesy, 82, 601-612. doi: 10.1007/s00190-008-0211-3.

Schön S, Kutterer H. (2007). A comparative analysis of uncertainty modelling in GPS data analysis. 130, 137-142. doi: 10.1007/978-3-540-49350-1_22.

Schuh H, Moehlmann L. (1989). Ocean loading station displacements observed by VLBI. Geophysical Research Letters, 16, 1105-1108. doi: 10.1029/GL016i010p01105.

Seeber G. (2003). Satellite Geodesy. Walter de Gruyter.

Seitz M, Angermann D, Bloßfeld M, Drewes H, Gerstl M. (2012). The 2008 DGFI realization of the ITRS: DTRF2008. Journal of Geodesy, 86, 1097-1123. doi: 10.1007/s00190-012-0567-2.

Sekido M, Fukushima T. (2006). A VLBI Delay Model for Radio Sources at a Finite Distance. Journal of Geodesy, 80, 137-149. doi: 10.1007/s00190-006-0035-y.

Sekido M, Kondo T, Kawai E, Imae M. (2003). Evaluation of GPS-based ionospheric TEC map by comparing with VLBI data. Radio Science, 38, n/a-n/a. doi: 10.1029/2000rs002620.

Shi C, Gu S, Lou Y, Ge M. (2012). An improved approach to model ionospheric delays for single-frequency Precise Point Positioning. Advances in Space Research, 49, 1698-1708. doi: 10.1016/j.asr.2012.03.016.

Shi C, Zhao Q, Geng J, Lou Y, Ge M, Liu J. (2008). Recent development of PANDA software in GNSS data processing. In: Proc. SPIE 7285, International Conference on Earth Observation Data Processing and Analysis (ICEODPA), pp. 72851S.

Shrivastava MN, Gonzalez G, Moreno M, Soto H, Schurr B, Salazar P, Baez JC. (2019). Earthquake segmentation in northern Chile correlates with curved plate geometry. Sci Rep, 9, 4403. doi: 10.1038/s41598-019-40282-6.

Sillard P, Boucher C. (2001). A review of algebraic constraints in terrestrial reference frame datum definition. Journal of Geodesy, 75, 63-73. doi: 10.1007/s001900100166.

Snajdrova K, Boehm J, Willis P, Haas R, Schuh H. (2005). Multi-technique comparison of tropospheric zenith delays derived during the CONT02 campaign. Journal of Geodesy, 79, 613-623. doi: 10.1007/s00190-005-0010-z.

Soja B, Nilsson T, Karbon M, Zus F, Dick G, Deng Z, Wickert J, Heinkelmann R, Schuh H. (2015). Tropospheric delay determination by Kalman filtering VLBI data. Earth, Planets and Space, 67. doi: 10.1186/s40623-015-0293-0.

Sośnica K, Bury G, Zajdel R. (2018). Contribution of Multi-GNSS Constellation to SLR-Derived Terrestrial Reference Frame. Geophysical Research Letters, 45, 2339-2348. doi: 10.1002/2017gl076850.

Sośnica K, Jäggi A, Meyer U, Thaller D, Beutler G, Arnold D, Dach R. (2015a). Time variable Earth's gravity field from SLR satellites. Journal of Geodesy, 89, 945-960. doi: 10.1007/s00190-015-0825-1.

Sośnica K, Jäggi A, Thaller D, Beutler G, Dach R. (2014). Contribution of Starlette, Stella, and AJISAI to the SLR-derived global reference frame. Journal of Geodesy, 88, 789-804. doi: 10.1007/s00190-014-0722-z.

Sośnica K, Thaller D, Dach R, Jäggi A, Beutler G. (2013). Impact of loading displacements on SLR-derived parameters and on the consistency between GNSS and SLR results. Journal of Geodesy, 87, 751-769. doi: 10.1007/s00190-013-0644-1.

Sośnica K, Thaller D, Dach R, Steigenberger P, Beutler G, Arnold D, Jäggi A. (2015b). Satellite laser ranging to GPS and GLONASS. Journal of Geodesy, 89, 725-743. doi: 10.1007/s00190-015-0810-8.

Sovers OJ. (1994). Vertical ocean loading amplitudes from VLBI measurements. Geophysical Research Letters, 21, 357-360. doi: 10.1029/93gl02648.

Sovers OJ, Fanselow JL, Jacobs CS. (1998). Astrometry and geodesy with radio interferometry: experiments, models, results. Reviews of Modern Physics, 70, 1393-1454. doi: 10.1103/RevModPhys.70.1393.

Spicakova H, Wijaya D, Böhm J, Schuh H. (2011). Atmosphere loading in VLBI analysis. In: GGOS Unified Analysis Workshop, Zurich.

Springer T, Dilssner F, Escobar D, Flohrer C, Otten O, Svehla D, Zandbergen R. (2011). NAPEOS: The ESA/ESOC tool for space geodesy. The European Geosciences Union.

Steigenberger P. (2009). Reprocessing of a global GPS network. Technical University of Munich.

Steigenberger P, Montenbruck O. (2020). Consistency of MGEX Orbit and Clock Products. Engineering, 6, 898-903. doi: 10.1016/j.eng.2019.12.005.

Steigenberger P, Tesmer V, Krügel M, Thaller D, Schmid R, Vey S, Rothacher M. (2007). Comparisons of homogeneously reprocessed GPS and VLBI long time-series of troposphere zenith delays and gradients. Journal of Geodesy, 81, 503-514. doi: 10.1007/s00190-006-0124-y.

Štěpánek P, Filler V. (2018). Cause of scale inconsistencies in DORIS time series. Studia Geophysica et Geodaetica, 62, 562-585. doi: 10.1007/s11200-018-0406-x.

Sun J, Bohm J, Nilsson T, Krasna H, Bohm S, Schuh H. (2014). New VLBI2010 scheduling strategies and implications on the terrestrial reference frames. J Geod, 88, 449-461. doi: 10.1007/s00190-014-0697-9.

Sušnik A, Grahsl A, Arnold D, Villiger A, Dach R, Beutler G, Jäggi A. (2020). Validation of the EGSIEM-REPRO GNSS Orbits and Satellite Clock Corrections. Remote Sensing, 12, 2322. doi: 10.3390/rs12142322.

Svehla D, Flohrer C, Otten M, Springer T, Zandbergen R, Dow J. (2010). Instantaneous Reference Frame Realization by Means of Combination of Space Geodesy Techniques Onboard Jason-2 Satellite. In.

Teke K, Böhm J, Madzak M, Kwak Y, Steigenberger P. (2015). GNSS zenith delays and gradients in the analysis of VLBI Intensive sessions. Advances in Space Research, 56, 1667-1676. doi: 10.1016/j.asr.2015.07.032.

Teke K, Böhm J, Nilsson T, Schuh H, Steigenberger P, Dach R, Heinkelmann R, Willis P, Haas R, García-Espada S, Hobiger T, Ichikawa R, Shimizu S. (2011). Multi-technique comparison of troposphere zenith delays and gradients during CONT08. Journal of Geodesy, 85, 395-413. doi: 10.1007/s00190-010-0434-y.

Teke K, Nilsson T, Böhm J, Hobiger T, Steigenberger P, García-Espada S, Haas R, Willis P. (2013). Troposphere delays from space geodetic techniques, water vapor radiometers, and numerical weather models over a series of continuous VLBI campaigns. Journal of Geodesy, 87, 981-1001. doi: 10.1007/s00190-013-0662-z.

Teunissen PJG, Montenbruck O. (2016). Springer Handbook of Global Navigation Satellite Systems. Springer International Publishing.

Thaller D. (2008). Inter-technique combination based on homogeneous normal equation systems including station coordinates, earth orientation and troposphere parameters.

Thaller D, Dach R, Schmid R, Hugentobler U, Mareyen M, Richter B. (2009). The Bernese

GPS Software for the analysis of GNSS, SLR and VLBI data and for the SINEX/NEQ combination. In: Working Group on Combination at the Observation Level, Warsaw.

Thaller D, Dach R, Seitz M, Beutler G, Mareyen M, Richter B. (2011). Combination of GNSS and SLR observations using satellite co-locations. Journal of Geodesy, 85, 257-272. doi: 10.1007/s00190-010-0433-z.

Thaller D, Krügel M, Rothacher M, Tesmer V, Schmid R, Angermann D. (2006). Combined Earth orientation parameters based on homogeneous and continuous VLBI and GPS data. Journal of Geodesy, 81, 529-541. doi: 10.1007/s00190-006-0115-z.

Thomas ID, King MA, Clarke PJ. (2006). A comparison of GPS, VLBI and model estimates of ocean tide loading displacements. Journal of Geodesy, 81, 359-368. doi: 10.1007/s00190-006-0118-9.

Titov O. (2009). A new estimator for VLBI baseline length repeatability. Journal of Geodesy, 83, 1041-1049. doi: 10.1007/s00190-009-0322-5.

Titov O, Tesmer V, Boehm J. (2004). OCCAM v.6.0 Software for VLBI Data Analysis. In.

Uhlemann M, Gendt G, Ramatschi M, Deng Z. (2015). GFZ global multi-GNSS network and data processing results. In: International Association of Geodesy Symposia. Springer International Publishing, Cham, pp. 673–679.

Villiger A, Dach R, Schaer S, Prange L, Zimmermann F, Kuhlmann H, Wübbena G, Schmitz M, Beutler G, Jäggi A. (2020). GNSS scale determination using calibrated receiver and Galileo satellite antenna patterns. Journal of Geodesy, 94. doi: 10.1007/s00190-020-01417-0.

Wang J, Liu Z. (2019). Improving GNSS PPP accuracy through WVR PWV augmentation. Journal of Geodesy. doi: 10.1007/s00190-019-01278-2.

Wang J, Wu Z, Semmling M, Zus F, Gerland S, Ramatschi M, Ge M, Wickert J, Schuh H. (2019). Retrieving Precipitable Water Vapor From Shipborne Multi-GNSS Observations. Geophysical Research Letters, 46, 5000-5008. doi: 10.1029/2019gl082136.

Wang K, Rothacher M. (2013). Stochastic modeling of high-stability ground clocks in GPS analysis. Journal of Geodesy, 87, 427-437. doi: 10.1007/s00190-013-0616-5.

Wu JT, S.C.Wu, G.A.Hajj, W.I.Bertiger, S.M.Lichten. (1993). Effects of Antenna Orientation on GPS Carrier Phase. Manuscripta Geodaetica, 18, 91-98.

Wu X, Abbondanza C, Altamimi Z, Chin TM, Collilieux X, Gross RS, Heflin MB, Jiang Y, Parker JW. (2015). KALREF-A Kalman filter and time series approach to the International Terrestrial Reference Frame realization. Journal of Geophysical Research: Solid Earth, 120, 3775-3802. doi: 10.1002/2014jb011622.

Wu Z, Wang J, Liu Y, He X, Liu Y, Xu W. (2019). Validation of 7 Years in-Flight HY-2A Calibration Microwave Radiometer Products Using Numerical Weather Model and Radiosondes. Remote Sensing, 11, 1616. doi: 10.3390/rs11131616.

Xia Y, Liu X, Guo J, Yang Z, Qi L, Ji B, Chang X. (2020). On GPS data quality of GRACE-FO and GRACE satellites: effects of phase center variation and satellite attitude on precise orbit determination. Acta Geodaetica et Geophysica. doi: 10.1007/s40328-020-00324-2.

Xu MH, Anderson JM, Heinkelmann R, Lunz S, Schuh H, Wang GL. (2019). Structure Effects for 3417 Celestial Reference Frame Radio Sources. The Astrophysical Journal Supplement

Series, 242, 5. doi: 10.3847/1538-4365/ab16ea.

Yaya P. (2002). Apport des combinaisons de techniques astrométriques et géodésiques à l'estimation des paramètres d'orientation de la terre.

Yuan LG, Ding XL, Zhong P, Chen W, Huang DF. (2009). Estimates of ocean tide loading displacements and its impact on position time series in Hong Kong using a dense continuous GPS network. Journal of Geodesy, 83, 999-1015. doi: 10.1007/s00190-009-0319-0.

Zajdel R, Sośnica K, Bury G, Dach R, Prange L. (2020). System-specific systematic errors in earth rotation parameters derived from GPS, GLONASS, and Galileo. GPS Solutions, 24. doi: 10.1007/s10291-020-00989-w.

Zajdel R, Sośnica K, Dach R, Bury G, Prange L, Jäggi A. (2019). Network effects and handling of the geocenter motion in multi-GNSS processing. Journal of Geophysical Research: Solid Earth. doi: 10.1029/2019jb017443.

Zelensky NP, Lemoine FG, Ziebart M, Sibthorpe A, Willis P, Beckley BD, Klosko SM, Chinn DS, Rowlands DD, Luthcke SB, Pavlis DE, Luceri V. (2010). DORIS/SLR POD modeling improvements for Jason-1 and Jason-2. Advances in Space Research, 46, 1541-1558. doi: 10.1016/j.asr.2010.05.008.

Zhu S, Reigber C, König R. (2004). Integrated adjustment of CHAMP, GRACE, and GPS data. Journal of Geodesy, 78. doi: 10.1007/s00190-004-0379-0.

Zus F, Dick G, Dousa J, Wickert J. (2014). Systematic errors of mapping functions which are based on the VMF1 concept. GPS Solutions, 19, 277-286. doi: 10.1007/s10291-014-0386-4.

Appendix

A List of stations

The following tables provide the GNSS and VLBI station information used in CONT05–CONT17. The co-location information is given in Table A.1, and the receiver and antenna information of the GNSS stations used in CONT05-CONT17 is given in Table A.2.

Table A.1 Co-located VLBI and GNSS stations in CONT campaigns. For each co-located site the latitude, longitude, and ellipsoid height of the VLBI station are shown. For the co-located VLBI–GNSS stations, coordinate differences to the co-located VLBI station are shown in the north (dN), east (dE), and up (dU) components. The co-located stations with large coordinate differences are marked with "**bold**".

VLBI Site	CDP	Lat. (°)	Lon. (°)	Ell. (m)	Site Contributing to CONT Campaigns					
	GNSS	dN (m)	dE (m)	dU (m)	C05	C08	C11	C14	V17	C17
ALGOPARK	7282	46.0	281.9	224.0	X					
	ALGO	33.5	105.3	–23.1+0.1						
BADARY	7382	51.8	102.2	821.6			X	X		X
	BADG	–61.9	73.5	–10.2						
BR-VLBA	7614	48.1	240.3	250.5					X	
	BREW	33.3	48.0	–11.9						
FD-VLBA	7613	30.6	256.1	1606.4					X	
	MDO1	**5046.0**	**–6726.0**	**392.5**						
FORTLEZA	7297	–3.9	321.6	23.1			X	X		X
	BRFT	45.5	35.7	–1.4						
GILCREEK	7225	65.0	212.5	332.1	X					
	FAIR	–45.9	–81.4	–13.1+0.1						
HART15M	7378	–25.9	27.7	1409.4				X		X
HARTRAO[a]	7232	–1.5	112.9	6.3	X	X	X			
	HARB	**307.2**	**2303.2**	**148.3+3.1**						
	HRAO	–40.8	271.9	4.7+0.1						
HN-VLBA	7618	42.9	288.0	295.6					X	
HOBART12	7374	–42.8	147.4	41.0			X	X		
HOBART26[b]	7242	221.5	194.7	24.1				X		X
	HOB2	95.9	48.7	0.1						
KASHIM11	7334	36.0	140.7	62.3						X
	KSMV	–24.1	18.3	–4.7						
KATH12M	7375	–14.4	132.2	189.2				X		X
	KAT1	–59.4	97.2	–5.0						
KOKEE	7298	22.1	200.3	1176.6	X	X	X	X		X
	KOKB	–41.8	18.0	–9.2+0.1						
	KOKV	–41.8	18.0	–9.2+0.1						
KP-VLBA	7610	32.0	248.4	1902.0					X	
LA-VLBA	7611	35.8	253.8	1962.4					X	
MATERA	7243	40.6	16.7	543.4				X		X
	MAT1	–51.4	44.7	–8.8						
	MATE	–43.7	37.3	–7.7+0.1						
MEDICINA	7230	44.5	11.6	67.2		X			X	
	MEDI	–59.6	–9.6	–17.1						
MK-VLBA	7617	19.8	204.5	3763.0					X	
	MKEA	–3.3	–87.3	–8.4						

Table A.1 – continued from previous page										
NL-VLBA	7612	41.8	268.4	222.2					X	
	NLIB	18.5	–62.9	–15.2						
NYALES20	7331	78.9	11.9	87.4	X	X	X	X		X
	NYA1	49.5	–94.1	–3.1						
	NYA2	136.3	–237.2	–5.9						
	NYAL[d]	52.9	–98.8	–8.8+5.2						
ONSALA60	7213	57.4	11.9	59.3	X	X	X	X		X
	ONS1	–56.0	–109.0	–14.8						
	ONSA	–60.0	–50.5	–13.7+1.0						
OV-VLBA	7616	37.2	241.7	1196.3					X	
PIETOWN	7234	34.3	251.9	2364.7					X	
	PIE1	54.3	24.3	–17.0+0.1						
SESHAN25	7227	31.1	121.2	29.4					X	
	SHAO	53.3	74.7	–7.4						
SVETLOE	7380	60.5	29.8	86.0	X	X				
	SVTL	57.6	–58.5	–9.3						
TIGOCONC	7640	–36.8	287.0	170.9	X	X	X			
	CONT	–13.6	–20.8	2.5						
	CONZ	–115.9	–30.0	9.7						
TSUKUB32	7345	36.1	140.1	84.6	X	X	X	X		
	TSK2	269.7	–145.9	–14.8						
	TSKB	281.2	–111.6	–17.5						
WARK12M	7377	–36.4	174.7	127.9			X	X		X
	WARK	44.3	–42.6	–16.6						
WESTFORD	7209	42.6	288.5	86.8	X	X	X	X		
	WES2	43.0	38.4	–1.7						
WETTZELL	7224	49.1	12.9	669.1	X	X	X	X		X
WETTZ13N[c]	7387	–121.8	18.3	3.4					X	
	WTZA	–87.1	105.8	–3.2+0.1						
	WTZR	–90.1	106.3	–3.1+0.1						
	WTZS	–24.7	85.8	–5.7+0.1						
	WTZZ	–88.6	105.9	–3.2+0.3						
YARRA12M	7376	–29.0	115.3	248.2				X	X	
	YAR2	65.9	131.8	–6.9+0.1						
	YAR3	72.4	148.7	–5.8						
	YARR	62.0	131.5	–6.9						
YEBES40M	7386	40.5	356.9	988.9			X	X		X
	YEBE	26.0	–149.7	–16.2						
ZELENCHK	7381	43.8	41.6	1175.1		X	X	X		X
	ZECK	64.8	–7.9	–8.8						

Table A.2 Receiver and antenna types of GNSS stations co-located with VLBI telescopes in CONT05–CONT17. The information is derived from the GNSS station log files.

Station	Campaign	Receiver	Antenna
ALGO	CONT05	AOA BENCHMARK ACT	AOAD/M_T NONE
BADG	CONT11–CONT17	JAVAD TRE_G3TH DELTA	JAVRINGANT_DM JVDM
BREW	CONT17	ASHTECH UZ-12	ASH701945C_M SCIT
BRFT	CONT11–CONT17	LEICA GRX1200PRO	LEIAT504 NONE
CONT	CONT11	SEPT POLARX2	ASH700936E SNOW
CONZ	CONT05	JPS LEGACY	TPSCR3_GGD CONE
	CONT08	TPS E_GGD	Same as above
	CONT11	LEICA GRX1200+GNSS	LEIAR25.R3 LEIT
FAIR	CONT05	ASHTECH UZ-12	ASH701945G_M JPLA
HARB	CONT05	TRIMBLE 4000SSI	TRM29659.00 NONE
	CONT08–CONT11	ASHTECH UZ-12	Same as above
	CONT14–CONT17	TRIMBLE NETR9	TRM59800.00 NONE
HOB2	CONT14	LEICA GRX1200GGPRO	AOAD/M_T NONE
	CONT17	SEPT POLARX5	-
HARO	CONT05	ASHTECH Z-XII3	ASH701945C_M NONE
	CONT08–CONT11	ASHTECH UZ-12	ASH701945E_M NONE
	CONT14	ASHTECH Z-XII3	Same as above
	CONT17	JAVAD TRE_G3TH DELTA	Same as above
KAT1	CONT14	LEICA GRX1200+GNSS	LEIAR25.R3 LEIT
	CONT17	SEPT POLARX5	Same as above
KOKB	CONT05–CONT17	ASHTECH UZ-12	ASH701945G_M NONE
KOKV	CONT11	JPS EGGDT	ASH701945G_M NONE
	CONT14–CONT17	JAVAD TRE_G3TH DELTA	Same as above
KMSV	CONT17	TRIMBLE NETRS	ASH700936E SCIS
MAT1	CONT14	TRIMBLE 4000SSI	TRM29659.00 NONE
	CONT17	LEICA GR30	LEIAR20 NONE
MATE	CONT14	LEICA GRX1200GGPRO	LEIAT504GG NONE
	CONT17	LEICA GR30	LEIAR20 NONE
MDO1	CONT17	JAVAD TRE_G3TH DELTA	TPSCR.G3 SCIS
MEDI	CONT08	TRIMBLE 4000SSI	TRM29659.00 NONE
	CONT17	LEICA GR10	LEIAR20 NONE
MKEA	CONT17	JAVAD TRE_G3TH DELTA	JAVRINGANT_DM NONE
NLIB	CONT17	ASHTECH UZ-12	TPSCR.G3 SCIS
NYA1	CONT05–CONT08	AOA BENCHMARK ACT	ASH701073.1 SNOW
	CONT11–CONT17	TRIMBLE NETR8	ASH701073.1 SNOW
NYA2	CONT17	JAVAD TRE_G3TH DELTA	JAV_RINGANT_G3T NONE
NYAL	CONT05–CONT08	AOA BENCHMARK ACT	AOAD/M_B DOME
	CONT11–CONT17	TRIMBLE NETRS	AOAD/M_B DOME
ONS1	CONT17	TRIMBLE NETR9	LEIAR25.R3 LEIT

Table A.2 – continued from previous page				
ONSA	CONT05–CONT14	JPS E_GGD	AOAD/M_B	OSOD
	CONT17	JAVAD TRE_G3TH DELTA	AOAD/M_B	OSOD
PIE1	CONT17	JAVAD TRE_G3TH DELTA	ASH701945E_M	NONE
SHAO	CONT17		Same as above	
SVTL	CONT05–CONT08	LEICA SR520	LEIAT504	LEIS
TSK2	CONT05–CONT11	TRIMBLE 5700	TRM29659.00	DOME
	CONT14	TRIMBLE NETR9	TRM59800.00	NONE
TSKB	CONT05–CONT11	AOA BENCHMARK ACT	AOAD/M_T	DOME
	CONT14	TRIMBLE NETR9	Same as above	
WARK	CONT14–CONT17	TRIMBLE NETR9	TRM55971.00	NONE
WES2	CONT05	ROGUE SNR-8000	AOAD/M_TA_NGS	NONE
	CONT08	ASHTECH UZ-12	Same as above	
	CONT11–CONT14	LEICA GRX1200GGPRO	Same as above	
WTZA	CONT11–CONT14	ASHTECH Z-XII3T	ASH700936C_M	SNOW
	CONT17	SEPT POLARX2	Same as above	
WTZR	CONT05	TPS E_GGD	AOAD/M_T	NONE
	CONT08	LEICA GRX1200GGPRO	Same as above	
	CONT11	LEICA GRX1200+GNSS	LEIAR25.R3	LEIT
	CONT14	LEICA GR2	Same as above	
	CONT17	LEICA GR50	Same as above	
WTZS	CONT11–CONT14	SEPT POLARX2	LEIAR25.R3	LEIT
	CONT17	SEPT POLARX4TR	Same as above	
WTZZ	CONT05–CONT08	TPS E_GGD	TPSCR3_GGD	CONE
	CONT11–CONT17	JAVAD TRE_G3TH DELTA	LEIAR25.R3	LEIT
YAR2	CONT14	ASHTECH UZ-12	AOAD/M_T	NONE
	CONT17	SEPT POLARX4TR	Same as above	
YAR3	CONT14	LEICA GRX1200GGPRO	LEIAR25	NONE
	CONT17	SEPT POLARX5	Same as above	
YARR	CONT14	LEICA GRX1200PRO	LEIAT504	NONE
	CONT17	SEPT POLARX5	Same as above	
YEBE	CONT11–CONT17	TRIMBLE NETRS	TRM29659.00	NONE
ZECK	CONT08	ASHTECH Z-XII3	ASH700936D_M	SNOW
	CONT11–CONT17	JAVAD TRE_G3TH DELTA	JAVRINGANT_DM	JVDM

B EOP results of GNSS and VLBI single-technique solutions

The following figures and tables presents the GNSS and VLBI EOP estimates from single-session solutions, as discussed in Chapter 4.

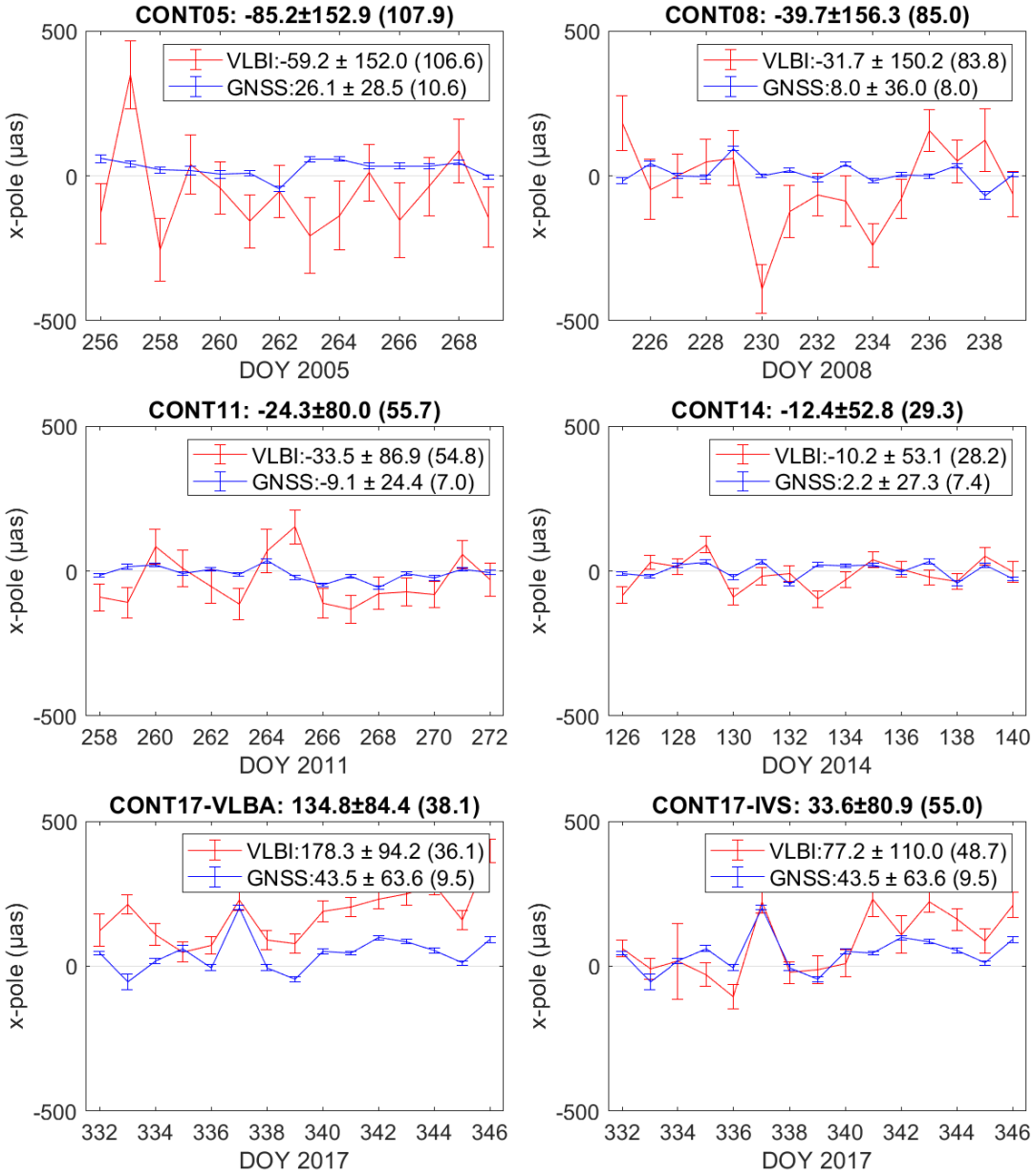

Figure B.1 Daily estimates of x-pole compared to the IERS EOP 14 C04 for GNSS (in blue) and VLBI (in red) and the corresponding uncertainty in CONT05–CONT17. The MEAN, STD, and formal errors (in parentheses) are shown in the legend. The MEAN and STD of the differences between GNSS and VLBI are shown in the title.

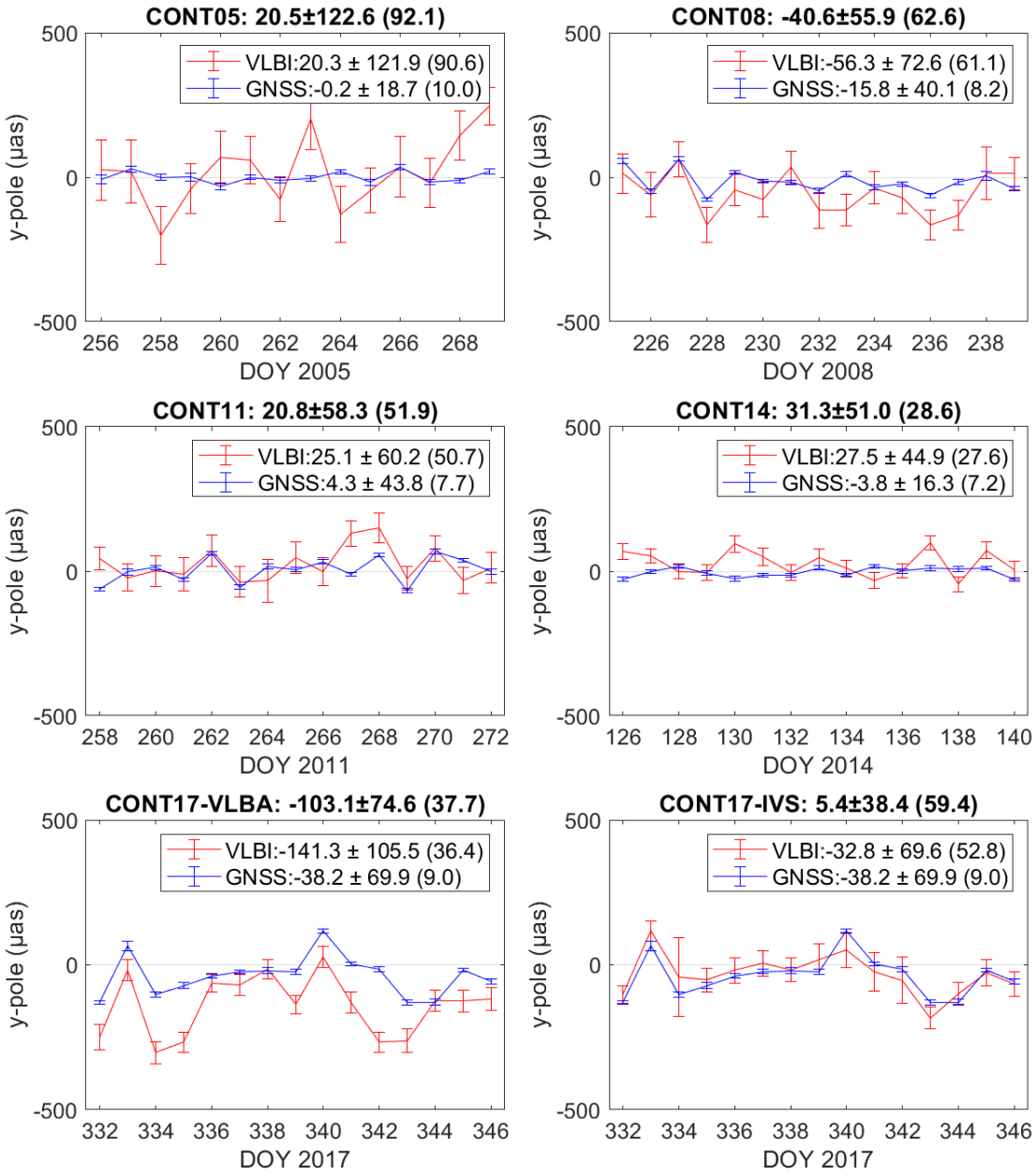

Figure B.2 Daily estimates of y-pole compared to the IERS EOP 14 C04 product and the corresponding formal errors for GNSS (in blue) and VLBI (in red) in CONT05–CONT17 campaigns. The MEAN, STD, and formal errors (in parentheses) are shown in the legend. The MEAN and STD of the differences between GNSS and VLBI are shown in the title.

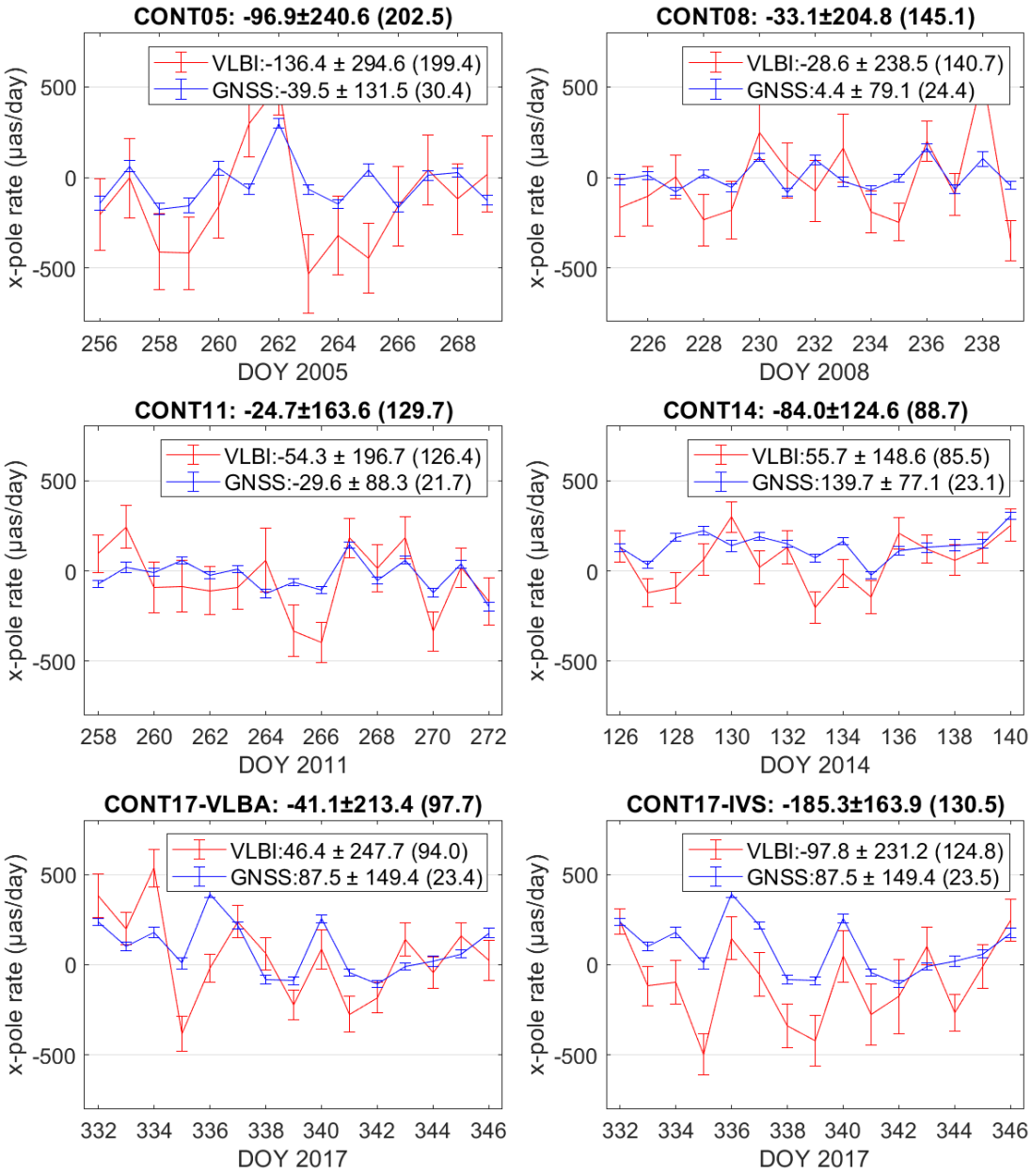

Figure B.3 Daily estimates of x-pole rate compared to the IERS EOP 14 C04 product and the corresponding uncertainty for GNSS (in blue) and VLBI (in red) in CONT05–CONT17. The MEAN, STD, and nominal uncertainty (in parentheses) are shown in the legend. The MEAN and STD of the differences between GNSS and VLBI are shown in the title.

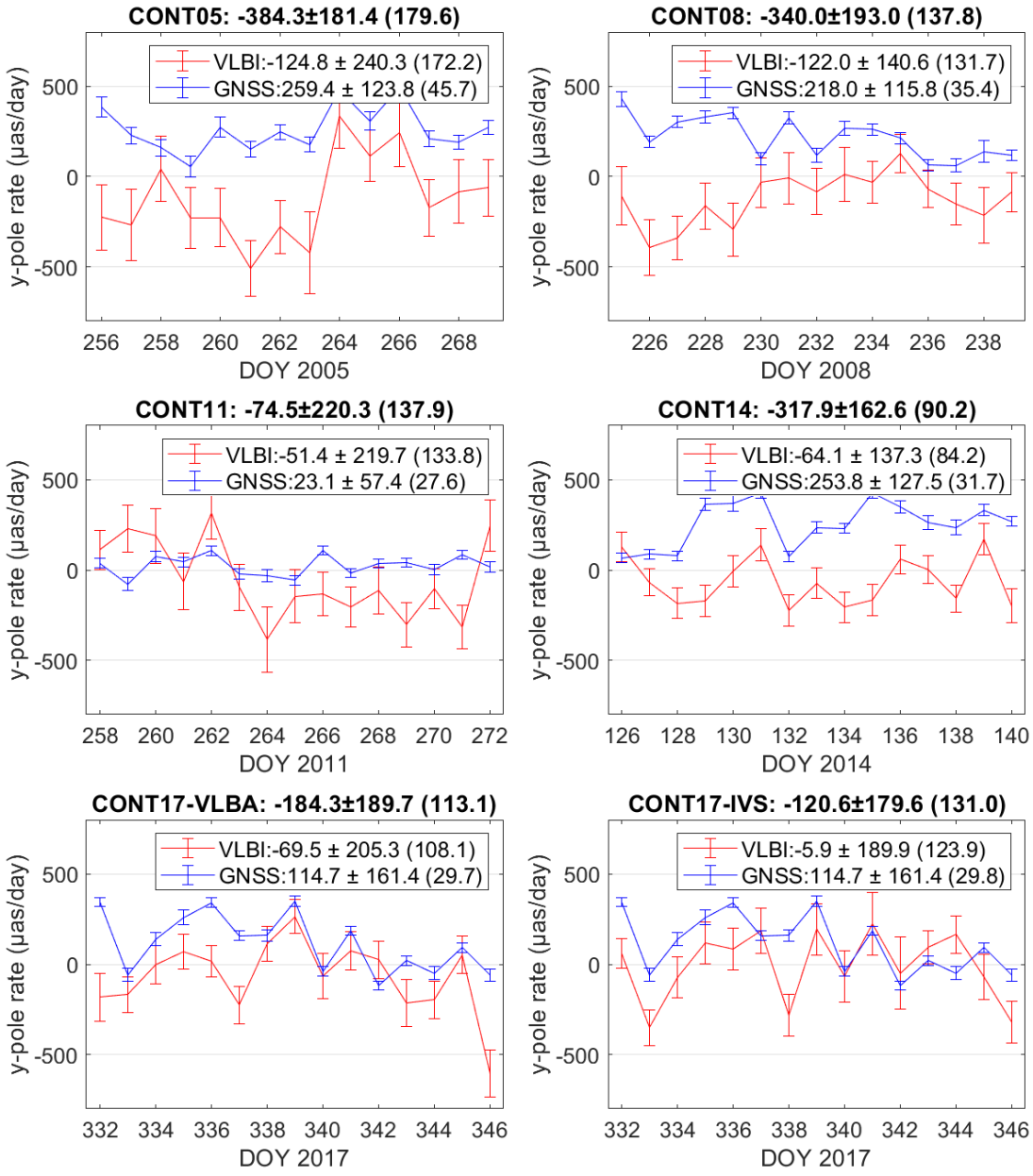

Figure B.4 Daily estimates of y-pole rate compared to the IERS EOP 14 C04 product and the corresponding uncertainty for GNSS (in blue) and VLBI (in red) in CONT05–CONT17. The MEAN, STD, and nominal uncertainty (in parentheses) are shown in the legend. The MEAN and STD of the differences between GNSS and VLBI are shown in the title.

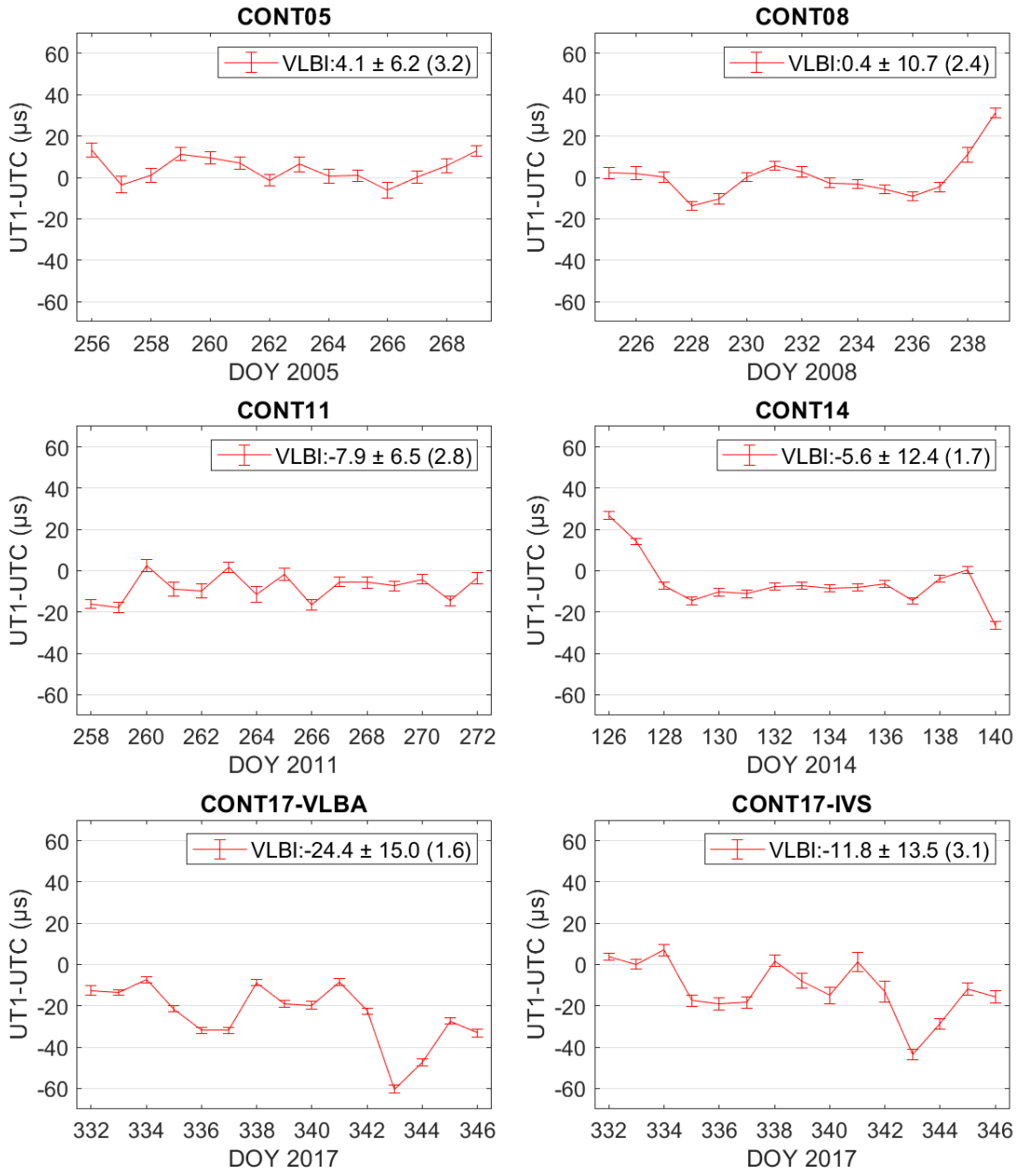

Figure B.5 UT1-UTC estimates of VLBI CONT campaigns compared to the IERS EOP 14 C04 product. The MEAN and STD values in each campaign are shown in the legend, and the value in parentheses shows the average uncertainty.

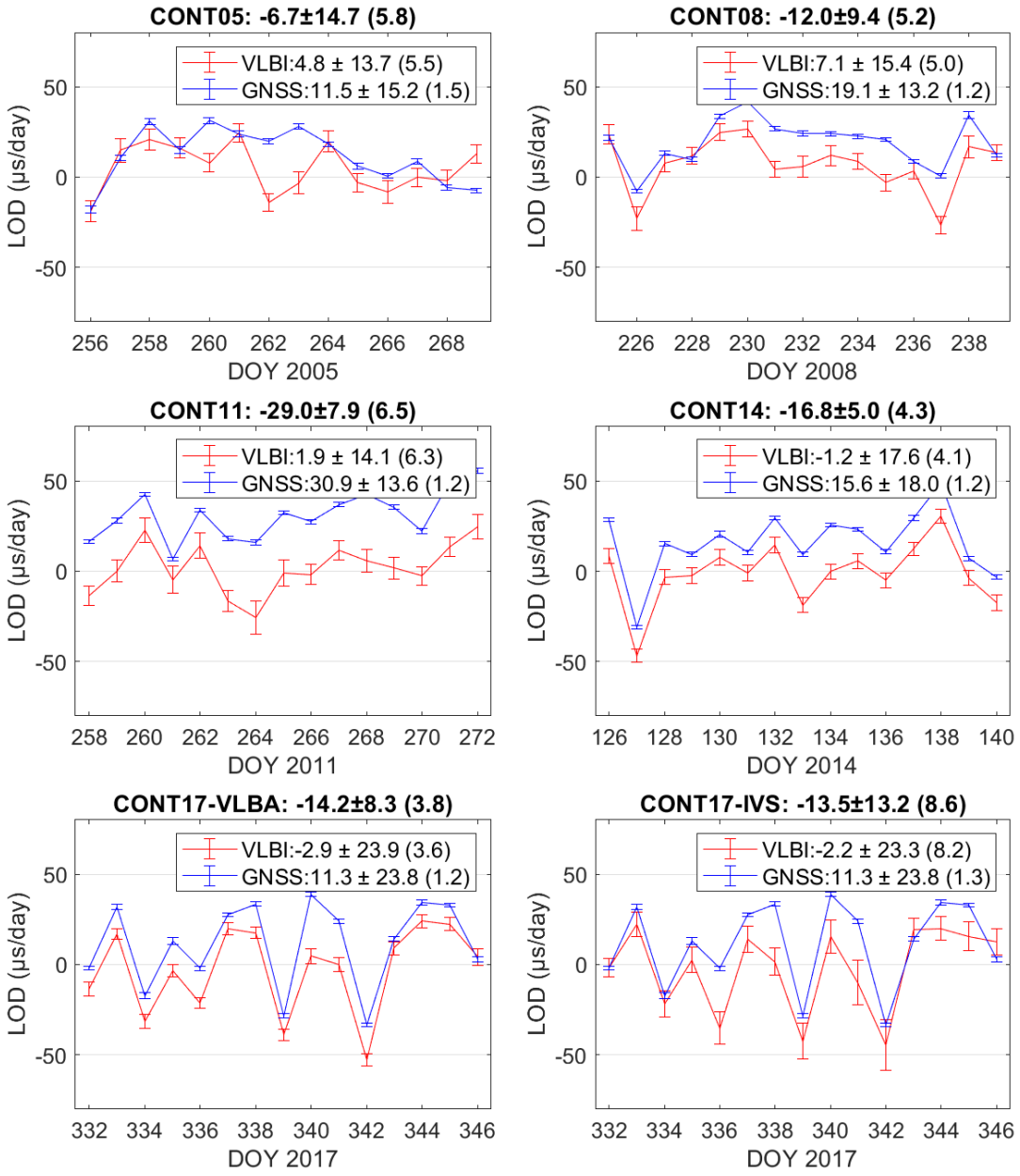

Figure B.6 LOD differences compared to the IERS EOP 14 C04 product and the corresponding uncertainty for GNSS (in blue) and VLBI (in red) in CONT05–CONT17. The MEAN, STD, and nominal uncertainty (in parentheses) are shown in the legend. The MEAN and STD of the differences between GNSS and VLBI are shown in the title.

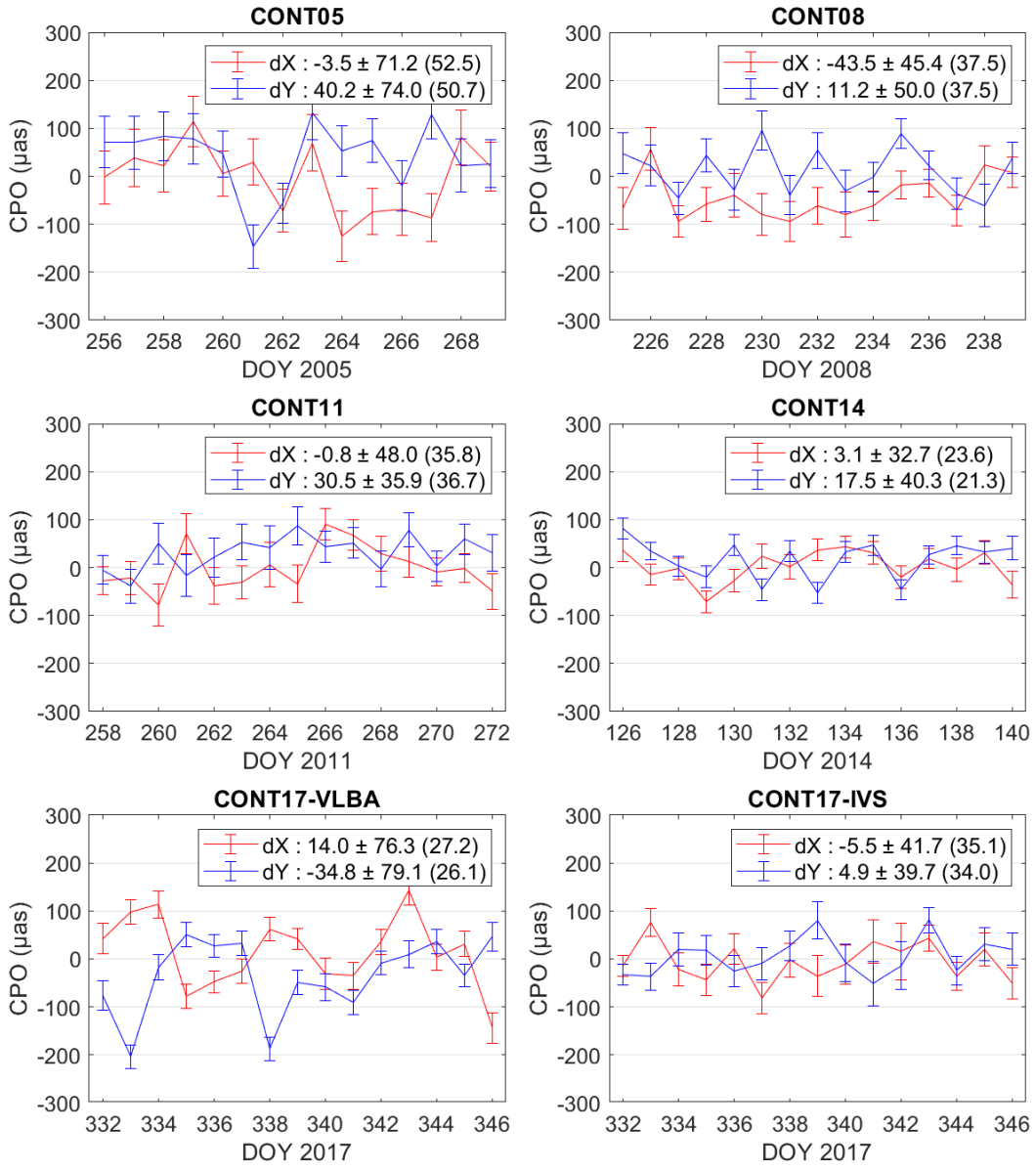

Figure B.7 Celestial pole offset estimates VLBI solution during CONT05–CONT17 compared to the IERS EOP 14 C04 product. The MEAN and STD are shown in the legend, and the number in parentheses shows the average uncertainty.

The following tables present the average values of the EOP comparison in all the CONT campaigns.

Table B.1 Average values of GNSS daily POD ERP WMEAN statistics compared to the IERS EOP 14 C04 product in CONT05–CONT17

EOP	rep	igs	co2	cf2	gf2	es2	gr2	mi2	jp2	em2
	Avg(abs(WMEAN))									
x-pole (µas)	15	23	14	47	47	32	18	13	19	24
x-pole rate (µas/day)	60	62	6	46	81	89	95	105	48	71
y-pole (µas)	13	7	26	25	20	19	31	26	17	28
y-pole rate (µas/day)	173	110	4	182	209	155	73	126	63	109
LOD (µs/day)	17.4	3.0	5.5	16.0	26.1	20.9	14.8	21.2	34.6	35.1
	Avg(WMEAN)									
x-pole (µas)	15	23	14	41	47	28	3	11	19	3
x-pole rate (µas/day)	33	31	5	–37	–57	–28	90	105	–30	–9
y-pole (µas)	–11	–6	23	25	14	–5	–31	–26	–15	–22
y-pole rate (µas/day)	174	110	–1	162	209	115	73	126	46	43
LOD (µs/day)	17.5	–0.6	5.0	16.0	26.1	20.9	14.2	21.2	34.6	35.1

Table B.2 Average values of GNSS daily POD ERP WSTD comparison between different GNSS solutions in CONT05–CONT17.

ACs	C04	rep	ig2	co2	cf2	gf2	es2	gr2	mi2	jp2	em2
	PM offsets (μas). Top left: x-pole, bottom right: y-pole										
C04		35	31	27	31	35	34	35	37	35	39
rep	36		22	25	27	27	24	26	29	30	31
ig2	35	22		21	21	22	17	19	15	19	21
co2	28	29	24		21	28	24	20	29	26	30
cf2	32	29	23	22		29	21	26	28	24	28
gf2	43	30	23	32	29		23	28	31	29	29
es2	35	26	14	26	24	25		24	24	23	27
gr2	36	23	17	24	27	30	18		26	26	32
mi2	42	28	14	31	31	30	21	24		25	27
jp2	36	28	21	30	28	27	24	26	28		29
em2	42	32	14	32	32	28	26	30	30	31	
	PM rates (μas/day) Top left: x-pole, bottom right: y-pole										
C04		102	90	84	98	118	108	104	102	149	155
rep	114		65	76	93	99	89	87	74	142	149
ig2	94	77		70	75	88	63	72	46	127	124
co2	90	99	82		91	110	92	85	85	154	148
cf2	119	112	89	115		119	75	103	93	146	146
gf2	163	149	115	159	133		114	104	119	145	148
es2	104	101	61	94	82	114		83	81	130	138
gr2	93	96	85	89	99	159	93		92	125	144
mi2	109	100	48	96	113	139	91	112		150	144
jp2	118	115	95	116	126	147	105	116	129		143
em2	113	118	79	104	110	133	90	109	103	99	
	LOD (μs/day)										
C04		16.1	17.0	14.6	15.7	17.1	16.9	13.5	16.0	14.7	18.6
rep			5.1	6.6	8.5	8.5	7.6	6.9	4.2	11.4	11.2
ig2				8.2	8.5	8.0	7.4	7.6	4.2	12.4	10.0
co2					8.3	7.5	7.8	5.3	7.0	10.7	11.8
cf2						7.2	6.9	7.6	9.3	12.4	11.5
gf2							5.8	7.9	8.9	12.0	11.3
es2								7.4	7.9	11.9	9.6
gr2									9.0	10.3	11.2
mi2										11.8	10.9
jp2											15.4

C Desciption of PANDA functions

The functions of the PANDA software are briefly explained in the following table. Note that only those mentioned in this thesis are presented.

Table C. 1 Description of selected PANDA software functions.

	Description	GNSS	VLBI	SLR
ambfix	Fixing the float ambiguity to integer	X		
ambchk	Check for the mis-fixed ambiguities	X		
clkfit	Fit the satellite or receiver clock time series, usually with polynomial function; check for the clock breaks for VLBI	X	X	
edtres	Check for the cycle slips and outliers for GNSS; check for the outliers, clock breaks, and baseline clock offsets for VLBI; check for the outliers, range and time biases for SLR	X	X	X
extclk	Extract the clock estimates from the PANDA internal file and output to the GNSS clock file format	X	X	
lsq	Least-squares adjustment	X	X	X
npt2rnx	Convert the SLR normal point files to the GNSS SINEX file format			X
oi	Orbit intergration, calculate the satellite orbit coordinate and partial derivatives of any time given the initial conditions	X		X
orbfit	Estimate the satellite orbit initial conditions given the reference orbit file; compare two orbits	X		X
precolc	Driver for integrated processing given the control information of individual technique, output the control file for integrated least-sqaures adjustment	X	X	X
preslr	Driver for the SLR data processing, output the control file, check the SLR observations files, satellite and station information			X
presrif	Driver for the GNSS data processing, output the control file, check the GNSS observations files, satellite and station information	X		
prevlbi	Driver for the VLBI data processing, output the control file, check the VLBI observations files, AGN and station information		X	
slr2log	Convert the SLR quality control information of station and observation to the PANDA internal file format			X
trimcor	Fix the clock jump in GNSS observation	X		
turboedit	Preliminary quanlity control for GNSS observations	X		

ISSN 2190-7110